Development of Micro-Computed Tomography Data Based Simulation Technique For Deformation and Strain Measurement of Densely Packed Electronics

by

Nakul Kothari

A dissertation submitted to the Graduate Faculty of
Auburn University
in partial fulfillment of the
requirements for the Degree of
Doctor of Philosophy

Auburn, Alabama
May 2, 2020

Keywords: Computed tomography, Finite Element Analysis, Electronics, Solder Joint, Void

Approved by

Dr.Pradeep Lall, Professor of Mechanical Engineering
Dr.Michael Zabala, Assistant Professor of Mechanical Engineering
Dr.Adil Bashir, Associate Professor of Electrical Engineering
Dr.Edmon Perkins, Assistant Professor of Mechanical Engineering
Dr.Vinamra Agrawal, Assistant Professor of Aerospace Engineering

Abstract

Rising pace of innovation and continuously increasing investments in research and developments has resulted in higher value added to each electronics equipment around us. This has also resulted in massive rise in demand in each segment of this industry. As of 2018, the semiconductor industry is the largest sector in the world, worth $248 billion. Growth of the consumer electronics industry can be largely accounted to miniaturization of the electrical components following the Moore's Law. This miniaturization and reduction in form factor has occurred in the electronics used in the defense sector as well and at a high cost. The proposed budget for the US Defense has gone from $574.5 billion in 2018 to $597.1 billion in 2019. The Air Force's procurement budget has increased by 5.9 percent from $47.73 billion in 2018 to $50.54 billion in 2019. A large part of this budget is annually allocated behind the research, development and procurement of missile or missile related technologies.

Constant efforts are made to maximize the life of the electronics used in the missiles and study the Remaining Useful Life of these electronics to improve the cost efficiency of the missile program. Improvements in maximizing the life of electronics or the remaining useful life, requires understanding of the current in-situ condition of the electronics used in these systems. This requires researchers be able to quantify and analyze the amount of deformations the small electrical sub-assemblies inside the systems may observe over its service life. This data can then be used to predict the

failure or analyze the extent of damage to predict and quantify its performance over its remaining life.

The existing popular methods used by the US Missile Command involves destructive testing of statistically representative selected samples of missile electronics which results in significant expensive. As per the Stockpile Recovery Program launched in 2015, performing simulations in of (mathematical models) has been cited as one of the ways to reduce the cost per unit of each missile and thus gain much required cost efficiency. This dissertation is thus on the development of non- destructive, non-invasive simulation and experimental techniques to quantify the deformation and strain occurring on the inside of the fuze electronics used in missile systems.

In this study the Author has used micro-computed tomography (micro-CT) data to make Finite Element models of a comprehensive fuze assembly and used the same micro-CT data to make experimental deformation measurements using a technique called Digital Volume Correlation.

Over the life cycle of a missile, the missile electronics are subjected to two categories of loading scenarios. One at the time of manufacturing and storage and other, during its service life. During manufacturing and storage, the electrical assemblies are subjected residual stresses left by the curing of potting thermoset resins or underfills and long hours of thermal aging during storage. During the service life, high-g and low-g mechanical shocks, vibration and sudden temperature changes are the most

common forms of loading experienced by missile electronics. In order to protect the electrical assemblies and components from these mechanical and thermal loads, they are often potted within thermoset adhesives. This design further makes the strain and deformation quantification more challenging as the electrical components and assemblies are hidden from the line of sight.

While current methods involve experimentation and testing on a sample set at intermittent stages during the life cycle of a missile, these methods are often destructive in nature. This study is based on use of micro-CT scan data to measure deformations and strains occurring on these electrical components, hidden from the line of sight due to protective adhesives. This is done using Finite element models (simulation technique) and use of micro-CT scan data based Digital Volume Correlation (experimental technique).

Conventional FE modeling approach is found to be prohibitively time consuming for modeling densely packed electrical assemblies. CAD modeling, assembly and meshing of numerous electrical components, big and small, with varied different material models is found to be the bottle neck and thus little to no literature exists on doing FE modeling of comprehensive fuze assemblies. This work involves development of a novel FE modeling strategy using micro-CT data to overcome the problem. An application of this technique would be to perform FE simulations of any field extracted electrical assemblies at any stage of its service life.

Digital Volume Correlation is a technique analogous to Digital Image Correlation for computing deformations and strains in a non-contact manner utilizing the voxel/pixel intensity data. This study reports on use of this technique to experimentally monitor the physical integrity of the electrical components by comparing two micro-CT scans and computing deformations and strains the components would have experienced over a particular time frame. A further application of this technique is explored by quantifying damage progression in the electronics as a function of time over the entire 3D domain on the assembly.

Chapter 1 gives a detailed introduction and literature review on the relevant topics. Chapter 2 denotes a brief introduction to X-ray micro-CT systems, micro-CT data and its usability. A detailed account of the simulation and experimental technique is given in Chapter 3. Chapter 3 also enlists case studies done to explore the capabilities of the technique developed. Chapter 4 and 5 are based on applications of the technique developed to investigate effect of voids in solder joints found in a popular electronic packaging in the present-day consumer electronics followed by Conclusions and Discussion in Chapter 6 and 7.

Acknowledgements

I am convinced that the research work I have done during my time at Auburn University is the best work I have produced in my career as a Mechanical Engineer so far. The decision to come to Auburn University is truly the best decision I have taken thus far in my professional career. I must acknowledge the ever so helpful Auburn Community; this includes every individual I have been in touch with during my time at Auburn. Somehow the place has always brought out the best version of people and this has brought out the best in me as well. The culture and environment at Auburn has truly motivated hard work, persistence, creation of knowledge, honesty and humbleness. I have grown as a person professionally and personally during my time at Auburn, Alabama and will proudly call Auburn my Home.

I would like to thank my elder brother for taking care of my parents ever so responsibly while I have pursued my career at Auburn University. This very act has allowed me to be in good spirits and keep my focus on my education and research work. I can never Thank my parents enough for affording me this opportunity and for always having shown nothing but unwavering support.

I have immense sense of gratitude towards Dr.Pradeep Lall, my Advisor. He has kept faith in me and given me opportunity to work on multiple projects. PhD work is not just about the knowledge creation through one's work but also much about the mental toughness one

must show to solve a problem. He has taught me this thoroughly and made me a much better engineer. His very approach towards going about his Job has taught me of self-belief, hard work, smart work, time management, being a good listener and a strong work ethic. He has truly given me a great platform to take my career to the next level and equipped me with the tools in plentiful.

I must acknowledge my Lab Mates who have always rooted for me, helped me and been in the trenches with me: Kalyan, Amrit , Vikas, Tony, Madhu, Ved, Jinesh, Vishal bhai, Aathi, and Kartik. I love you guys and can't really thank y'all enough. I want to mention a special sense of gratitude towards Shantanu Deshpande, Robin Muthukumar and Rohit Kanungo for their invaluable support, friendship and brotherhood. I have looked upto all three of you and glad to have y'all with me during my time at Auburn. I also wish to thank Jay Patel for being the best roommate and friend I could have asked for.

My PhD work has involved working with several experimental setups and Mr. John Marcell and Mr.Jason Smith have come out clutch all the time in getting the equipment setup. I wish to acknowledge Dr.Suhling and the Mechanical Engineering Staff and my PhD committee members for helping me out and enable be towards getting my Degree. I again wish to thank every individual stated above and many more I have not had a chance to mention above. Thank you!!

Table of Contents

List of Figures

Chapter 1 Introduction and Literature Review

1.1 Research Motivation

The reliability of the sophisticated electronics found inside any missile systems today is the key to rapid detection, tracking and interception of enemy targets. In recent times, these electronics have become much denser, complex and sophisticated. The missile systems are required to be launch ready at any given instant and also required to be highly reliable not only at delivery, but also after transportation, handling and 10 to 20 years of dormant storage in harsh environments worldwide [AMRDEC 2015]. Thus, there is a need to constantly assess the physical and electrical integrity of the sub- assemblies to ensure the mission readiness of these systems.

Some of the popular missile systems currently used by USA Department of Defense are the Hellfire missile which cost approximately $48,000. It is reported that the traditional way of reliability testing of these missiles cost from minimum $18, 8000 to maximum of $56, 4000. This involves testing of 12 samples from a monthly manufactured batch. Failure of 2 samples result in rejection of an entire batch [Howard 1997]. Thus, US Army Missile Command has started encouraging newer, better cost saving technologies for stockpile assessment of such missile systems.

Destructive forms of experimental testing result in sacrificing the sample and it still may only result in a binary response and fail to point towards the subtle cause of failure. Thus,

there is a need to develop non-destructive experimental techniques to detect failure and quantify damage. This would help save much cost without sacrificing the sample in testing. The experimental technique and the simulation technique mentioned in this study, is developed with a direct intent to aid the existing non-destructive experimental techniques currently used in this domain for intermittent assessment of physical integrity of the missile systems during their service life.

1.2 Overview of Missile Fuze

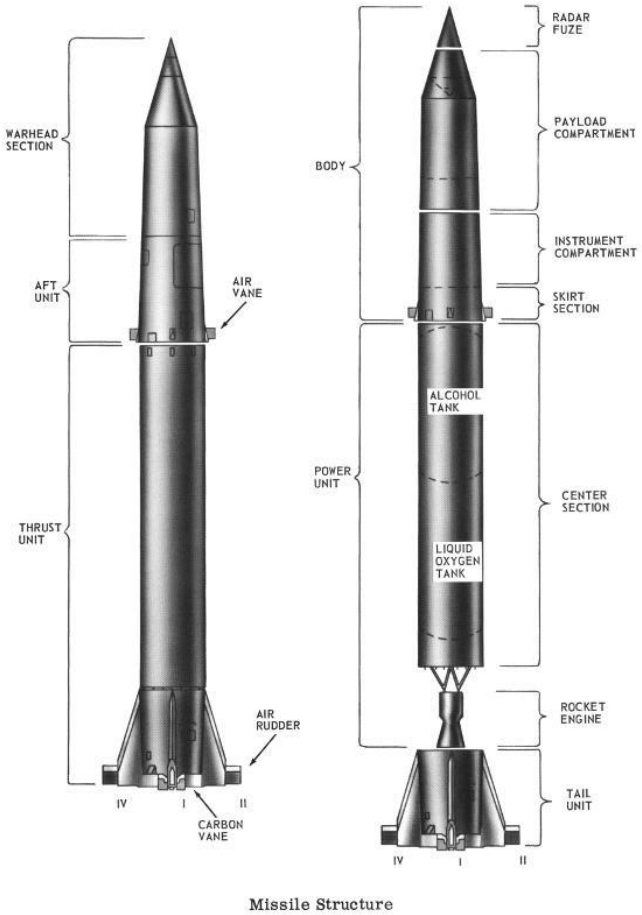

Figure 1: Missile Structure and location of fuze assembly [Department of Archive and Special Collection]

Figure 1 shows a general structure of a missile and location of the fuze assembly. A missile fuze is a subsystem of a missile that activates the warhead mechanism when it comes on the vicinity of the intended target. It is also responsible to keep the warhead in a safe condition during all prior phases of its service life. The fuze is thus utilized only once in its service life to activate the warhead. The fuze may undergo several years of service life after being deployed, from long times in missile storage silos undergoing thermal ageing to occasional low g, high g shocks experienced during personnel handling and logistics to vibration during pilot training missions to extreme temperature changes while being flown across continents. It is still expected to be functional, surviving all the above-mentioned harsh environments and perform its function in milliseconds when the missile is fired. In comparison, other missile sub systems like guidance systems may recover from transient malfunctions, target-tracking radars may experience numerous false alarms without significantly compromising their utility, and missile airframes may flex and recover, but the fuze-warhead process is singular and irreversible. The quality required of fuze designs is usually specified by two values: functional reliability, which ranges typically from 0.95 to 0.99 for complex missile fuzes and to 0.999 for projectile and bomb contact fuzes and safety reliability, for which a failure rate not greater than 1 in 106 must be proved prior to release of items for service usage [Fundamentals of Naval Weapons Systems].

1.2.1 Functions of a Fuze Assembly

As per the book “Fundamentals of Naval Weapons Systems” published by the Weapons and Systems Engineering Department, United States Naval Academy the following are the major functions of the fuze:

1. Keep the weapon safe: This is done by Safing and Arming device, a sub assembly of the fuze that makes sure that the warhead would not detonate until it has reached the target.
2. Arm the weapon: A warhead is meant to explode only of it is armed, the arming operation is done by different mechanisms in different types of fuzes.
3. Recognize or detect the target: This function is performed by a mechanical or electrical sensor that detects whether the target is close enough to be contained within the damage volume of the warhead.
4. Initiate the detonation of the warhead: A warhead usually contains a powerful but relatively insensitive high explosive that can only be initiated by the heat and energy from a primary explosive. The primary explosive is a component of the fuze subsystem and is normally loaded in the detonator.

1.3 Types of Fuze

Fuze types are broadly classified as Mechanical Fuze or Electrical Fuze.In this study an electrical fuze is used. Based on the working principle, they are further classified as follows:

1. Proximity Fuze
2. Time Fuze
3. Point detonating fuze
4. Delay Fuze
5. Command detonate fuze

The fuze type used in this study is electrical impact delay fuze named FMU143.

1.4 Working principle of an Impact Delay Fuze

1.4.1 Electrical Fuze Working Principle

Electrical fuzes in general can be activated either by means of a lanyard, or by means of electrical energy. If a fuze is electrically activated, the electrical signal can both be a source of energy and contain commands. An electrical pulse from the delivery aircraft charges capacitors in the fuze as the bomb is released from the aircraft. Arming and functioning delays are produced by a series of Resistor/capacitor networks in the fuze. The functioning delay is electromechanically initiated, with the necessary circuits closed by means of shock-sensitive switches. The electric fuze remains safe until it is energized by the electrical charging system carried in the aircraft. Because of the safety interlocks provided in the release equipment, electrical charging can occur only after the bomb is released from the rack or shackle and has begun its separation from the aircraft; however, it is still connected electrically to the aircraft's bomb arming unit. At this time, the fuze receives the energizing charge required for selection of the desired arming and impact times.

1.4.2 Working Principle of Impact Delay Fuze

Impact delay fuze are equipped with sensors, mechanical or electrical, meant to detect contact/impact and associated deceleration. Upon sensing the impact, a time delay circuitry is employed to ensure detonation after the missile may have broken the exterior hard structure of the target. FMU-143 is meant for hard shelled targets and example of this would be hard concrete bunkers. Fig shows image of an FMU143 impact delay fuze.

The FMU143 fuze is shown in Figure 2. It is of a cylindrical shape, 2.5 inches in length and 2 inches in diameter. From the X-ray imagery there are three board assemblies, held together by a skeletal structure through the periphery. The electrical components are mounted in a through-hole type mounting configuration. The entire electrical assembly is potted inside thermoset epoxy resin for protection from harsh environments. There are more than 50 parts, electrical components and mechanical components combined.

This device was chosen as the primary test vehicle because it is representative of a densely packed electrical assembly and in particular one that researchers or engineers do not make CAD models and FE models of owing to the prohibitively time-consuming efforts that would go into it.

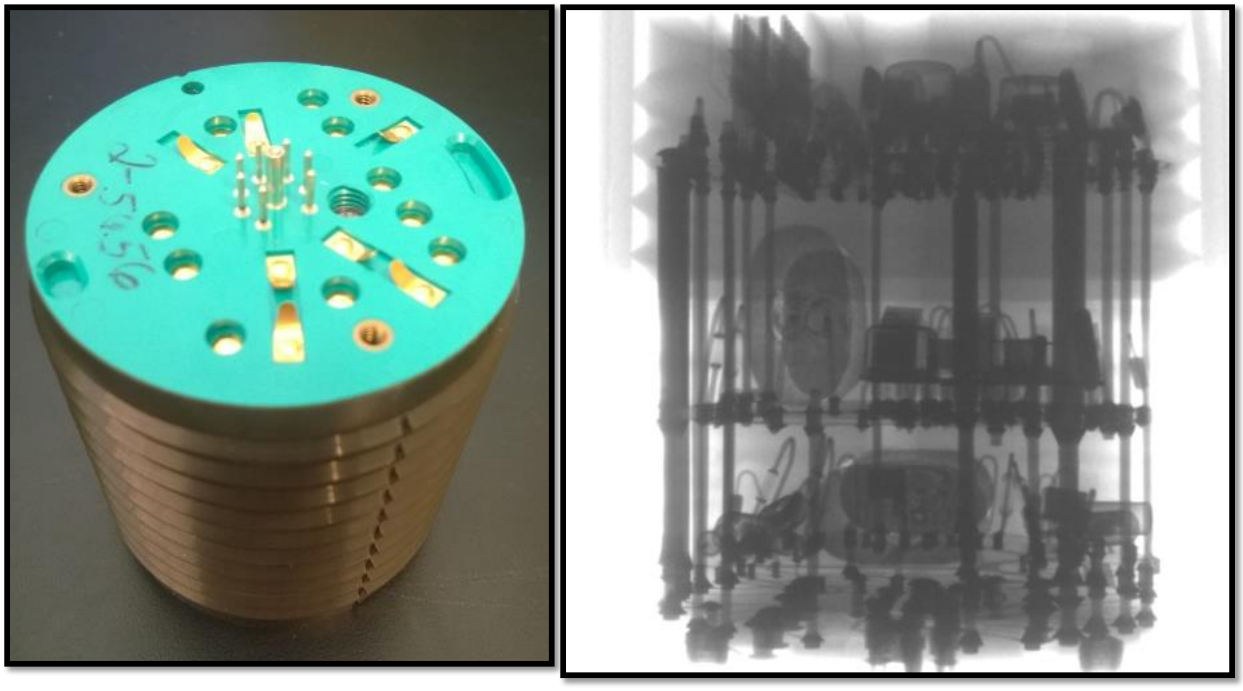

Figure 2: FMU143 fuze assembly

1.5 Life Cycle of a Fuze

Fuze assembly is subsystem of a missile and thus designed with shelf life of approximately 10 years or more. A typical fuze assembly used in a common missile system may undergo a series of harsh environments from the time of manufacturing to assembly, storage, launched, being armed and finally being detonated. The fuze assemblies are put into storage for long durations before being taken out on missions or practice runs. During the missions, they may or may not be fired, and if not fired, it may return back to storage before being deployed again. During this life cycle, it is subjected to thermal ageing, high g and low g mechanical shocks, vibrations, sudden temperature changes. The fuze electronics is always expected to be mission ready. In order to ensure that such a high value component remains fail safe, engineers often build in redundancy in the system by putting in back up circuitries, protective potting adhesives and other means to ensure the proper functioning of fuze electronics.

1.6 Overview of X-ray CT Scanners

CT scanners stand for Computed Tomography scanners. “Tomography” is a technique of representing cross sectional data of any object by means of x-rays or ultrasound or radio waves. An Italian radiologist named Alessandro Vallebona invented tomography in early 1900s. It used radiographic film to see a single slice of the body [Vallebona 1931]. This discovery came few decades after the discovery of X-rays by Wilhelm Röntgen. These two discoveries permitted seeing inside objects without literally opening them.

As and when computers gained more and more computational power, this field progressed further. In the late 1960s, Godfrey Hounsfield and Allan McLeod Cormack developed the

world’s first x-ray computed tomography system. A Nobel Prize in the field of medicine was awarded in 1979, for their contribution. The first clinical CT scan of a patient was taken at Atkinson Morley's Hospital, in London, England. The patient, a lady with a suspected frontal lobe tumor, was scanned with a prototype scanner, developed by Godfrey Hounsfield and his team at EMI Central Research Laboratories in Hayes, west London. The scanner produced an image with an 80 x 80 matrix, taking about 5 minutes for each scan, with a similar time required to process the image data. In comparison, the micro-CT scanner used in this study can record a 2048 x 2048 matrix in 97 minutes, thanks to the much-improved computational power today. Figure 3 shows the CT scanner that Godfrey Hounsfield and his team developed.

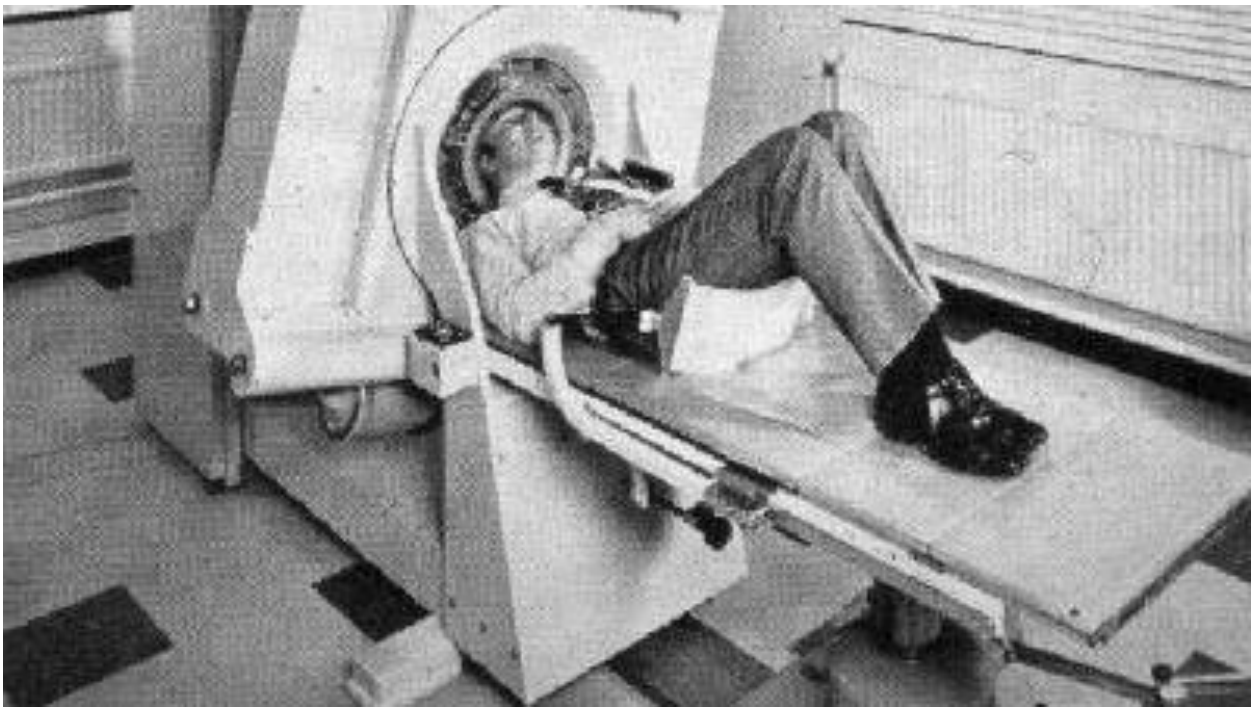

Figure 3: First CT scanner at Atkinson Morley’s Hospital [[impactscan.org]]

1.7 Overview of Image Reconstructions

Image reconstruction is a broad technique used to create a 3D image from a 2D image. For a 2D image, it is pixels that stores the grayscale intensity data that determines the characteristics of the image. Analogous to pixels for a 2D image, for a 3D image, it is the voxels that store the intensity data and determine resolution of the image. For a 2D image, the grayscale intensity of the pixel can range from 0 to 255 (8-bit image). For a 3D image, the voxels have gray scale intensity values ranging from 0 to 65535 (16 bit). In general, a 3D scan can be projected in to multiple 2D images. Thus, a 3D image is simply an intersection of multiple 2D images. Thus, a 3D image may be reconstructed from any technology that may produce a 2D pixel data, that is, X-ray, magnetic resonance imaging, ultrasound, optical microscopy or radio waves.

In standard images, the object may still overlap each other and thus the details in the 3rd dimension may be often hidden from the line of sight. Thus, it is not possible to reconstruct a 3D image with much accuracy using standard images. A workaround this problem would be to use, x-ray images. X-rays penetrate through the objects in its path and create a shadow with varying gray scales as per the amount of resistance given by the objects in its path to the passage of x-rays. It is this attribute of x-ray images that allows for successful 3D reconstruction of overlapping parts, like human body organs, tissues or organic matter.

1.8 X-ray and CT Scanning as a Non-destructive technique in Electronics Packaging

X-ray Computed Tomography technique is more advanced non-destructive technique as compared to other techniques like infrared-thermography, ultrasound, and X-ray imagery. It is capable of giving sub-micron scale resolution and slice by slice imagery enables complete inspections of electronic packages in a non-contact, non-destructive way. Previously researchers have implemented industrial 2D x-ray inspection techniques to locate defects in automobile engines [Izumi S. 1993], detection of defects in solder joints [Sumimoto T. 2002], inspection of electronic packages, wirebonds [Maur F, 2003; Kovacs R 2005] successfully. Automated solder inspection technique was developed using Artificial Neural Network trained algorithm, alongside 2D X-ray imaging [Teramoto A. 2007]. Real time X-ray radiography was coupled with reconstruction algorithms and 3D models of packages were reconstructed to find defects in solder joints [Oppermann M 2009, Tsuritani H 2011], evolution of phase growth in solder balls [Tsuritani H 2007]. In this study Computed Tomography is extensively used on system level electronics like Fuze devices and also on component level electronics like BGAs and QFN packages. The author has used the CT scan data acquired in a non-destructive way and further attempted to augment its utility into finite element modeling framework.

1.9 Conventional Finite Element Approach

The finite element method (FEM), is a numerical method for solving engineering problems of solid structures, civil structures, applied thermodynamic problems, heat transfer, fluid flow and also several other multi-physics types of problems. The finite element method formulation of the problem results in a system of algebraic equations that yield approximate values in comparison to results from close form solutions. The method subdivides a large problem into smaller, simpler geometry that are called finite elements. The simple equations that model these finite elements are then assembled into a larger system of equations that models the entire problem. FEM then uses variational methods to approximate a solution by minimizing an associated error function.

Conventional FE modeling approach requires the user to CAD model the geometry of the part. If it is an assembly, then multiple parts may be CAD modeled and assembled. The CAD model may then be imported to a FE modeling platform where these parts or assemblies are carefully meshed with a certain element type, namely a hexahedral element, shell element or tetrahedral element. Upon meshing, the model may be given the appropriate boundary conditions and loads and at this point the model would be ready to solve. Figure 4 below shows a process flow of the conventional FE modeling approach.

Figure 4: Conventional FE Modeling Approach

In this conventional approach we make several assumptions during the CAD modeling approach as follows:

1. There are no manufacturing defects in the part modeled
2. The part modeled represents an ideal geometry of the part without any dimensional tolerances
3. The part to be modeled has perfect symmetry

The assumptions stated above are sources of errors for a FE model results. This practice of using the conventional approach is most often used in the design stage and thus these sources of error are often considered as trivial and the variation in results are considered within the minimum error of the FE result.

1.10 Micro-CT Data Based FE Modeling Approach

In the medical industry, FE techniques have been used extensively. The unique and complex geometry of human anatomy has pushed researchers to use Computed Tomography (CT) or MRI scanned data to create FE models. Structural analysis on skeleton biomechanics using finite element methods has been much useful [Taddei 2006]. Researchers in the past have created hexahedron FE mesh from CT scanned data [Wei 2014]. Researchers in the past have used the Computed Tomography (CT) data of individual human body parts , for example bones, lungs, femur to perform FE simulations [Rahman 2009][Diemente 1991][Tao 2007] [Wei-Chun 1993].Finite Elements have been used to study human hand of a cadaver where the model was created using micro-CT data [Battula 2004]. Choy et al [Choy 2012] have studied the human skull using FE models created using the Micro-CT data and DICOM images. The biggest short coming in these finite element models is that they only involve one material type and do not have parts within other parts. Use of contact elements, multi point constraints or having nodes of the parts merged at the interface would be mandatory to model such assemblies.

In this study one of the primary objectives is to create an FE model of a part that is already manufactured, and field deployed. It may have been subjected to multiple harsh environments but still within the shelf life and acceptable performance standards. The part to be modeled may have been several years back and would have sustained deformations and strain but within acceptable performance standards. Fuze electronics are designed to have a shelf life of at least 10 years. Also, the part to be modeled has more than 50 electrical and structural components potted inside the resin. CAD modeling, assembly and meshing of these many parts is what makes the current approach prohibitively time consuming.

Ability to FE model the true as-is geometry of these high value electrical assemblies would give the ability to study how the assembly would behave in varied harsh environments treating keeping in consideration the true accumulated damage. The number of manufacturing defects that regularly occur in manufacturing, through-hole, surface mounting procedures are widely published upon. Ability to incorporate these defects in the FE model would add much fidelity and confidence in the FE modeling of these electronics. Figure 5 below shows the new process flow for the proposed method.

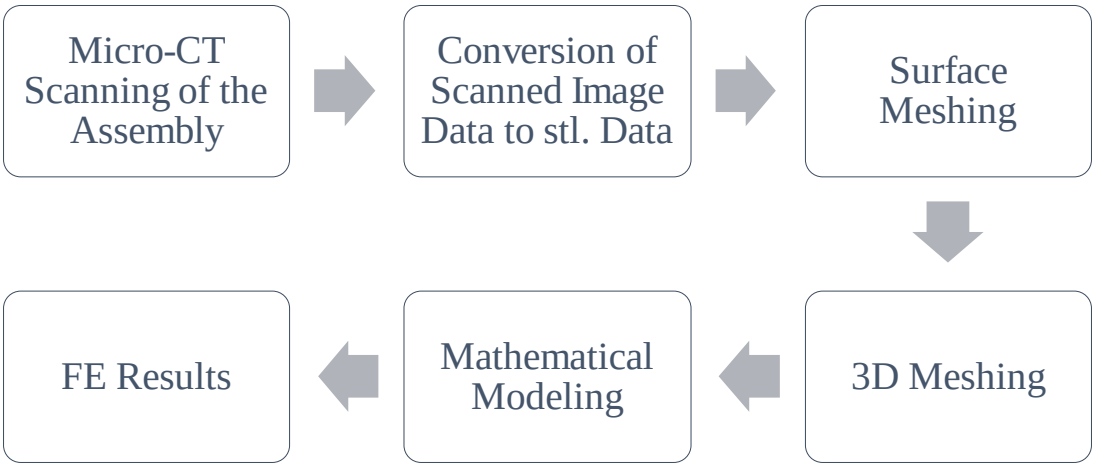

Figure 5: Proposed FE Modeling Approach

1.11 Digital Volume Correlation

Failure and damage in electronics can be detected by several existing non-destructive methods like x-rays, computed tomography, acoustic methods [Lall 2014][Ma 2005][Sakai 2016].Though these methods enable the researchers to accurately measure locate the failure location, it does not allow for measurement of deformations at the failure locations. Full field deformation measurement techniques like 2D Digital Image Correlation(DIC) and 3D Digital Image Correlation only help measure displacement on surfaces in the direct line of sight of the recording device used while the failure site is often on the inside if the component, not visible on the outer surface. In this case, the parts have to be cross sectioned to expose the failure sites and perform further deformation measurement techniques under various environments. Thus, the sample under test has to be sacrificed and may not be viable for any further experimentation and possible extended service life. In this study we have overcome this problem by using Digital Volume Correlation (DVC), capable of full field deformation in a 3D space. The technique uses micro-CT data of the scanned part under deformation for deformation measurements.

This technique has been previously demonstrated by the authors for ball grid-array assemblies [Lall 2015], [Lall 2016]. DVC has been used by researchers to measure strain and deformations over vertebrae [Tozzi 2016], [Palanca 2016] and trabecular bones [Gilliard 2014]. The method uses the gray scale values (in these case radio densities) of the x-ray image slices of the material being scanned to compute deformations and strains.

Much work has been done to study damage progression as a function of loading. Researchers have used finite element modeling to study damage progression in solder balls of BGA packages subjected to mechanical shock using input G method [Yamin 2011] and Energy Partitioning Damage Evolution model [Ladani 2010].Researchers have used Digital Image Speckle Analysis to study progression of deformations and strains in lead-free solder joints subjected to thermal cyclic aging [Luhua 2005]. The technique used in this study is a full field measurement technique and since it uses micro-CT data, it does not require cross sectioning to expose the region of interest or surface preparations to create gray scale values over region of interest.

Digital Volume Correlation (DVC) is a full field displacement and strain measurement technique analogous to 2D Digital Image Correlation (DIC), but computing displacements in a 3D space.

This deformation measurement technique is different with respect to strain gauge measurement technique, in a way that, this technique is capable of giving a full field

displacement or strain field. Use Strain gauge or Moire Interference techniques require surface preparation and still may only give strain values where the strain gauge is affixed.

Like Digital Image Correlation, selection of subset size and search volume governs the fidelity of the DVC solution. Subset size for DVC denotes a volume of pixel grid. Maximum search volume is the volume within which the displaced voxel can be found. Selection of a search volume size lesser than the resultant displacement would result in the faulty results as the displaced voxel would lie outside the search range, selection of a larger search volume would increase the solve times by a cubic relationship. The correct subset size was found by applying a known translational displacement to the fuze and computing that displacement by running DVC computations for various subset sizes.

In this study we have used this technique to experimentally compute the deformations and strains occurring in the fuze electronics when subjected to high g mechanical shock or an isothermal temperature load. This technique has been widely published on in the health care industry, where researchers use the CT scan data or the MRI scan data to compute deformation and strains on human body parts. In this study, an attempt has been made to use this technique to add to the existing capabilities of the technique, an ability to record damage progression in fuze electronics as a function of time. More details about this technique can be found in the Chapter 4.

1.12 Objectives

There are 6 main objectives to this study:

1. Develop a technique to convert the micro-CT scan data of the fuze electronics in to a finite element mesh
2. The resultant mesh must be compatible with Implicit and Explicit FE solvers
3. The resultant mesh must show good dimensional accuracy in comparison to the true dimensions
4. The technique must be applicable to different types of electronic packages, independent of shape, size and number of sub-components. This would allow for comprehensive FE modeling of any densely packed electronics in significantly less amount of time. It would also help account for the manufacturing defects and physical damage in the FE model, thus allowing FE modeling of any field extracted electronics.
5. Apply the developed technique to suitable problems in electronics packaging area. In this case, the author has applied the technique to study the effect of voids on thermos-mechanical reliability of solder joints.
6. Develop a methodology to record damage progression in electronics over its entire 3D domain as a function of time, using Digital Volume Correlation. The method developed would help monitor the physical integrity of the electronics at any instance during its service life. This would also give leading indicators of impending mechanical failure in electronics.

Chapter 2: X-Ray Micro-Computed Tomography

Computed tomography is a non-destructive tool capable of inspecting entire 3D domain of any structure, capturing features both external and internal. This attribute has made the CT scanners much useful and widely used in the industry for obtaining accurate geometrical information with very good accuracy. This chapter describes the principle of CT scanners,

the test setup that is used in this study, the raw data of the CT scanners and surface tessellation files (.stl files).

2.1 Computed Tomography Principle

CT scanners can be broadly classified in two types, an industrial CT system and a medical CT system. Irrespective of the type, every CT system has an x-ray source, a rotary chuck or a rotary table and an x-ray detector.

In a CT system, the X-ray source emits a series of x-rays at set voltage and current, which passes through the part to be CT scanned. Some of the x-rays are absorbed within the part, some get scattered and some get transmitted. The process of x-ray energy intensity reduction through its passage through the part is called x-ray attenuation. The attenuated x-rays do not reach the x-ray detector. The x-ray detector detects the x-rays reach it with varying intensities and uses this data to reconstruct a 3D geometry of the part. The gray scale of the voxels of this 3D scan thus represent the x-ray attenuation capability of the different regions of the part scanned. It is this attribute of the x-ray attenuation that can be exploited to detect the regions of interest in a scanned volume and convert into a surface tessellation file for creation of FE models. Figure 6 shows the schematic of the x-ray micro CT system.

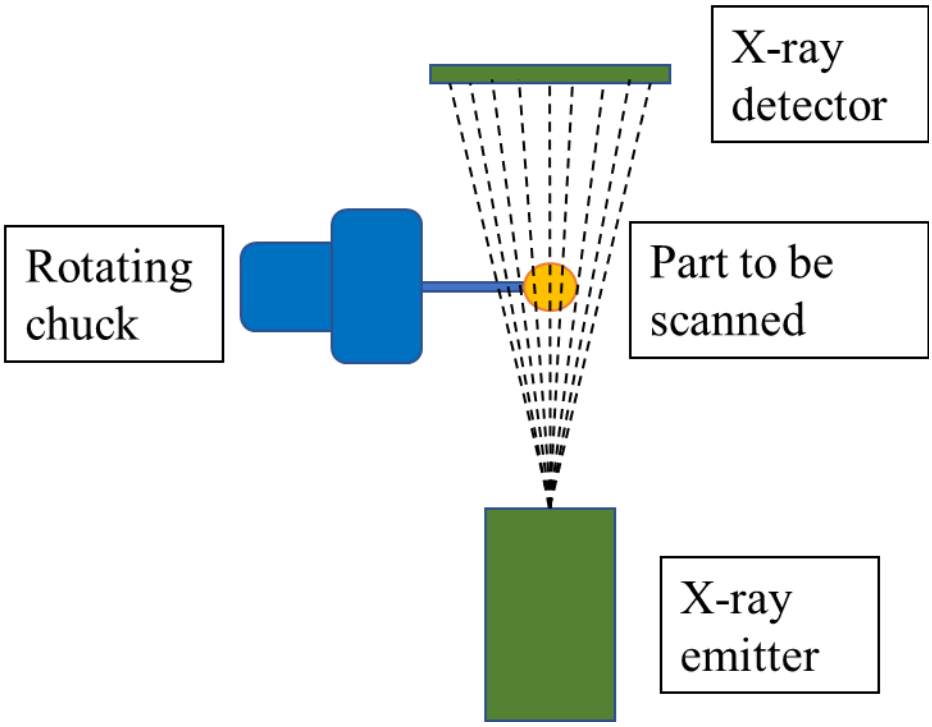

Figure 6: Micro CT Sytem Schematic

2.2 Comparison between Medical Grade CT scanners and Industrial CT scanners

This is an industrial Cone Beam CT system. In a medical grade CT system, the part is held constant and the emitter and the detector rotate, while an industrial CT system the part rotates, and the emitter and the detector are held constant.

Other notable differences in an industrial CT scanner and a medical grade CT scanner are in the material type it may be meant to scan, the applied energy and the resolution of the CT scanner. While the medical grade CT scanners have maximum applied energy less than 200KeV, the industrial CT scanners are found to have maximum applied energy up to 15MeV [Cantatore, 2011].

The resolution of the industrial CT scanners is found to be 10 to 50 microns, whereas the resolution of the medical CT scanners is found to be 1-2 mm. The industrial CT scanners can be further classified in to 4 types, depending on the achievable resolution:

1. Nano CT
2. Micro CT
3. Macro CT
4. Linear Accelerators

Shows a graph of achievable resolution with respect to measuring range.

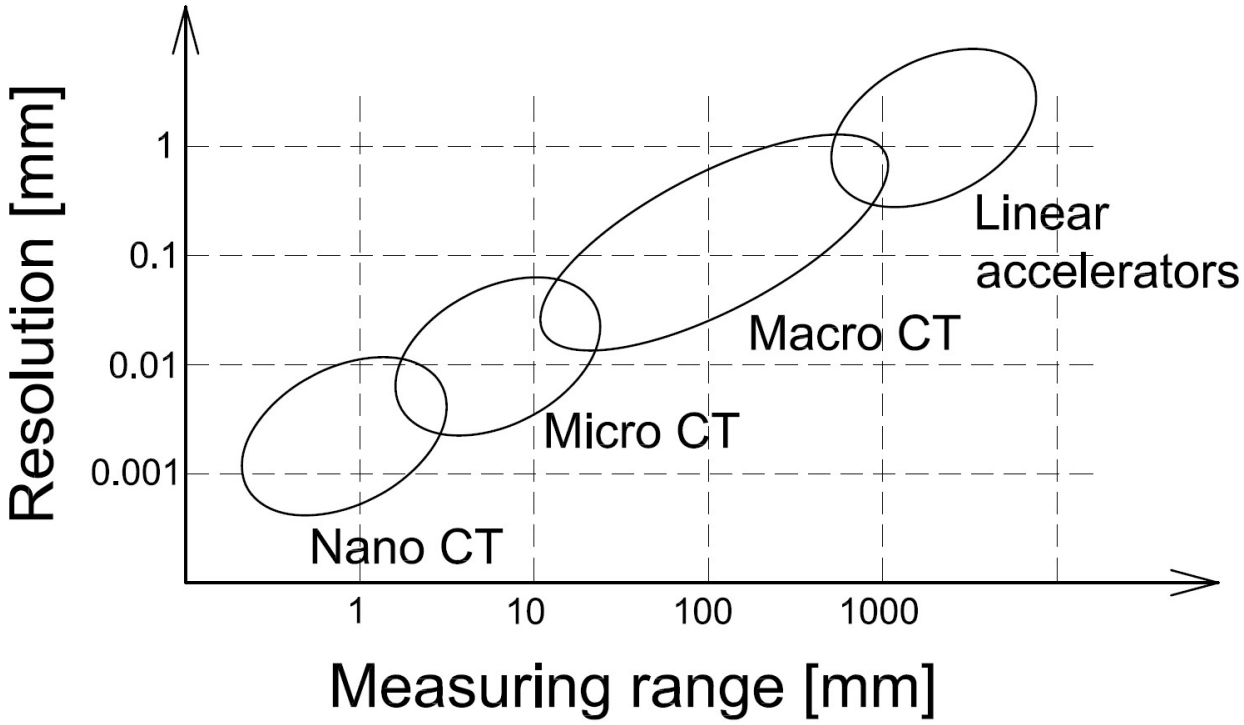

Figure 7: Achievable Resolution Vs Measuring Range [ASTM E1441 00:2005]

2.3 Basics of X-ray

The x-rays are electro-magnetic waves. X-rays are produced when an accelerated beam of electrons are retarded by a metal object. This target object most commonly is the anode. The electrons from a hot cathode hit the anode. Now, the cathode electrons interact with the orbital electrons of the anode, resulting in conversion of kinetic energy to thermal energy and electromagnetic energy. 98% of this energy is found to be the thermal energy. The resulting emission consist of Bremsstrahlung radiation and radiation that is related to

excess energy of the accelerated electrons. It is this excess energy that is emitted as photon of the x-ray with a constant peak value wavelength. This is often called Kα radiation. These spectrum peaks are different from material to material and thus also known as characteristic radiation [Cantatore 2011].

Energy of each photon in x-ray beam is determined as

$$\mathrm{E} = \frac{hc}{\lambda} \tag{1}$$

Here h = Plank's Constant,

c = speed of light,

λ = wavelength

2.4 Basics of X-ray Attenuation

When x-rays encounter any form of matter, they are partly transmitted and partly absorbed. It is found experimentally that:

$$I \propto x \tag{2}$$

Here I= Intensity of X-rays

x = distance

In differential form

$$\frac{-dI}{I} = \mu dx \tag{3}$$

Where μ = linear absorption coefficient

After integration

$$I_x = I_0 e^{-\mu x} \tag{4}$$

Here

I_0 =incident beam intensity

I_x = transmitted beam intensity

(4) states that for the x-rays passing through a part, the amount of x-ray energy transmitted after passing through the part is not only a function of the linear absorption coefficient, but also a function of the thickness of the part itself. This equation can be further modified to introduce the material density ρ.

$$I_x = I_0 e^{-(\frac{\mu}{\rho})\rho x} \tag{5}$$

The factor $\frac{\mu}{\rho}$ is known as the mass absorption coefficient or the mass attenuation coefficient. It is this coefficient that is commonly reported rather than the μ. This coefficient is a constant and is also independent of the physical state of the material, namely solid, liquid or gas. The mass absorption coefficient of the substance containing more than one element is a weighted average of the mass absorption coefficients of its constituent elements [Cantatore 2011].

2.5 CT Number

CT number is defined as relative comparison of x-ray attenuation of each voxel of material with an equal volume of water [Cantatore 2011].

$$CT\ Number = \frac{\mu_{material} - \mu_{water}}{\mu_{water}}\ 1000 \tag{6}$$

Here the CT number is expressed in Hounsfield units and μ is the attenuation coefficient of the x-ray beam. Vacuum has a value of -1000 HU and water has a value of 0 HU for reference.

CT number will be further utilized in this research to perform global thresh hold segmentation to selectively pick the regions of interests in a scan to be converted into a FE model.

2.6 X-ray Micro CT Equipment

In the NSF CAVE3 Research Labs at Auburn University, there is a YXLON Cougar Industrial Micro CT system. Shows the assembly lay out of the machine. There are overall cameras attached on the ceiling wall of the machine, X-ray Insulator, X-ray detector, tilt rotation arm for the detector, micro CT movable tray, X-ray generating tube, vacuum generator, vacuum pump, high voltage power supply and a control unit. The vacuum

system is used to maintain a vacuum in the x-ray generator tube. The x-ray generator tube has a carbon electrode as anode and a tungsten filament as the cathode.

Upon starting the x-ray generating sequence, one sets the voltage and the current through the YXLON FGUI software. A beam of electrons is generated having the user specified energy and intensity. This beam of electrons goes and hits the tungsten filament that serves as the cathode. Upon impact x-rays are generated through the x-ray emitter tube. The X-rays penetrate through the part to be scanned and come through the other side of the part and reach the detector. The sensors on the x-ray detector detect the x-rays of reduced energy and convert this data of the x-rays into signals that are now transmitted to the Micro CT reconstruction computer. There are two computers in the system, one for controlling the CT scan tray and the FGUI module and the other for reconstructing the raw data of the micro CT system. The CT reconstruction computer has large Random-Access Memory (RAM) and a graphic card to aid the computational process and support the graphic intensive Volume Graphics software. These two computers simultaneously exchange data during a CT scan to continuously store the raw data generated.

Figure 8: Micro CT System Layout (1)

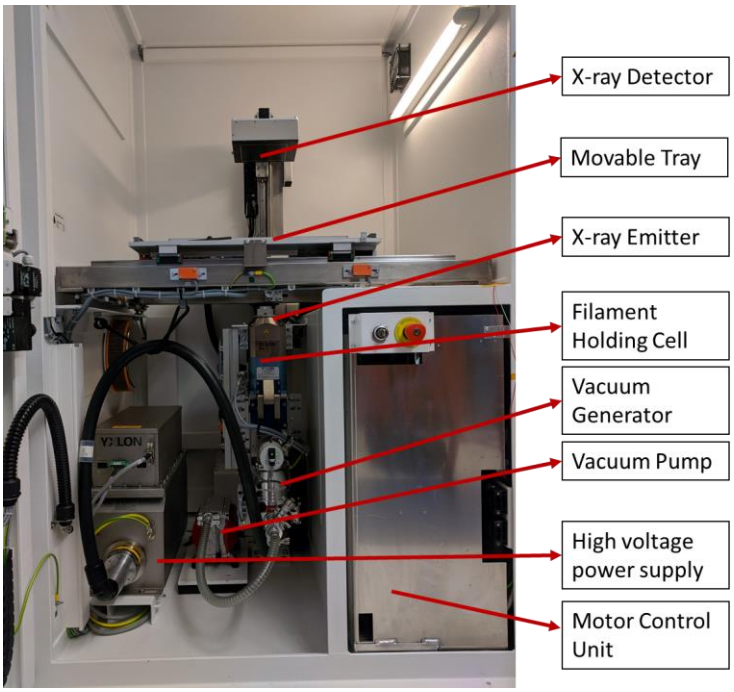

Figure 9: Micro-CT system Layout (2)

2.7 X-ray Micro CT Parameters

Micro CT system requires generation of x-rays at certain user specified parameters that directly affect the imaging quality and ability to seek out the details that the user wants. There are three attributes to a CT scan raw data that can be user adjusted.

1.Penetration Depth

2.Sharpness of Features

3.Resolution of Scan

These three attributes decide the quality of the x-ray image being recorded and eventually the quality of the CT scan. These three attributes can be adjusted by altering following four parameters:

1. Voltage
2. Current
3. Distance between emitter to part and part to detector
4. Number of images recorded
5. Part orientation

2.7.1 Voltage

Voltage at which the anode is maintained determines the energy spectrum of the x-rays. Higher the voltage, higher is the amount of energy per x-ray and thus higher is the penetration depth of the x-ray. Increasing the amount of energy per x-ray, increases the probability of the x-ray to get attenuated as it passes through the part and still traverse through the thickness and come out on the other side. Thus, for CT scanning or for x-ray inspection of parts with heavier element material composition, example, lead or mercury, and for parts with large thickness, the voltage needs to be increased.

Since increasing the voltage increases the penetration depth of the x-rays, increasing the voltage for the same part, beyond a limit results in loss of information. An x-ray image represents the attenuation it experienced per material part it passed through. Thus, increasing the voltage beyond a certain limit may result in trivial attenuation though certain relatively low radio density materials. Thus, this results in loss in details. This phenomenon becomes evident through a 'washed out' x-ray image. This can be observed in Figure 10 below. It can be seen that, the excess energy also reduces the dimensional accuracy of the features. Keeping the current very low may result in excessive attenuation through the par and this may give an excessively dark image.

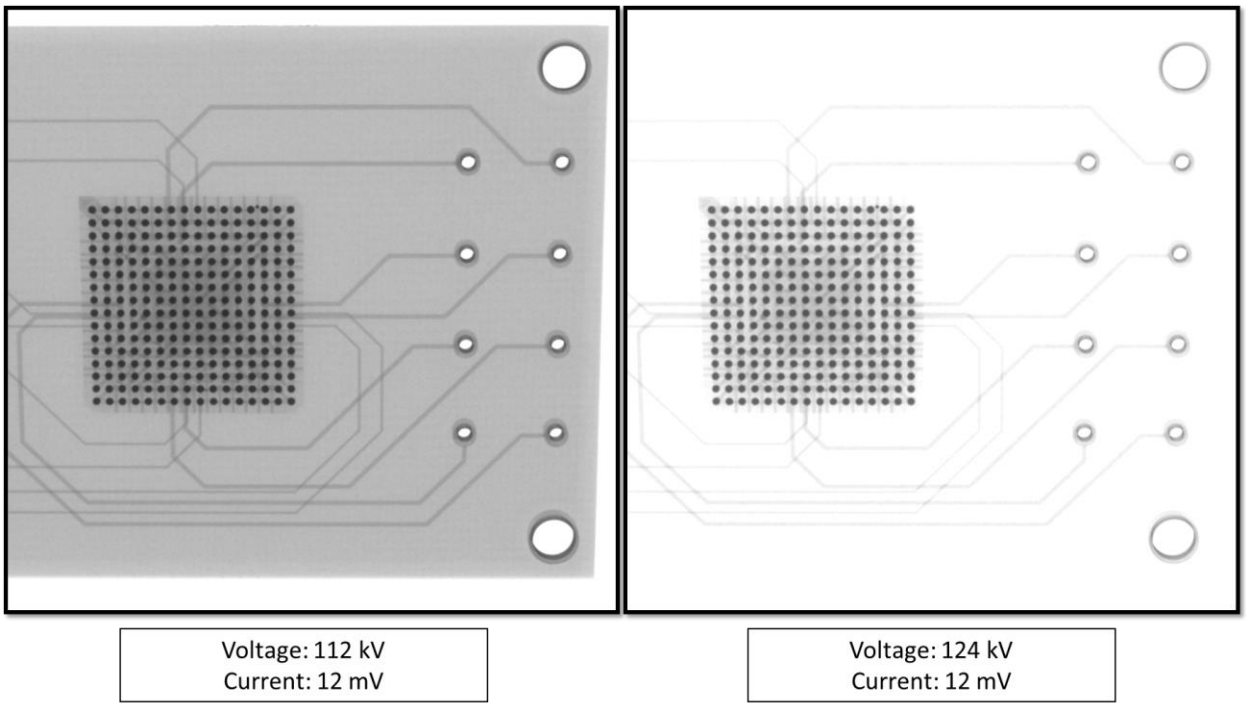

Figure 10: Difference in x-ray image quality on increasing voltage

2.7.2 Current

Current at which the anode is maintained, determines the sheer number of electrons forming the electron beam for x-ray generation. Increasing the current, increases the number of x-rays produced. An increase in x-ray density results in increased attenuation per volume and thus will result more features being recorded. Thus, increasing the current increases the sharpness of the x-ray image.

Similar to voltage, increasing the current beyond a certain limit results in washed out images and loss of dimensional accuracy. This can be seen in figure below. Keeping the current too low may result in fuzzy edges because of lack of details.

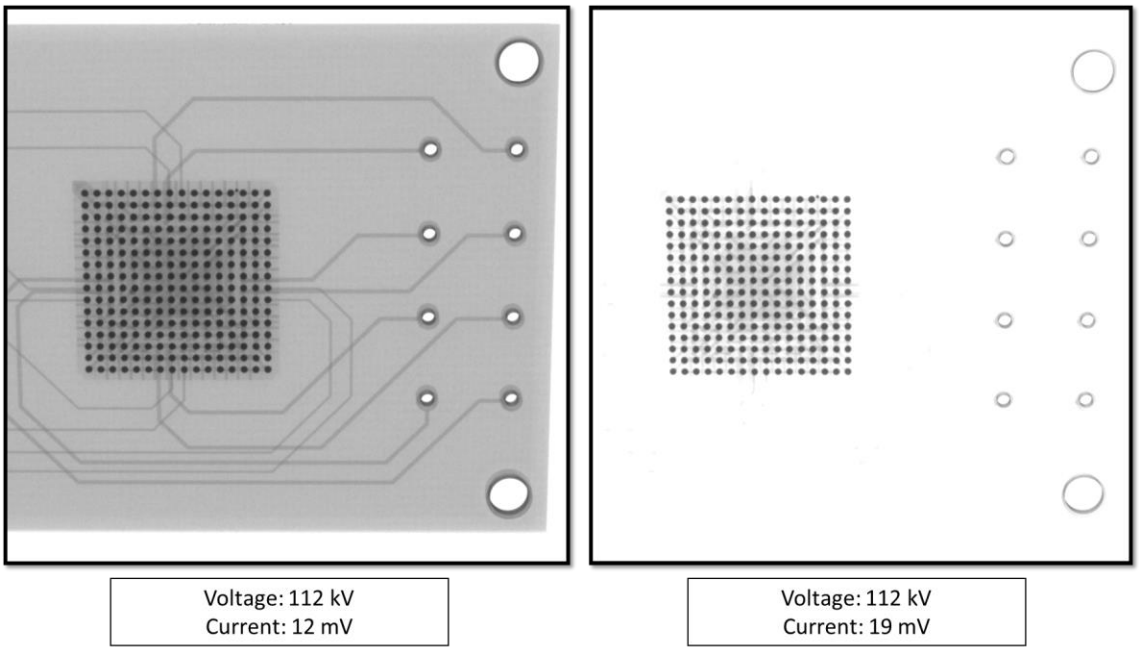

Figure 11: Difference in x-ray image quality on increasing current

Finding the optimum voltage and current requires the user to make measurements of a known feature size seen in the x-ray image and attempt to get as close as possible by a trial and error approach.

2.7.3 Distance between Emitter to Part and Part to Detector

The part to be scanned is always mounted on a horizontal three-point chuck in the YXLON Micro CT system. The Figure 12 shows the placement of part, emitter and detector. These two distances enable the user to zoom in and zoom out for the x-ray image being recorded. Thus, it directly helps determine the resolution of the scan. In the micro CT system, the part remains at a fixed position while the emitter and the detector may be moved up and down. As the emitter is brought closer to the part, the x-ray projection (shadow) formed on the backside will get scaled up resulting in a more zoomed in image and vice versa.

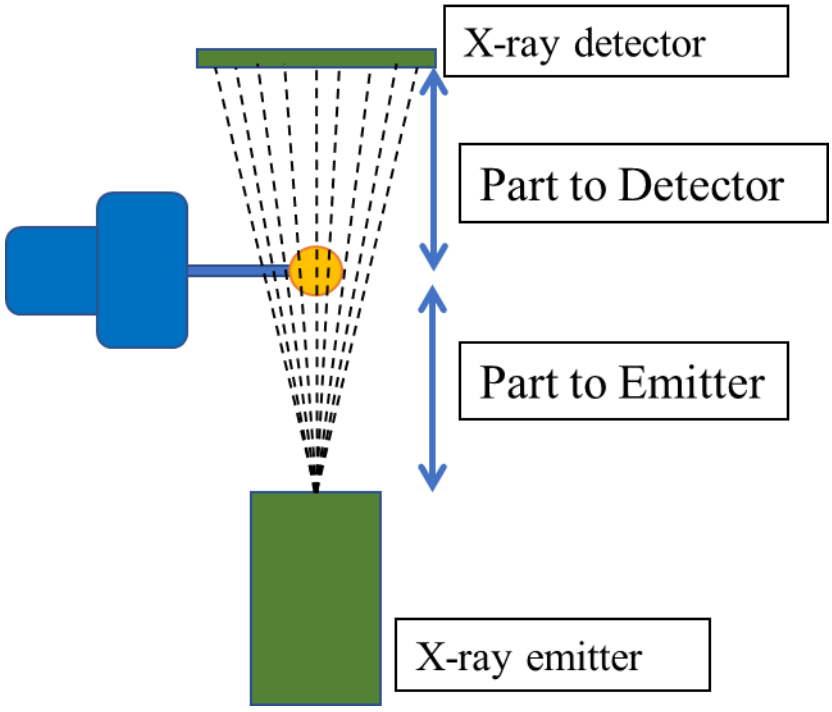

Figure 12: Distance between Part to Emitter and Part to Detector

2.7.4 Number of Images Recorded

The number of X-ray images recorded as the part rotates through 1 full rotation also determines the resolution of the scan. If 512 images are recorded through one full rotation, it translates to the dividing the entire 3D domain being scanned into 512 part along the three axes. Thus, the size of each unit cube within the scanned domain would be $(1/512)^3$. The edge length of this unit cube is the resolution of the scan and the cube itself is called a volume pixel or a voxel. Thus, recording more images per full rotation increases the resolution of the scan. The YXLON micro CT system has options for a 512, 1024 and 2048 scan configuration. As the number of images recorded increase, the resolution also increases by a factor of two. This increase in number of images also results in more computation time. The computation time increases by cubic factor.

2.7.5 Part Orientation

Depending on the geometry of the part, some features may get hidden behind others while the part is CT scanned. This may lead to those features appearing broken or sparse. This is because lack of enough x-ray energy to reach those regions and experiencing the attenuation before reaching the detector. An example of this is shown in figure (wirebonds). Right scan orientation is also very important for small electronic packages like Ball Grid Array (BGA). These packages have a square grid of solder ball. This repetitive geometry is also known to induce geometry reconstruction errors. Parts with repetitive geometry may, CT scanned with lesser number of images (512) is found to be much prone to these errors because of lack of clear boundary definition to compute the material vector flow in the geometry reconstruction algorithm.

2.8 The Raw Data of CT Scanners

2.8.1 Gray Scale Image

To detect the region of interest in an x-ray image, image segmentation algorithms are commonly used. All image segmentation algorithms utilize the gray scale data of the pixels in the image to detect the boundaries or cluster similar group of pixels or binarize the image. This gray scale data of the pixels can be imported into software like MATLAB or Python in the matrix form. A 3D matrix can be formed for a CT scan data. This 3D matrix contains slice by slice information of the scanned data with each layer storing the planar information of each slice that is one voxel apart. Figure 13 shows a cross section of a solder ball of a BGA package. In the Figure 13, gray scale values of each pixel are shown. The recorded images are 16bit unsigned integer type images. The gray scale values range from 0 to 65,536. The marked boundary represents the approximate border of the solder ball. The dark region is the solder ball and the bright white region is the surrounding material or in this case air. It is this pixel data at the periphery that is used by the image segmentation algorithm to differentiate between the background and the region of interest.

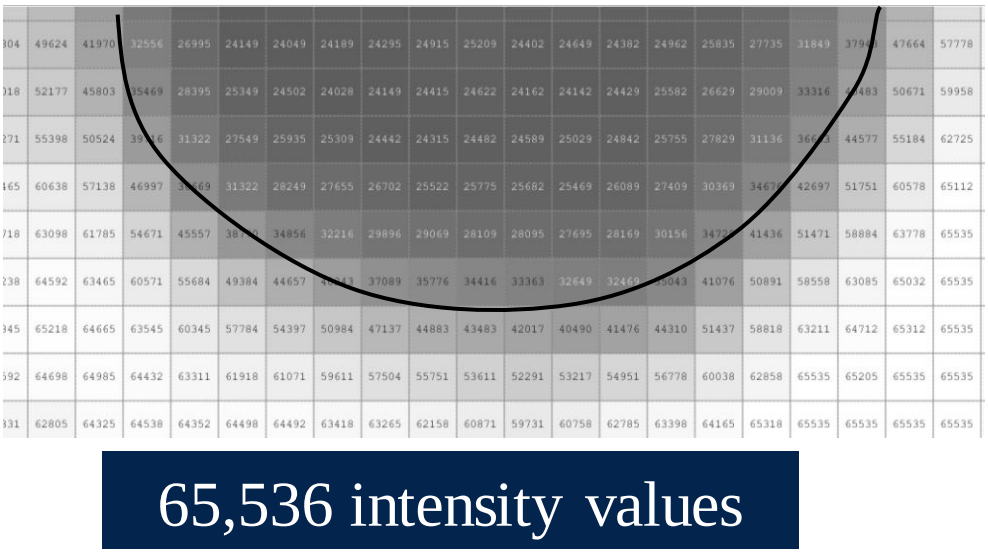

Figure 13: Pixel data of a solder ball

Typically, the voxel value uses the 16-bit unsigned form to save RAM space on the computer. More precise gray scale data can be obtained by using the 32-bit images, which range from 0 to 4,294,967,269.

2.8.2 DICOM Image Series

The gray scale data of the CT scanners is stored as a DICOM image data. DICOM is an acronym for Digital Imaging and Communications in Medicine. It is a current standard to store Medical Imaging data and a data structure type for storing medical data from MRI scanners or CT scanners or other similar systems. The YXLON Cougar CT scanner also stores the raw data as a DICOM data. Shows an example of a typical DICOM image series. The DICOM image series stores the x-ray images recorded as the part undergoes one full rotation.

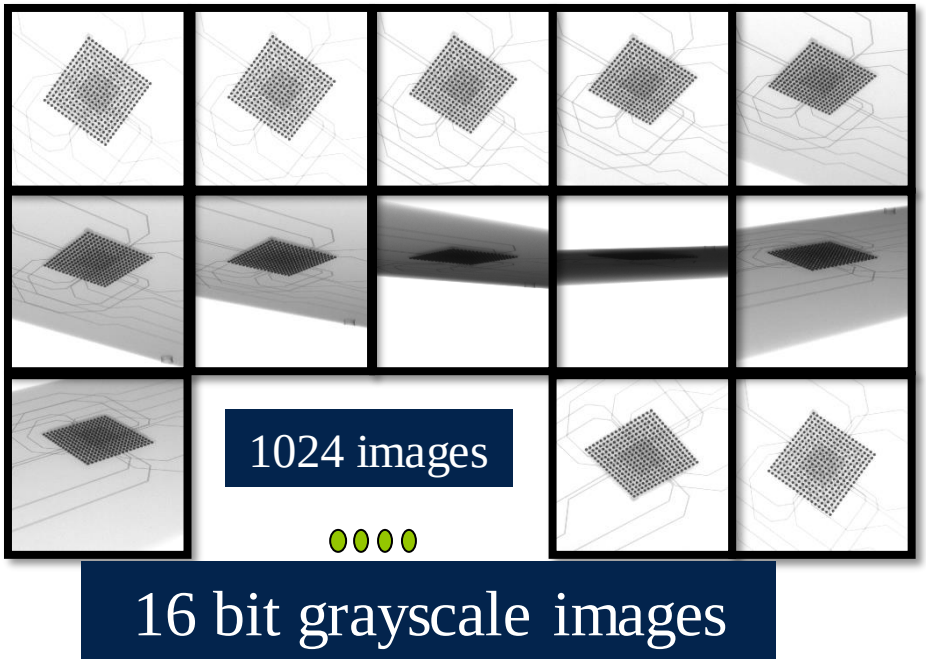

Figure 14: A DICOM image series

2.8.3 Gray Scale image Histogram

Figure 15 shows the x -ray image and its histogram. The x-axis shows the gray scale values of different regions of the object and the y -axis shows the y-axis shows the number of voxels of that region for that gray scale value. Higher the grayscale value denser the part is. Different gray scales windows with corresponding materials are marked in the figure. The right most window designates the highest density material, solder balls. This is followed by the surrounding the PCB board and copper vias and finally the surrounding air and fixture. As we can see from the image, the most abundant material in the image is the air, followed by the PCB, followed by the solder balls. This is corresponding to the y-axis data for each material in the histogram.

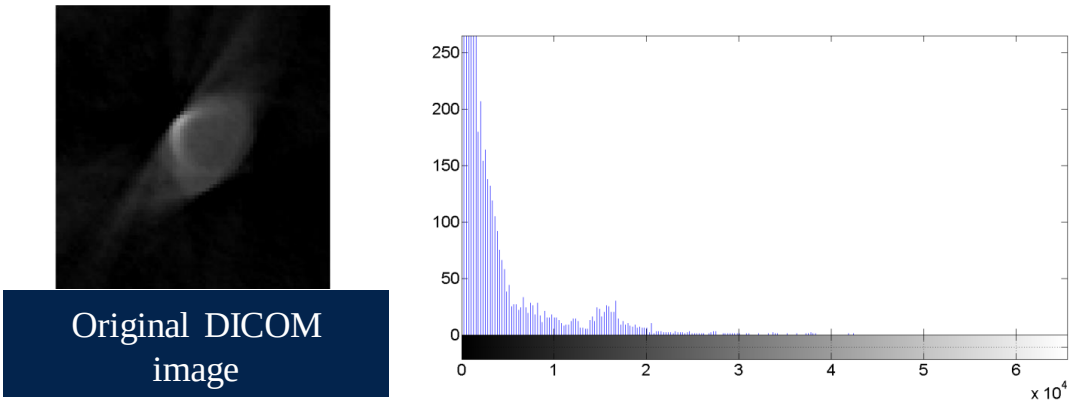

Figure 15: Histogram of a DICOM Image

2.9 Voxels and ISO Surfaces

The gray scale images of the data are unique to each voxel. The voxel represents a gray scale value in a 3D grid. Each voxel represents the x-ray density property of the CT scan. Since the x-rays loose energy as it passes through an object, air shows up as low-density material relative to everything else. Analogous to this, the voxel values of any solid part are found to be lesser on the surface with respect to the values found on the inside of the part.

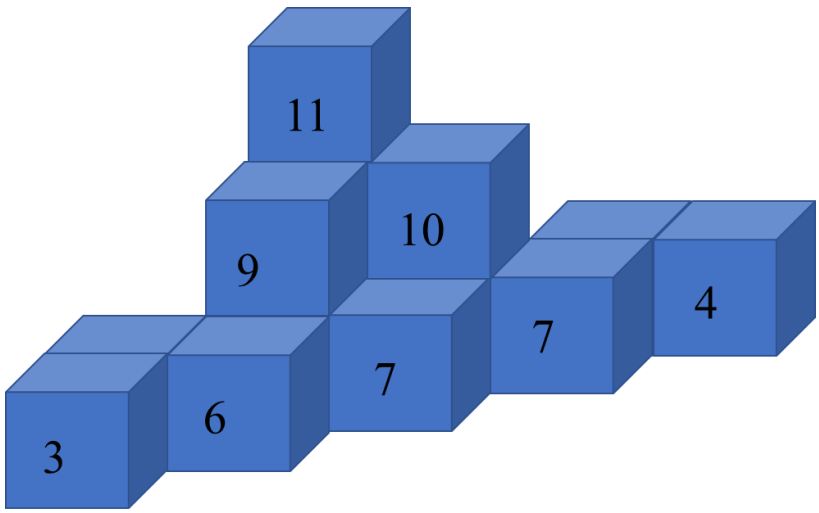

Figure 16: Voxels with Gray Values in 3D Image

A surface of voxel faces with the same value is known as an iso-surface. Thus iso -surface is a set of points or voxel faces of the same constant forming a continuous function formed in a 3D domain. Figure below shows different iso-surfaces of a BGA solder ball.

The region of interest within a 3D CT scan data is selected using the corresponding iso-surface value. Image segmentation algorithms require selection of the region of interest within the CT scan data using the appropriate iso-surface value. An error in the selection of iso-surface value leads to errors in geometrical dimensions of the selected region of interest.

2.10 Coordinate System of CT scanner

Figure 17 shows the global coordinate system of the micro CT scanner. The XM and YM axis lie on the horizontal. The rotating chuck has the XM axis as its axis of rotation. ZD is the distance from the horizontal plan to the detector and ZT is the distance from the horizontal plan to the emitter. As per the geometry of the part, the CT tray is moved around to orient the part above the X-ray emitter. The Table 1 shows a sample CT configurations table. Upon scanning the part, the Volume Graphics software opens the raw data that is the x-ray images of the part as shown in Figure 14.

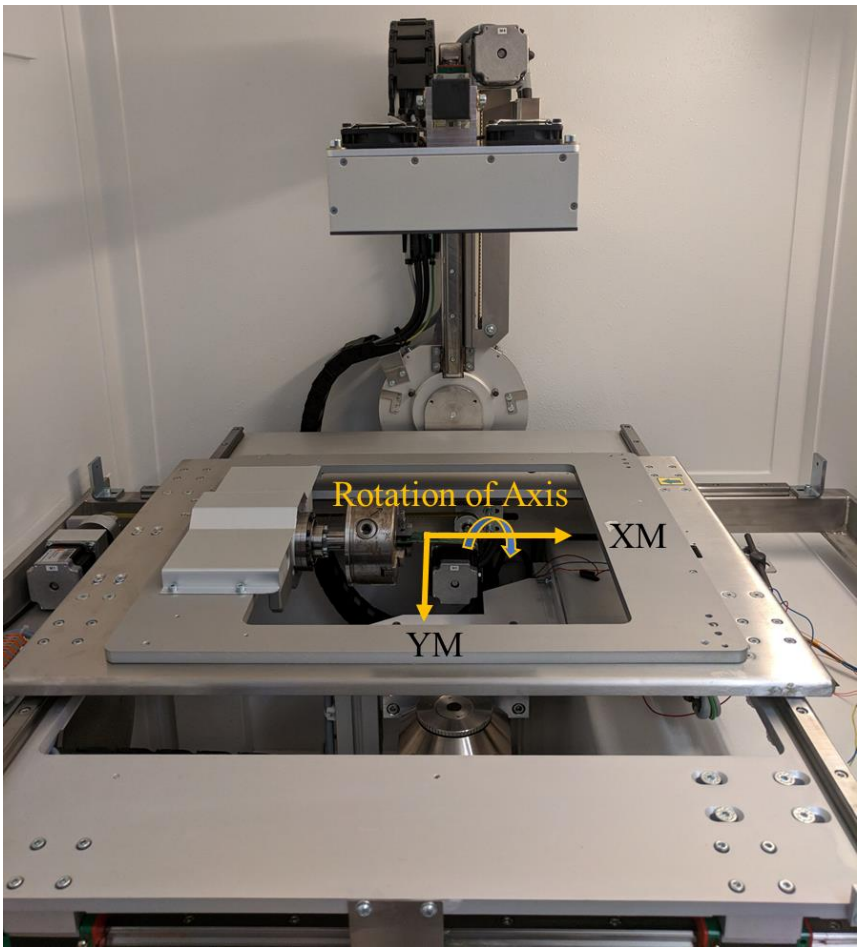

Figure 17: CT Axes and Part Configuration

Table 1: Sample CT scan Variables

Scan Variable	Values
XM	146463
YM	163660
ZT	-137026
ZD	103517
TiltD	0
RotCT	53092

2.11 Uncertainty in Dimensional Measurement using CT Scanners

In this study, the micro CT scan data of missile fuze electronics has been used for creation of FE models and for deformation measurement using Digital Volume Correlation. Presence of good dimensional accuracy of the reconstructed geometry is of prime importance for the fidelity of the model and the technique itself. There are multiple factors that affect the dimensional accuracy of the scanned geometry. This section gives a brief overview of various sources of errors and lists their possible root causes. Following are the five main sources of errors and their root causes:

1. Errors in Software and Data Processing
    1. 3D Reconstruction
    2. Threshold determination
    3. Surface regeneration
    4. Data reduction
    5. Data correction
2. Measurement Object
    1. Surface roughness
    2. Penetration depth, dimension and geometry
    3. Beam Hardening
    4. Scattered radiation
    5. Material Composition
3. Operator Settings
    1. Source Current
    2. Acceleration voltage
    3. Magnification

4. Object orientation
5. Number of images
6. Spatial resolution
7. Detector exposure time

4. Environmental Effects
    1. Temperature
    2. Vibration
    3. Humidity
5. Hardware
    1. X-ray source: energy spectrum, focus, stability of the beam
    2. Detector: Thermal drift, beam scattering, contrast sensitivity, pixel variance, noise, lateral resolution
    3. Mechanical Axis: Geometrical errors, mechanical stability

All the factors stated above are plausible sources of errors that one need to account for. Errors mentioned under Software and Data processing are fundamentally due to underlying deficiencies in the algorithms employed for data processing. Improper Threshold value selection leads to exclusion or inclusion of model geometries that may be relevant or irrelevant respectively. Depending on the resolution of the CT scan this error may be further compounded if the scan resolution is low leading to jagged edges. Accuracy of surface regeneration algorithms rely on density of sampling points on the surface to be reconstructed. A very high number of sampling points may overfit the scanned surface and capture surface noise. A relatively lesser number of sampling points may connect (bridge) sample points via surfaces that may not be connected at all.

Errors mentioned under the header of Measurement Object are pertaining to the geometry, topology and composition of the object being CT scanned. Objects with higher atomic number and density tend to have a higher resistance to the passage of x-rays. For example, CT scanning objects with Lead (Pb) can be very erroneous. Lead may absorb majority of the x-rays passing through it, barely allowing any x-rays to pass through it and reach the detector. Due to this a black spot appears on the X-ray data with loss of details hidden behind this high-density material.

Thickness of the part also leads to similar errors. Higher the thickness, more is the x –ray energy absorption as it passes through the part. Objects made of relatively lower density materials but with thickness high enough to block majority of x-ray energy to pass through causes the same error mentioned earlier as with respect to object with higher atomic number or material density.

A common artifact encountered in micro-CT scanning is beam hardening. It causes the edges of the scanned part to seem brighter than the center, even if the part is made of one uniform homogenous material. This error is caused because of the increase in mean X-ray energy, or “hardening” of the X-ray beam as it passes through the scanned part. The x-ray beam coming out of the emitter is a polychromatic beam, made of x-rays with varying energy levels.

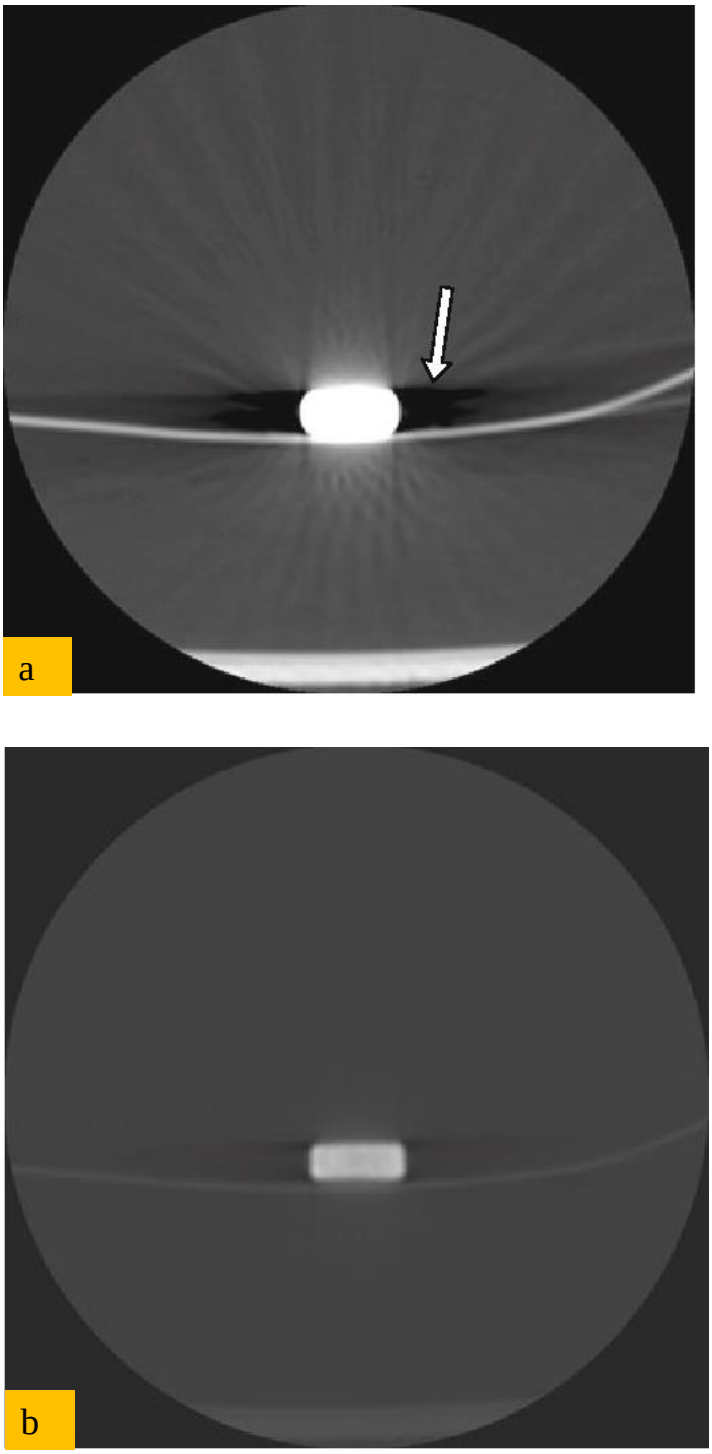

Figure 18: (a) Scan with beam hardening (b) scan without beam hardening [Hayashi 2010]

Due to this, the lower energy x-rays may get attenuated in areas where there are no artifacts and higher energy x-rays may not get attenuated at all in areas with artifacts. This results

in a reduction in overall intensity of the x –ray image and also has a higher average energy than the incident beam. This also results in reduction of effective attenuation coefficient of the part being CT scanned. In X-ray images of sufficiently high density, atomic number material, this error shows up as an artificial darkening in the center region and a corresponding brightening near the edges.

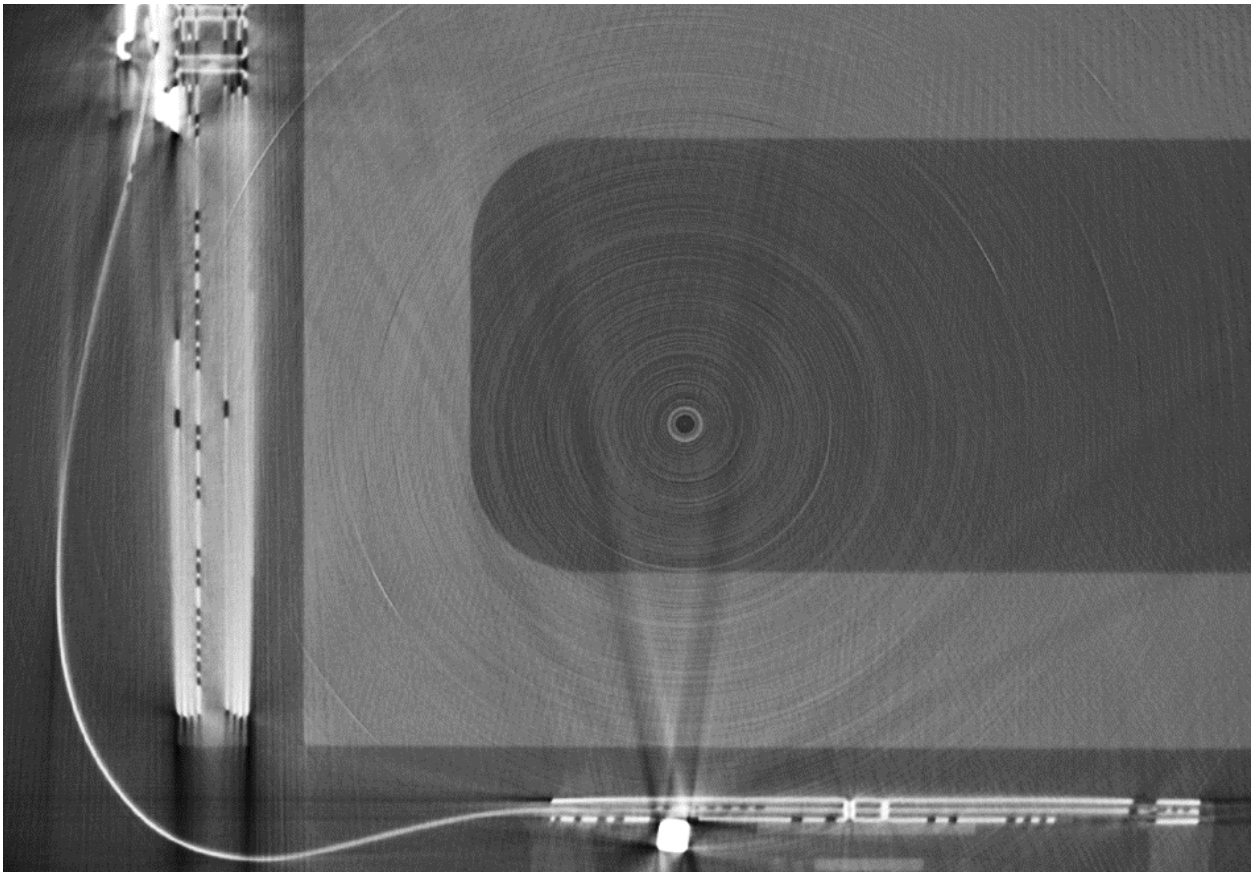

Figure 19: Ring artifact in CT scan [Muehlhauser 2010]

Ring Artifacts are another type of error where in artificial rings appear on the scanned geometry. It is caused by random shifts in output from the individual CT scan detector which cause the same x-ray at the same location to have different values along the part as the part rotates. This is a rather random error that is caused by change in scan parameters.

Sources of errors mentioned under the heading of operator setting are the most commonly found errors in CT scans. Higher operating current and voltage result in loss of details at the edges as the x-rays with higher energy pass through the edge locations without getting much attenuation, thus retaining the same energy as it reaches the detector. A lower current also results in lesser contrast and poorly focused images.

Spatial resolution plays a very important role in reducing the dimensional error in the scan. A lower resolution scan, like a 512 x 512 x 512 may have a voxel size bigger than the smallest feature of interest in the part being CT scanned. The least count of the dimension increases as the spatial resolution decreases. For the same spatial resolution if the number of images and the scanning time is reduced, lesser data is available for the reconstruction algorithm for volume reconstruction. This causes an increase in the amount of interpolated geometry in the final reconstructed volume.

Errors caused by environmental effects arise from the surroundings the CT scanner may be installed in. Maintaining the room with the machine at a constant set temperature and use of vibration isolators are common practices to avoid such errors.

Errors caused by hardware are often due to user negligence and equipment. Constant recalibration of the CT scanner helps align the x-ray beam, refocus the beam and calibrate the detector screen sensors. Errors caused due to improper positioning of the X-ray tray may cause the part to go out of the X-ray cone projections. This results in loss of data. Such errors can be easily avoided by rotating the part prior to scan to make sure it does not go

beyond the line of sight of the x-ray cone at any time during its complete revolution. These errors are also termed as geometrical errors. Mounting parts on a fixture that may move while it is being scanned also causes errors. It is of prime importance that the part being CT scanned is firmly held on to the fixture and does not move while being CT scanned. Figure 20, Figure 21 and Figure 22 show the CT scans of a fuze device. The scan was acquired at the scan parameters as listed.

Figure 20: CT scan of the Fuze device, orientation 1

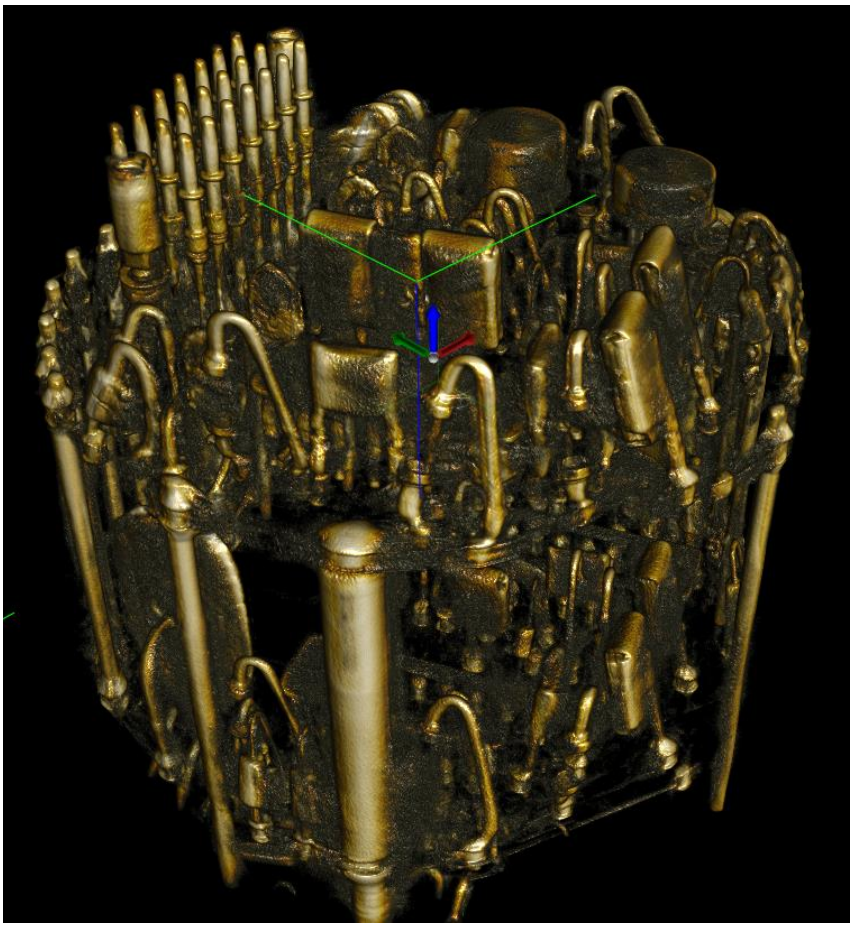

Figure 21: CT scan of the Fuze device, orientation 2

Table 2: Scan parameters for Fuze CT Scan

Scan Parameters	Value
Voltage	140kV
Current	25microAmps
Scan type	1024 X 1024 X 1024

Figure 22: CT scan of the Fuze device, orientation 3

Chapter 3: Micro-CT to Finite Element Conversion

This chapter aims to address the process of Micro-CT data to finite element model conversion. It draws a comparison between the conventional process and its advantages, disadvantages, applications and applications. It addresses the motivation, advantages, and disadvantages for the Micro-CT data based parallel technique and its unique application. It then describes the process and different algorithms in the process in detail and shows test cases undertaken to study the ability of the technique developed.

3.1 Conventional Finite Element Modeling

The finite element method is the very important technique in structural mechanics that analyzes the geometry in question by discretization approach. The basic concept in the physical interpretation of the Finite element modeling is the discretization of the mathematical model into smaller geometry sub-domains of the same components called finite elements or just elements. The behavior of each element is expressed in terms of a finite number of degrees of freedom characterized as the value of an unknown function, or functions, at a set of nodal points.

Measurable quantities like deformation, strains, and stresses are computed at the integration points of each element and these values are interpolated at the nodes by use of shape functions or basis function and displacement functions. Each type of element may have a different type of shape function (linear, quadratic, cubic, polynomial) that

determines the way the element may get deformed when acted upon by a load. Each type of element may also have different number of integration points. More the number of integration points, lesser the interpolation error at the nodes. But with an increase in integration points, even the sheer number of calculations increase, resulting in longer solving times.

Finite element analysis is ubiquitous today and has found profound application in engineering today. Problems of computational fluid dynamics, solid mechanics, applied thermodynamics, heat transfer, multi-disciplinary or multi-physics problems like electro-mechanical, electro-thermal, and thermo-mechanical sciences can all be modeled and solved using this approach. The technique is rigorously used to design components, assemblies or systems prior and study their behavior under varied loading environments to simulate real life scenarios.

In conventional Finite modeling approach, the user models the geometry in a CAD modeling software and then meshes the geometry. Further, loads are applied, and boundary conditions are given, and the model is simulated. Depending on the geometry and the nature of the loads, the element type may be selected. In this approach the underlying assumption is that the all geometrical details are reflective of the ideal desired part geometry, the geometry of the model is free of any manufacturing details like texture, surface finish, manufacturing defects. The finite element model is made to study the behavior of the part at the beginning of the parts life cycle.

In majority of applications of this technique, the above stated assumptions are commonly made and serve the purpose. In this research, an attempt is made to bypass these assumptions and study the behavior of the part considering manufacturing physical defects, physical damage the part may have sustained, leading up to the time it is being analyzed. Conventional Finite element modeling approach to model these details may be prohibitively time consuming and still fail to address capture the real as-is geometry. As mentioned in the earlier chapter, in applications like missile electronics, where the life of the electronics go beyond multiple decades and still may be expected to perform when field deployed are example scenarios where such Micro-CT data based geometry may help capture the real as-is geometry. This technique has also been in use in the Medical industry to design the prosthetic legs , design artificial vertebrae and several other applications .

3.2 CT Data to Finite Element modeling conversion in medical industry

As per the literature review the common steps involved in use of this technique has been as shown in Figure 23. Due to the presence of lesser number of components, most often one or two, the process is much simpler and easier. A CT scan may show much more details and scan geometries around the region of interest too that may not be of any use to the analysis at hand. The user may get to accomplish these tasks using several different image segmentation or 3D meshing algorithms. Image segmentation is a technique that allows selectively picking regions of interest and omitting the regions one is not interested in an image or volume. The selection is based on the bases of pixel (or voxel) intensity values. This selection can be implemented using multiple different algorithms designed for this

purpose. Presence of lesser number of components and the more often the components having drastically different intensities value, allows for easy selection.

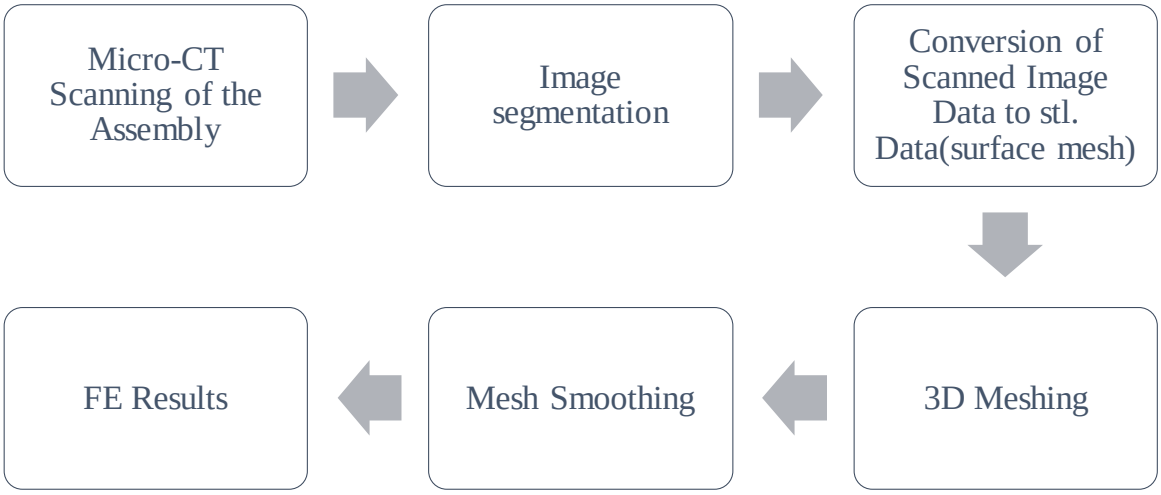

Figure 23: Micro CT to Finite element Mesh conversion in the medical industry

Rahman et al [Rahman 2009] and Taddei [Taddei 2006] [Guo 2011] has published on use of Mimics Medical Imaging Software to perform image segmentation of a standalone femur bone surrounded by tissue. Bao [Bao 2010] has also used CT data to make FE models of tibia bone to study stresses. Global threshold segmentation was used to distinguish between the bone and the surrounding tissue. Image segmentation of bone from tissue is relatively straight forward as the contrast between the region of interest (bone) and rejection region(tissue) is most ideal. Researchers have also used CT data to make finite element models of lungs, where the window of x-ray image pixel intensity for Lungs was known prior to the CT scanning operation based on published data [Li 2007]. Knowing this intensity range would ensure accurate image segmentation of the lungs from it's surrounding materials. This range of pixel intensity for different materials used in different electronic packages is not published and may never be published as the window of intensity values for the same material would change of the package architecture changes (BGA to Flipchips).

Researchers have used CT data to make FE models of skull and skull implant using Mimics software. Predefined setting for segmentation of skull were used to make the FE model [Shweta 2011]. Similarly [Wong 2003] used CT data of the vertebral body(bone) and manually made ligaments for their study. This literature review points towards a trend of use of CT data to make finite element models in cases where a single high-density material like bone is the region of interest and human body parts like lungs where the pixel intensity windows are already known. In contrast, electrical components like Fuze, BGAs, QFNs have multiple high-density materials like copper and solder next to each making accurate image segmentation more difficult and result in error prone surface geometry.

3.3 Micro-CT Data to Finite Element model conversion for Electronics

Initial attempts at repeating the procedure as shown in Figure 23 led to erroneous image segmentation. This was because of the presence of higher number of material (elements) per given volume. Because of this the surrounding material around the region of interest with other similar materials lead to excess of deficient region of interest selection. Due to this error, there was a need to correct this geometry or repair this geometry. These procedures included addition or subtraction of artificial surfaces in order to make the selected region of interest match the real part. This warranted use of special algorithms meant to repair/ manipulate 3D surfaces.

Also, finite element modeling of electronic assemblies often has presence of multiple sub-components big and small. Being able to control the mesh size of each sub-component is of prime importance to make a finite element that is truly compatible to be run using the

implicit or explicit finite element solvers. This required use of algorithms that allow for control over number of elements.

This chapter describes a step by step procedure for the stated tasks, mathematical basis for each algorithm and progression of mesh after each step. It also enlists a short study to investigate the dimensional accuracy of the procedure. Towards the latter half the chapter, two practical applications of this technique to fuze electronics has been noted. Figure 24 shows the steps involved the conversion of micro-CT data to FE mesh developed for electronic components.

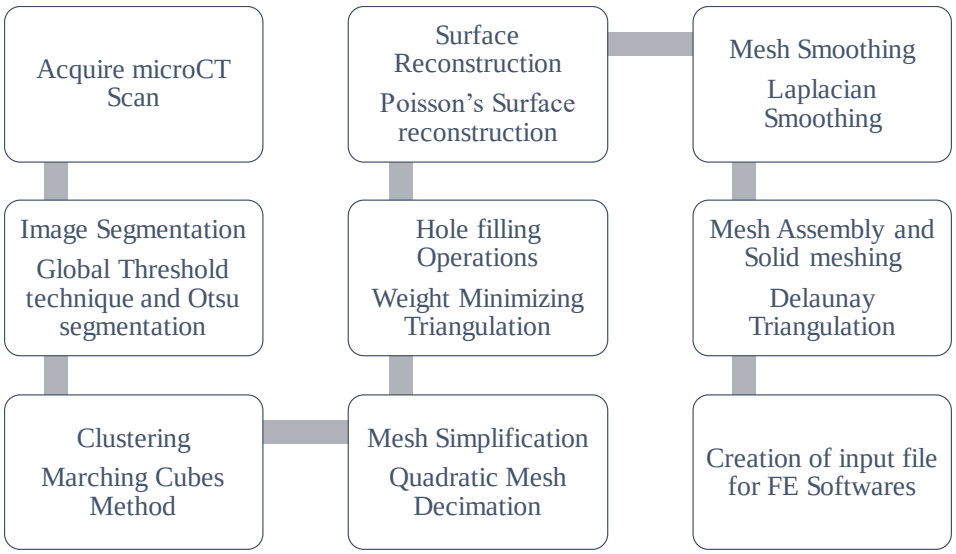

Figure 24: Micro-CT to Finite Element mesh conversion process

3.3.1 Image segmentation

In this step, boundaries of the model are identified based on the range of greyscale value in the DICOM files. In semiconductor devices, different materials are often stacked on top of each other. Each layer has different gray-scale value owing to its material density, thickness, and atomic number of the components. Difference in grayscale value in a volume represents changing internal structure or material regime of the device. This is then used to identify clear material boundaries at multi-material interface such as bind-EMC-chip interface. Pixel based thresholding to identify different geometries and extract specific elements is a technique known as Global Threshold image segmentation. Figure 24 shows the global threshold image segmentation. The original dicom image shows a circular object at the center. Global thresholding algorithm requires input in the form of a pixel intensity value. All the pixels with the intensity above this number are selected and the image is binaries as per this input pixel value. The shortcoming of the technique is the selection of the pixel intensity value. This value is user selected and the selection criteria is the user's perception of the boundary pixels in the image. This remains as the major source of error causing segmentation of unwanted pixels.

Otsu method which uses cluster-based image thresholding was used to process the images. This analysis techniques provides result in the bi-color format. The colored region represents the selected geometry and the black image represents the background noise. Algorithm assumes bimodal distribution, i.e. image consist of pixel belonging to either the object or the background [Otsu 1979].

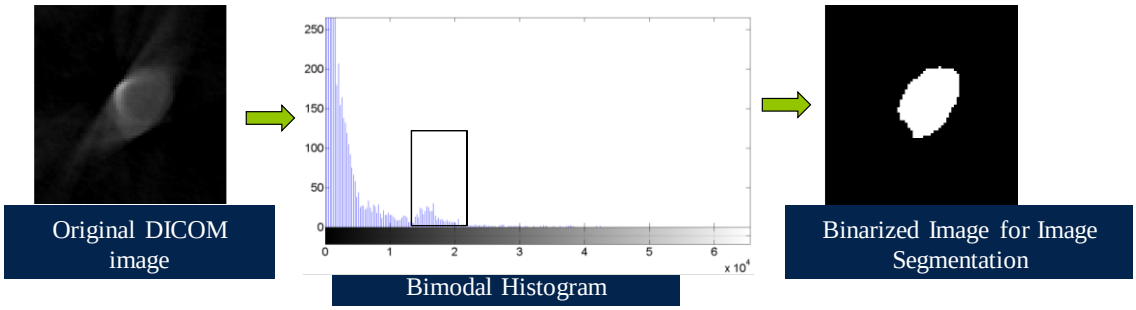

Figure 25: Global thresholding technique for image segmentation

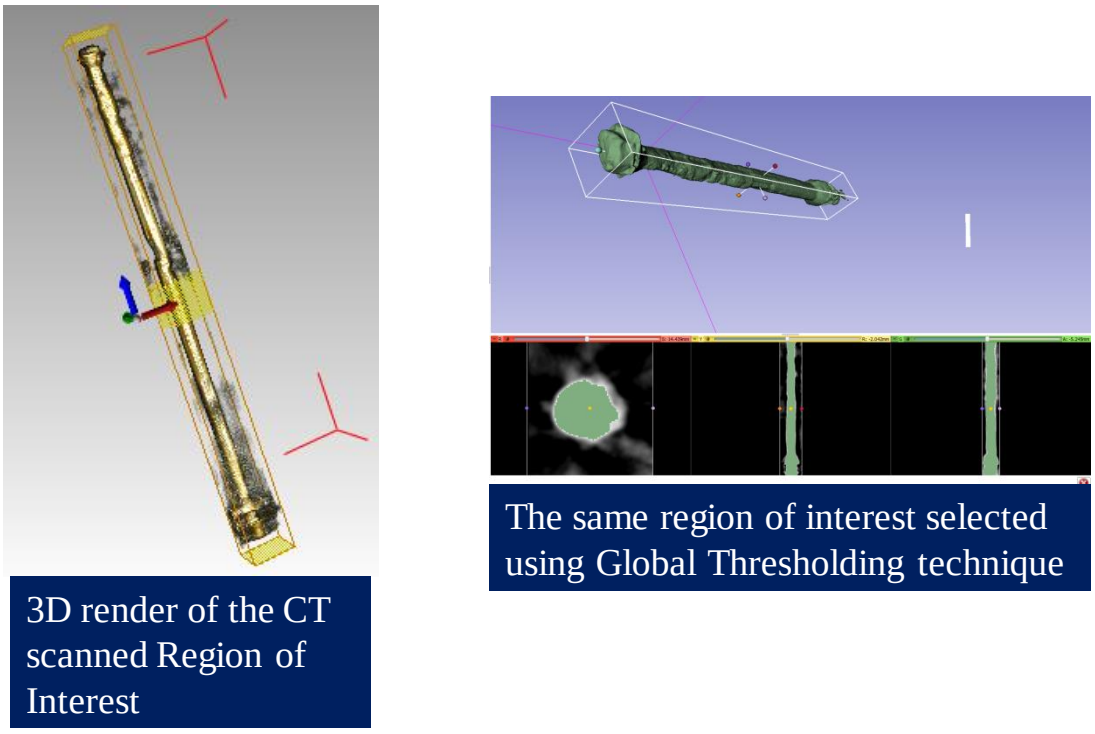

Figure 26: Comparison of CT scanned render of ROI and ROI selected via Global

3.3.1.1 Thresholding technique

The algorithm is used to calculate the optimum threshold that allows separation of two classes so that variance in each class is minimum and variance between two distributions is maximum.

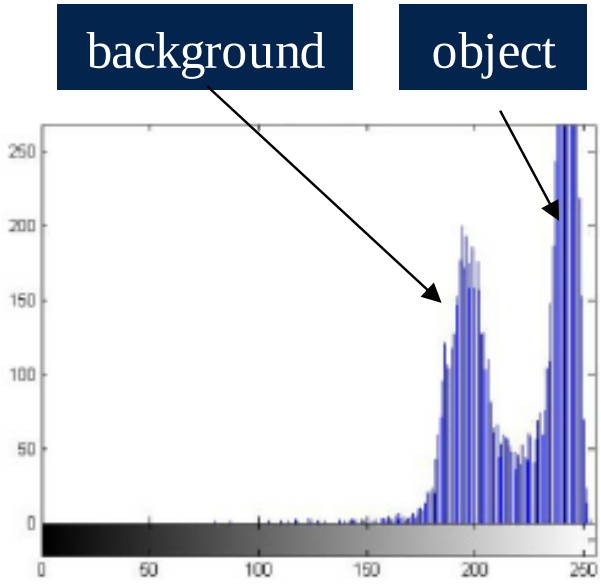

Figure 27: Bimodal distribution of pixel intensities for Otsu segmentation

The within class variance is computed based on the weighted sum of the variance in the two classes and calculated as,

$$\sigma^2_{within} = w_0(t)\sigma^2_b(t) + w_1(t)\sigma^2_o(t) \quad (7)$$

Where, w is weight, "o" and "b" represents two classes of object and background, and σ_{within} is the within class variance for objected and background. The variance within the classes is minimized and variance between classes is maximized to formulate following functions,

$$\sigma^2_{between}(t) = \sigma^2_T(t) + \sigma^2_{within}(t) \quad (8)$$

$$\sigma^2_{within}(t) = w_b(t)[\mu_b(t) - \mu_T]^2 + w_o(t)[\mu_o(t) - \mu_T]^2 \quad (9)$$

Where, $\sigma^2_T(t)$ is the combined variance, μ_T is the combined mean, w is weight of each class, and o and b represent class object and background respectively. The weights used for the calculation of the within class variance are based on the probability of gray scale values in the object and the background distribution.

$$w_b(t) = \sum_{i=0}^{t-1} p(i) \quad (10)$$

$$w_o(t) = \sum_{i=0}^{N-1} p(i) \quad (11)$$

Where, [0, N-1] represents grayscale levels in the image including object and background. Probability of each of the grayscale levels is represented by p(i). The combined mean of the object distribution and the background distribution is calculated by,

$$\mu_T = w_b(t)\mu_b(t) + w_o(t)\mu_o(t) \quad (12)$$

The between class variance can be expressed in terms of the means of the distributions by substituting Equation 12 into Equation 13

$$\sigma^2_{between}(t) = w_b(t)w_o(t)[\mu_b(t) - \mu_o(t)]^2 \quad (13)$$

Each of the threshold levels were then successively testes to maximize the between-class variance allowing for identification of grayscale levels. Marching cubes algorithm was used for extracting a polygon mesh of an iso-surface from three-dimensional discrete field based on identified greyscale values.

The dimensional accuracy of the part being segmented is found to be better than that of the part segmented using Global Threshold segmentation as there is no human intervention involved. Though, the Otsu segmentation requires the dicom data of the ROI to have a bimodal distribution as shown in Figure 27.

3.3.2 Marching Cubes Algorithm

At the end of the image segmentation process, the region of interest throughout the dicom data is selected as per the pixel intensity value. The dicom data series is made of a series of 2D x-ray images with segmented ROI marked out. Inorder to convert this 2D data of the ROI to a 3D volume, marching cubes algorithm is used. Marching cubes algorithm is a test to determine whether a given arbitrary point lies within a given boundary within which the ROI exists. A schematic of the working of the algorithm in 2D is shown in Figure 28.Figure 28 (a) shows the region of interest with a grid of certain resolution superimposed on it. Thus the space with the ROI is divided into an arbitrary number of cubes. Now the corner of every cube is tested to check if it lies inside the ROI or outside as marked and shown in the figure with the red dots. Now for every cube some corners are found inside and some corners are found outside the object, the surface of the ROI must pass through that cube, intersecting the edges of the cube in between corners of opposite classification. This procedure is repeated multiple times with a finer grid to improve the dimensional accuracy of the ROI. The intersection points can now be connected as shown in Figure 28 (c) to obtain the ROI. This is also known as a quadtree (for 2D) and octree (for 3D) approach [Lorensen 1987, 1992, 1994].

This procedure can be translated onto a 3D domain as shown in Figure 29. The 3D volume can be superimposed by a 3D grid and each corner of the cube of the ROI within can be

tested as shown earlier. Now a cube could have all its corners marked to either be inside or outside with its edges being intersected by the ROI. At this point, algorithm needs to connect the intersecting points but this may not be as simple as the 3 points or more points could be connected in multiple ways and not just one as was the case for 2D. Doing this procedure for all the cubes inside the 3D space may be too time consuming and thus an alternate approach is used which is using a 'lookup table' with all possible combinations of a corner in a cube being inside or outside. This comes out to be 256 combinations as there are 8 corners (2^8). After accounting or mirror triangulation positions and identical triangulations, it is found that there are 14 unique combinations of triangulations possible. Using the look up table the procedure of finding the correct combinations of intersecting points to connect is found out.

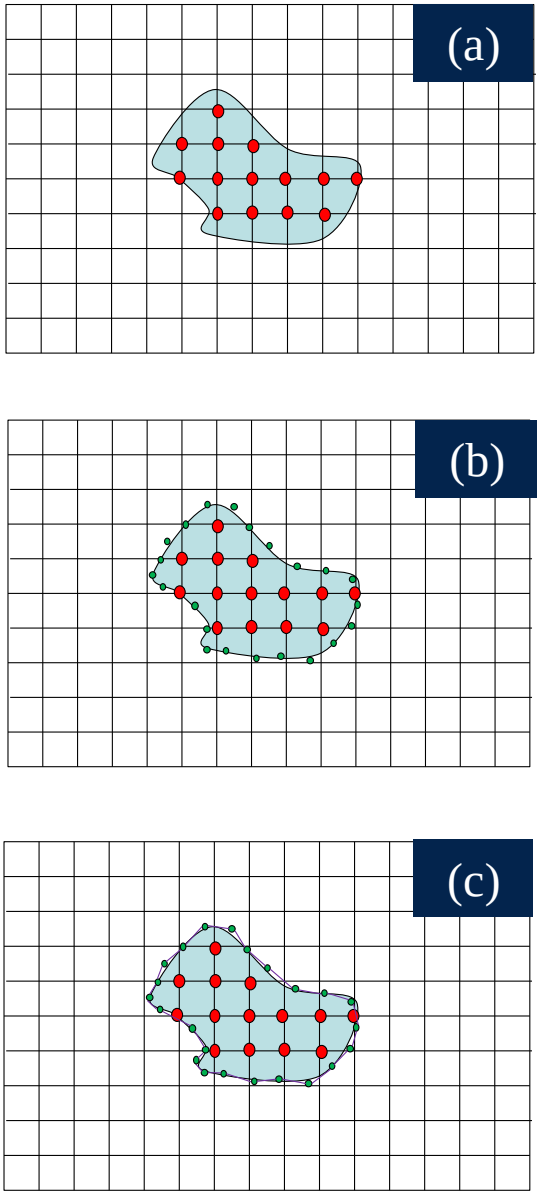

Figure 28: (a) ROI intersected by grid (b) higher resolution grid made to find new intersection points closer to the ROI boundary (c) the selected final intersection points connected to form a bounded region

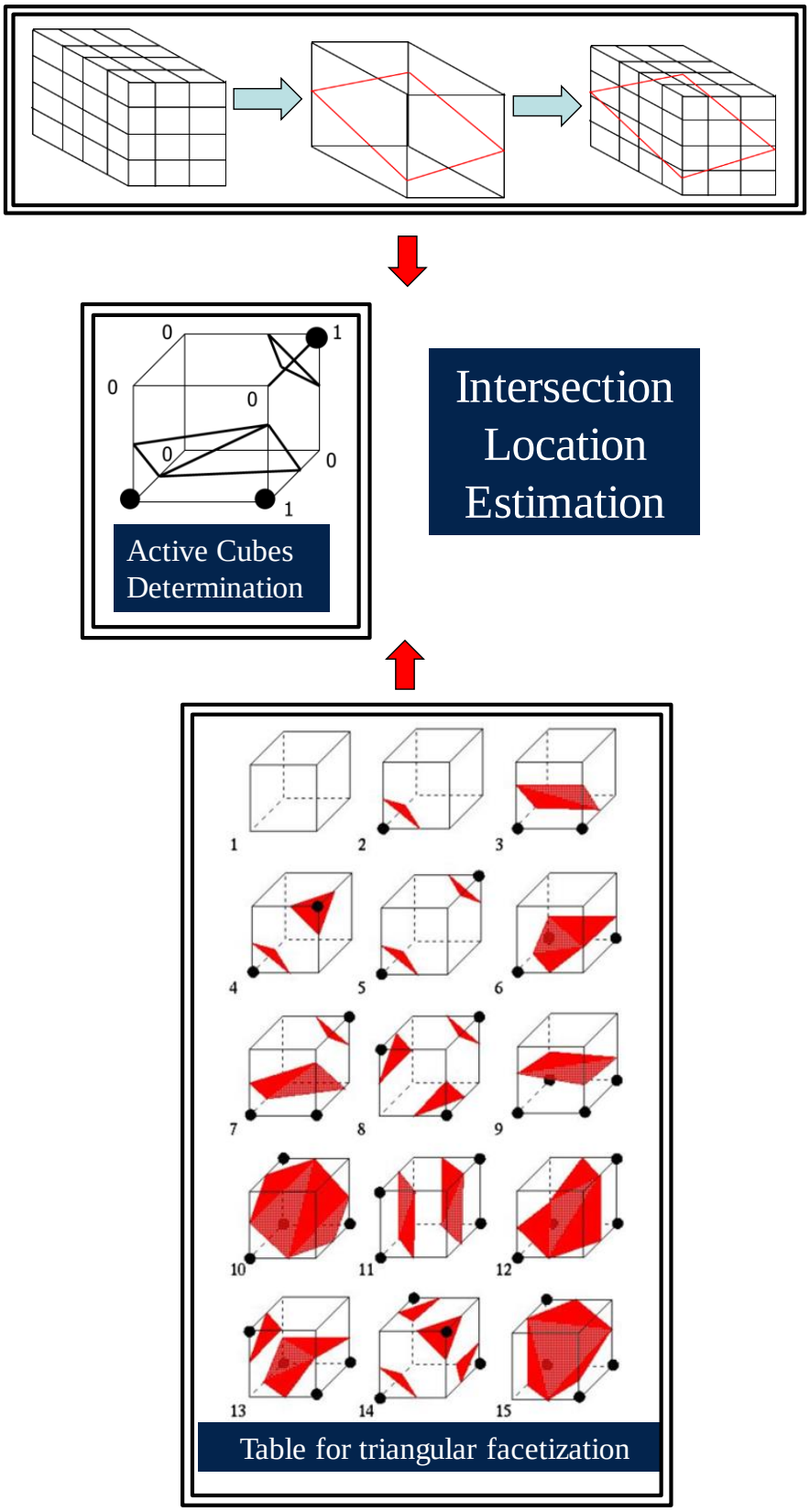

Figure 29: Marching Cubes Algorithm in 3D [Cirne 2013]

3.3.3 Minimum Weight Triangulation Hole Filling Algorithm

Because of the errors in image segmentation because of the presence of large number of material parts, there may be certain regions in the ROI that may get omitted during segmentation step. This omitted region shows up as a 3D surface with a hole. Since the real surface does not have this feature, the image segmented 3D model with a hole needs to be filled by an artificial surface. This can done by minimum weight triangulation hole filling operation.

The hole filling operations in this work is done by applying the Minimum Weight Triangulation method to fill a polygonal hole formed by the boundary edges forming the hole. As per this algorithm a random triangle is generated inside this polygon and this triangle splits the polygonal into smaller sub polygons recursively until no new polygons can be created. The criteria that governs the creation of the triangles is governed by minimization of weight of the triangles, which is done by controlling the area, edge length, dihedral angles [Hoffman 2006] [Liepa 2003]. The weights on the triangles are defines as an ordered pair of (angle, area). A weight set L is defined as

$$L_{angle} = [0, \pi] X [0, \infty), 0_{Langle} = (0,0) \tag{14}$$

The ordering in L_{angle} is designed to give precedence to dihedral angles over area and penalize large dihedral angles.

The weighting functions defined as

$$\Omega_{angle} : V^3 \rightarrow L_{angle} \tag{15}$$

$$\Omega_{angle}(v_i, v_m v_k) = (\mu(v_i, v_m v_k), \Omega_{area}(v_i, v_m v_k)) \quad (16)$$

Where $\mu(v_i, v_m v_k)$ is the maximum dihedral angle between $(v_i, v_m v_k)$ and existing adjacent angles. The triangulation algorithm using this weighting will yield the triangulation that minimizes the maximum dihedral angle. Figure 30 shows a comparison of a part with a hole and the same part after the hole filling operation.

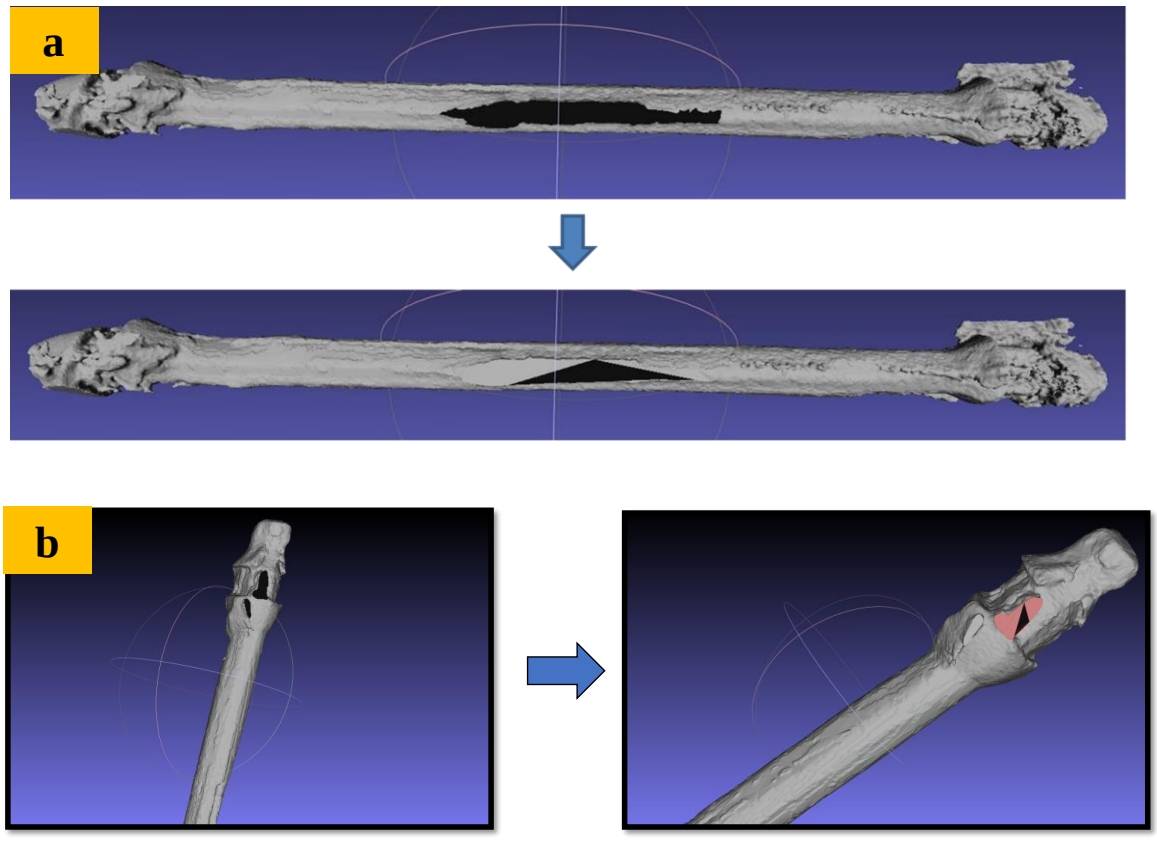

Figure 30: Example of Hole filling operation

3.3.4 Poisson Surface Reconstruction

The 3D model generated by the marching cubes algorithm is often found to be ‘blocky’. Also, the surface triangular mesh is often found to be unevenly distributed. These two features of the mesh are not favorable for finite element analysis. Poisson surface reconstruction replaces the existing surface of the 3D model by a new surface that forms a convex hull and has triangular elements evenly distributed.

In the Poisson surface reconstruction method, a 3D indicator function χ , is defined such that it has a value of 1 for points inside the model and a value of 0 for points outside the model. The gradient of the indicator function is a vector field of zeros everywhere apart from the points near the surface where it is equal to the inward pointed surface normal as shown in Figure 31 . The points on the surface are generated using a quadtree or octree approach as mentioned in the earlier section of marching cubes algorithm. A schematic of this approach is shown in Figure 32 [Kazhdan 2003, Berger 2014].

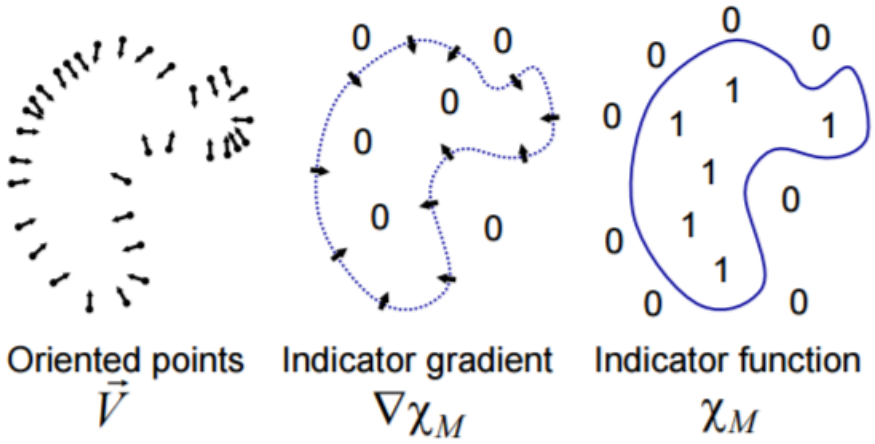

Figure 31: Poisson surface reconstruction procedure for finding the indicator function [Kazhdan 2006]

Thus, the gradient of the indicator function are oriented point samples. The indicator function can thus be computed by inverting the gradient operator or finding the scalar

function χ whose gradient best approximates the vector field, defined by the samples in a least squares sense.

$$\min_{\chi} \|\nabla\chi - V\| \tag{17}$$

Application of the divergence operator allows for the problem to be transformed to a standard Poisson's problem:

$$\nabla.\nabla\chi = \Delta\chi = \nabla.V \tag{18}$$

Once solved, the surface is found via χ with a suitable surface.

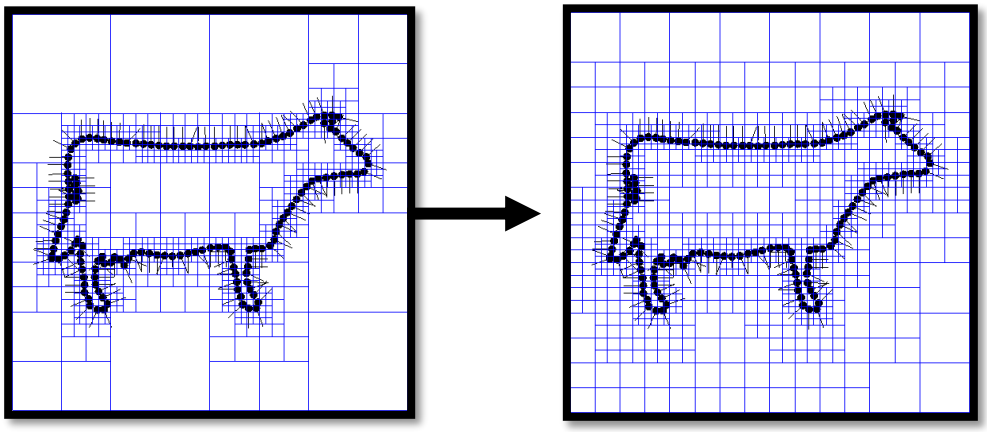

Figure 32: Quadtree approach for Poisson surface reconstruction [Kazhdan 2003]

At the end of the Poisson surface reconstruction step a 3D model with an evenly distributed mesh is created. Though at this point the number of surface elements is often found to be very large. The number of elements and size of elements on the surface can be controlled by use of quadratic mesh decimation algorithm.

3.3.5 Mesh Decimation and Smoothing

The STL data contains point cloud and their unit normal vectors arranged in triangulated surfaces. A raw surface after surface fitting has a very dense mesh. Very small element size is computationally expensive and tedious for processing. The process of removing extra vertices and faces from mesh by simplifying the surface without losing the surface features is called mesh decimation. This step produces moderately coarse mesh which is essential for simplified computation. This reduction was performed based on quadratic error matrix [Garland 1999]. The edge collapse algorithm reduces an edge into single vertex, i.e. two vertices are merged into one. The method is based on iterative contraction of vertex pairs (v_i, v_j) which needs to be replaced by a vertex v during the process of mesh simplification,

$$(v_i, v_j) \rightarrow \bar{v} \qquad (19)$$

Garland set of planes to each of the vertices.

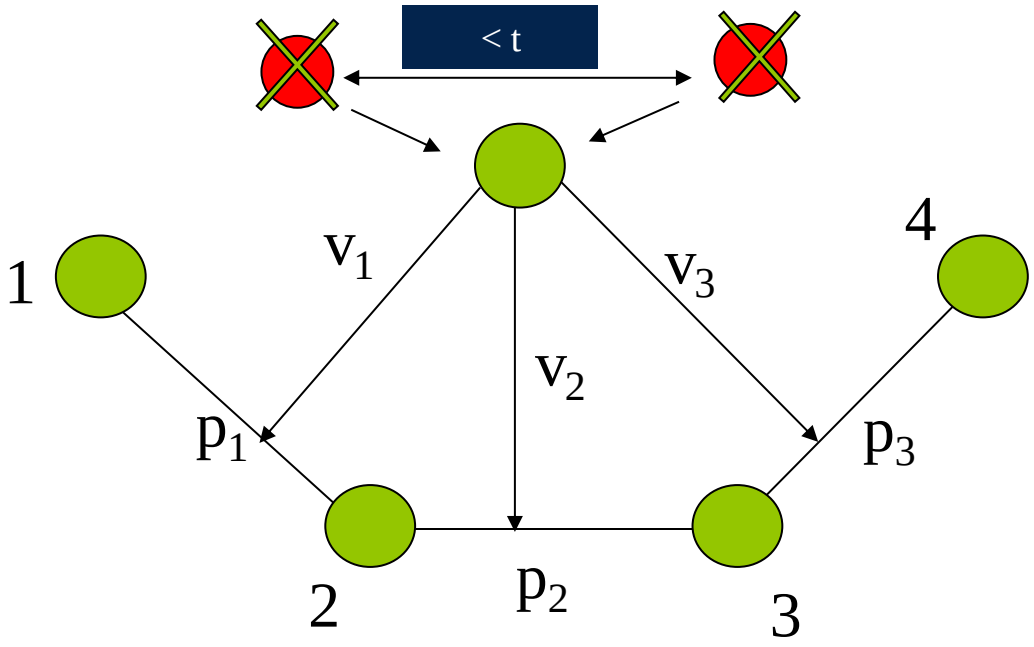

Figure 33: Schematic iterative contraction of vertex pairs

The decision and order of the edge collapse depends in the computed error, which is based on the distance of the point to the plane. A vertex in 3D space may be represented as,

$$\nu = [\nu_x, \nu_y, \nu_z, 1]^T \tag{20}$$

A plane p, in cartesian 3D space may be represented as,

$$ax+by+cz+d=0 \tag{21}$$

Where, $a^2+b^2+c^2=1$The distance D of the vertex from the plane may be represented as,

$$D^2 = (p^T\nu)^2 = (p^T\nu)^T(p^T\nu) \quad = \nu^T Kp\nu \tag{22}$$

Where $Kp=pp^T$. The error of each vertex is defined as the sum of the squared distances to all the planes to which the vertex belongs and is represented as follows,

$$\Delta\nu = \sum_{P\in planes(\nu)} D^2\nu = \nu^T\left(\sum_{P\in planes(\nu)} K_p\right)\nu \tag{23}$$

Where planes (ν) represents all the triangles that meet at the vertex. The edge in the mesh is contracted when the resulting quadratic error is equal to the quadratic error of the two vertices,

$$\bar{\Delta\nu} = \Delta\nu_i + \Delta\nu_j \tag{24}$$

In the current model, quadratic decimation has been used to reduce the number of edges by 75% for each component.

At the end of the quadratic mesh decimation process the final output achieved is as shown in Figure 34.

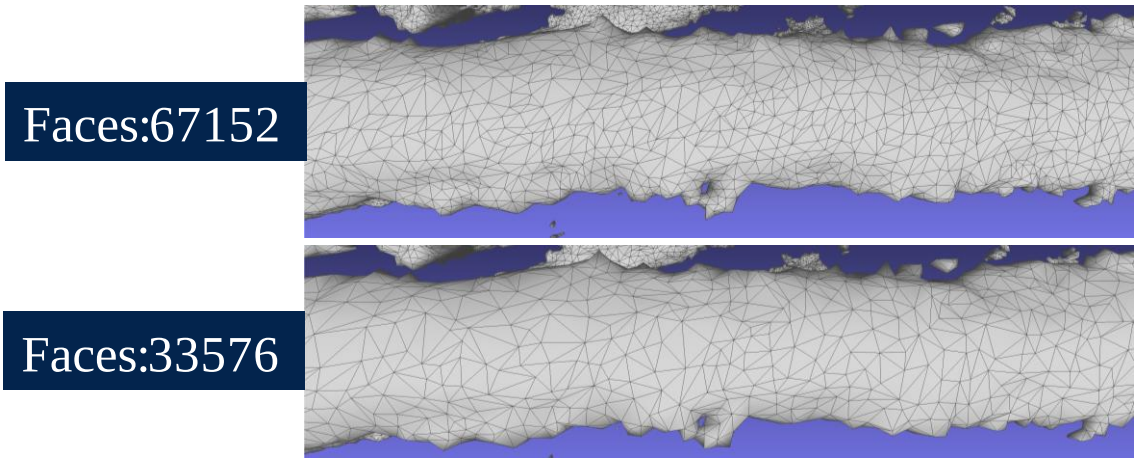

Figure 34: Output after quadratic mesh decimation

3.3.5.1 Laplacian smoothing

Once the mesh decimation was performed, Laplacian smoothing was used to smoothen the mesh. In this process, vertices of the mesh are incrementally moved in the direction of Laplacian as shown in Figure 35.

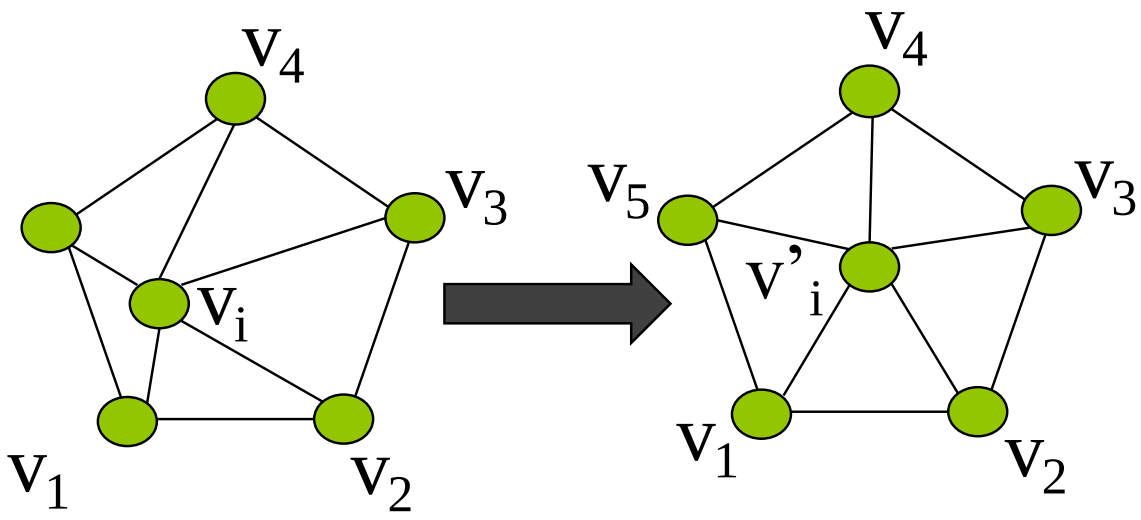

Figure 35: Laplacian Smoothing operation schematic

The differential version of smoothing equation is,

$$\frac{\partial X}{\partial t} = \lambda L(X) \tag{25}$$

Where C is a vector of the vertices of the mesh, L is the Laplacian, and λ is a scalar that controls the diffusion speed. The continuous form of the Laplacian operator is,

$$\nabla^2 f = \sum_{i=1}^{n} \frac{\partial^2 f}{\partial x_i^2} \tag{26}$$

Where the subscript "i" corresponds to each of the independent variables. There are a few different approximations for the Laplacian operator. For a linear approximation of the operator, the smoothing equation can be written as

$$X(n+1)=(I+\lambda dtL)X(n) \tag{27}$$

The desirable property of diffusion smoothing is that it does not modify the connectivity of the mesh or add or delete any of the vertices. The process of smoothing instead focuses on modifying the position of the vertices. In addition, the discrete Laplacian smoothing can be implemented in a manner such that the smoothing operation requires information from its immediate neighbors. The size of the neighborhood is small and does not increase with the increase in the size of the mesh [Ji 2005]. The discrete approximations of the Laplacian Operator take the general form

$$L(x_i) = \sum_{j \in N_1(i)} w_{ij}(x_j - x_i) \tag{28}$$

There are several options in calculations of the weights including (a) simple approximation also called the umbrella operator is one in which the Laplacian uses equal weights, such that $W_{ij}=1/m$, where m is the number of nearest neighbors of x_i. Using the simple approximation defines the Laplacian as the vector from the vertex in question to the barycenter of the first ring neighbors. The advantage of the linear operator is that it does not change in the smoothing process and thus never needs to be recalculated. (b) scale-dependent Laplacian or the scale dependent umbrella operator uses Fujiwara weights proportional to the inverse distance between the vertices. The scale dependent Laplacian operator is represented by $w_{ij}=1/|e_{ij}|$. The advantage of this method is that it preserves the distribution of triangle sizes. The scale dependent Laplacian needs to be recalculated as the vertices move. (c) Curvature normal approximation in which the tangential component of the Laplacian is eliminated using weights represented by,

$$w_{ij} = \cot\alpha_j + \cot\beta_j \tag{29}$$

Where, α_j and β_j are the angles opposite the edge in the two triangles that share the edge. In this study, the umbrella operator has been used for mesh smoothing.

3.3.6 Final Mesh Assembly

After using the Laplacian smoothing algorithm, the resultant mesh is a 3D surface mesh with triangular elements. Figure 36 shows the progression of mesh from step 1, image segmentation to the mesh after Laplacian smoothing operation. The top image shows why the surface after the initial image segmentation process is not suitable for use in finite element analysis.

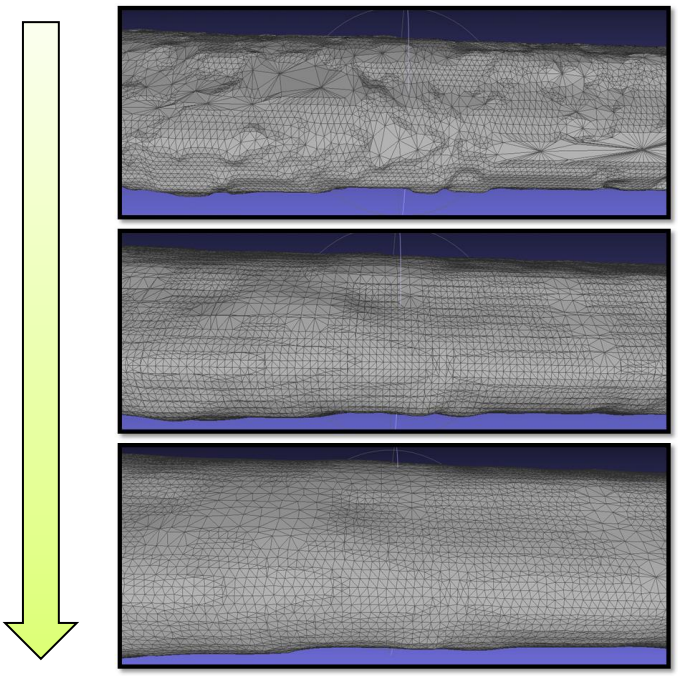

Figure 36: Progression of mesh from image segmented 3D surface model to a smoothed 3D surface model

Figure 37 shows the comparison of capacitor plate as a CT scan render prior to applying the entire conversion process and shows the same capacitor plate after the process. The black colored region showing in the initial image is the noise introduced in the scan data because of the size and number of parts in the fuze component.

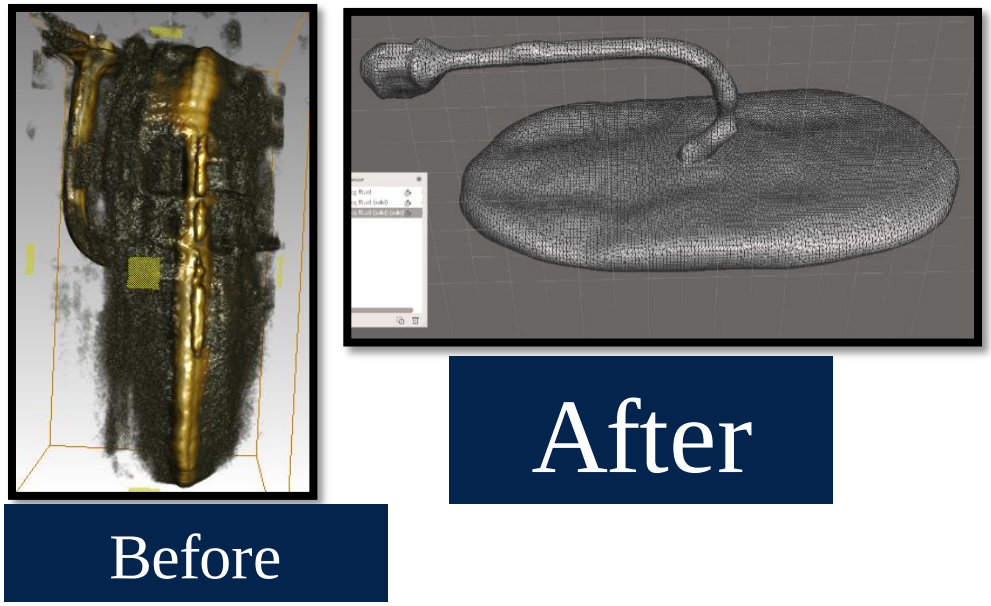

Figure 37: Comparison of CT scanned render and CT data converted meshed part

This model is in surface tessellation file format and is exported into Hypermesh for further meshing and assembly. The procedure stated until this point is repeated individually on the different regions of interest that need to be incorporated into the final model. These different models are imported in Hypermesh where they are assembled as shown in Figure 38.

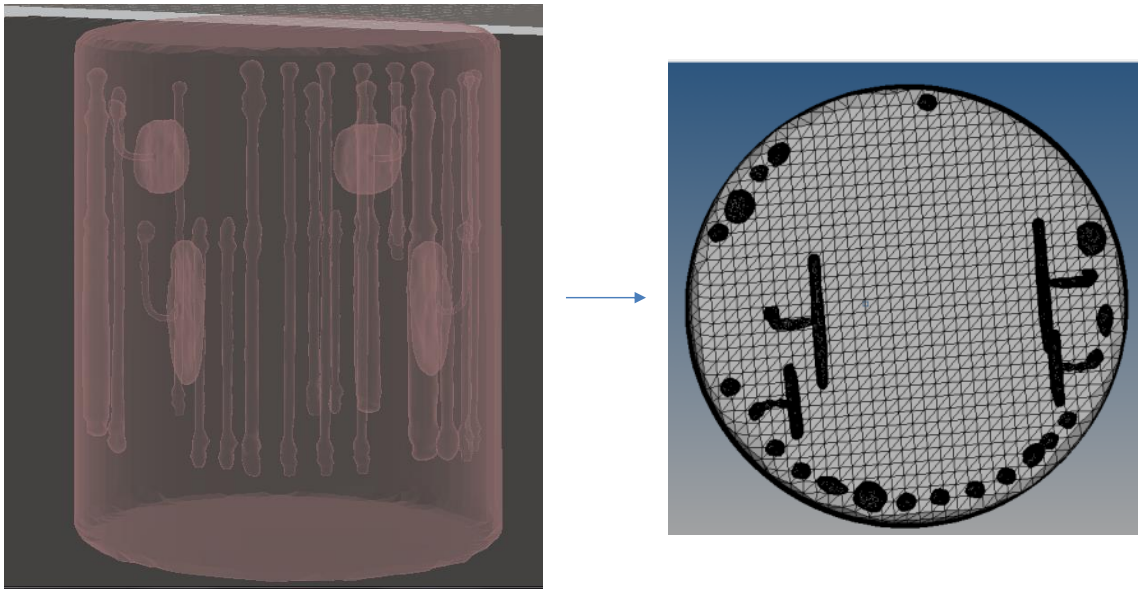

Figure 38: Mesh assembly in Hypermesh software

The fuze device in the study has a total of 24 components with the 24th component being the cylindrical block of resin. Each component was isolated, repaired and cleaned up individually. Each component after the surface mesh cleanup procedure is still a surface mesh and not a solid mesh. This section describes the procedure to assemble the individually meshed components and embed them in a cylindrical resin block. Each component would be sharing nodes with the surrounding resin at the interface. Figure 39 shows the steps involved in assembling the mesh

Figure 39: Procedure for Mesh assembly

3.3.6.1 Parent Assembly Template

Assembling components in a finite 3D space is done in CAD modeling software by defining position of each component with respect to a reference. The reference can be any point, line, face, axes or datum planes. This procedure is possible to do since the all the dimensions are known to the user. In case of assembling micro-CT scanned meshed parts with irregular geometry, making relative distance measurements of each component with respect to one reference can be a very time consuming and error prone task. Thus a novel approach has been developed to make an assembly of meshes with unknown relative measurements.

Using the process of image segmentation, rather than thresholding individual components, the threshold range is selected in a way that all the visible components in the scanned DICOM data are selected together. This selection picks up all the components although having some amount of white noise at the boundaries. Figure 40 shows the thresholded region and the template mesh with some amount of white noise.

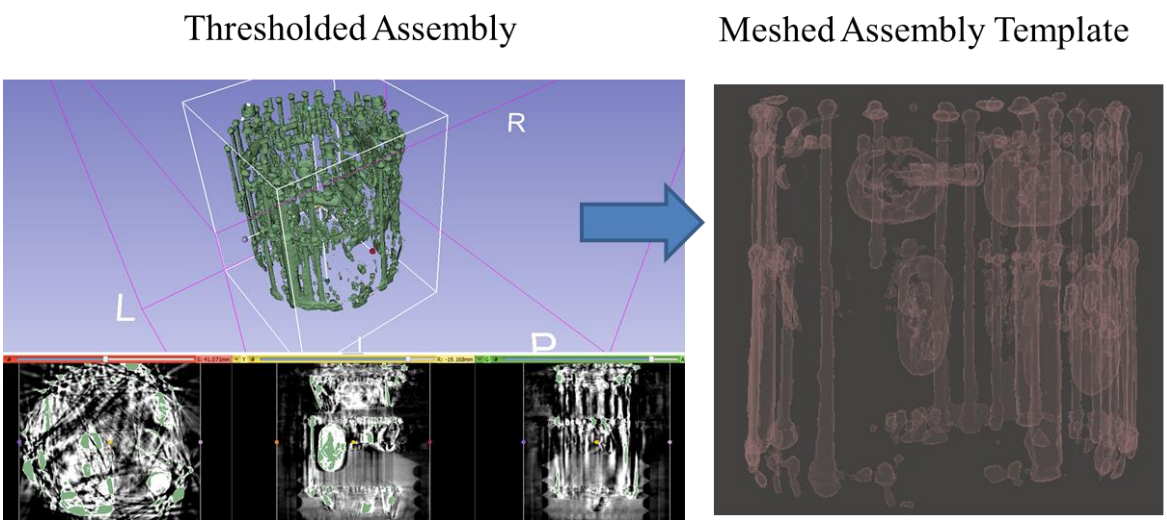

Figure 40: Template creation for part placement

3.3.6.2 Components in Template

The meshed assembly template thus formed has all the components positioned in a finite 3D space in an as-is condition. Next, each component was imported individually and placed and aligned with its counterpart in the template as shown in Figure 41.

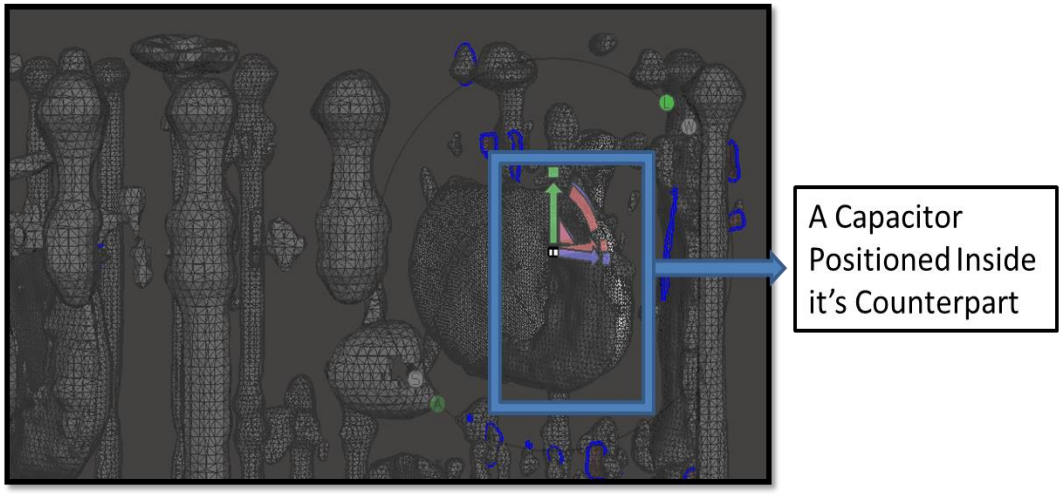

Figure 41: Part placement inside the template

3.3.6.3 Solid Tetra Mesh

An assembly of all surface meshed components is created by following the procedure above. The final step would be to solid mesh the components using tetrahedral elements using the already present surface triangular elements as the seed mesh. Moreover, this was done in a way that the tetrahedral mesh of the surrounding resin did not extend into the components embedded inside and interfere with its own solid mesh. This is done using an existing functionality in the Hypermesh software based on Delaunay triangulation algorithm. Figure 42shows a cross section of a meshed fuze assembly.

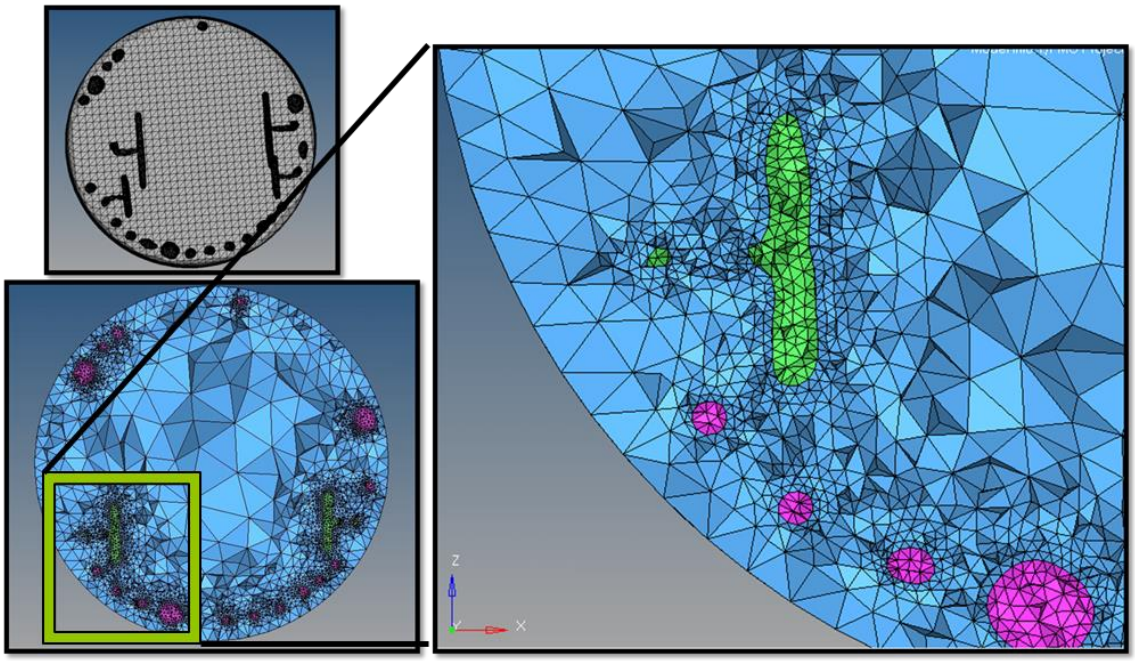

Figure 42: Cross section view of meshed assembly with nodes merging at the component interface

The nodes merging at the interface ensure compatibility and prevent use of contact elements or multi point constraints. The meshed assembly had 1,342,998 elements. This fully meshed model can be exported into an input file compatible with any Finite Element Solver package.

3.3.7 Dimension Accuracy Check

The sub-components thus converted after the entire process are assembled and solid meshed. One of the underlying premises of using CT scanned data for Finite element analysis is to use the real as-is geometry. Thus, it is of prime importance that the final resultant meshed parts have a very good dimensional accuracy. This section throws light on dimensional accuracy of the parts.

There are multiple sources of error as far as dimension related errors go. The x-ray imagery or the dicom data set may be treated as the standard target dimensions to achieve. Given this, conversion of image segmented 3D model into a Poisson surface reconstructed 3D data is a first source of error. The surface fitting process may use sampled points near the surface that may not essentially lie on the surface. Fitting the broken geometry or the geometry with hole with an artificial surface is a source of error. Quadratic mesh decimation meant to reduce the number of elements also produces certain amount of mesh shrinkage further affecting the dimensional accuracy. Mesh smoothing algorithms also result in mesh shrinkage for every iteration run. Thus, it is important to investigate the dimensional error involved.

In this section, dimensions of 4 components measured using CT scan data and those measured after the FE model conversion process have been compared and shown. Figure 43 shows the pin connector component. The image to the left denotes the FE model and to the right denotes x-ray image, also considered as the source for the real dimension. The achieved dimension and the real dimension are found to within 1% error. Similarly

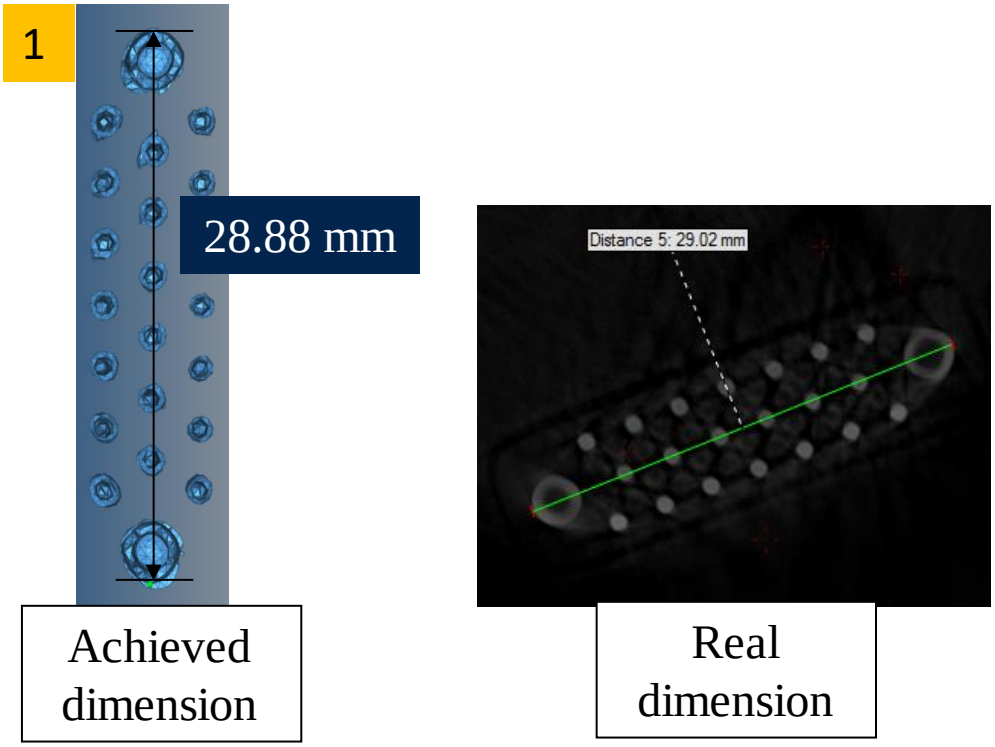

Figure 43: comparison of dimensions of a component

Table 3: Dimension comparison

Sr No.	Real Dimension (CT scan data)	Achieved Dimension	%Error
1	29.02mm	28.88mm	0.40%
2	24.81mm	24.21mm	2.41%
3	11.18mm	10.99mm	1.69%
4	1.60mm	1.56mm	2.5%

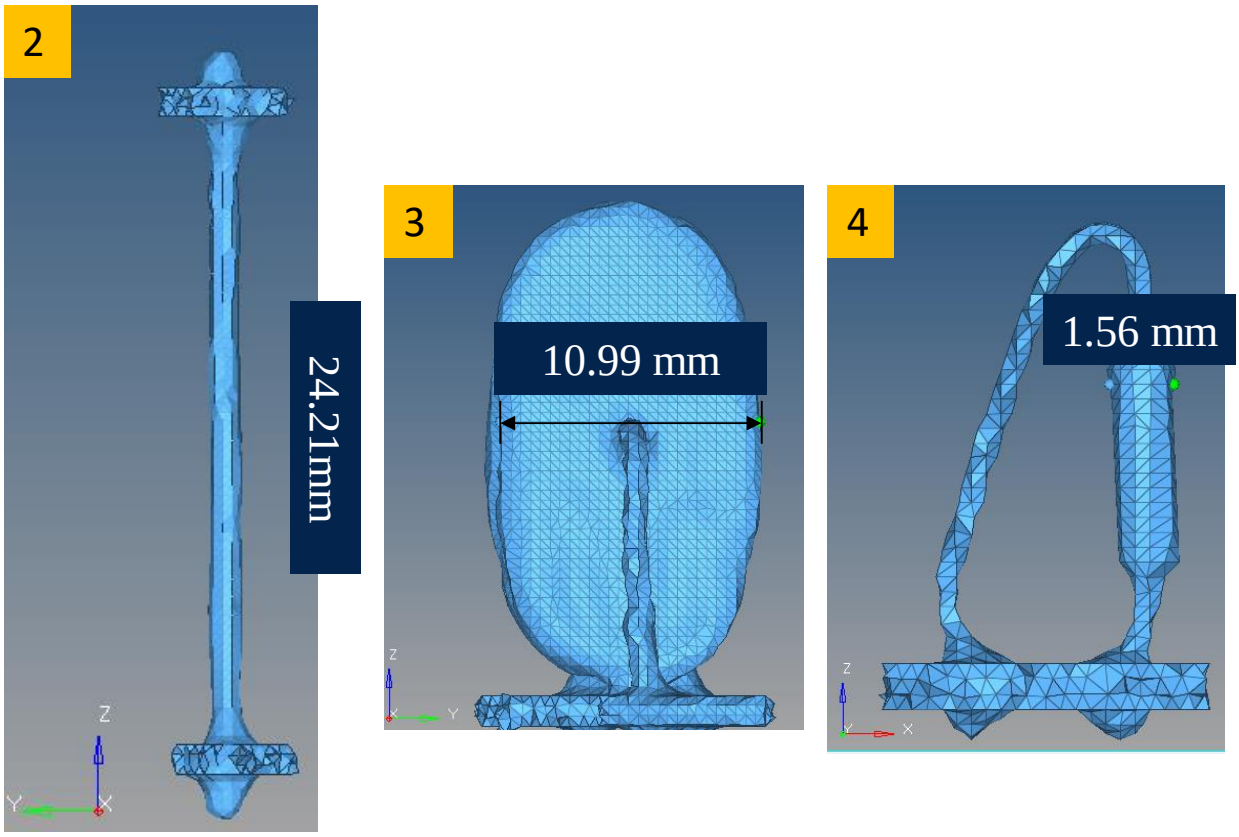

Figure 44: Achieved dimensions for remaining components

Figure 44 and Table 3 show the comparison of real and achieved dimensions. All the parts are found to be within 2.5% error. The dimensional accuracy can be further improved by better image segmentation procedure.

3.3.8 Examples of other meshed models

One of the objectives of this research is to make the developed method generic and applicable to wide range of electronic packages. While fuze electronics is an example of a big assembly converted into a finite element model, smaller board level electronic packages like Ball grid array packages, QFN packages, underfilled packages are examples of commonly found electronic packages in consumer grade and defense grade electronics. Each of these packages were micro-CT scanned and meshed.

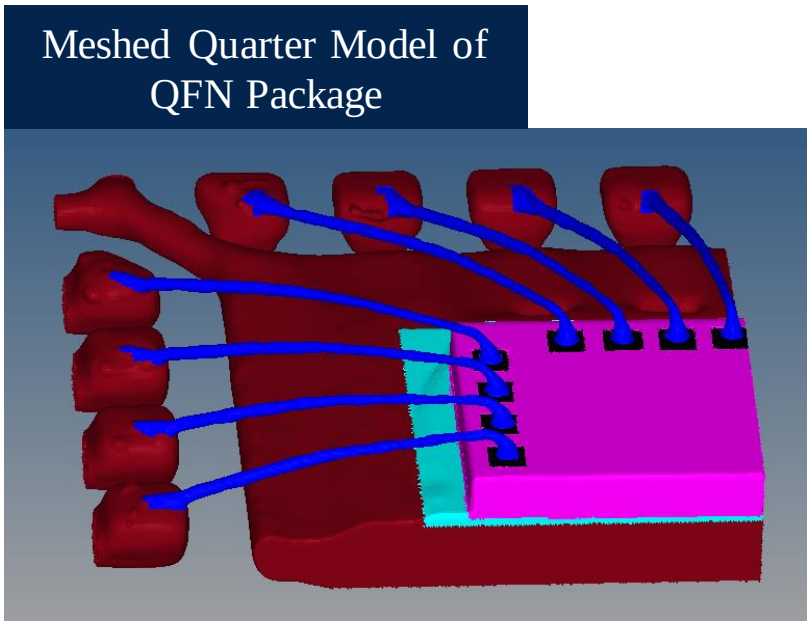

Figure 45: QFN package with wire bonds

The meshed QFN model shown in Figure 45 shows the quarter symmetry model made. This model is a hybrid of CT to mesh converted parts like the lead-frame, leads, solder joint, wire-bond and CAD modeled parts like silicon chip and die attach. The procedure to incorporate the CAD modeled geometry with the CT to mesh converted geometry gives an important ability to incorporate parts that are no detected by CT scan. Parts like Silicon Chip, die attach, copper pads underneath the solder joint are impossible to be detected distinctly by the CT scan.

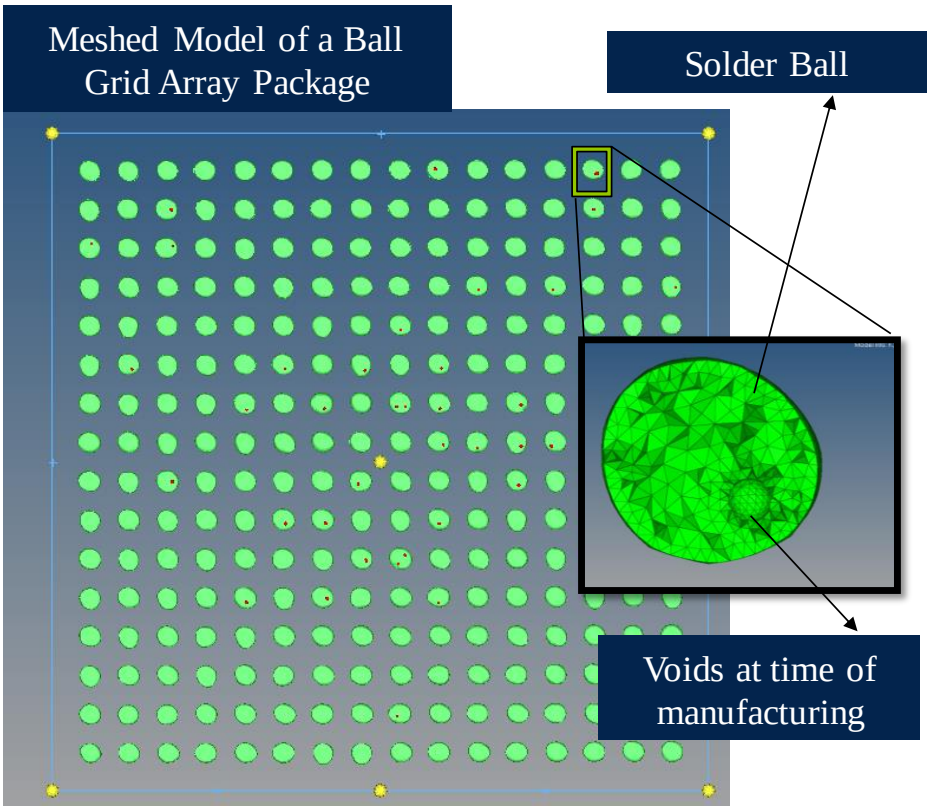

Figure 46: BGA solder balls with voids

Figure 46 shows Ball Grid array package solder balls with voids detected inside of the solder joint. The red dots visible are the voids inside the solder joint. Voids inside the solder joint get detected easily in a CT scan, but in order to mesh it a different procedure has been developed. The voids are meshed separately alongside the solder joint and recorded as a separate entity set. The meshed voids are then deleted to create an empty space in that location that serves as the void as shown the zoomed-in view of the solder joint.

Figure 47 and Figure 48 show a CT to mesh converted underfilled board assembly meshed in Hypermesh and imported to ANSYS APDLM. This model is also a combination of CT to mesh converted model and CAD geometry meshed model. Multipoint constraints were

used to establish load transfer across underfill-solder joint and PCB and underfill-solder joint and package interface.

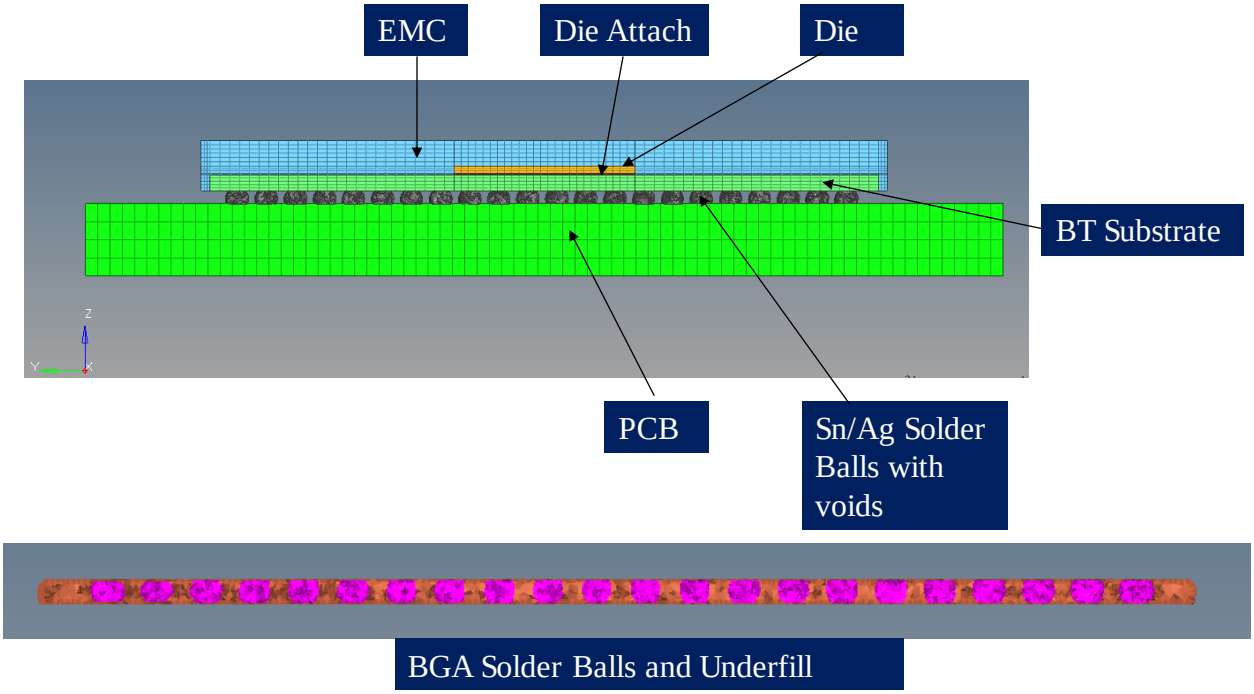

Figure 47: Underfilled BGA assembly

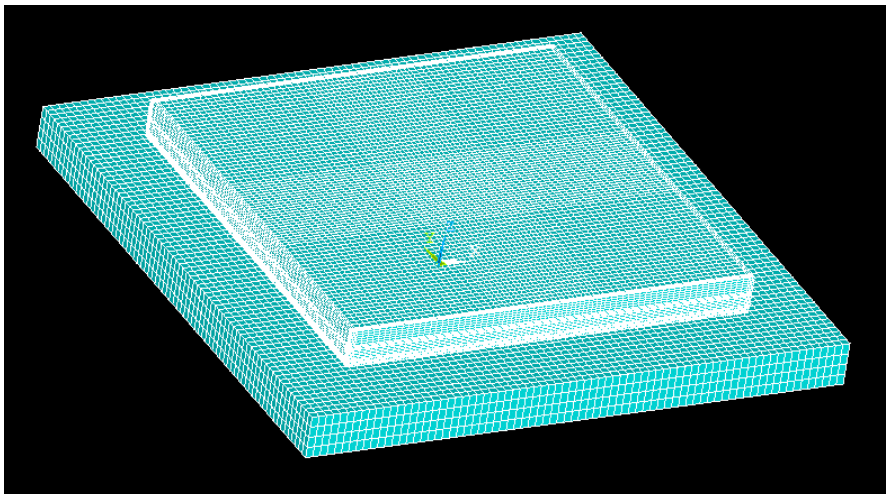

Figure 48: Underfill model imported into ANSYS APDLM

The different meshed models in this section show the ability of the prcess developed to mesh electronic components of different size, shape and also incorporate geometries that

don’t get detected by the CT scanners. In the next sections, two tests studied to test whether the CT to mesh converted models can run efficiently by explicit transient FE solvers and two on implicit solvers solver is stated.

3.3.9 Digital Volume Correlation and Application

Digital Image Correlation is a popular technique in experimental mechanics. The DIC technique correlates two images using the subsets matching algorithm. A subset is a group of pixels considered for correlation. The subset can be on the form of a grid of pixel arrays, for example a 5 X 5 or a 15 X 15 array of pixels. Each subset can be matched using its aggregate intensity values. The following Figure 49 shows two subsets, which the intensity can be seen as the height value in the z-direction [Wei 2017].

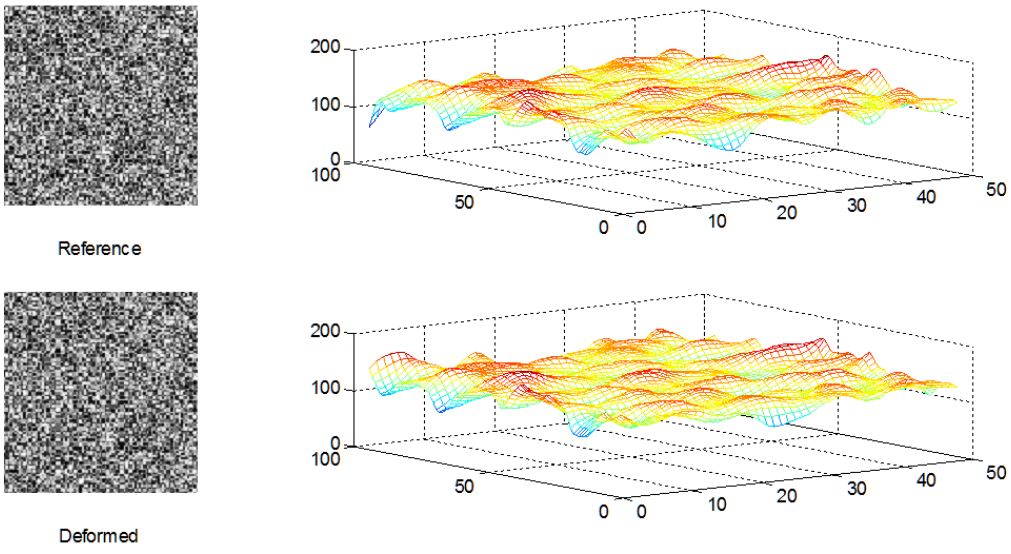

Figure 49: Example of Two DIC images and its Intensity

There are many correlation criterions:

(1) Least Squares

(2) Normalized Least Squares

(3) Unbiased Normalized Least Squares

(4) Scalar Product

(5) Correlation Coefficient

(6) Normalized Cross Correlation

(7) Zeroed Normalized Cross Correlation

(8) Fast Fourier Transform.

Each criterion has a mathematic representation, which is listed as the following:

The Least Squares:

$$\mathrm{LSQ}(u,v) = \sum_{x,y}[I_1(x,y) - I_2(x+u, y+v)]^2 \tag{30}$$

x, y: location in the reference image

u, v: deformation vector component

I_1: reference image

I_2: deformed image

The Normalized Least Squares:

$$\mathrm{NLSQ}(u,v) = \frac{\sum_{x,y}[I_1(x,y) - I_2(x+u,y+v)]^2}{\sqrt{\sum_{x,y} I_1(x,y)^2 \sum_{x,y} I_2(x+u,y+v)^2}} \tag{31}$$

Unbiased Normalized Least Squares:

$$\mathrm{UNLSQ}(u,v) = \sum_{x,y}\left[\frac{I_1(x,y) - \bar{I_1}}{\sqrt{\sum_{x,y}[I_1(x,y) - \bar{I_1}]^2}} - \frac{I_2(x,y) - \bar{I_2}}{\sqrt{\sum_{x,y}[I_2(x,y) - \bar{I_2}]^2}}\right]^2 \tag{32}$$

$$\bar{I_1} = \frac{1}{2M+1}\sum_{i=-M}^{M}\sum_{i=-M}^{M} I_1(x,y)$$

$$\bar{I_2} = \frac{1}{2M+1}\sum_{i=-M}^{M}\sum_{i=-M}^{M} I_2(x',y')$$

The Scalar Product:

$$\mathrm{CC}(u,v) = \sum_{x,y} I_1(x,y) \cdot I_2(x+u,y+v) \tag{33}$$

Normalized Cross Correlation:

$$\mathrm{NCC}(u,v) = \frac{\sum_{x,y} I_1(x,y) I_2(x+u,y+v)}{\sqrt{\sum_{x,y} I_1(x,y)^2 \sum_{x,y} I_2(x+u,y+v)^2}} \tag{34}$$

The Zeroed Normalized Cross Correlation:

$$C(u,v) = \frac{\sum\sum[I_1(x,y) - \bar{I_1}][I_2(x+u,y+v) - \bar{I_2}]}{\sqrt{\sum\sum[I_1(x,y) - \bar{I_1}]^2 \sum\sum[I_2(x+u,v+v) - \bar{I_2}]^2}} \tag{35}$$

$$\overline{I_1} = \frac{1}{(2M+1)^2} \sum_{i=-M}^{M} \sum_{j=-M}^{M} I_1(x+i, y+j)$$

$$\overline{I_2} = \frac{1}{(2M+1)^2} \sum_{i=-M}^{M} \sum_{j=-M}^{M} I_2(x'+i, y'+j)$$

The Fast Fourier Transformation:

$$< f, g > = IFFT(\overline{\mathrm{FFT}(f_{pad})} \circ \mathrm{FFT}(g_{pad})) \tag{36}$$

$\circ$ is vectorized production

$\overline{\mathrm{FFT}}$ is the conjugate of FFT Transform

The criterion is to find the best match between two subsets, which the local minimum should be avoided. The following equations shows the peak of correlation coefficients in the two-dimensional domain. The peak is the best match point between the subsets. The ideal correlation criterion should differentiate the cross-correlation coefficient value around the best match point.

In a deformation field, there is a relation between the rotation and strain, in the 2D, if we only consider the rotation, every point should remain the same on the plane. Therefore, the normal stains are zero in the following equation:

$$\frac{\partial u}{\partial x} = 0.0 \tag{37}$$

$$\frac{\partial v}{\partial y} = 0.0 \tag{38}$$

u is the displacement in x direction

v is the displacement in y direction

The gradient of displacement field is the following:

$$\begin{bmatrix} 0.0 & \frac{\partial u}{\partial y} \\ \frac{\partial v}{\partial x} & 0.0 \end{bmatrix} \tag{39}$$

If we consider the full gradient field, the deformation matrix can be decomposed into a normal strain, shear strain matrix and rotation matrix:

$$\begin{bmatrix} \frac{\partial u}{\partial x} & \frac{\partial u}{\partial y} \\ \frac{\partial v}{\partial x} & \frac{\partial x}{\partial y} \end{bmatrix} = \begin{bmatrix} \frac{1}{2}\left(\frac{\partial u}{\partial x} + \frac{\partial u}{\partial x}\right) & \frac{1}{2}\left(\frac{\partial u}{\partial y} + \frac{\partial v}{\partial x}\right) \\ \frac{1}{2}\left(\frac{\partial u}{\partial y} + \frac{\partial v}{\partial x}\right) & \frac{1}{2}\left(\frac{\partial v}{\partial y} + \frac{\partial v}{\partial y}\right) \end{bmatrix} + \begin{bmatrix} 0 & \frac{1}{2}\left(\frac{\partial u}{\partial y} - \frac{\partial v}{\partial x}\right) \\ \frac{1}{2}\left(\frac{\partial v}{\partial x} - \frac{\partial u}{\partial y}\right) & 0 \end{bmatrix} \tag{40}$$

The first term, the symmetric component, is strain tensor, and the second term, the skew-symmetric component, is rotation matrix. In general, the deformation matrix can be written as the following:

$$\frac{\partial u_i}{\partial x_j} = \frac{1}{2}\left(\frac{\partial u_i}{\partial x_j} + \frac{\partial u_j}{\partial x_i}\right) + \frac{1}{2}\left(\frac{\partial u_i}{\partial x_j} - \frac{\partial u_j}{\partial x_i}\right) = \epsilon_{ij} + \omega_{ij} \quad (41)$$

ϵ_{ij}: strain components

ω_{ij}: skew rotation components

Digital Volume Correlation (DVC) is a full field displacement and strain measurement technique analogous to 2D Digital Image Correlation (DIC) where deformation field is computed by computing the correlation between the grayscale values in the pixels of the two acquired images. In DVC, correlation between the greyscale values of corresponding voxels of two 3D regions of interest is computed. The greyscale values in case of a 3D volume depend on the corresponding material's radio density and atomic number.

There are several DVC algorithms published on, the most widely used involve greyscale-based correlation and feature based correlation [Li 2007] [Lall 2015] [Palanca 2016] [Gillard 2014]. In this study, we have used a greyscale-based correlation algorithm. To improve the computation time, a finite element-based geometry discretization method was used to compute deformation instead of a voxel-based geometry discretization.

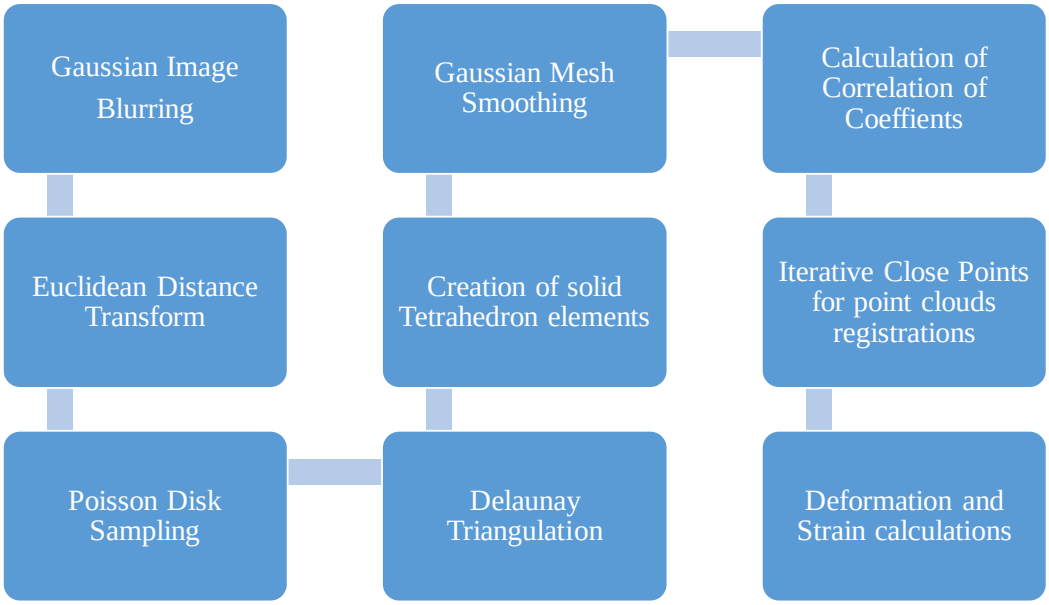

Figure 50: Process flow for FE based DVC

The input DICOM data sets from reference and deformed scans are blurred using a Gaussian mage blurring technique. This removes the high frequency noise from the image data sets. Based on the iso-surface value and Euclidean distance transform plotted on the reference and deformed image sets, Poisson disk samples are generated on every image inside the iso- surface boundaries identified by the iso-surface values. This creates a point cloud over the 3D geometries above the input iso-surface threshold.

Once the point clouds are created, using the point as the node, a Delaunay Triangulation is computed over the points to compute the optimal number of triangulations (tetrahedron elements) possible over the point cloud. A normalized cross correlation algorithm is used to compute the correlation coefficients and find the matching subsets.

$$C = 1 - \frac{\sum_{i=1}^{L}\sum_{j=1}^{M}\sum_{k=1}^{N}\left(V_{ijk}-\bar{V}\right)\left(V'_{ijk}-\bar{V}'\right)}{\sqrt{\sum_{i=1}^{L}\sum_{j=1}^{M}\sum_{k=1}^{N}\left(V_{ijk}-\bar{V}\right)^2\left(V'_{ijk}-\bar{V}'\right)^2}} \quad (42)$$

To account for the rigid body rotations and translations in the deformed scan with respect to the reference scan, Iterative Close Points algorithm was used. DVC technique is susceptible to errors arising out of misalignments in the deformed scan with respect to the reference scan in terms of rigid body translation or rotation. In this work, the fuze the assembly is scanned after every 7 mechanical drop events and thus prone to human error in mounting the assembly at the exact same position with respect to the reference scan. This error in misalignments in the deformed scan is removed by using a principal component analysis-based technique to compute rotations and translations. This done by making a shape aware coordinate system for the two-point clouds using origin based on the centroid of all the points and axes with directions along which the model varies the most.

Consider a set of points p_i to q_i with centroid location c. Formulate a matrix P such that ith column is p_i.

A 3X3 covariance matrix is formulates as

$$M = P.Q^T \quad (43)$$

Eigenvectors of the covariance matrix represent principal directions of shape variation and Eigenvalues indicate amount of variation along each eigenvector.

Let c_D and c_R be centroids of deformed and reference point clouds. Let p_i be coordinates of a random point in the deformed point cloud and p_i' be the coordinates (location) of the point after the alignment. Equation below applies the required rigid translation and rigid rotation to the deformed point cloud and aligns it with reference point cloud.

$$p_i' = c_R + R.(p_i - c_D) \tag{44}$$

Here R is the rotation matrix calculated for the two reference and deformed orthonormal matrices. This is an initial course alignment step. Now, for each transformed deformed cloud point, the closest reference cloud point is assigned as its corresponding point. This is done formulating matrix P as whose ith column is vector p_i-c_D and matrix Q as q_i-c_R. Cross covariance of these two matrices is formed as

$$M = P.Q^T \tag{45}$$

Now the rotation matrix R is found as a matrix that maximizes the trace $Tr[R.M]$. This rotation matrix is found iteratively till a user specified maximum iteration is reached. This procedure aligns the two-point clouds and now the displacement vectors are computed for each node. The Iterative Close Points algorithm is summarized in

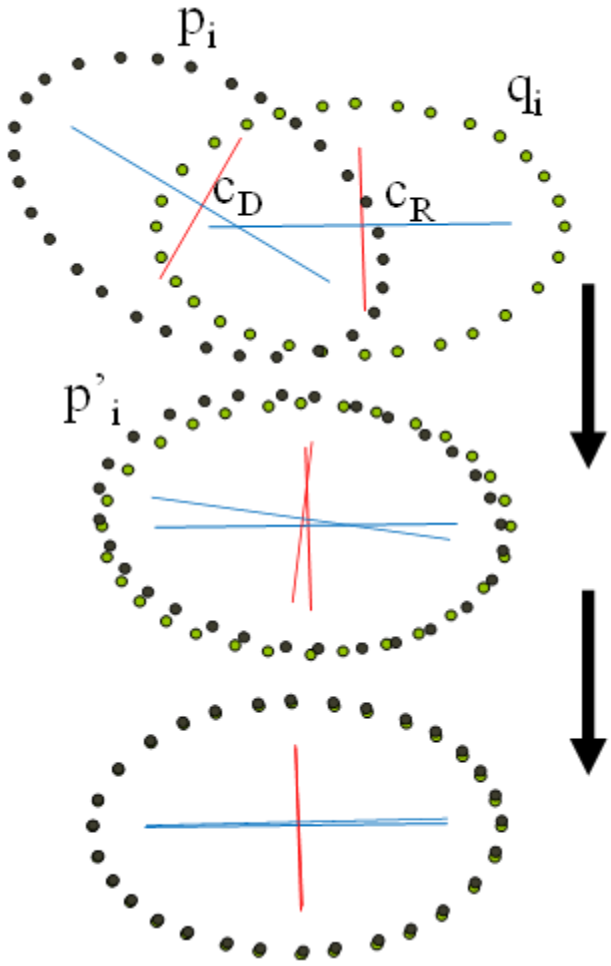

Figure 51: Iterative close points algorithm

After computed the displacement vectors for each node, the displacement at any location is computed by the linear interpolation using the closest nodes. The displacement at any location *(x,y)* will be calculated by a basis function with the degree freedoms .

$$U(x,y)=\sum_{j=1}^{N} C_j \Phi_j(x,y) \tag{46}$$

This summarizes the DVC calculations. This algorithm was developed in house and more details can be found in the reference [Lall 2017].

3.3.9.1 DVC Results for two successive CT scans

DVC computations require determination of several parameters depending on the part being analyzed. These parameters include the iso-surface value threshold. All the iso-surfaces above this input threshold value are picked in the DICOM image data. This parameter determines the geometry over which the DVC computations would be made. Next, the density of Poisson Disk samples created over the selected geometry would determine the geometrical details that would be captured while creating a tetrahedron mesh. Delaunay triangulation over these samples in a 3D space helps determine the number of elements required to mesh the geometry. Analogous to Digital Image Correlation, DVC also requires a subset size and search region in which the best match for the specified subset would be found.

The parameters set out for the DVC scan may be tested for resultant accuracy by taking two successive scans of the part. In this test case, the first scan is treated as reference scan and the second one as the deformed scan. Here the reference scan is the fuze prior to being heat up for acquiring the deformed scan. The second scan is the CT scan acquired after heating the fuze till 100^0C and letting it cool down to room temperature of 24^0C and a wait period of 60 minutes.

The DVC algorithm was run on this data set. In an ideal case, the deformation contour plots along each axis must show zero deformations all along the volume of the part as the reference scan acquired prior to heating the fuze would be at ambient temperature and the second scan acquired would be after allowing the fuze to cool down to ambient

temperature. Figure 52 shows the deformation contour plot for DVC algorithm run on the fuze device. Prior to acquiring the second scan the fuze assembly was also removed and loaded back in to allow it cool down. This procedure was followed to test the accuracy of DVC with iterative close points algorithm that would remove the rigid body translation and rotation. This procedure was followed to replicate a more realistic scenario.

As seen from the contour plots in the Figure 52, the deformations are not zero ever where, but found to be close to zero. This can be attributed to the randomness in creation of samples and Delaunay triangulation of the two domains. The two geometries have different number of samples and elements created each time, even though the all the parameters are kept constant. This difference in creation of point clouds, results in error in DVC computations.

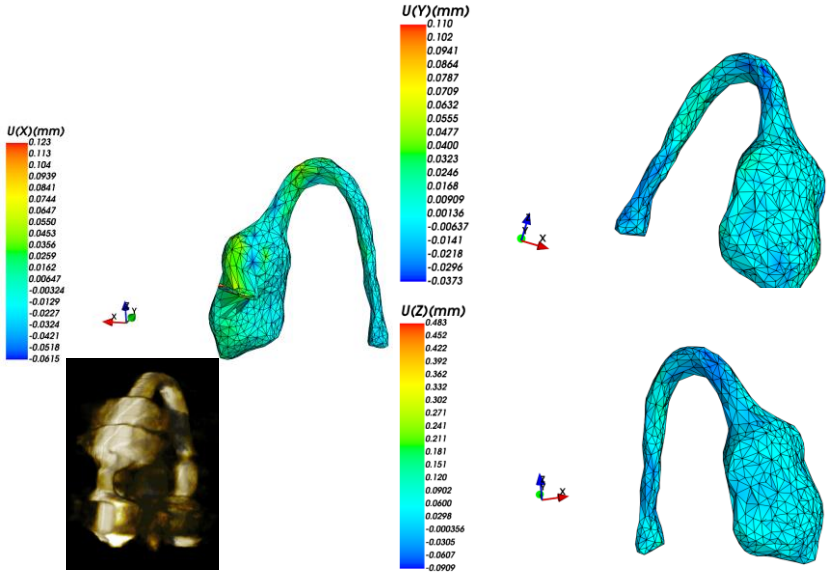

Figure 52: Calibration scan results showing deformation contour plots

Chapter 4 Validation Test Cases

In this section, 4 test cases to investigate the utility of the CT to Mesh conversion process developed earlier is elaborated on. Validity of the FE model results with the experimental data and ability of the resultant mesh to run through transient explicit FE simulation has been tested.

4.1 Test Study for BGA 256 package subjected to Three Point Bend Load

The process of conversion of CT data to a Finite Element mesh stated in prior sections is tested on PCB with a BGA256 package. The intent of the study is to test the accuracy of the results of the FE model made using the developed technique. A BGA (Ball Grid Array) package with 16 X 16 grid of solder balls is known for its relatively higher I/O count in comparison to the packages of similar dimensions. It has also gained popularity for the package architecture offering improved reliability and ease of manufacturing. The solder balls while under reflow self-align and thus offer a much higher yield.

In this test case, a FR4 PCB with PBGA 256 package with SAC 305 alloy is subjected to a three-point bend load. Displacement data from Universal tensile testing machine (Instron) is collected. 4 strain gauges are attached to the back side of the PCB with the package and the assembly is subjected to a three-point bend flexure test. A load of 100N is applied on the simply supported beam at the center location on the package top surface. The load vs displacement output for the test from the Instron machine is recorded. Simultaneously, real time strain data from the 4 strain gauges is also recorded while the flexure test is underway.

The peak displacement and Load Vs Displacement data found at the PCB's bottom center region and the 4 strain values from the strain gauges are used to compare against the same data recorded from the FE model created of the package in created in Hypermesh and run in Ansys APDLM.

4.1.1 Experimental Setup

The package assembly with strain gauges and respective connections to a data acquisition setup is shown in Figure 53.

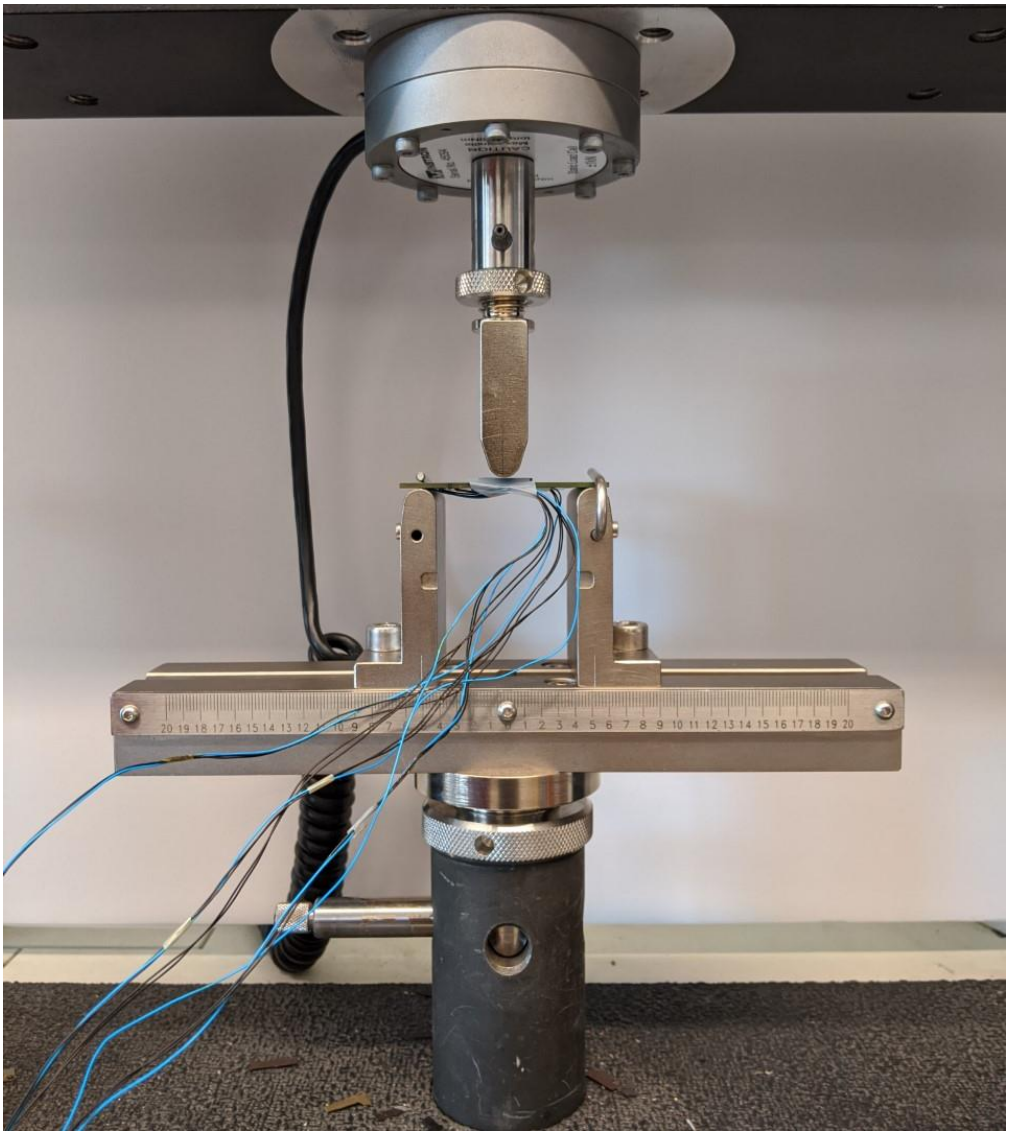

Figure 53: Three-point bend setup with PBGA 256 package board

A load of 100N applied at the rate of 1N per minute was applied to the assembly. A span length of 61mm with 1.5mm over-hang on both sides was setup for the test. Figure 54 shows the PCB back side with the strain gauges attached. Strain gauges numbered 1 and 2 are on attached at symmetric location about the center line of the BGA package. In a three-point bend test the strain should be symmetric along the center line at these two locations. Strain gauges 1 and 2 were made to orient along global X axis direction that is along the length of the PCB where the strain would be highest relative to Z axis in lateral direction and Z axis along out of plane direction.

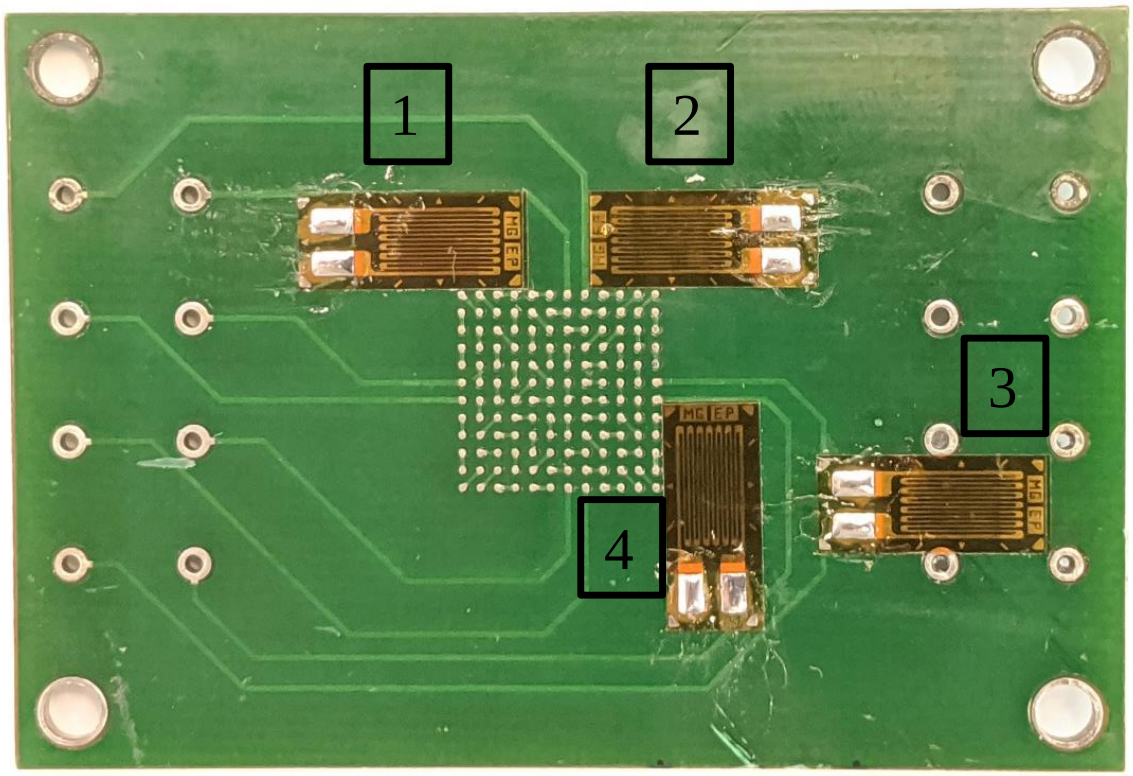

Figure 54: Location of 4 strain gauges at the back side of PCB

Strain gauge number 3 is also aligned along x direction but further towards the support, away from the center line. The expected X direction strain should be relatively lesser in comparison to strains at location 1 and 2. Strain gauge number 4 was attached near the

bottom corner of the PBGA package aligned along the Z axis. The Strain along Z axis would be the least in comparison to any other strain gauges.

4.1.2 Finite Element Model Setup

The package assembly was CT scanned for capturing the solder joints. The solder joint CT scans with the real as is shape and voids were converted into a 3D tetrahedral mesh. The PCB and the package were meshed separately in Hypermesh using hexahedral elements. The meshed solder balls with voids and the mesh assembly is shown in Figure 55 and Figure 56.

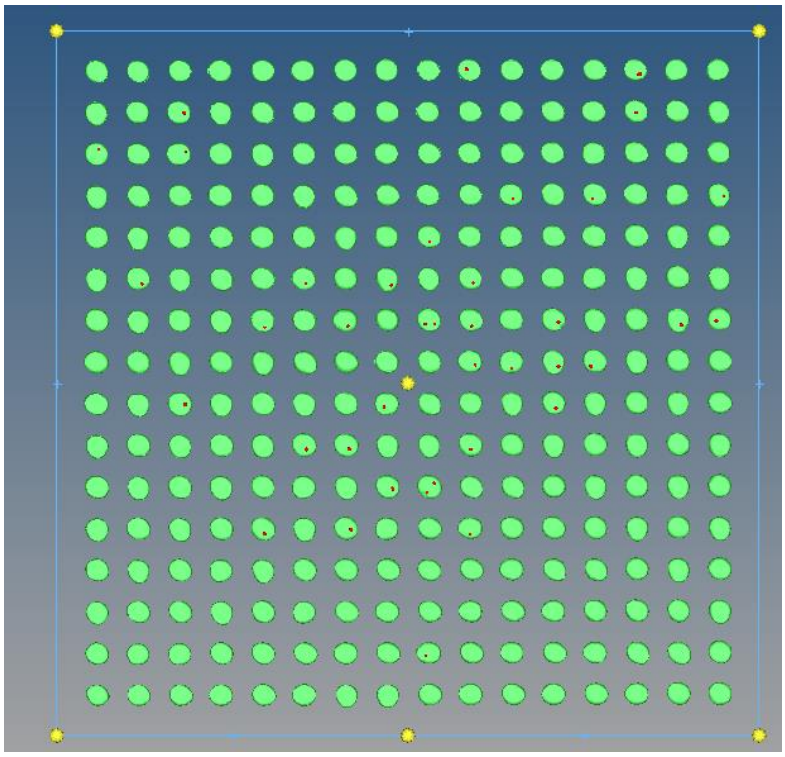

Figure 55: Mesh of BGA256 solder ball with voids

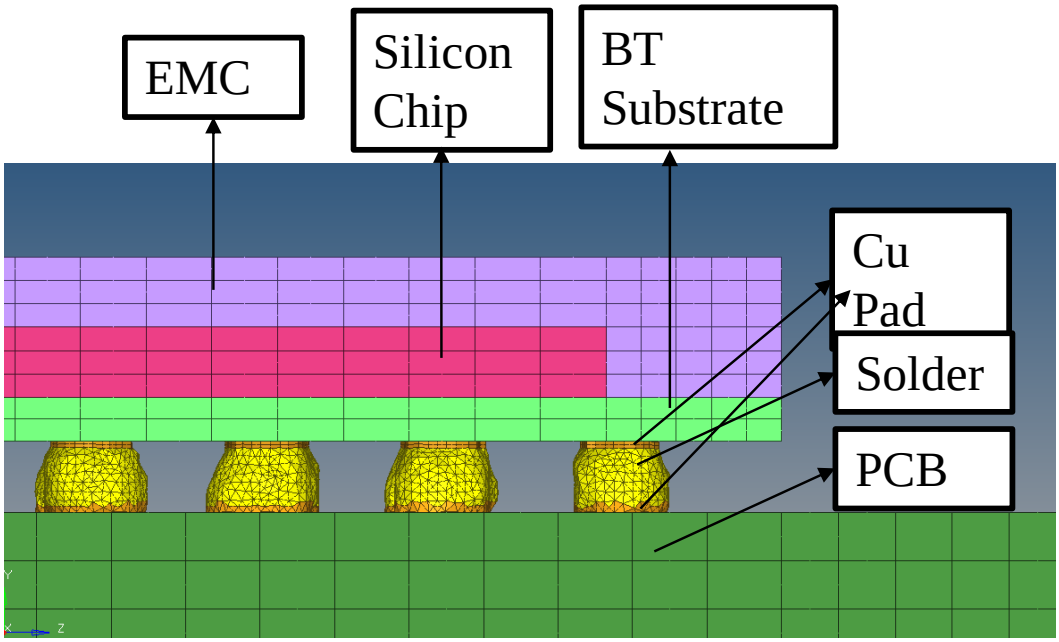

Figure 56: Mesh assembly with different components in the package

The interface from PCB to Solder balls and Solder balls top to copper pad and package was tied using multi-point constraints. This mesh assembly was imported to Ansys APDLM and boundary conditions for three point bend test were applied as shown in Figure 57.

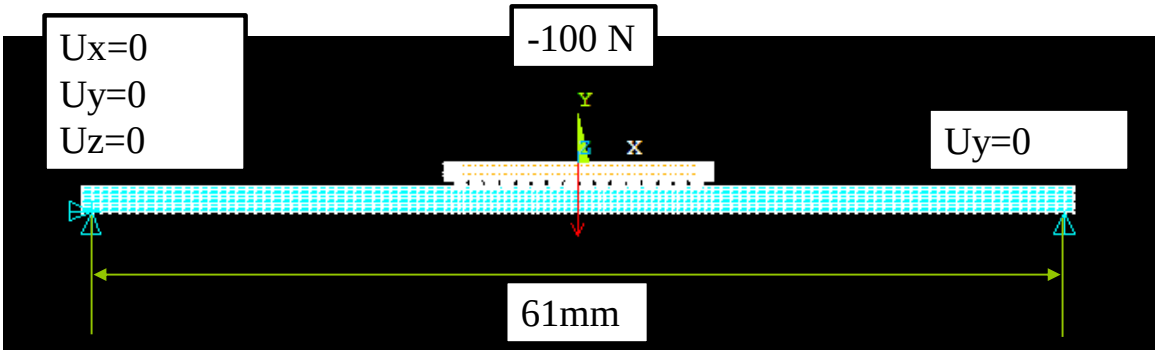

Figure 57: Boundary conditions and load application

Table 4 Shows the material properties applied to each component in the package assembly.

Table 4: Material Properties for PBGA 256

Component	**E (GPa)**	**υ**
EMC	25.52	0.3
Si Chip	163	3.5
Die-attach	3.1	0.35
Solder, SAC305	54	0.34
BT Substrate	12.5	0.3
Cu Pad	129	0.34
PCB	17 (X, Y),7.43 (Z)	0.39, 0.11

SAC305 solder alloy material properties were applied to the solder. The material properties were obtained from [Lall 2015]. Figure 58 shows the locations for the extraction of strain in the model as per the location of the strain gauges on the board and the dimensions of the strain gauge itself.

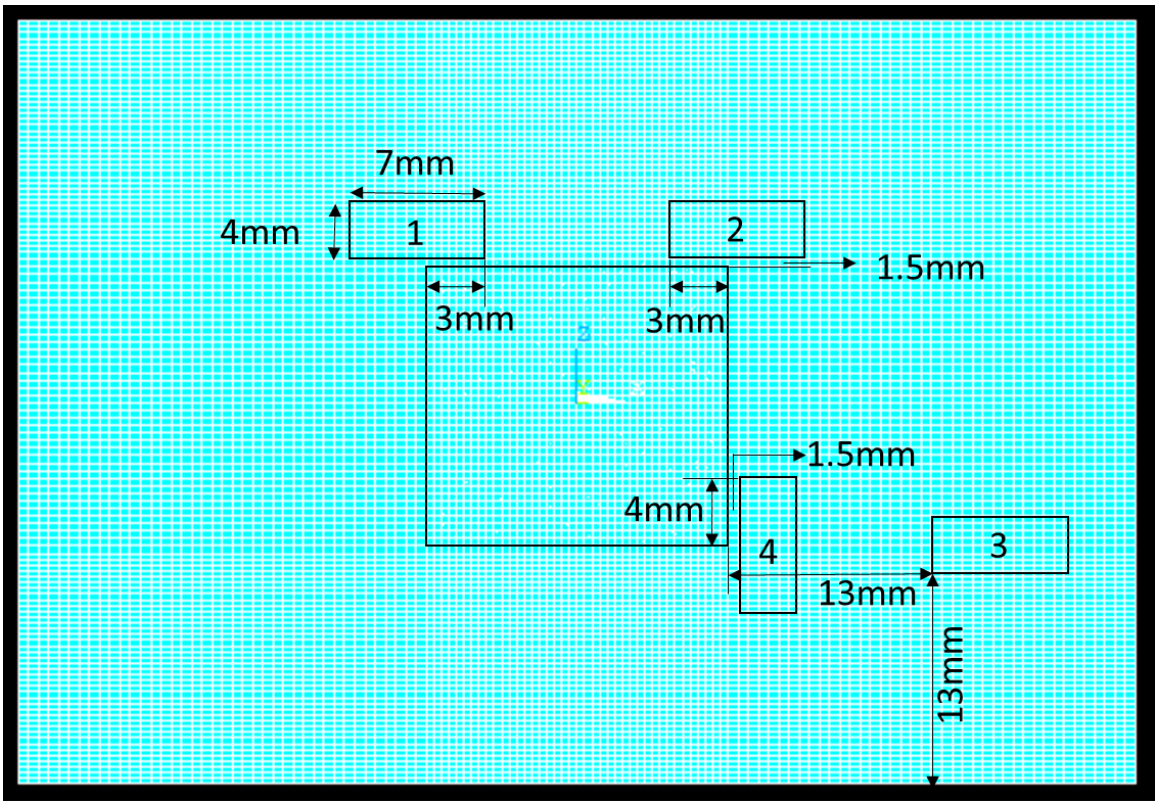

Figure 58: Strain extraction points on the back side of the PCB in FE model

4.1.3 Results and Conclusions

Contour plot for Y displacement found from the FE model results is shown in Figure 59.Load Vs Displacement data found experimentally and from the FE model are shown in Figure 60.

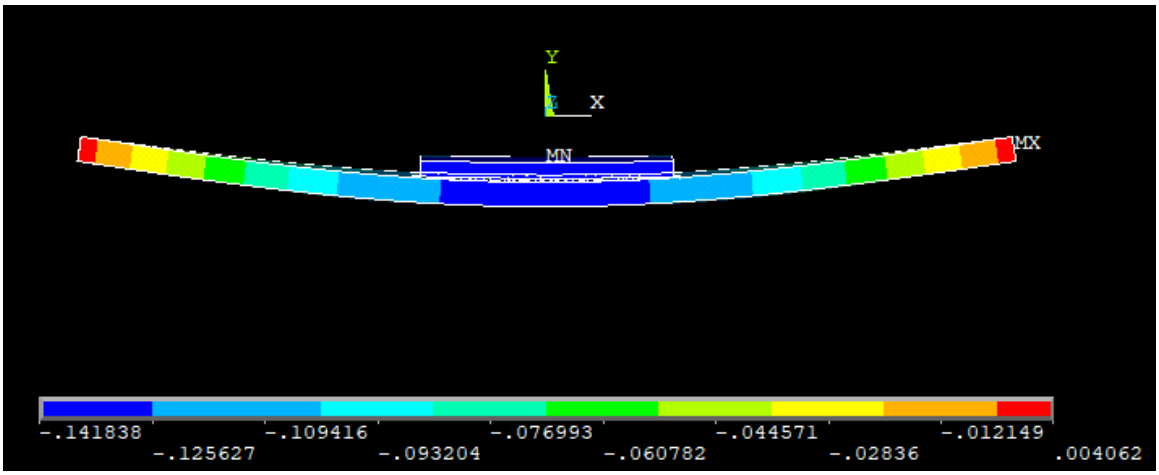

Figure 59:Contour plot of Y displacement

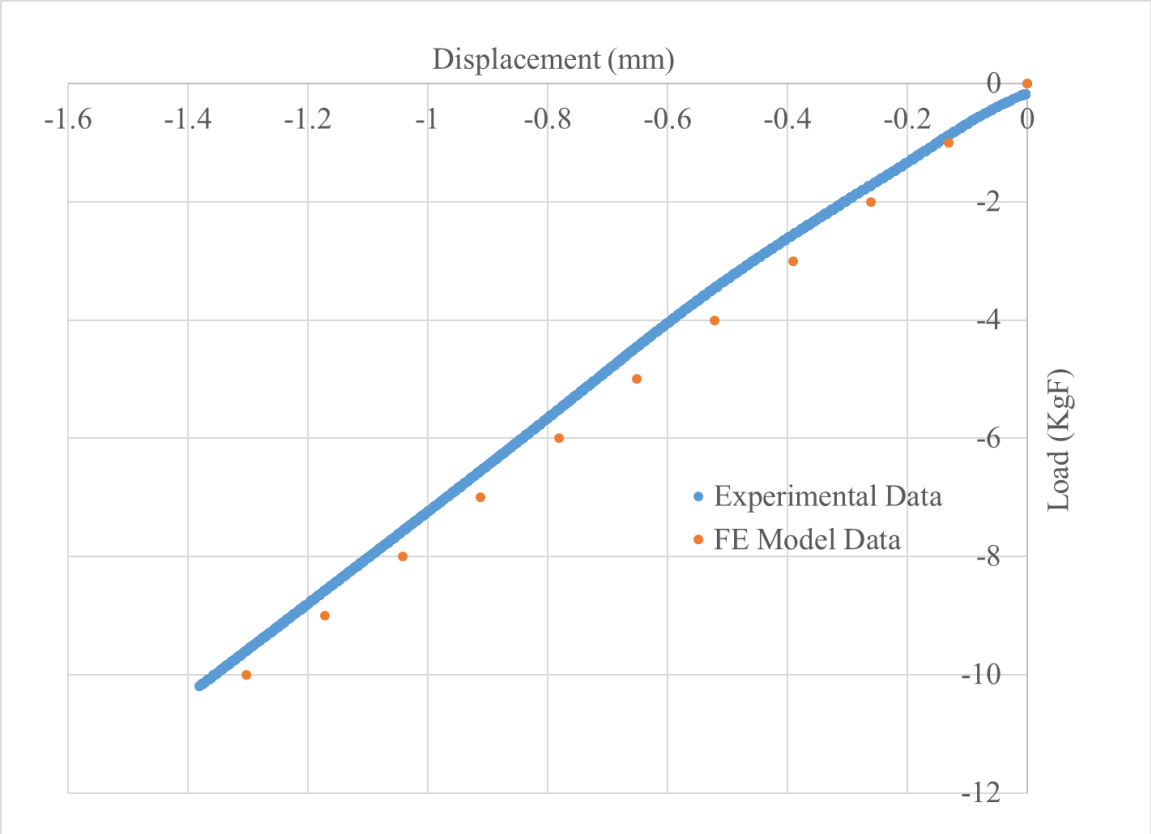

Figure 60: Comparison of experimental and FE model Load Vs Displacement results

The displacement result from the FE model was extracted at the PCB bottom side center node. The graph shows good correlation between the FE model and experimental load Vs displacement data. Though the maximum displacement obtained from the experimentation was found to be 1.38 mm while that found from the FE model was 1.301mm. This result is summarized in Table 5. A 5.72% error was found in the FE model results in comparison to the experimental data.

Table 5: Comparison of Displacements

	Max Displacement Comparison
Experimental Result	1.381 mm
FE Model Result	1.301 mm
Error%	5.72%

Strains in X direction or Exx were extracted from the from the 4 locations shown in Figure 58. Table 6 shows the comparison of strain for the experimentally obtained strain gauge data and the FE model results.

Table 6:Comparison of strain

	1 Exx strain	2 Exx strain	3 Exx strain	4 Ezz strain
Experimental Result	0.0046	0.0050	0.0014	X
FE Model Prediction	0.004016	0.004065	0.00116	0.000051
% Error	12.6	18	17.14	

Strain data found at location 4 was found to be smaller than the resolution of the strain gauge and thus deemed unfit to report. The resolution of the strain gauge is 0.1% change in resistance. An error ranging from 12% to 18% was found for locations 1,2 and 3. Though this error is reasonably acceptable. The reason for this error may be attributed to the bigger size of the strain gauge, the small mismatch in the location of the node with respect of the center of the strain gauge and minor variabilities in application of boundary conditions in the FE model with respect to the experimentally displacement. Also, the material properties

applied to the FE model were not experimentally tested and verified. Also, the strains and displacements predicted by the FE model were found to be under predicting the value obtained via experimentation which is what should be expected.

Upon examining the strain more, it was observed that the strain values for 1 and 2 were nearly symmetric but the mismatch could be attributed to the small error in strain gauge placement. Strain at location 1 and 2 were found to be higher in comparison to the 3 as expected.

In conclusion the test case for the PBGA256 package showed acceptable error in displacements and strain measurement. The CT data to FE mesh technique used for making the PBGA 256 model was found to underpredict the displacement and strain. The nature of strain distribution obtained from the FE model also was found to be in tandem with the experimental results from the three-point bend test.

4.2 Test study for Explicit Solver

A fuze device is often subjected to harsh environments, with high g mechanical shock being the most dominant form of loading it undergoes. In this study, the fuze has been subjected to a 10,000g mechanical shock event using an explicit FE solver Abaqus CAE. The use of an explicit solver would fully test the mesh quality as it depends on the element size. The fuze device discussed earlier was meshed using the micro-CT data to finite element model procedure described earlier. Figure 61 shows the meshed cross-section of the fuze device.

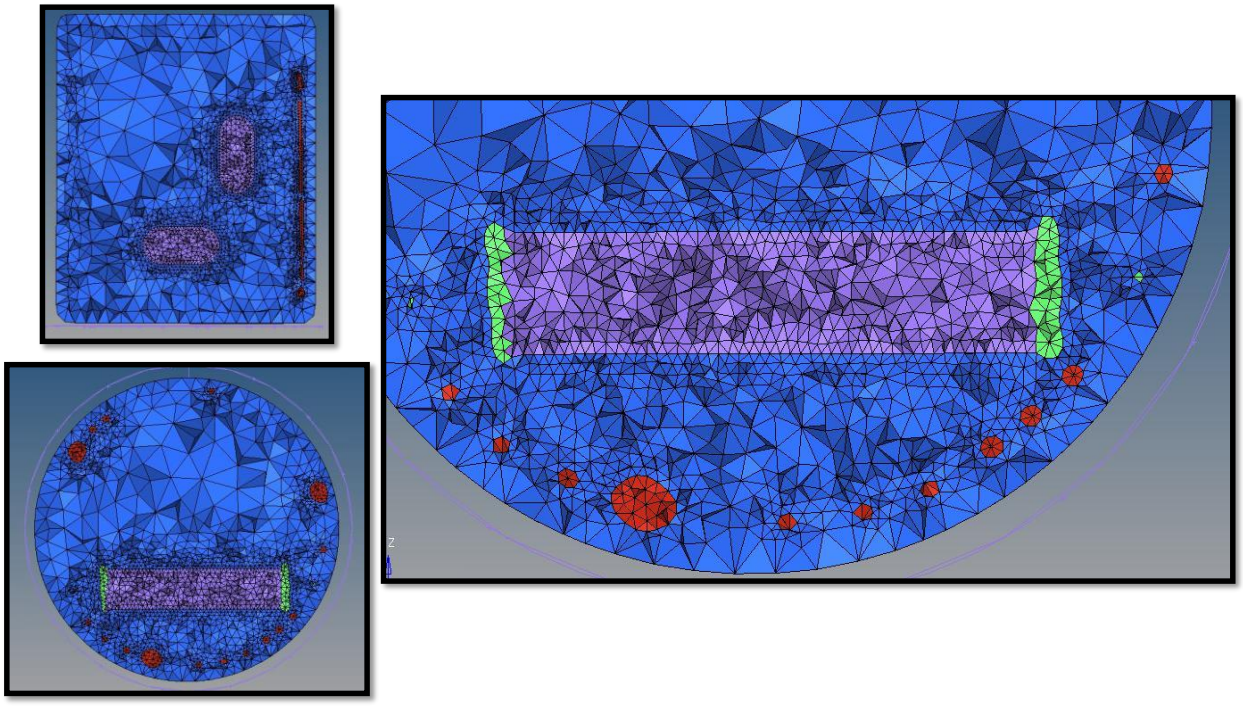

Figure 61: Meshed Fuze cross -section

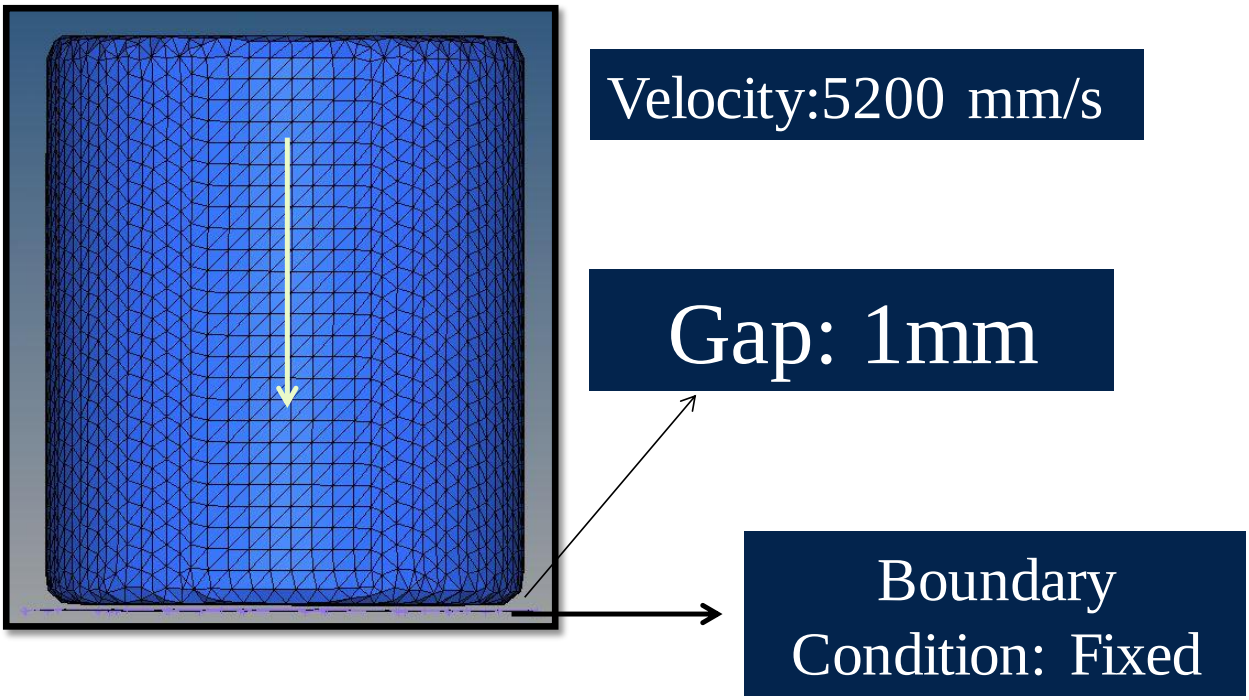

Figure 62: Finite element model setup for explicit drop simulation

To apply a 10,000g load, a predefined velocity field of 5200mm/s was applied on all nodes of the model. The reference point of the rigid surface was fixed and elements R3D4 and C3D4 were used in the model. Figure 63 shows the contour plot of averaged Von Mises stresses over the cross section of the 4-capacitor plated embedded inside the resin.

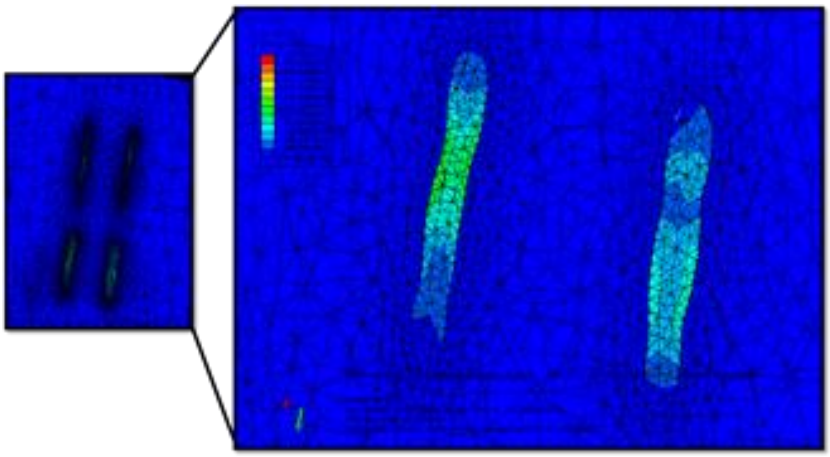

Figure 63: Contour plot of Von-Mises Stress over Capacitor plate cross section

As seen in the Figure 63 and Figure 64, the stress contour changes over the resin and capacitor interface while satisfying compatibility conditions. Figure 64 shows the stress contour plot over all the capacitors.

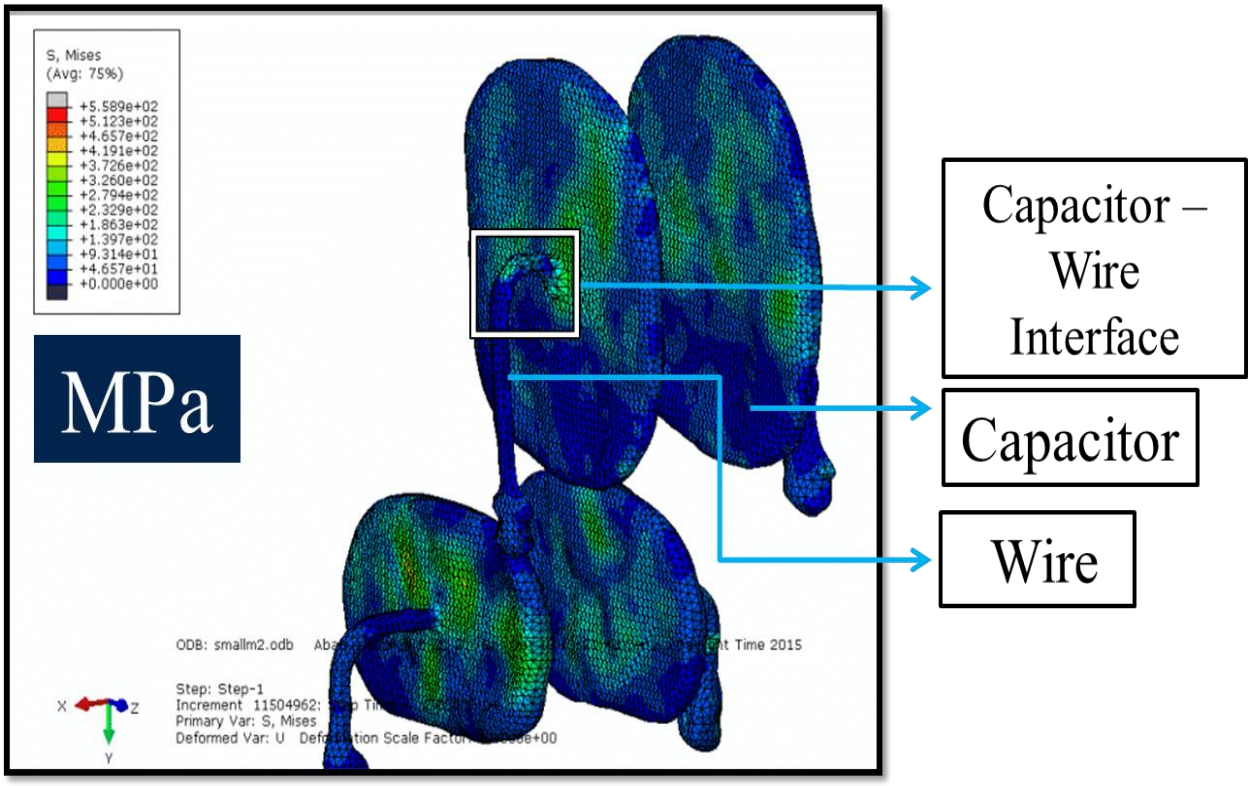

Figure 64: Von Mises Contour Plot over capacitor plates

Figure 64 shows the capacitor sub-assembly, made of connecting wire and the capacitor. The capacitor-wire interface shows higher stress values relative to the surrounding region as one would expect as the wire tends to separate and come closer to the capacitor. Thus, a test case of a highly dynamic, non-linear FE model, made using the micro-CT data has been shown in this study. Figure 65 and Figure 66 show progression of Von Mises stresses on the capacitor plates and the protective cage during the drop event. The Figure 67 and Figure 68 show the stress and strain at the critical nodes , showing the ability of the model

made to run as expected and able to give design insights an engineer could seek at by using the process developed. The intent of these results is to show the similarity of the CT to mesh converted FE models to any other regular FE models and the design insights that could be achieved leveraging the advantages of the process developed.

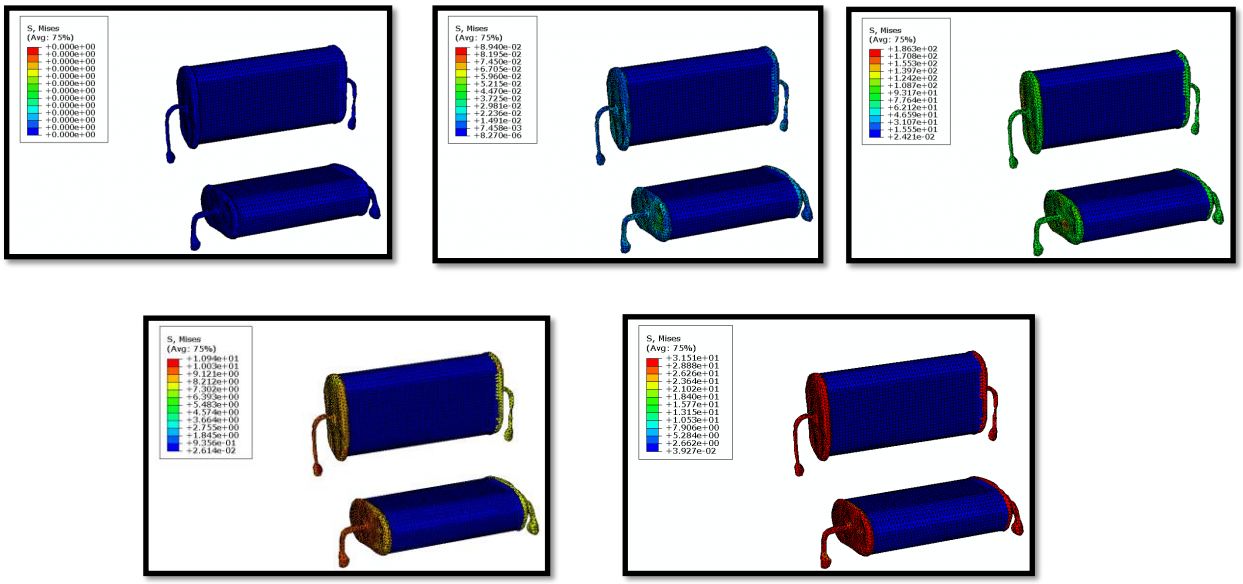

Figure 65: Progression of Von-mises stresses over the Capacitor plates

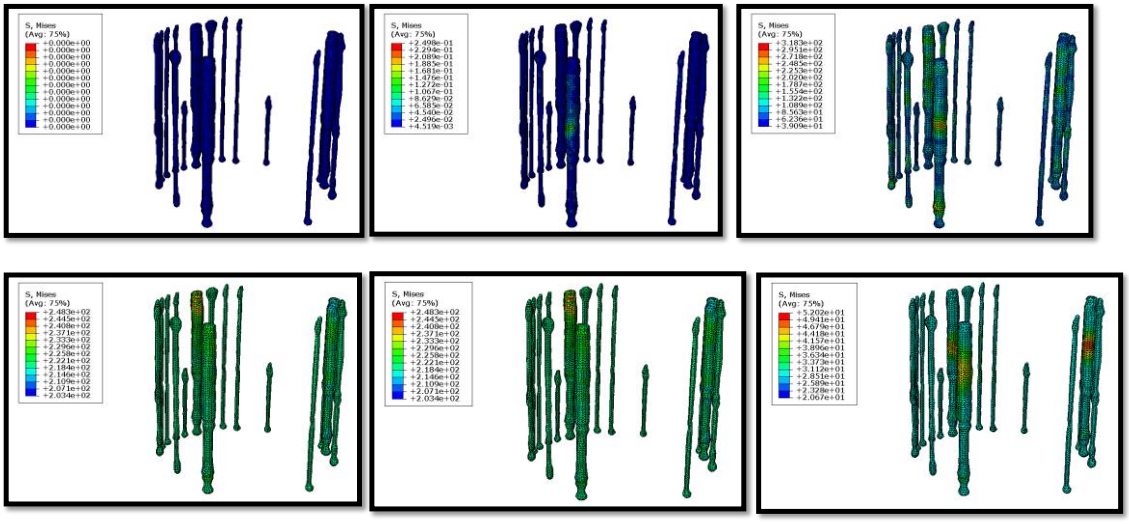

Figure 66: Progression of Von-Mises stresses over the Protective cage structure

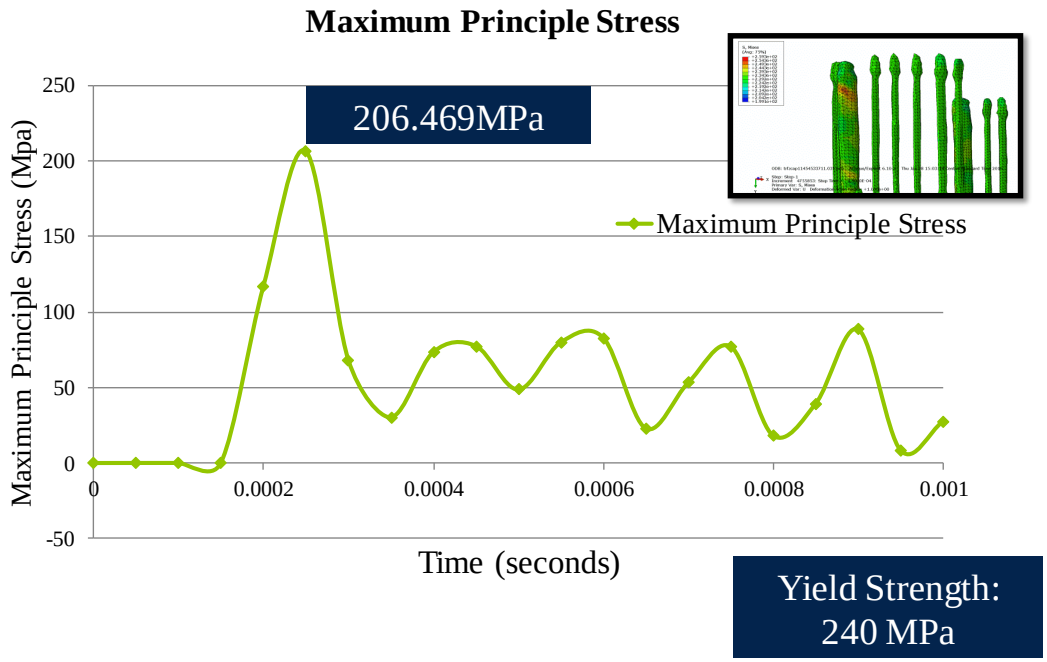

Figure 67: Maximum Principle Stress on the critical node of the critical protective cage member

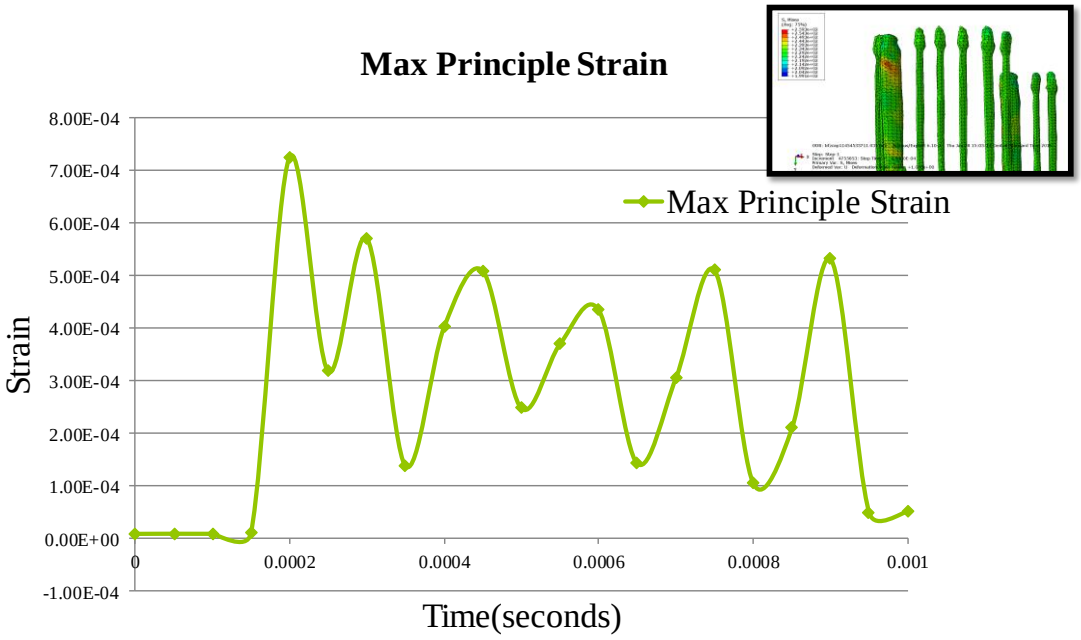

Figure 68: Maximum Principle Strain on the critical node of the critical protective cage member

4.2.1 Conclusions from the test study

Using the CT scanned data to make finite element models has been studied and researched on in the medical industry. All the data fully visible in a micro-CT scanner, has been converted into a finite element mesh that is the high-density material detected by the micro-CT scanner. The low-density material (resin), not detected by the x-ray too was incorporated in the final model. The method developed allowed for a direct conversion of the micro-CT data into a finite element, thus removing the time-consuming conventional CAD modeling step. Thus as-in geometry was used to make the model rather than the idealized geometry that we usually use when using conventional CAD modeling process. The method developed gave good control over the mesh density element size and allowed for mesh refinement over regions of interest. This functionality would make the model fit for both implicit and explicit solvers. Control over number of elements can help in faster solving times for models run using implicit solver and control over element size would help in achieving faster solving time for models run using explicit solver. The method allowed for nodes merging at the interface of the embedded components thus helping prevent use of contact elements and multi point constraints.

The next section illustrates a second case study where a thermal load is applied to a fuze device and the ability of the CT to mesh converted geometry to predict the nature of deformation after the application of load is investigated using experimental data and finite element modeling.

4.3 Test Study for Fuze under application of Thermal load with Micro CT data and Digital volume correlation

The YXLON μCT Cougar system at CAVE facility in Auburn University is used for studying the fuze. The YXLON μCT Cougar Machine is a CT scanning machine with a resolution of less than 1 μm and a measurement resolution of 0.1 μm. The scanner is capable of 70 to 160 kV voltage and 200 μA current. The x-ray microscopic computed tomography (μCT) system has been used to generate the 16-bit digital volume data. The x-ray detector has ability to image the x-ray attenuation of x-rays through the object. The electronic assembly of interest has been scanned to create a volume render with 1024X 1024 slices along each axis to perform DVC when the fuze is under an application of a thermal load.

In order to apply a thermal load, two flexible element heaters of 1-inch width were pasted on the top 1-inch band of the fuze. A thermocouple was inserted between the element heater and the cylindrical surface of the fuze to monitor the surface temperature of the fuze. Figure 69 shows the fuze attached with element heater and a thermocouple and mounted inside the micro-CT scanner.

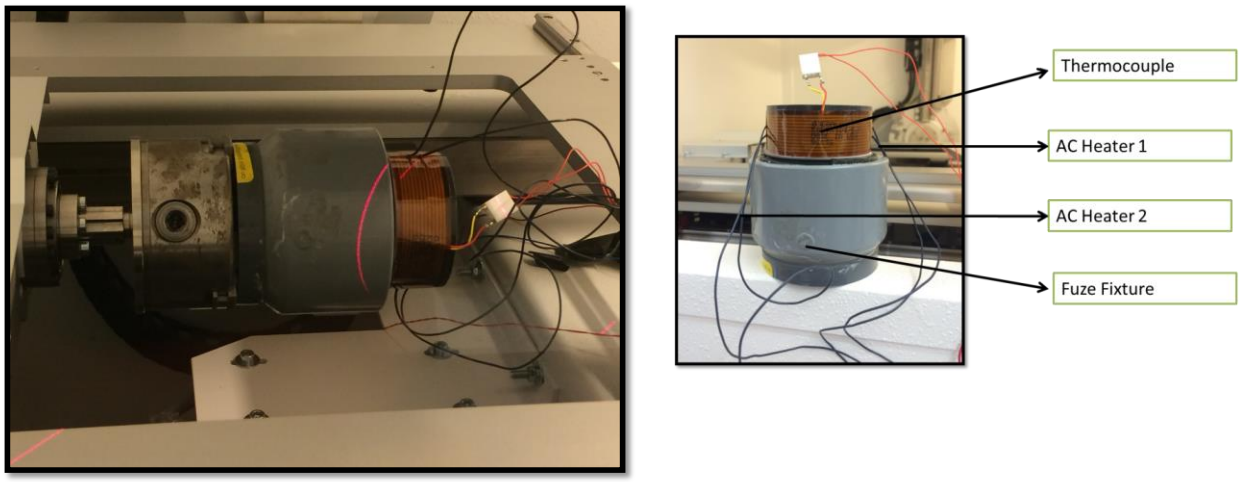

Figure 69: Fuze with element heaters and thermocouple

The Figure 70 shows a flowchart of the test plan for this study. A reference scan of the fuze without any external load applied was recorded. Next step was to apply a thermal load with AC element heaters. The element heaters were made to go a 100^0C and were maintained at that temperature using a temperature controller module and with feedback coming from the thermocouple placed between the fuze surface and the element heater. The reference and the deformed scan were then used for DVC calculation. The reference scan was also used to create a FE mesh, thus capturing the as-is geometry.

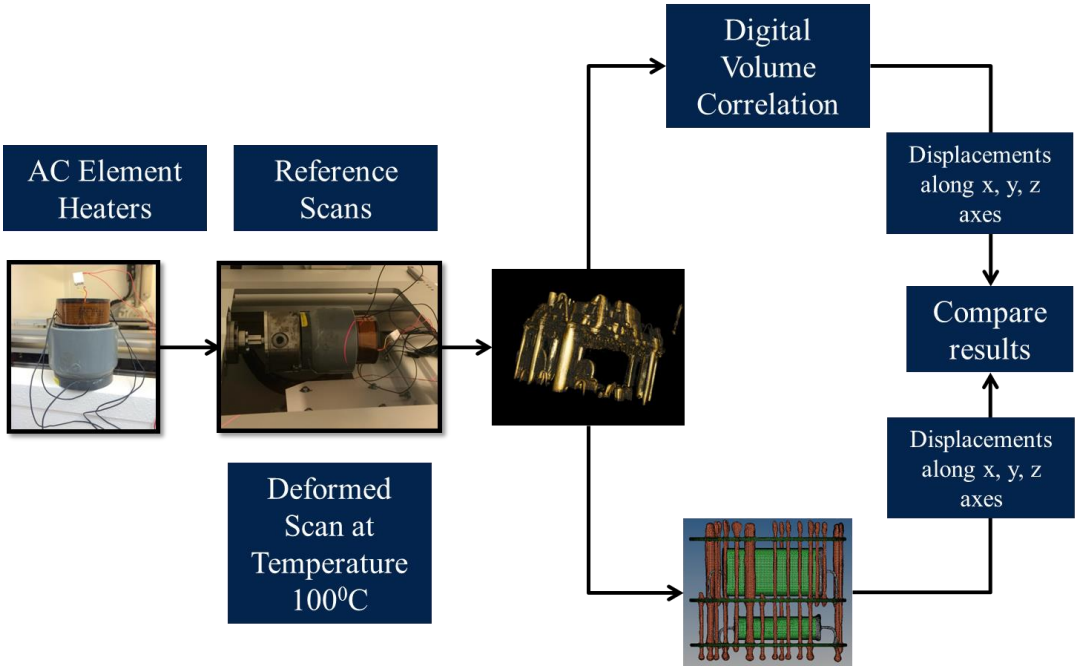

Figure 70: Flowchart for test plan

The results from the DVC and the finite element analysis have been compared and discussed further ahead in this study.

4.3.1 Micro-CT Data to Finite Element Mesh

Conventional Finite Element (FE) analysis done by making a CAD model of a part takes a prohibitively long duration because of the complexity of the part, the time required to model an accurate geometry and assemble them in CAD as per the dimensions of the real part. The common steps involved in the procedure to convert micro-CT data into FE mesh are image segmentation, conversion to the 3D surface model, meshing and FE analysis.The sub micron accuracy of the micro-CT data ensures good representation of the real geometry.The process developed, involves use of image segmentation, surface reconstruction and surface smoothing to refine the scanned topography. Noise removal from the scanned data, and surface smoothing, mesh refinement in Region of

Interest(ROI).Figure 71 is the process flow of steps involved in conversion of micro-CT data into FE mesh.

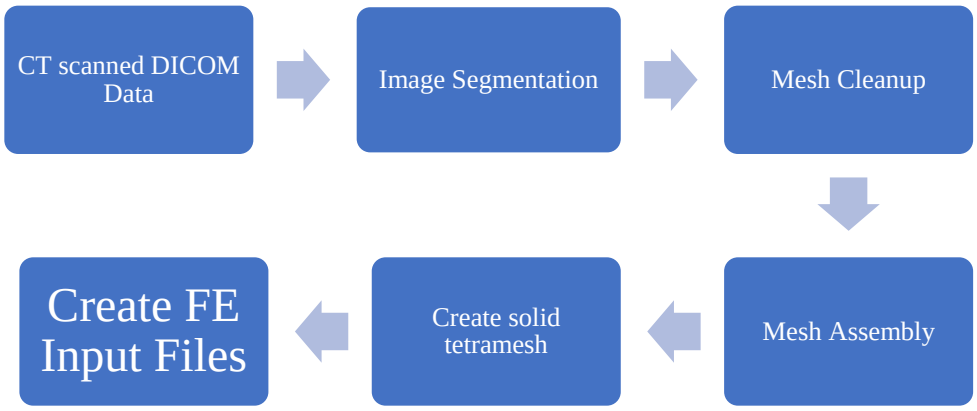

Figure 71: Flowchart for CT scanned data to FE Mesh conversion process

The reference scan taken for the DVC computation was used to convert the scanned data into an FE mesh. The advantage of using this method is that it allows the user to directly convert the CT scanned data into a finite element mesh without CAD modelling procedure. Using the CT scanned data ensures that the true as-is geomtry of the sample is captured. The method developed also provides good control over the mesh and allowes for fine remeshing in the regions of interest. The solid tetra mesh created, using Delauney triangulation has nodes merging at the interface of the different material boundaries and no use of contact elements that add to the non-linerity of the prolem.

Figure 72 shows the meshed model of the fuze. The board assmeblies, resin, the skeletal structure and the two capapcitors have been modeled with nodes merging at the interface.

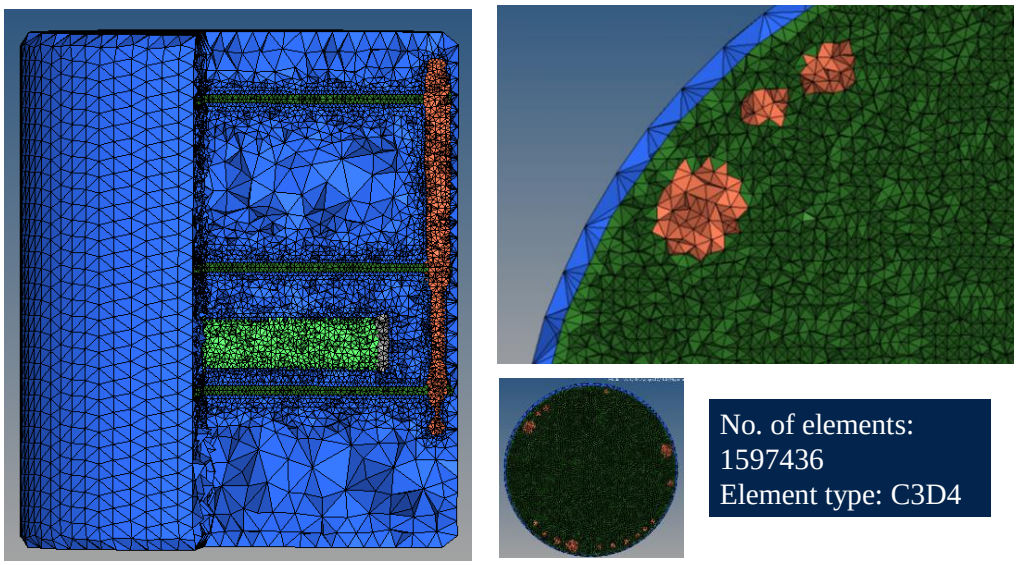

Figure 72: Cross sectional view of the meshed model

The meshed model was imported an ABAQUS Finite Element software for further analysis. Figure 73 shows the thermal load and the boundary conditions applied to the meshed model.

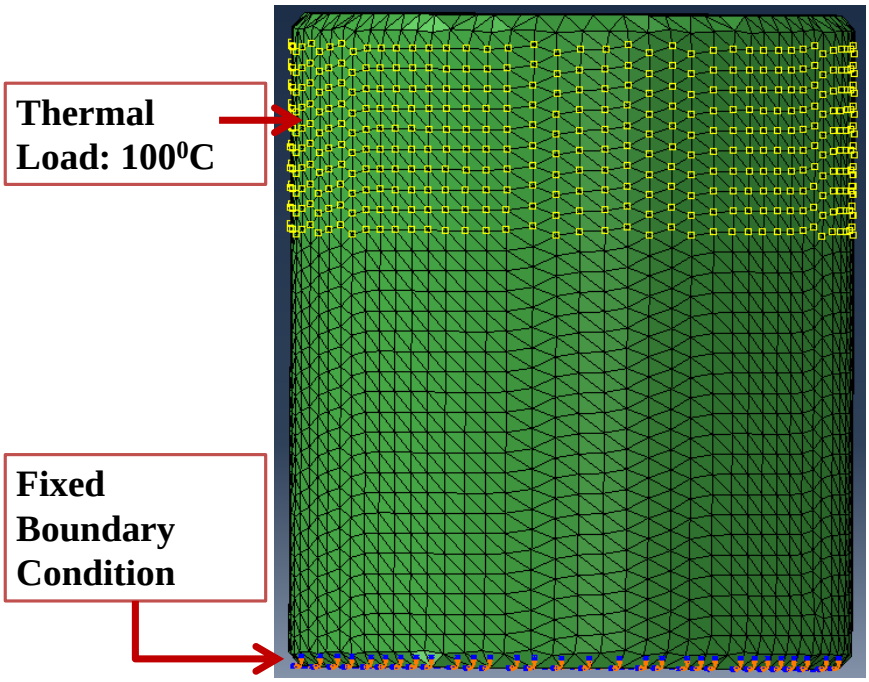

Figure 73: FE model with load and boundary conditions

A constant thermal load of 100^0C as applied the location same as that of the element heaters. The fuze model was a given a fixed boundary condition along the three axes at the bottom surface of the model and the cylindrical surface of the fuze under the element heaters.

4.3.2 Material Property Characterization

In order to make a reliable FE model to predict deformations and strains, material properties of the resin and the skeleton structure to hold the board assemblies were important. Fuze device are inherently made for a very long shelf life. But, exposure to prolonged thermal aging, low g shocks, moisture may affect the material properties of the potting resin. The skeletal structure holds the board assemblies, is located along the periphery of the fuze and is potted inside the resin. This structure is also subjected to internal stresses developing from the resin cure apart from the exposure to harsh environments mentioned earlier. To account for this, Young's modulus of the resin and the skeletal structure were found using nano-indentation technique.

Nano-indentation was done using Olive-Pharr method, where the Young's modulus is calculated from the unloading part of the load vs displacement curve [Oliver 1992]. 25 indents were made on the polished sample. The Figure 74 shows a box plot of the Young's modulus calculated for every indent.

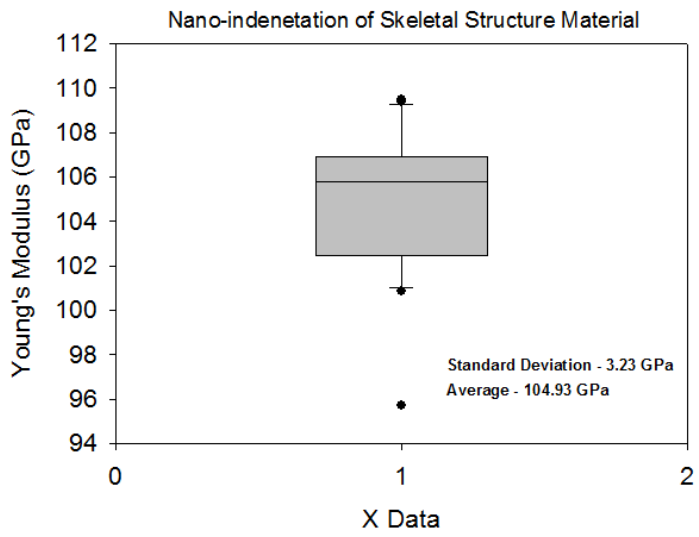

Figure 74: Box plot for Young's modulus

The box plot showed data spread between 101 GPa to 109 GPa with a low standard deviation of 3.23 GPa and an average of 104.93 GPa.

The EDX analysis was done to find the material composition of the skeletal structure material. The skeletal structure being potted inside the resin and the small dimensions of the skeletal rods made it difficult to separate the skeletal rod from the resin and perform test to find out the coefficient of thermal expansion under a thermos-mechanical analyzer. In order to gauge the coefficient of thermal expansion for this material, EDX analysis was performed on a cross sectioned sample. Figure 75 shows the EDX scan of a polished cross section of one of the skeletal structures surrounded by the resin and solder material.

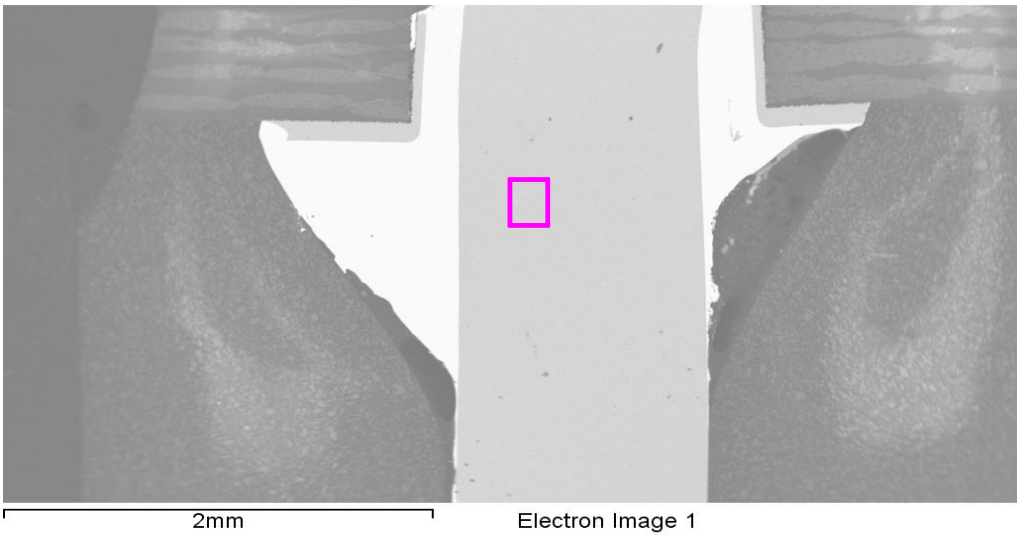

Figure 75: EDX scan for the skeletal structure material

Table 7: Elemental composition from EDX analysis

Element	Weight%	Atomic%
C K	2.99	15.69
Co K	-0.03	-0.04
Ni K	0.56	0.60
Cu K	77.91	77.20
Hf L	18.57	6.55
Totals	100.00	

Table 7 shows the elemental composition of the area scan.

The elemental composition shows the material to be type of copper alloy.

4.3.3 Results

As per the test protocol set earlier, DVC was run on the fuze assembly subjected to 100^0C thermal load. Prior to DVC computations for the deformed scan it was important to select the correct subset size and the maximum search region. This was done by multiple DVC computations at different subset sizes to achieve a known translation motion applied on the fuze device.

Prior to application of the thermal load the scanning tray holding the fuze was translated in along its length by 0.15 mm. Using the translated fuze scan as a deformed scan, DVC computations were run at subset sizes of 5 , 7 and 9 voxels with maximum search region being twice the applied translation in voxels. Subset size 7 was found to detect accurately 0.15mm translation motion. In this study, DVC computations have been run on multiple smaller volumes found within the large scanned volume. This was done to reduce the computation time. Selecting a large volume size increases the computation time by a power of three as the number of voxels increase over all the three axes. The Figure 76 below shows the location the volume over which the DVC computations were run.

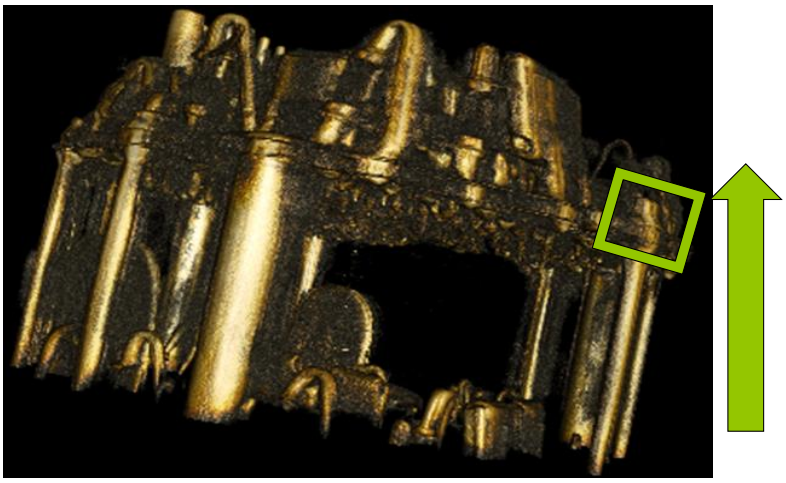

Translation of **0.15 mm**

Figure 76: 0.15 mm translation scan and location for DVC calibration

Figure 76 Figure 77 shows the contour plot of DVC computations along the length of the fuze, that is, along Y axis for subset size of 7 and 9.

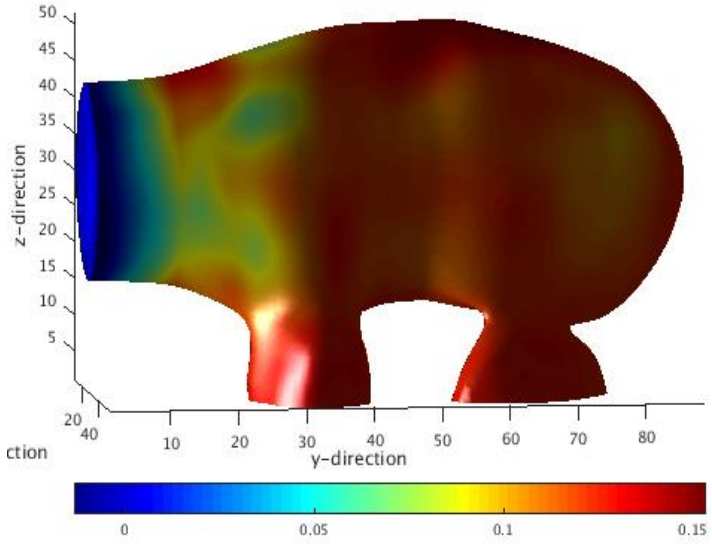

(a)

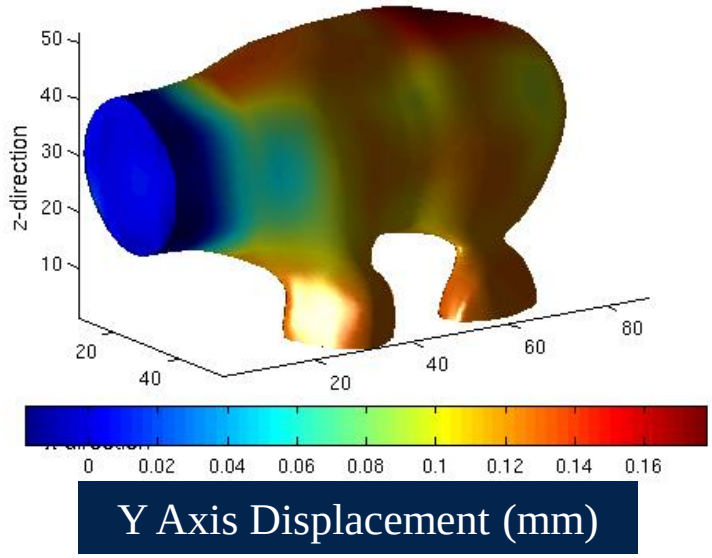

(b)

Figure 77: (a) Y axis displacement, subset size 7 , (b) Y Axis displacement, subset size 9

Figure 77 (a) is displacement contour for subset size of 7 and fig (b) is displacement contour for subset size of 9. In Figure 77(a), majority of the volume having a single colored contour represents translation motion. On Comparing Figure 77(a) and (b), it can be clearly observed that displacement contour for subset size 7 has more evenly spread contour at 0.15 mm translation than the displacement contour for subset size of 9. The color contour in the bottom most part of the contour plot results from poor correlation coefficients as voxels in that region of the deformed scan are newly introduced in the selected volume with respect to the reference volume. Figure 78 show DVC computations for one of the skeletal structure rods.

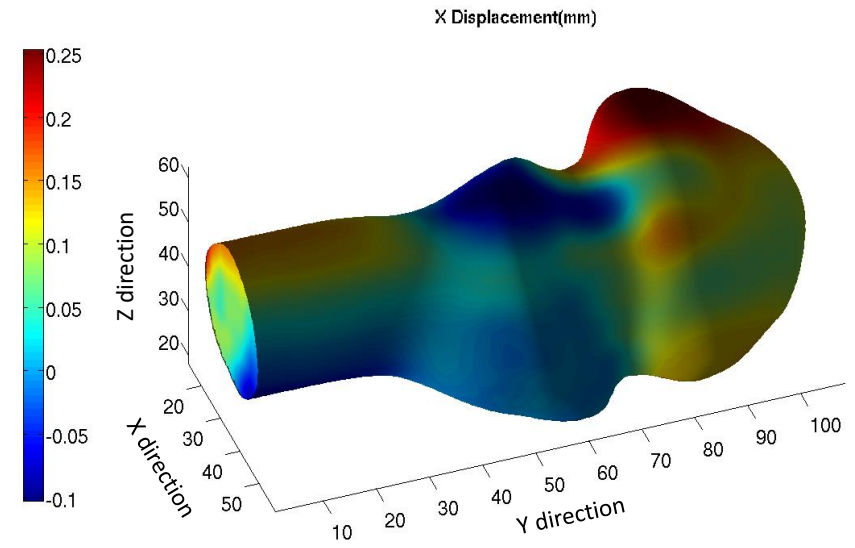
X Displacement(mm)
0.25
0.2
0.15
0.1
0.05
0
-0.05
-0.1
Z direction
60
50
40
30
20
X direction
20
30
40
50
Y direction
10
20
30
40
50
60
70
80
90
100

(a)

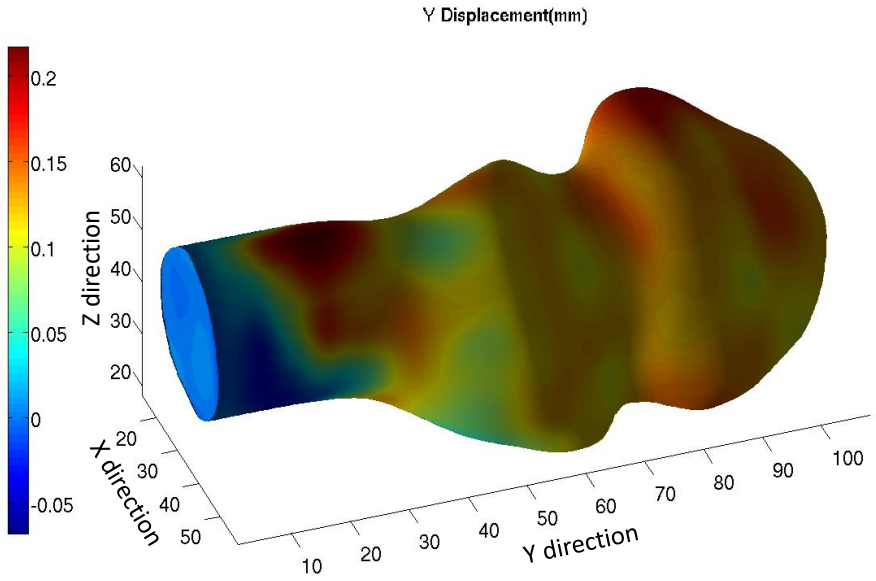
Y Displacement(mm)
0.2
0.15
0.1
0.05
0
-0.05
Z direction
60
50
40
30
20
X direction
20
30
40
50
Y direction
10
20
30
40
50
60
70
80
90
100

(b)

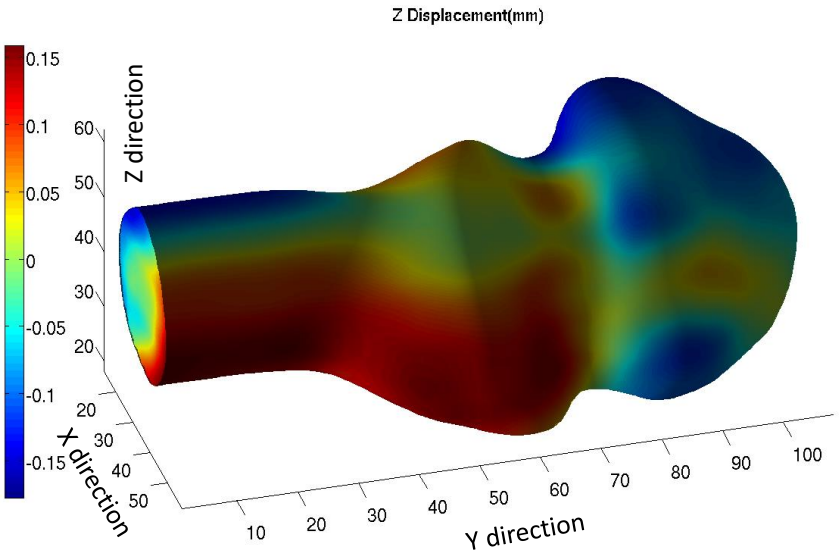

(c)

Figure 78: (a) Displacement along x direction, (b) Displacement along y direction, (c) Displacement along z direction

Figure 78 shows the location of the rods in the fuze assembly. The displacement contour is for a 100^0C thermal load.

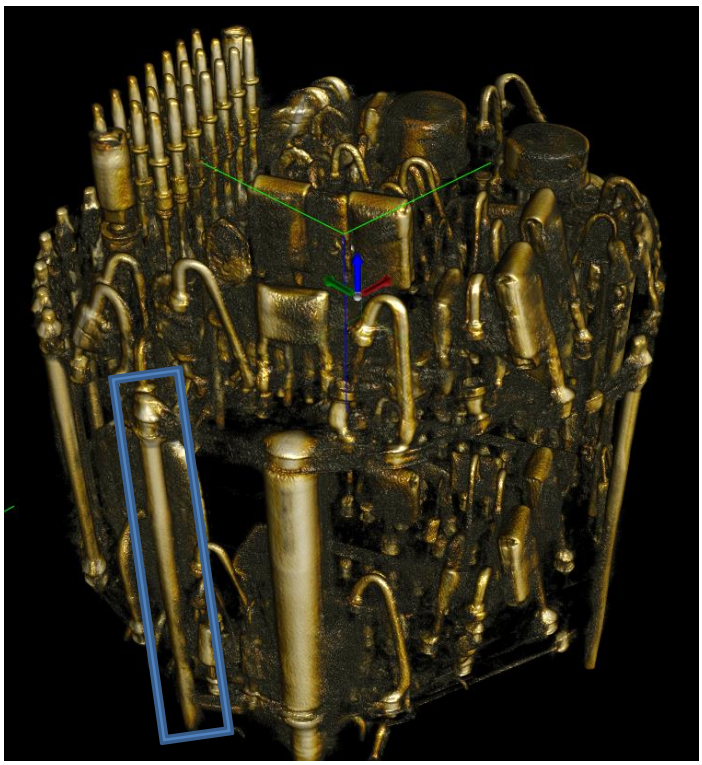

Figure 79: Location of the rod in the fuze

From the displacement contour plots in x direction and y direction in Figure 78, it is seen that the rod has a tendency to displace radially inwards. Along the Z direction the rod has a tendency to move to the Z direction, the part of the rod closer to the outer surface more so than the part on the inside that is showing a blue colored contour. These experimental results were found to be in agreement with the nature of displacement found from the results of the FE model made using CT scan data.

Figure 80 shows displacement normal for the rod in X, Y, Z axes.

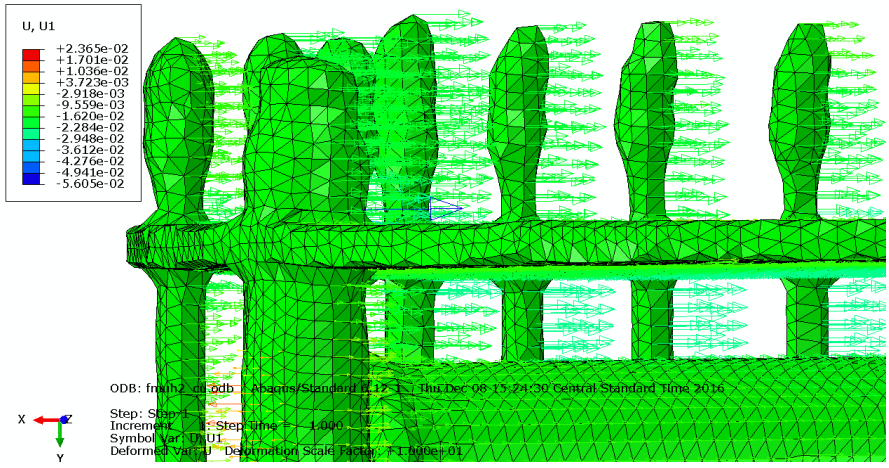

(a)

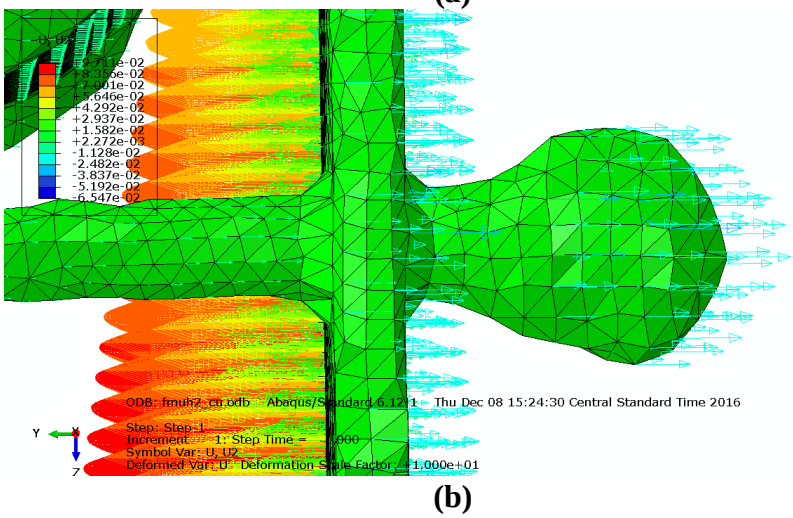

(b)

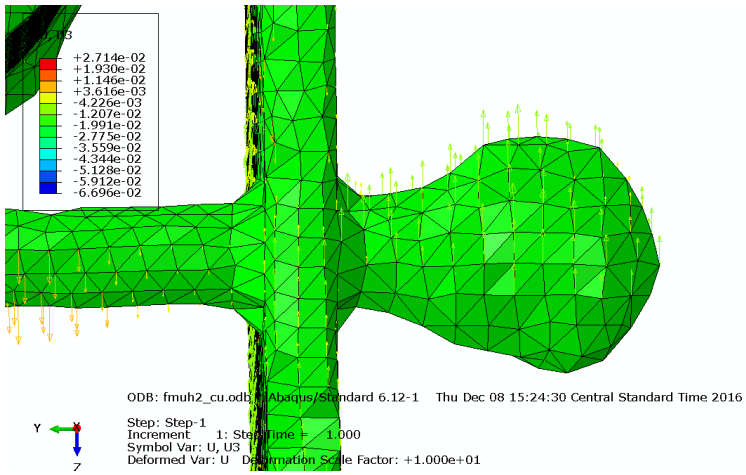

(c)

Figure 80: (a) Displacement direction along X axis, (b) Displacement direction along Y axis, (c) Displacement direction along Z axis

This shows that DVC computations and the FE model could correctly predict the displacement profile of large densely packed electrical fuze assembly. Figure 82 shows the DVC computation results for electrical components located on the top board assembly. Figure 81 shows the location of the electrical component on the top board assembly. The part is located along the periphery of the cylindrical surface being heated.

Figure 81: Location of the electrical component on the top board assembly

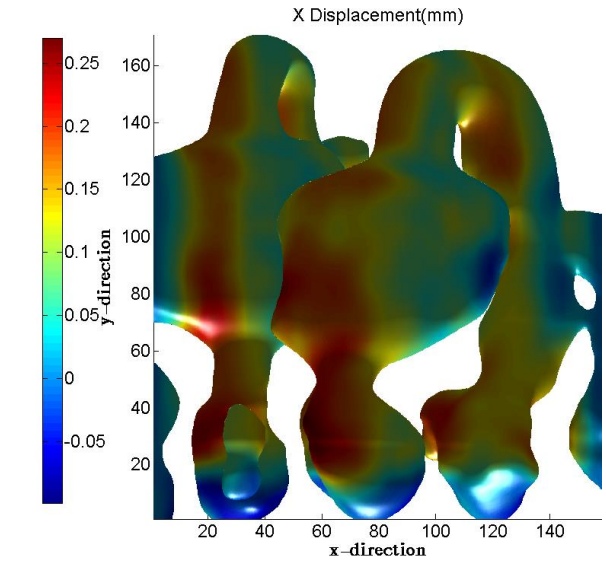
X Displacement(mm)
0.25
0.2
0.15
0.1
0.05
0
-0.05
y-direction
160
140
120
100
80
60
40
20
20
40
60
80
100
120
140
x-direction

(a)

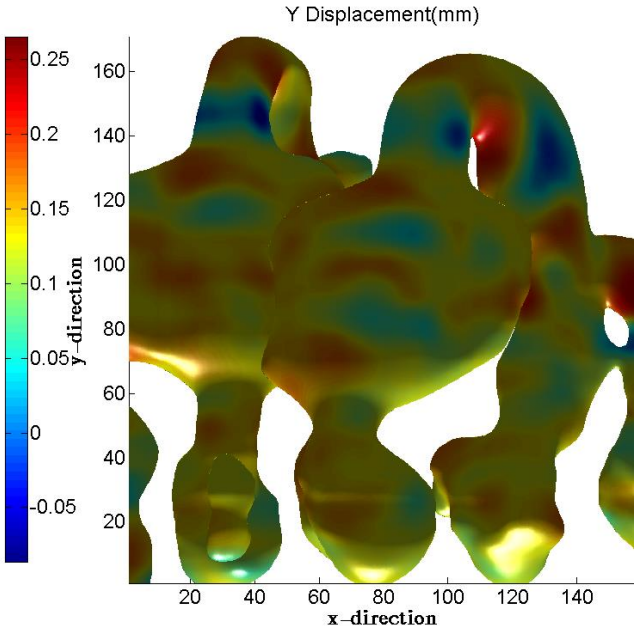
Y Displacement(mm)
0.25
0.2
0.15
0.1
0.05
0
-0.05
y-direction
160
140
120
100
80
60
40
20
20
40
60
80
100
120
140
x-direction

(b)

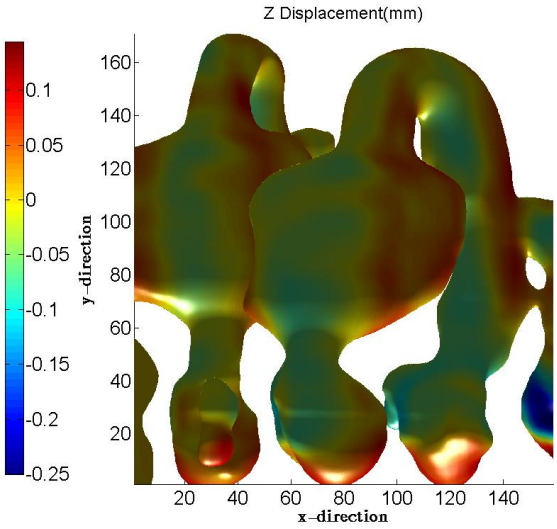

(c)

Figure 82: (a) Displacement along x direction, (b) Displacement along y direction, (c) Displacement along z direction

Figure 82 displacement contour plots for the electrical component show the component moving towards negative x direction, displacing upwards in the positive y direction and radially inside in the positive z direction. Similar nature of displacement was observed also for the rod discussed earlier. The base of the electrical component in within is soldered to the PCB board that is not visible in the Figure 82 as it is low density material and is thus not detected by the micro-CT machine.

4.3.4 Conclusions

In this work, a full field displacement measurement, DVC has been successfully used to analyze displacement contour over a large densely packed capacitive fuze. Micro-CT data of the test vehicle in a deformed and undeformed state was used for the DVC computations. This was done without cross sectioning or sacrificing the test vehicle. The parameters for the DVC computations were found by applying a known translation displacement to the test vehicle and back calculating that translation using DVC algorithm. A thermal load was

applied to the fuze to record a deformed CT scan. The deformed scan and the reference scan were used for DVC computations. As a second part of the study, a FE model was made using the micro-CT data of the fuze. The FE simulation results were compared to the DVC results to understand the utility of micro-CT scan data to use DVC as a viable experimental tool to study densely packed electrical assembly and to make FE models to predict displacements. Nano-indentation and EDX analysis was used to obtain the material properties for the FE analysis. This ensured usage of the in-situ material properties, accounting for the material degradation in the field extracted parts. It was shown that the FE model was able to correctly predict the displacement profile with respect to the DVC experimental results.

The deformation results from the FE and the DVC in terms of values were found to be not matching. The deformations computed by the FE analysis were found to be much conservative and off by an order of magnitude. Prior research in this field has shown the voxel-based displacement calculation scheme of DVC and mesh-based calculation scheme of FE software introduce error because of the difference in the location of nodes (in case of FE models) with respect to voxels in DVC calculations. Presence of large number tetrahedral elements is also known to make the model stiff. Also, the component studied is a fuze assembly with several sub-assemblies and different materials that have gone degradation during its service life apart from those that have already been measured and incorporated in the model.

In summary, the use of micro-CT data in deformation measurement using DVC as an experimental tool for large electrical assemblies has been shown for the first time. This method has been used before in the medical industry in studying the deformation over bones and in the electronics industry for deformations and failure in small ball-grid array packages, but not for large densely packed electrical assemblies. The micro-CT data was also used to create a FE model with multiple parts without use of contact elements and multipoint constraints. The findings presented in this study indicate that the FE model created using the micro-CT data was able to predict the displacement profile of the model with respect to the DVC results but not deformation values.

4.4 Test Study for Fuze under application of Drop Shock Load and Thermal load with Micro CT data and Digital volume correlation

In this study, a fuze device has been subjected to a test plan that reflects the storage life and service life of a missile system. A missile system during its service life may be subjected to high temperature storage life followed by high g mechanical shocks when flown out on missions and then again put back in storage if not fired. I order to replicate this complex scenario; the fuze has been subjected to mechanical shock loads followed by a thermal load. Digital Volume Correlation (DVC), a non-destructive full field displacement measurement technique, analogous to Digital Image Correlation has been used to track deformation at discreet location in the fuze device. The 3D data for the DVC technique was acquired using the micro-CT scanner.

In order to implement this test plan, a fuze assembly was subjected 30 consecutive mechanical shocks at 30,000 g, followed by as isothermal heating load of 100^0C. This cycle was repeated twice. In order to perform the DVC measurements, the fuze was scanned in a pristine state before initiating any mechanical shock testing. The fuze was then scanned after the 30^{th} drop. Thus, the pristine scan served as the reference scan and the scan after the 30^{th} drop served as the 1^{st} deformed scan. Comparing these two scans helped us quantify the damage sustained on electrical components inside the fuze during the 30 consecutive mechanical shocks. After the scanning the fuze at the 30^{th} drop event, the fuze was again scanned after subjecting it to the thermal load of 100^0C. Thus, now the scan after the 30^{th} drop and the scan after the thermal load were compared to quantify the damage after the isothermal heating of the fuze. This procedure mentioned above was repeated twice. Also,

the scan data before the isothermal heating step was used to construct an FE model using the micro-CT data to FE modeling procedure. More details on this procedure may be found in [Lall 2016] [Lall 2017]. The deformations recorded by DVC for the isothermal heating and the thermal FE simulations have been compared for the two test cycles. The Figure 83 shows a schematic of the test protocol.

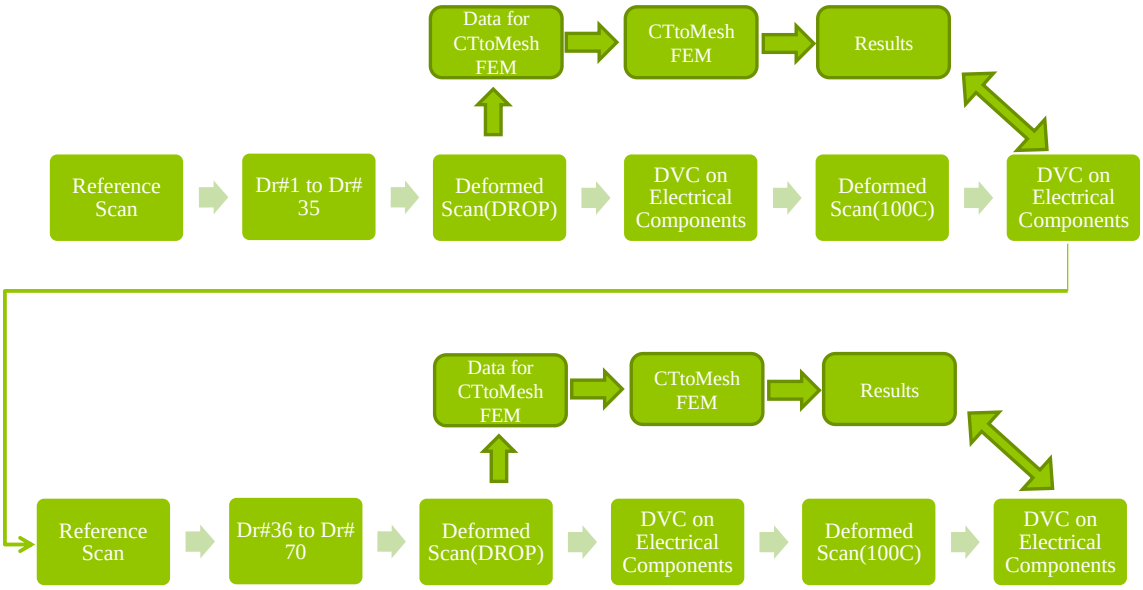

Figure 83: Test Protocol

In order to subject the fuze to high g mechanical shock, a Dual Mass Shock Amplifier (DMSA) was used. The drop tower with DMSA and the fuze were calibrated for 30,000 g. A drop height of 50 inches was found to achieve the desired g level. While the 30,000 g level was read at the fixture of the containing the fuze, a g level of ~6,300 g was recorded on the fuze device. Figure 84 shows the locations where the g levels were recorded.

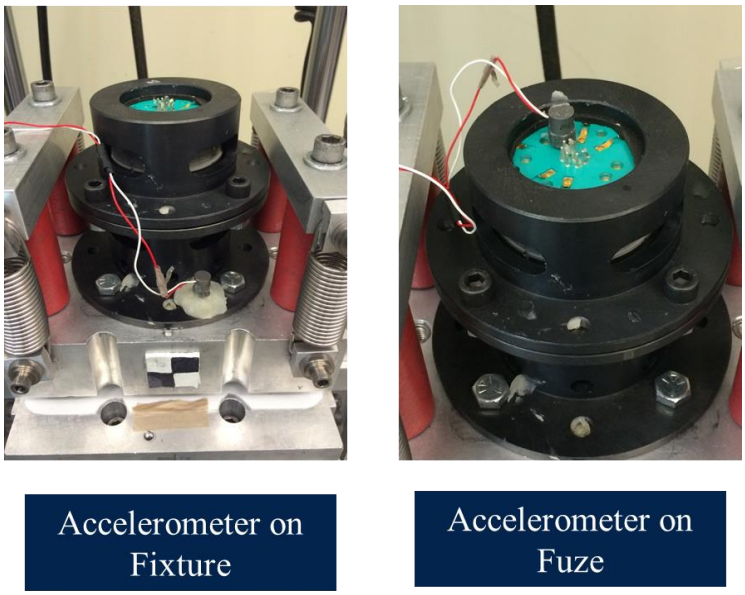

Figure 84: Locations where the g levels were recorded on the fixture and the fuze assembly

Figure 85 shows the accelerometer output for the g levels recorded at the two different locations, on the fixture and on the fuze. Multiple accelerometer signals in the graph show repeatability of the mechanical shock amplitude on the fuze.

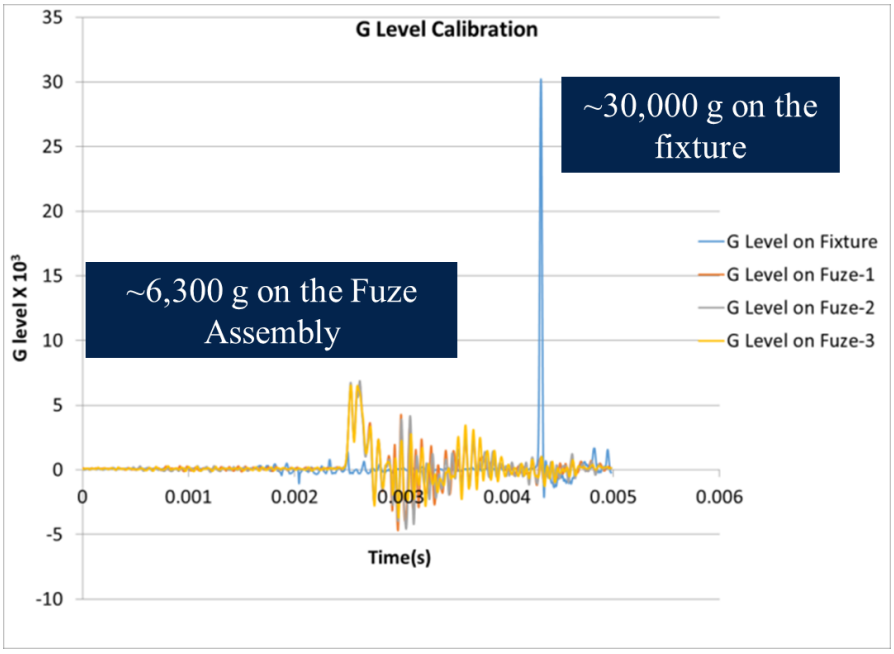

Figure 85: g levels recorded on the fixture and the fuze

The thermal load was applied using 2 one inch wide element heaters pasted on the top one inch cylindrical surface of the fuze device. This area of the fuze also houses the top board assembly out of the three board assemblies in the fuze.

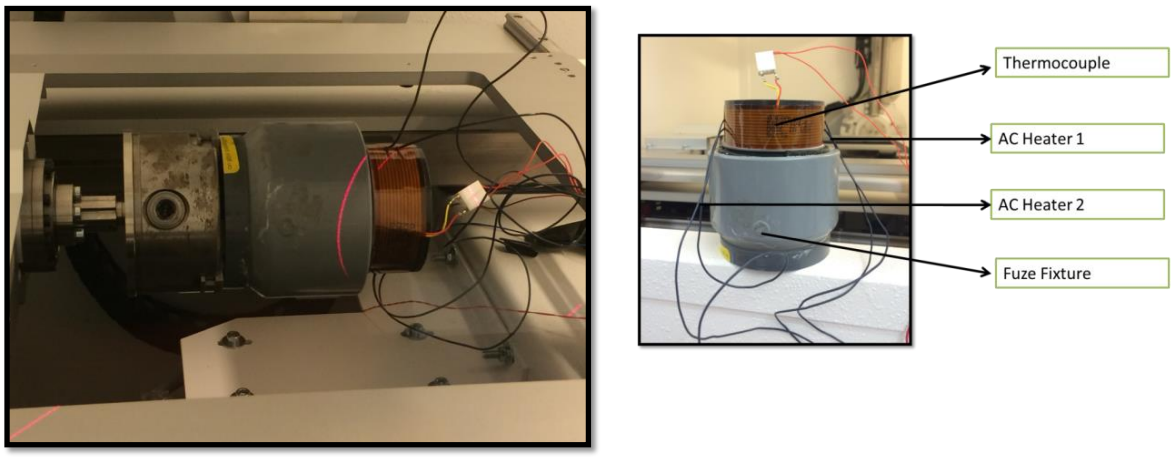

Figure 86: Test setup for isothermal load

Figure 86 shows the 2 element heaters with a feedback thermocouple loop to maintain the 100^0C load while being CT scanned.

It is the hypothesis of this study to have the developed experimental method not only accurately predict the deformations and strains but be able to record the deformation and strain history as a function of time or drop numbers in this case. This would prove the usefulness of the methods in predicting the potential nature of deformation and areas of impending failure in densely packed electrical assemblies in a complete non-destructive way.

Figure 87 shows the meshed model of the fuze. The board assmeblies, resin, the skeletal structure and the two capapcitors have been modeled with nodes merging at the interface.

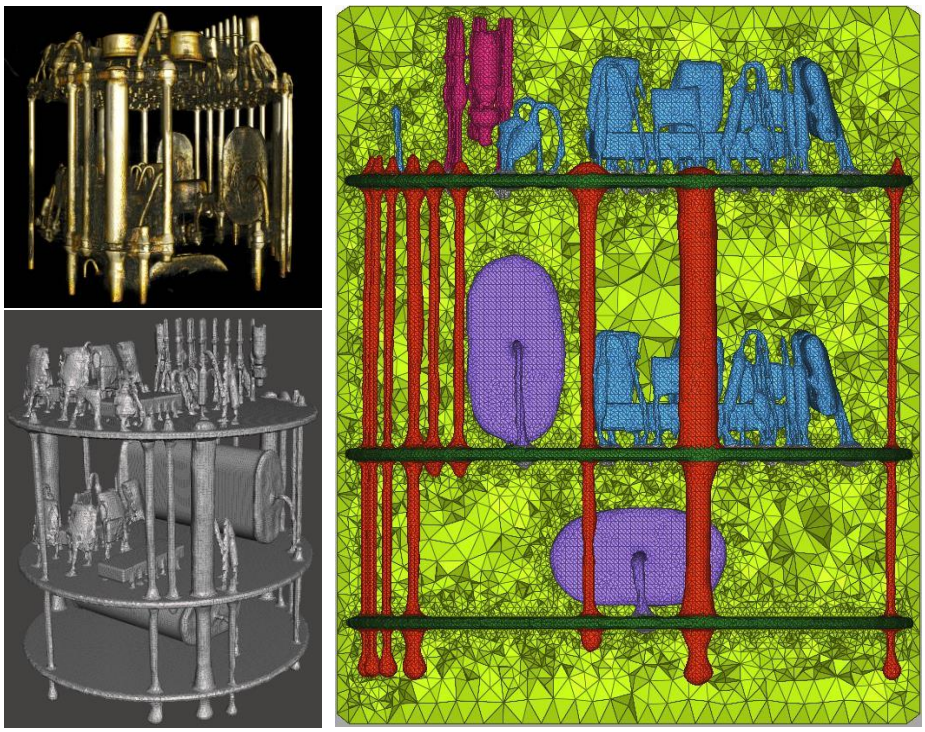

Figure 87: Meshed model with nodes merging at interface

The meshed model was imported in ABAQUS Finite Element software for further analysis. Figure 73 shows the thermal load and the boundary conditions applied to the meshed model.

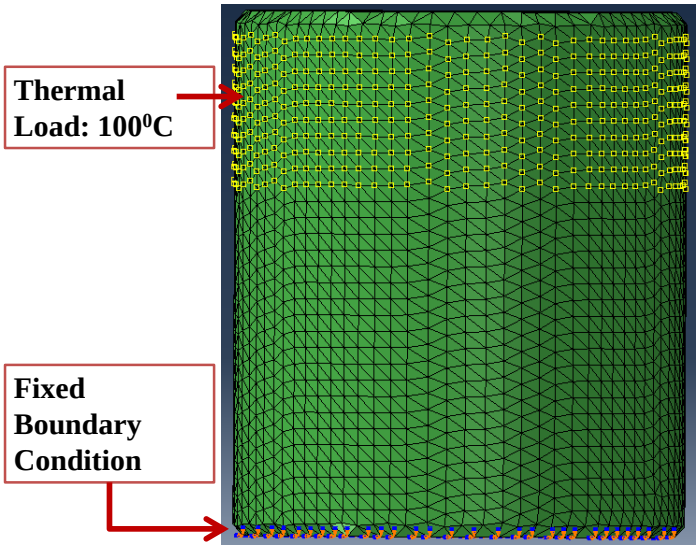

Figure 88: FE model with load and boundary conditions

A constant thermal load of 100^0C as applied the location same as that of the element heaters. The fuze model was a given a fixed boundary condition along the three axes at the bottom surface of the model and the cylindrical surface of the fuze under the element heaters.

The material property input to the FE model was made based on experimentally measured Young's modulus and co-efficient of thermal expansion of the potted resin and the structural cage holding the three board assemblies of the fuze. More details on the input material properties can be found at [Lall 2017].

4.4.1 Results

The fuze was subjected to 2 cycles of mechanical shocks and isothermal loading as stated earlier. The fuze assembly was CT scanned before and after each loading cycle. DVC calculations were performed comparing each micro-CT scan to the one before. The table below shows the instances at which DVC calculations were performed.

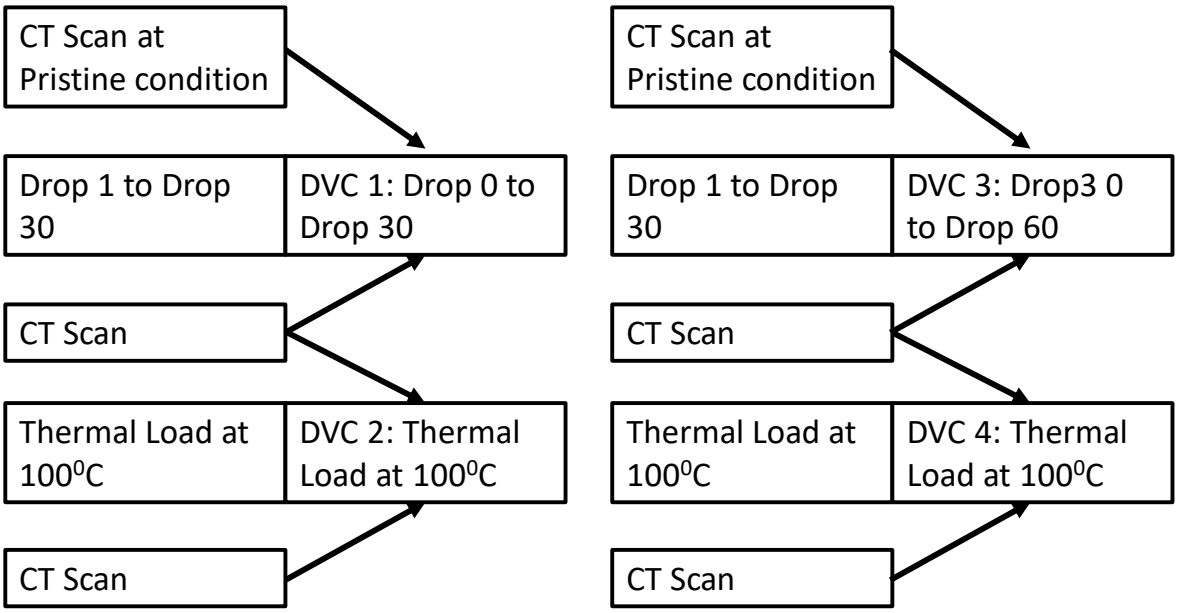

Figure 89: DVC Computations

Prior to performing DVC computations, the CT scan data from before and after the application of thermal load was made to overlap keeping the origin constant. The Figure 90 shows the overlapped scans.

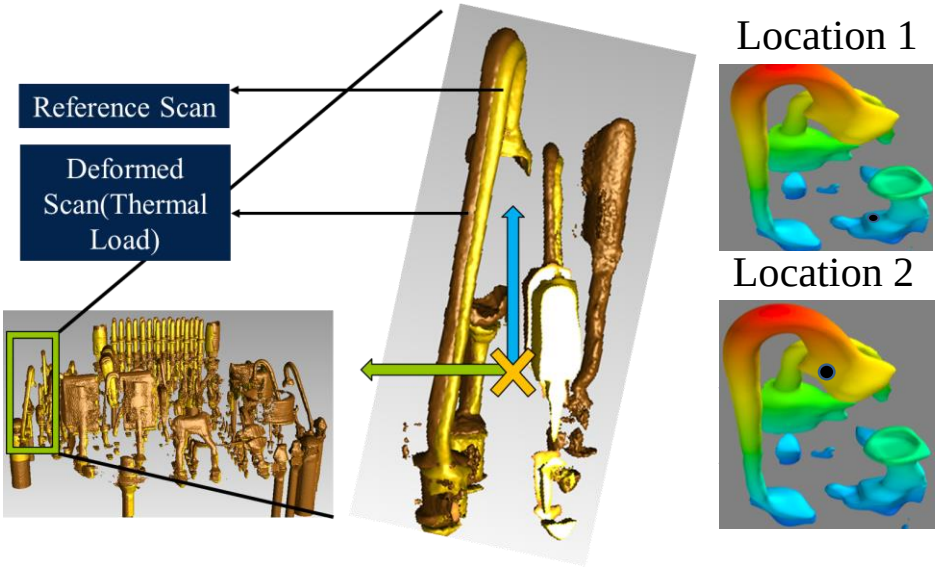

Figure 90: Nature of deformation by overlap of CT scans before and after the application of thermal load

Upon the application of thermal load, the top board assembly bent upwards and resulted in the electrical parts on it move radially outward as shown in the figure above.

As hypothesized earlier, the developed experimental and simulation tools must be able to accurately predict the true nature of deformation. The results from DVC and micro CT data-based FE model must be able to accurately give the same nature of deformation.

DVC computations were performed at the above mentioned four instances. The computations were performed on pre-selected 2 electrical components. Both the selected electrical components are found on the top board assembly, around which the thermal load is applied. The computations for deformations and strain were done over the entire convex

hull of the selected components' iso-surface. In order to obtain damage progression or quantify damage accrued after each different loading sub-cycle, deformation and strain values were extracted at different locations. These locations were kept constant for each scanned volume. These locations have been named as Electrical Component 1 (EC1) and Electrical Component 2 (EC2).Figure 91 shows the locations of the two electrical components on the top board assembly.

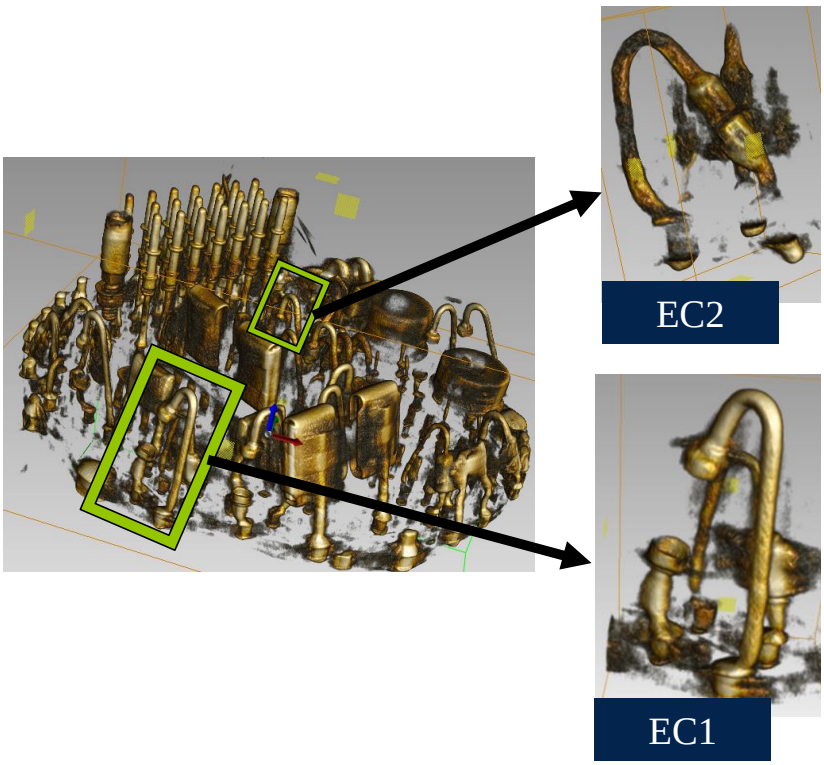

Figure 91: Locations for EC1 and EC2

These extracted values were then plotted to analyze the progression and damage because of different loading sub-cycles. Figure 95 shows the damage progression along x, y and z axis. This shown component has been named as Electrical Component 1 (EC1) through the study. The di-electric of the component being a relatively low dense material is not visible in the CT data.

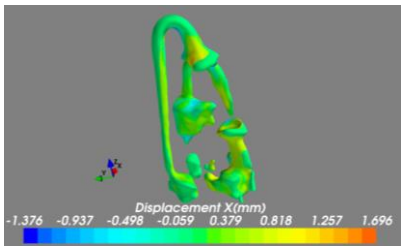

Drop 0 to Drop 30

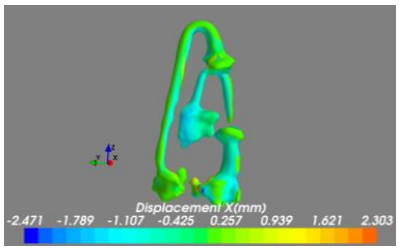

Thermal Load at Drop 30

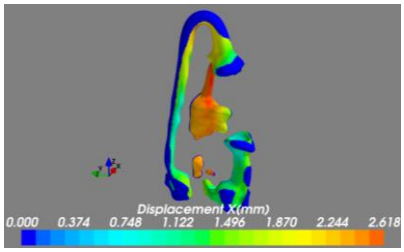

Drop 30 to Drop 60

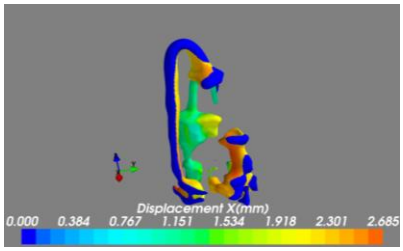

Thermal Load at Drop 60

Figure 92: Displacement in X axis for EC1

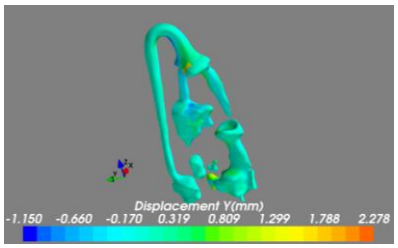

Drop 0 to Drop 30

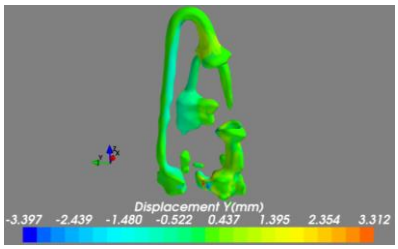

Thermal Load at Drop 30

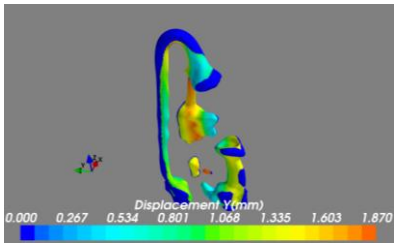

Drop 30 to Drop 60

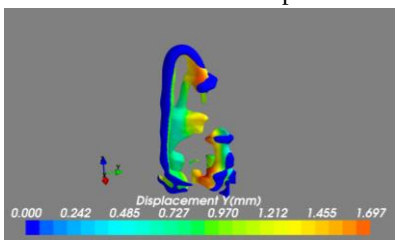

Thermal Load at Drop 60

Figure 93: Displacement in Y axis for EC1

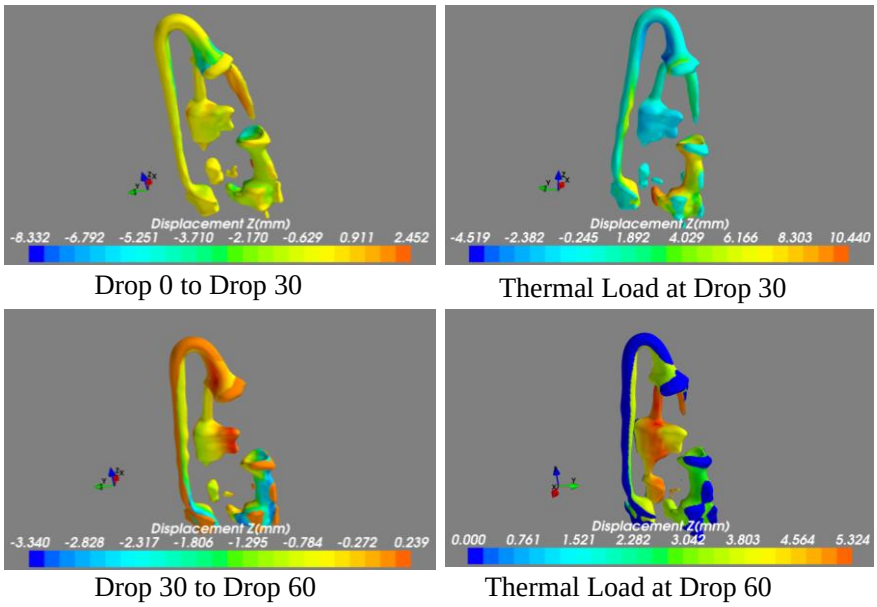

Figure 94: Displacement in Z axis for EC1

The contour plot of the deformation for EC1 shows the component to be displacing in the positive Z and positive Y direction. This indicates the PCB to be displacing upwards upon application of thermal load. This displacement has been quantified in the deformation histories graph in Figure 95.

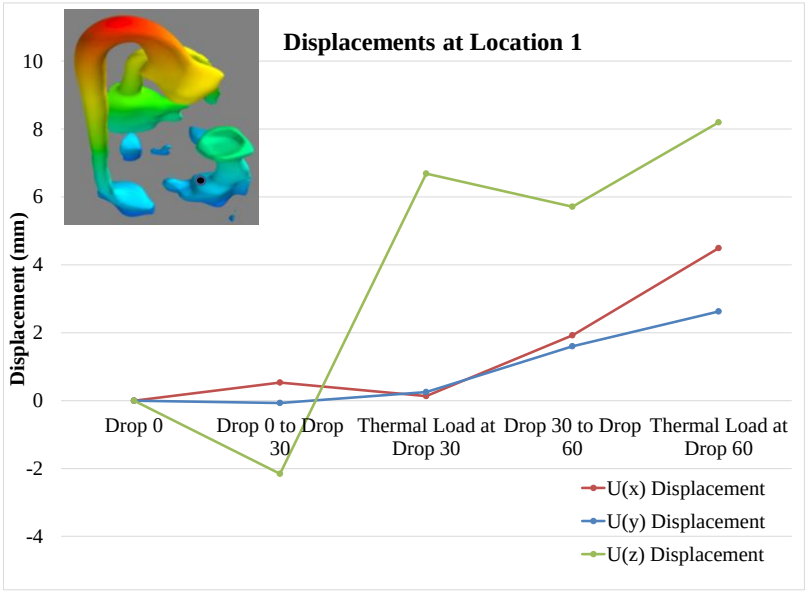

Figure 95: Displacements for EC1 at Location 1

The deformation history above shows the location 1 on EC1 to have considerably higher deformations along Z axis for application of thermal load vs application of 30 high g mechanical shocks. This shows that the thermal expansion of components in the fuze at a higher temperature may cause more damage to the fuze with respect to high g mechanical shocks. Figure 96 and Figure 97 show the progression of normal strain and shear strain at the same location on EC1.

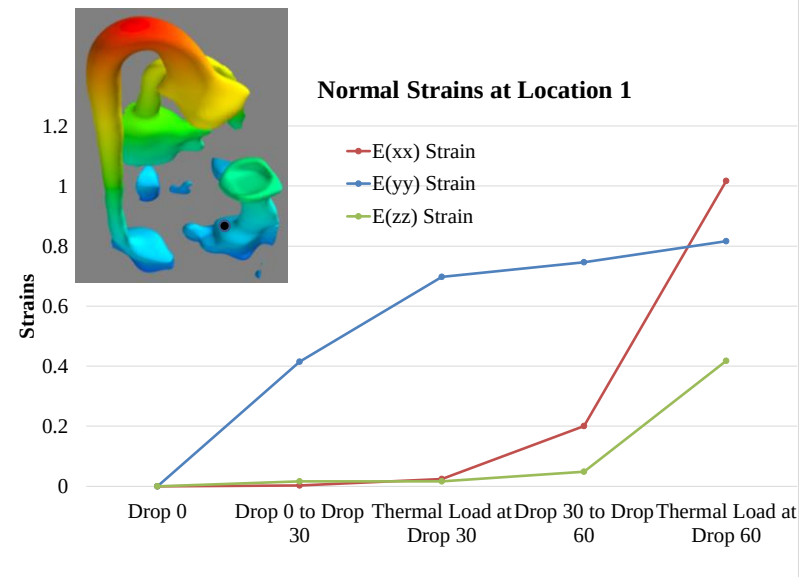

Figure 96: Normal Strains for EC1 at Location 1

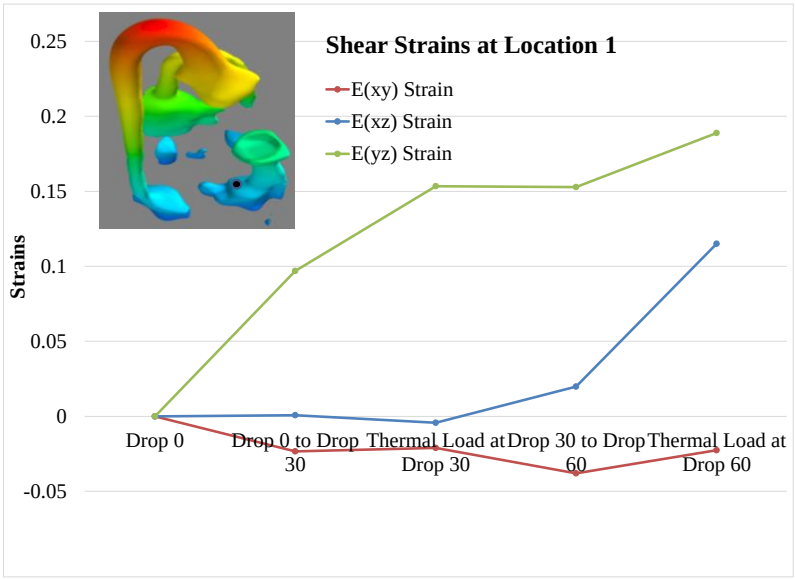

Figure 97: Shear Strains for EC1 at Location 1

Figure 98 shows the damage progression in terms of deformations along the 3 axes at location 2.

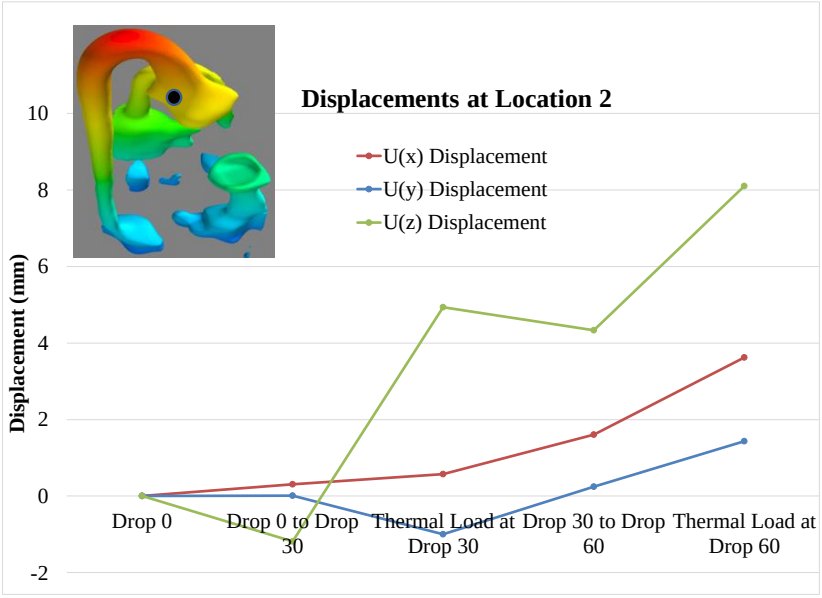

Figure 98: Displacements for EC1 at Location 2

Figure 99 and Figure 100 show the progression of normal strain and shear strain at the same location on EC1.

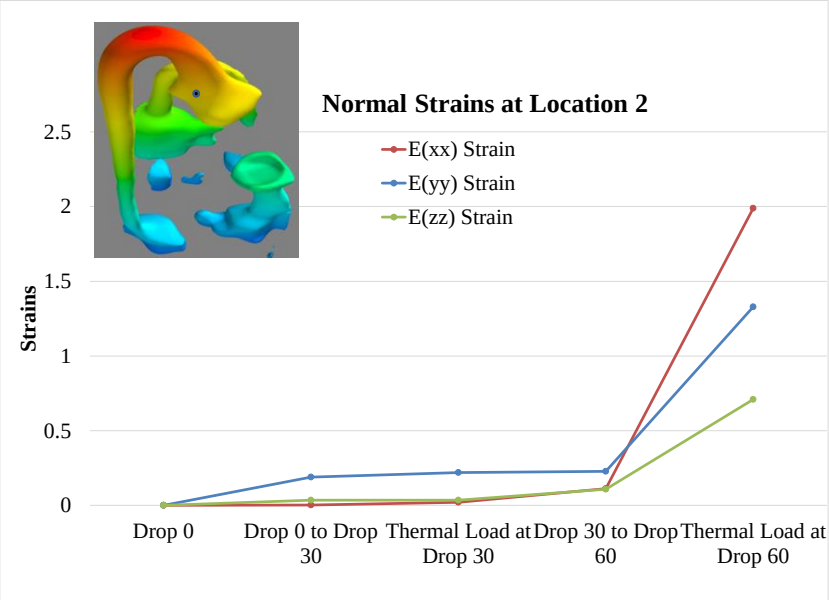

Figure 99: Normal Strains for EC1 at Location 2

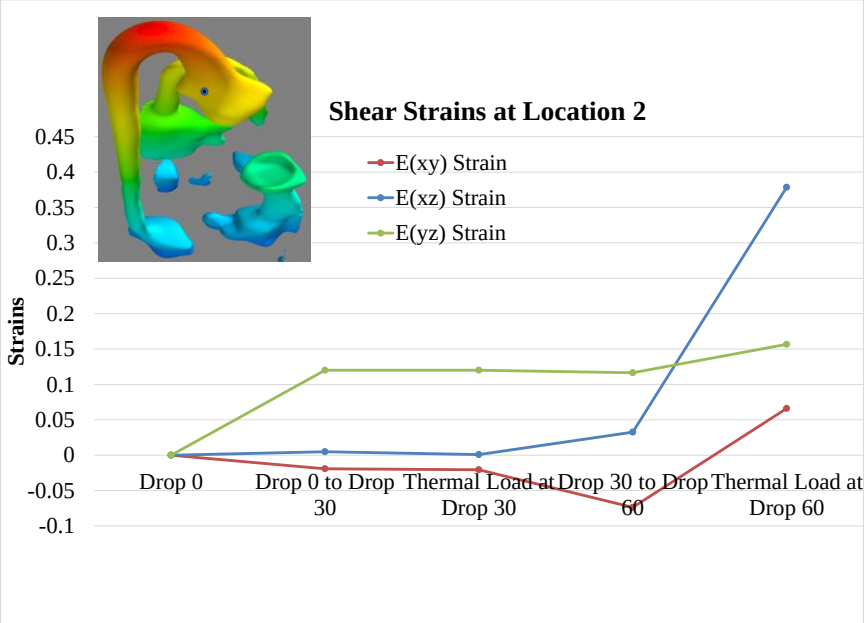

Figure 100: Shear Strains for EC1 at Location 2

The normal and shear strain histories at location 1 with respect to location 2 show that the deformation of the part along the positive Y direction is a causing a rise in the shear strain along YZ plane. The high mismatch in the shear strain at the two locations indicates the

possibility of shear failure between the dielectric and the bottom part of the EC1 component.

Figure 101 and Figure 102 shows the deformation histories at two locations, for the EC2 located in the center of the through hole board assembly.

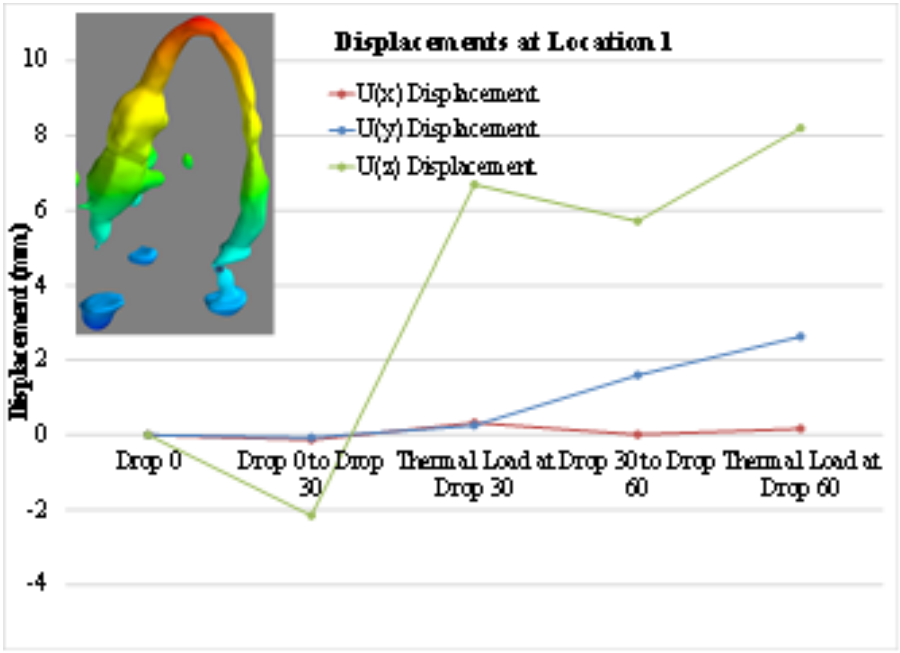

Figure 101: Displacements for EC2 at Location 1

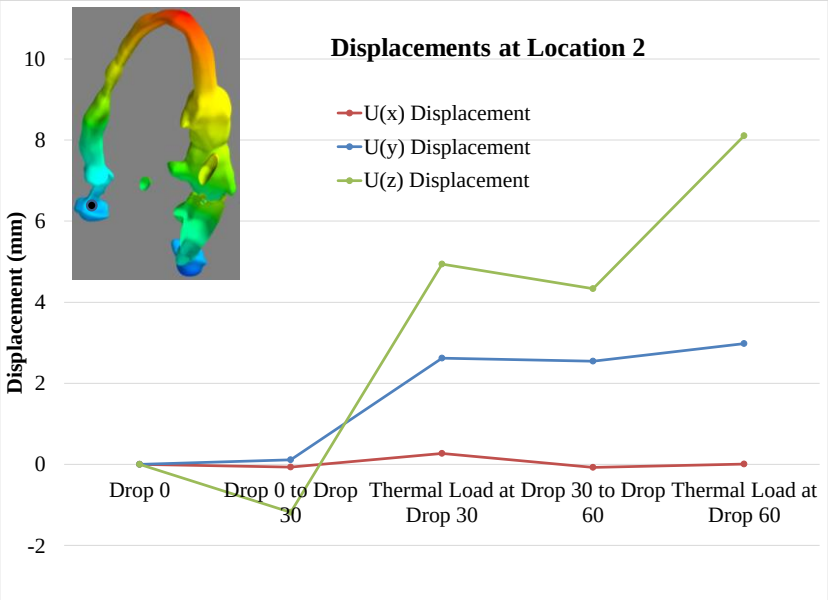

Figure 102: Displacements for EC2 at Location 2

The deformations for the EC2 show the same trend as EC1. The component is displacing in positive Z direction more upon application of thermal load vs application of high g mechanical shocks.

A static Finite Element model with a 100^0C thermal load was run. Below the shows a vector plot of displacements on the top board of the fuze assembly. ABAQUS CAE was used for this study. The thermal load was applied as a predefined field onto the model in to steps. The first step, where the predefined temperature field for the fuze was 22^0C. The second step had a predefined field of 100^0C. The nodes on the bottom half and the surrounding cylindrical area were marked to have the rotations and deformation constrained along all three axes,

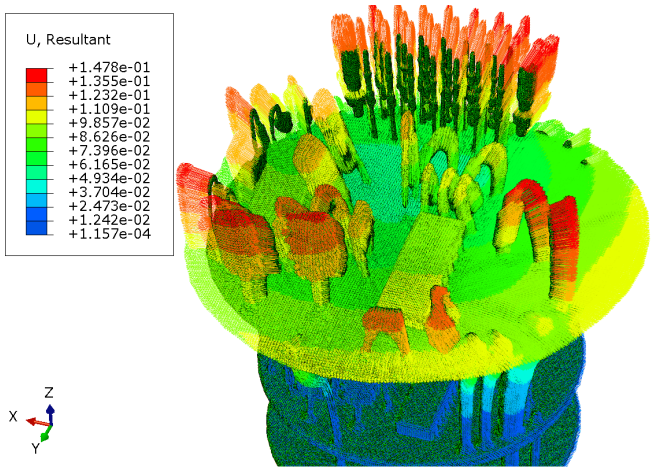

Figure 103: Vector plot of displacements on top board

The vector plot shows the top board bending upwards and the parts on the board moving radially outward as shown by the vector directions marked in the contour plot above. The absolute deformation values found using the three methods were not found to be matching. This could be attributed to the large number of parts and their real material properties were unaccounted. With these densely packed assemblies having more than 50 components all having different material types, the accurate displacement measurements were not possible. Though, the results from the FE model and DVC show the usefulness of the methods to accurately predict the nature of displacement.

Chapter 5: Study on Effect of voids on Thermo-mechanical Reliability

QFN packages have gained much popularity in the semiconductor industry for consumer electronics because of the thin profile, low inductance and low weight. This has made QFN packages much desirable in the other applications as well. Solder interconnects always have some amount of part to part physical variability in parameters like solder joint height, shape, distance to neutral point, location, size and number of macro voids. Assessment of thermal cycling fatigue reliability requires methods to accurately model the variance in the part and interconnect geometry including the presence of solder-voids and joint imperfections [Schubert 2003]. Solder interconnects of the same package assembly are not all the same. The most common FE modeling approaches to calculate characteristic life, assumes ideal geometry of the solder interconnect but fail to take into consideration this within part geometric variability. Published studies that do consider this variability, fail to take into account all the variabilities in the same FE model. Lall and all have published earlier on micro-CT data-based FE modeling of QFN solder interconnects with voids for one thermal cycle, considering linear material model for the solder [Lall 2018]. Researchers have included CAD modeled voids to study the effects of voids on therma l cyclic fatigue reliability of lead-free solder interconnects [Terasaki 2005], [Schwerz 2011] [Yubing 2005]. In this chapter the authors have first used micro-CT data-based FE model of the QFN package. Using the micro-CT data of the each QFN package has ensured representation of all the variances in the part and the interconnect geometry along with the

macro-voids. Secondly, a full factorial design of experiments was implemented to systematically study the effect of location, size and number of voids.

In the first study, Darveaux model for solder joint fatigue with Anand constants for SAC305 solder material was used to compute number of cycles to failure using FE. Characteristic life of QFN packages subjected to thermal cycling load of 250^0C to 125^0C was found previously in [Lall 2018]. We have used the micro-CT scan data of these QFN packages to make FE models and computed characteristic life of packages with part-to-part variations subjected to the same thermal cyclic load. The characteristic life obtained experimentally and from FE model has been compared. This is done to investigate the effect of considering the real as-is geometry of the parts on the resultant ΔW_{avg}, number of cycles to failure and resultant characteristic life of the sample set studied. QFN packages have gained much popularity in the consumer electronics because of the thin profile.

From the first study mentioned briefly above, it was concluded that presence of void in the vicinity of the corner solder joint has an effect on location of maximum non-linear plastic work. In response to these results a detailed study regarding the effect of location, size and number of voids on the maximum non-linear plastic work was undertaken. Though the effect of macro-voids on thermo-mechanical BGA reliability is well published upon, little literature can be found on effect of macro-voids of QFN solder joint reliability subjected to HTSL thermal cycling loads. Also, the dimensions of the solder joint of a QFN package are very different comparison to its counterpart in BGA packages. This inherently brings the macro-voids closer to the crack path on the package side. It is widely reported that, for

HTSL/HTOL loading conditions, macro-voids in solder balls depending on their size and location near the package side or the PCB side may cause an accumulation of shear stress in comparison to a no-void solder ball. When the void may be in the path of the package side crack path, the effective length of the solder joint reduces resulting in early failure. Lall et al have published earlier on micro-CT data-based FE modeling of QFN solder interconnects with voids for one thermal cycle, considering linear material model for the solder [Lall 2019]. Researchers have included artificially modeled voids to study the effects of voids on thermal cyclic fatigue reliability of lead-free solder interconnects of BGA packages. [Terasaki 2005], [Schwerz 2011] [Yubing 2005]. In this study, a detail study has been undertaken using finite element modeling of a 32 pin QFN package solder joints with artificially introduced voids. The FE model was done on QFN solder joints with artificially introduced voids of different sizes and locations. A thermal cyclic load of 125^0C to -40^0C as per AECQ-100 was used for the study. Effect of void size, void location and number of voids on non-linear plastic work per volume after two thermal cycles was tracked at different cross-sectional locations and effect of each factor was individually quantified using a full factorial DOE approach.

5.1 Investigation of effect of void on QFN solder joint thermo-mechanical reliability

5.1.1 Introduction

QFN packages have gained much popularity and are widely used because of their thin profile, low weight and low inductance. This has led to improved mechanical, electrical and thermal performance. Also, in comparison to lower I/O count BGA packages, QFN packages are much preferred as replacements because of ease of production, shorter track lines, better thermal performance and the better mechanical shock performance due to lower weight [Bernard 2007]. Though these advantages mainly cater to the consumer electronics space, the higher resistance to mechanical shock induced failure and good thermal energy venting via the large pad has also made these packages popular choice in defense electronics. These reasons have warranted much research to study the reliability of QFN packages and its first and second level interconnects.

QFN packages are found to be much different in comparison to other traditional packages, where the leaded terminations are soldered to the PCBs. A QFN package has no lead, the bottom plane of the package has solder lands that are directly soldered to the PCB solder pads. The package also has a large heat sink on the bottom plane in the middle of the package to vent the heat. This thermal pad efficiently conducts the heat away from the component as the package usually sits at a standoff height of 50 to 75 micrometers. The wire bonds serve as the first level interconnect in the package.

Voids in solder joints occur due to oxidation and flux evaporation within the solder joint. This is a common form of defect found in QFN packages like other packages. In general, solder voids result to lower heat transfer rate, lower current carrying capability, and lower

strength and fatigue life [Lee 2002]. Voiding related problems have been largely reported on by researchers. It was reported that the thermal resistance of a package is significantly affected by a large void as compared to distributed voids of equivalent percentage [Otiaba 2011]. Biswal et al have reported on adverse effects on the thermal conductivity of the power module by the size and quantity of voids [Biswal 2005]. Researchers have reported on impact of voiding size and location on the thermal reliability of BGA packages. It was found that voids on the chip side had lesser impact on the thermal fatigue reliability in comparison to voids on the PCB side. The voids not along the apparent path of crack propagation had little to know impact on the thermal fatigue reliability in BGA packages [Qiang 2006].In spite of these findings the small feature size of the QFN package solder joint in comparison to the BGA package solder joint, in particular the ratio of volume of solder void to volume of solder joint, greatly increase the influence of voids on the characteristic life.

COTS (commercial of the shelf) QFN packages of the same type and series are manufactured in bulk but differ from each other when it comes to location of voids, number of voids in the solder joint. Majority of the literature on thermal fatigue life of solder in QFN packages do not take into consideration this part to part variation and assume ideal geometry [Hoe 2012]. Characteristic life is often computed using Darveaux's method for thermal fatigue life prediction [Darveaux 1998].

Modeling the real as-is geometry of the solder in the QFN package with manufacturing defect may improve the fidelity of the model. This technique has been published upon by

several researchers from the medical field [Choy 2012] [Batulla 2004] [Parashar 2016]. In this study, authors have used CT scan data of a QFN board assembly to make a FE model. Similar approach was presented by Lall [Lall 2017] [Lall 2016]. Authors used x-ray images (DICOM data) to reconstruct the solid geometry of fuze electronics potted in resin. Electrical components such as capacitors, SOIC packages, PCB, supporting structure, solder, can transistors and connector pins were extracted one at a time and then combined into single FE model.

In this study, a 32pin QFN package mounted on PCB was subjected to thermal cycling load till failure and the number of cycles to failure was found. Alongside this a FE model was made with Anand viscoplastic properties defined and number of cycles to failure was computed.

The FE modeling approach developed initially prevented the use of contact elements or multi point constraints in the FE model citing increased computation time [Lall 2016]. But this also required use of tetrahedron elements throughout the model. In this study QFN packages undergoing bending due to the application of thermal load required use hexahedron elements to prevent the under estimation of deformation due to parasitic shear locking in tetrahedron elements. The authors have overcome this by making a hybrid model of CAD modeled QFN package and CT to mesh converted solder joints with voids. The solder joints with voids are modeled using the STL. Data and thus tetrahedron elements and the rest of the model is meshed using hexahedron element. The resultant model was subjected to 2 thermal cycles with ANAND parameters for the SAC305 solder joint

defined. Number of cycles to failure was computed using the FE model and compared against the same found experimentally.

QFN packages are being widely used in the industry because of their excellent performance and lowered cost. The thin and light design of the QFN packages, improved mechanical and thermal performance, shorter track lengths and better drop and shock load reliability in comparison to similar I/O count BGA packages have also made them more popular. Because of these advantages, these packages have also gained much utility in the much harsher environment applications in the defense applications. Because of these reasons, first and second level interconnect thermo-mechanical reliability [Lall, 2018], [Xi, 2014], delamination failures [Zhaowei, 2011] [Abdullah, 2007], moisture ingress [Wu 2018] are some areas much researched upon for the QFN packages.

QFN packages are soldered directly to the PCB Cu pads and have no lead, the bottom plane of the package has solder lands that are directly soldered. The QFN packages have a large heat sink that gives it good thermal characteristics and usually have a solder height of 50 to 75 microns. In comparison, BGA solder joints have a height varying from 350 microns to 550 microns.

Researchers have also published on effect of macro voids on thermal cyclic fatigue reliability of different package types. Lau et al published on effect of voids on Bump Chip Carrier package solder joints. Larger void percentage resulted in larger creep strain, larger void size resulted in larger creep strain and solder joints with voiding percentage less than

20% had no effect on the fatigue reliability [Lau 2002]. For BGA solder joints it is published that increase in number of voids towards the PCB side did not have an effect on the thermal cyclic fatigue reliability [Yu 2006]. Ladani et al concluded that the small voids near the damage area arrest damage propagation thus increasing the propagation life, but because of the shorter damage initiation life, they may still reduce the overall reliability. Also, it was reported that reliability increases as the void size increased from 1 to 15% and then dropped for voids bigger than 15% [Ladani 2006]. SAC 305 solder material is also known to have a lower fatigue life while under tensile loads in comparison to shear loads and multiaxial loads [Deshpande, 2019]. This behavior further warrants investigation of effect of presence of voids in SAC305 solder joints. Researchers have also reported that equivalent plastic strain and shear strain for solder joint with void is not always larger than the solder joint without a void. From the mechanical shear test done on the joint scale solder joint it was also reported that the fatigue strength may not be affected by voids in Pb-lead and SAC solders if the voids do not participate on the initiation and propagation of cracks. The authors reported that the effect of voids was small enough to be neglected in case of CSP packages [Kim 2004].

The research stated above came from the studies conducted on the BGA solder joints, Flip chip solder joints, bumped solder joints and for Chip Scale Packages. Apart from these findings, the small size of the QFN package solder joint in comparison to the BGA package solder joint, in particular the ratio of volume of solder void to volume of solder joint may increase the influence of voids on the characteristic life. Earlier authors have reported on a comparison between thermal cyclic fatigue characteristic life for 32-Pin QFN packages

found using experimentation and FE modeling using, ANAND viscoplastic material model and Darveaux model for fatigue life prediction. It was reported that the location of the solder joint with the maximum non-linear plastic work per volume may change depending the on the size of the void in the solder joint in the vicinity of the corner solder joint. Also the FE modeling technique employed use of multi point constraints and micro-CT data based finite element modeling technique [Lall 2019].

In this study, the authors have addressed the effect of macro voids on QFN solder joints by use of finite element models with varying number, size and location of voids. Two void sizes, three locations and solder joints with one void and two voids have been studied as per full factorial design of experiments approach.

5.1.2 Test Vehicle

In this study, 32 pin QFN packages with SAC305 solder joints and 1 mil wire bond were used. Figure 104 shows an optical image and x-ray imagery of the package and Table 8 show the physical dimensions of the package used. YXLON micro-CT Cougar system was used for CT scanning the part. The part was mounted on to a plastic fixture into the 3-jaw chuck and a full revolution while x-ray images were being recorded. 1024 images were captured during the 1 full rotation resulting in a resolution of 0.016 mm voxel edge. Figure 105 show the reconstructed volume in the Volume Graphics software meant for data visualization. The low-density materials like the epoxy molding compound and the silicon die are not visible in the 3D reconstruction as they have relatively much lower density in comparison to the heavier elemental compositions in solder, lead frame, leads and wirebonds.

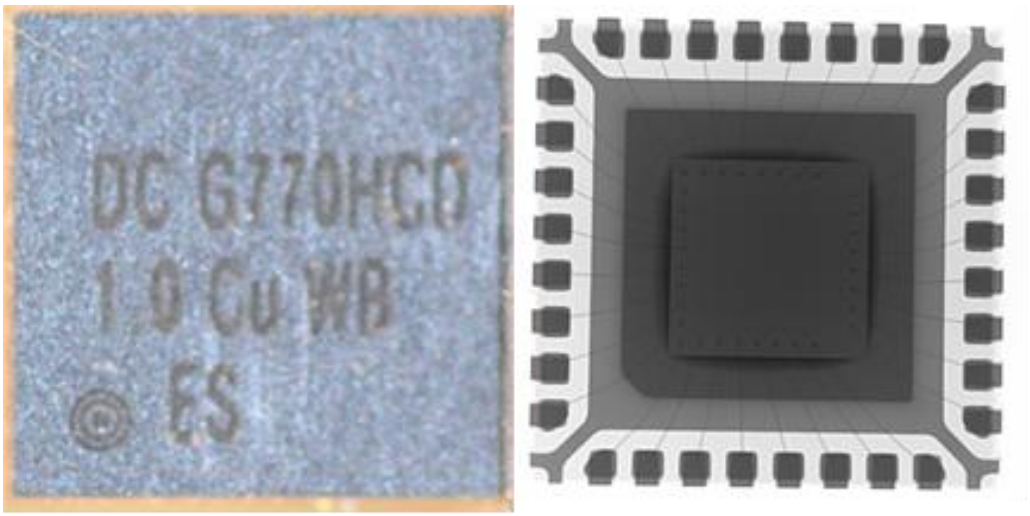

Figure 104: 32 Pin QFN (a) Optical Image (b) X-ray Image

Table 8 - Package Dimensions

Parameter	Dimensions (mm)
Width	5.02
Length	5.02
Height	0.7
Pitch	0.5
Wire Diameter	25.4 µm
Pad Thickness	0.9 µm

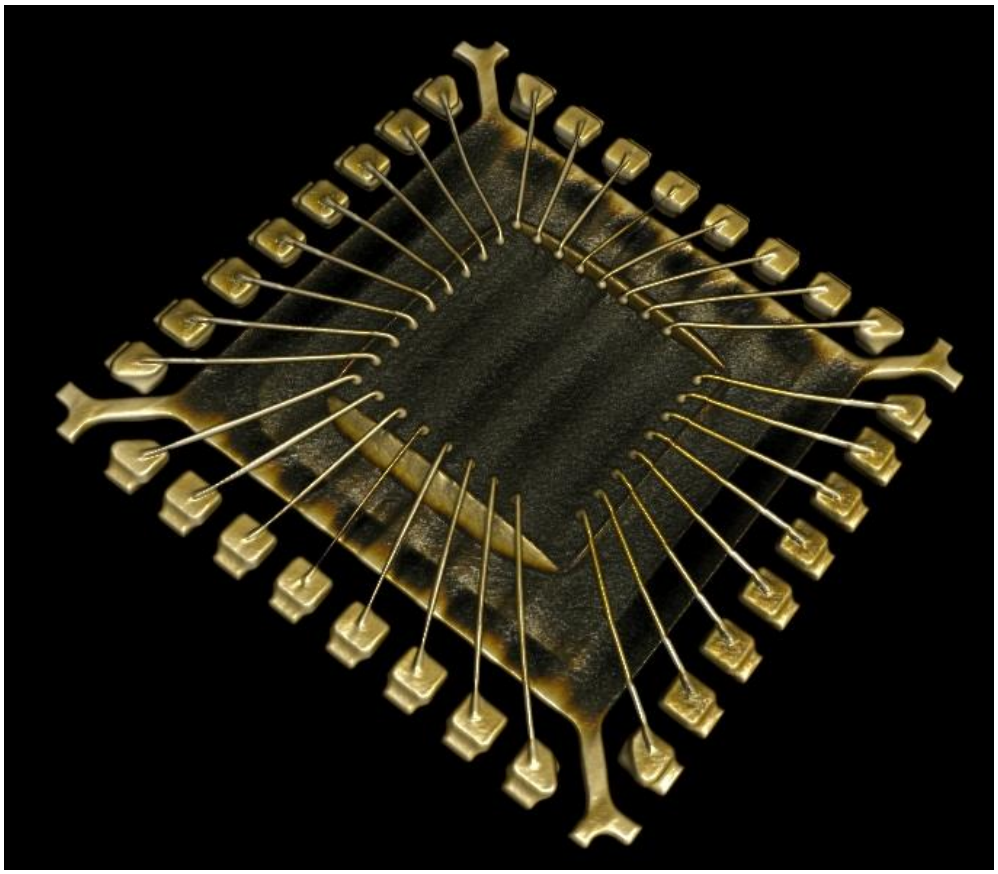

Figure 105 : 3D Reconstructed Package

5.1.3 Finite Element Modeling of QFN package

The procedure stated in the prior was repeated on all the solder joints and the stl. Data with surface triangular elements was obtained. This stl. Data was imported in Hypermesh and a solid tetramesh was created using the surface triangular mesh as the base seed mesh. The Figure 106 shows the final triangular solid mesh of the CT to mesh converted solder joints with voids.

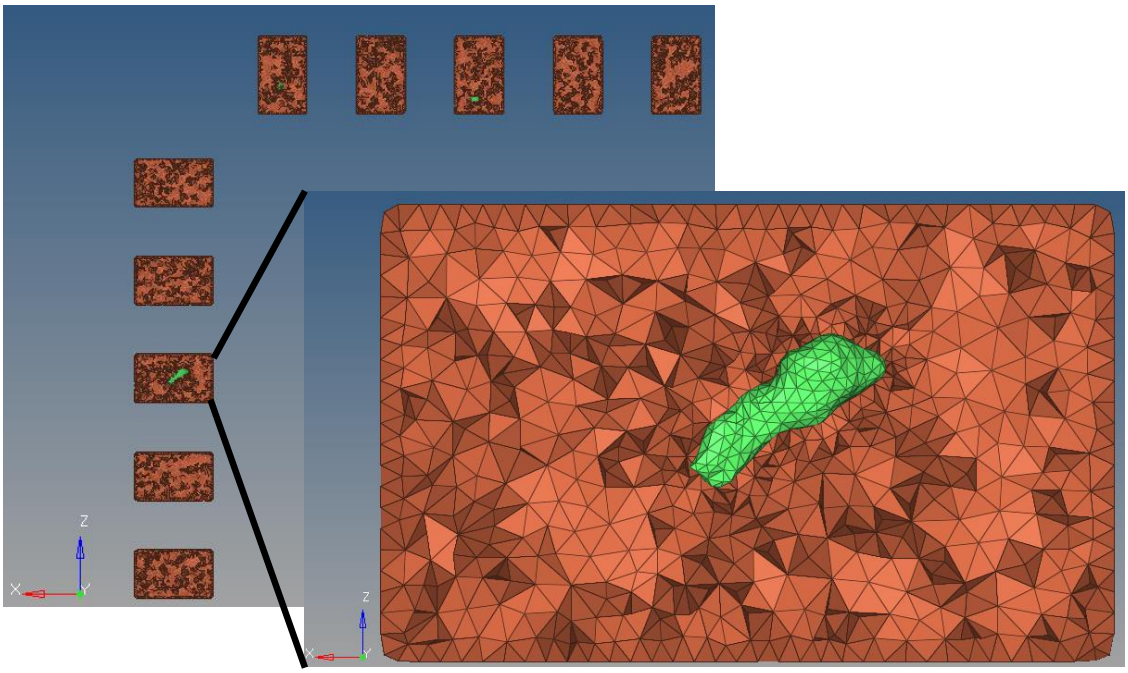

Figure 106: CT to mesh converted solder joints with voids

The solder joints were imported in Hypermesh and assembled with the rest of the CAD modeled and hex meshed QFN package and PCB. As different element types were assembled in the model, multipoint constraints approach was used to establish connectivity between the solder joint and PCB copper pad on the PCB side and solder joint and lead on the package side. A cross section of this assembly is shown the Figure 107:

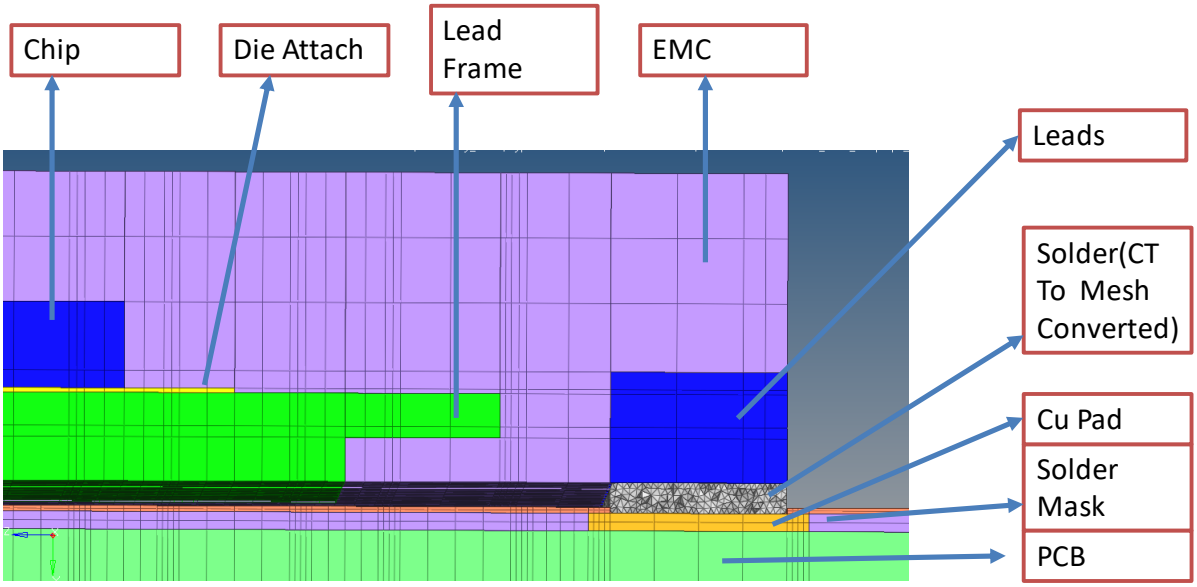

Figure 107: cross sectional view of the assembly

Linear elastic properties were assigned to all materials except for solder joint. Material properties are tabulated in Table 9. Die-attach material was identified as CRM-1076NS. This is high CTE silver die-attach specifically designed for QFN applications. The lead frame material was C194 alloy. EMC was green mold compound with very high filler content. This resulted into highest young's modulus and lowest CTE.

Table 9: Table of material Properties

Component	E (GPa)	CTE (ppm)	υ	Reference
EMC	24	10	0.3	[Vandevelde 2012]
Si Chip	163	0.28	3.5	[Lall 2003]
Die-attach	10	45	0.35	[Lall 2003]
Lead-frame	121	16.7	0.34	[Vandevelde 2012]
Solder Mask	3100	30	0.3	[Lall 2003]
Cu Pad	129	16.3	0.34	[Lall 2003]
PCB	23.8 (X,Y) 12.2 (Z)	12.42, 57	0.39, 0.11	[Lall 2003]

Table 10: Anand Model Parameters for SAC305 Solder

Property	**Value**
S_0	21MPa
Q/R	9320 1/K
A	3501 1/sec
x_i	4
m	0.25
h_0	1.8×10^5 MPa
$\hat{s}$	30.2 MPa
n	0.01
a	1.78

Table 10 shows the SAC305 solder Anand Model parameters found using experimental testing [Basit 2014]. SOLID 185 was used to mesh the hexahedral and tetrahedron elements of the solder and the rest of the parts. CONTACT170 and TARGET171 were used as the contact elements for forming the contact pairs for Multipoint constraints. The set of nodes meant for multipoint constraint-based contact definition were used to create Target and Contact elements, namely TARG170 and CONTA171 elements. ANSYS prescribes defining the softer of the materials in contact as the Contact and the relatively harder material as the Target. Other criteria for this definition is based on mesh density. The material with denser mesh is recommended to be defined as Contact and the relatively less dense mesh as the Target. In this model the contact was established between the copper and the solder at the bottom and solder and leads at the top. Figure 108 shows the location of the contact pairs formed. A fairly course mesh was used for meshing the QFN package and the PCB while a relatively denser mesh was used for modeling the solder joints. This was done to minimize the number of elements as an implicit FE solver was to be used for solving the FE model. The model created also had Anand parameters defined for the solder material further adding to the complexity of the model. The assembly was then subjected to thermal cyclic loading. Constant temperature was applied in stepwise manner to whole assembly. Peak temperatures were 125°C and -40°C. Higher temperature was defines as reference or stress-free point, and one full cycle was analyzed. Dwell time at highest and lowest point were 10 minutes and ramp time was 20 minutes. The boundary condition applied to the model are shown in the Figure 109.

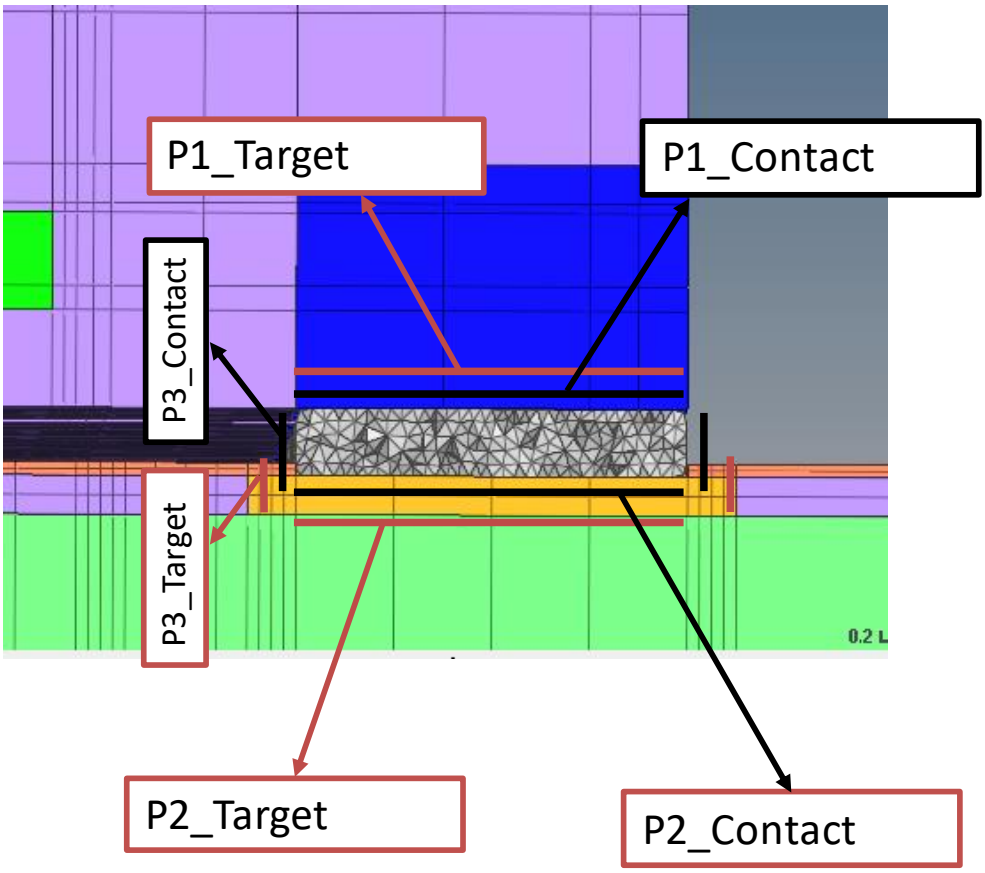

Figure 108: Location of contact pairs

A quarter model with voids was selected to aid computation time. Quarter with highest number of voids was selected for the study.

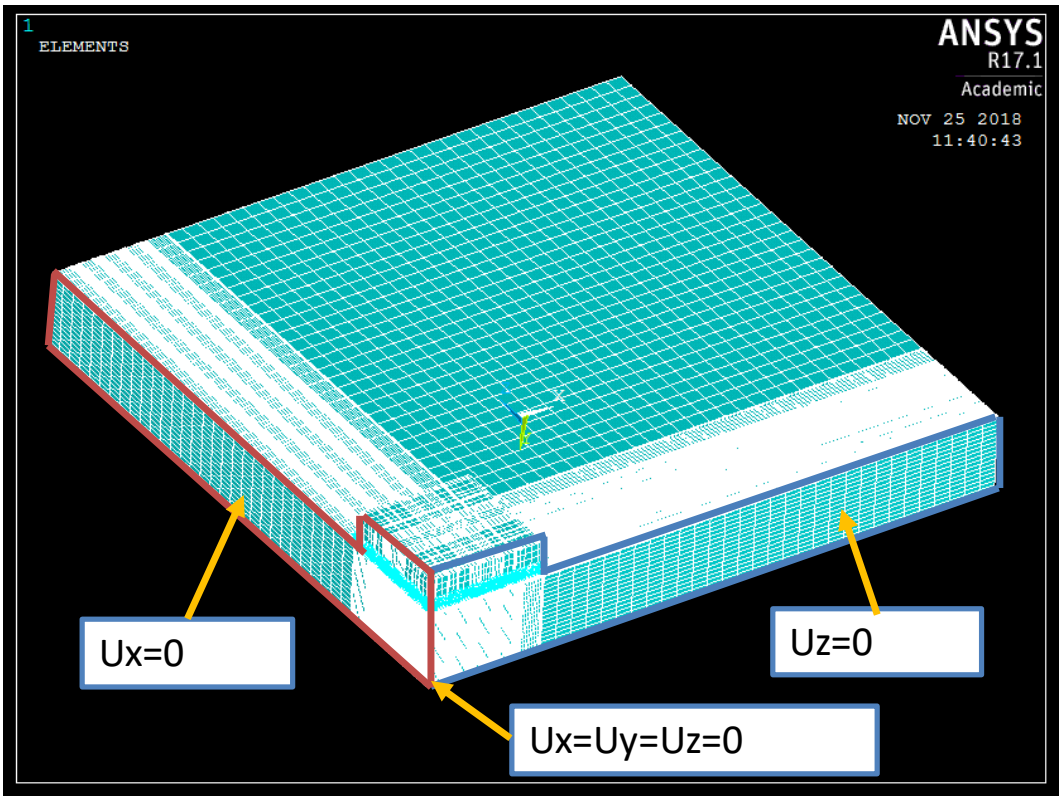

Figure 109: Boundary Conditions for the FE model

5.1.4 Anand Viscoplastic Model

Previously, Anand [1982] has developed a constitutive model to describe the material that depend on operating temperature and strain rates. Anand model has unified a stress equation, a flow equation, and an evolution equation to characterize both the creep and rate-dependent plastic performance of the solder alloy.

In one-dimension uniaxial loading case, stress equation can be written by;

$$\sigma = cs; c < 1 \tag{47}$$

Stress Equation:

$$\sigma = \left(\frac{s}{\xi}\right) \sinh^{-1}\left\{\left[\frac{\dot{\varepsilon}_p}{A} \exp\left(\frac{Q}{RT}\right)\right]^m\right\} \tag{48}$$

Flow equation:

$$\dot{\varepsilon}_p = A \exp\left(-\frac{Q}{RT}\right)\left[\sinh\left(\xi\frac{\sigma}{s}\right)\right]^{1/m} \tag{49}$$

Final version of stress-strain relation:

$$\sigma = \left(\frac{1}{\xi}\right)\sinh^{-1}\left\{\left[\frac{\dot{\varepsilon}_p}{A}\exp\left(\frac{Q}{RT}\right)\right]^m\right\} \tag{50}$$

$$\left\{\hat{s}\left(\frac{\dot{\varepsilon}_p}{A}\exp\left(\frac{Q}{RT}\right)\right)^n - \left\{\left[\hat{s}\left(\frac{\dot{\varepsilon}_p}{A}\exp\left(\frac{Q}{RT}\right)\right)^n - s_0\right]^{1-a} + (a-1)\left[h_0\left[\hat{s}\left(\frac{\dot{\varepsilon}_p}{A}\exp\left(\frac{Q}{RT}\right)\right)^n\right]^{-a}\varepsilon_p\right]\right\}^{1/1-a}\right\}$$

Nine anand constants are A, ξ, Q/R, m, h_0, a, s_0, $\hat{s}$, and n. The Ultimate Tensile Strength (UTS) can be attained by simply assuming that ε_p goes to infinity.

$$\sigma^* = \text{UTS} = \sigma\Big|_{\varepsilon_p\to\infty} = \frac{\hat{s}}{\xi}\left[\frac{\dot{\varepsilon}_p}{A}\exp\left(\frac{Q}{RT}\right)\right]^n \sinh^{-1}\left[\frac{\dot{\varepsilon}_p}{A}\exp\left(\frac{Q}{RT}\right)\right]^m \tag{51}$$

Substituting this maximum tensile stress back in Equation (50**)**

and rewritten as

$$\sigma = \sigma^* - [(\sigma^* - cs_0)^{1-a} + (a-1)\{ch_0(\sigma^*)^{-a}\}\varepsilon_p]^{1/1-a} \tag{52}$$

The detailed anand model and procedure to compute the nine anand parameters have been discussed in earlier publications by the authors [Lall 2014].

5.1.5 Experimental Results

Thermal cyclic experiment was performed on QFN packages. Resistance of the package was measured in-situ and 20% rise of resistance in more than 2 daisy chained pairs per package was defined as the failure criteria. 19 packages were subjected to test as per AEC-Q100 standard as shown in Figure 111. The CT to mesh converted solder joint were found to have rectangular cross-section similar to that observed in Figure 110.

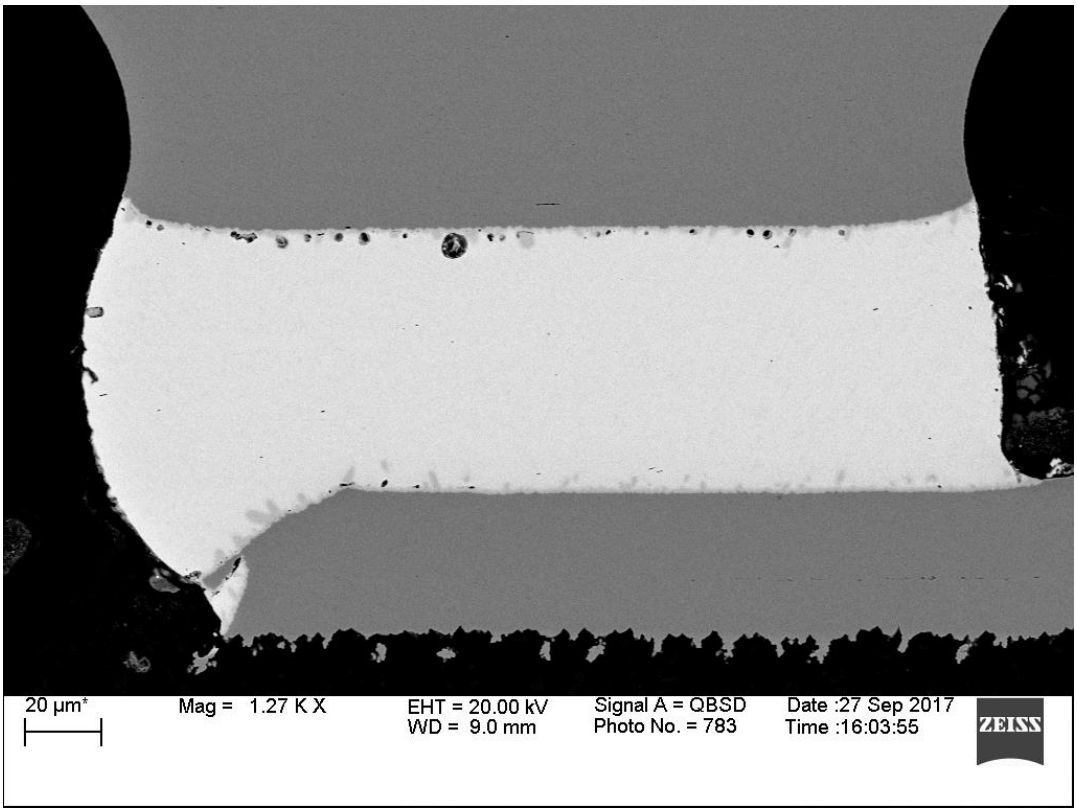

Figure 110:Cross-section of good solder joint

The packages were cycled to failure and number of cycles to failure for each package was recorded. A Weibull plot was made for the failed samples to note the characteristic life. Weibull distribution is shown in Figure 111. The characteristic life, which is the number of cycles to failure for 63% of all parts tested is represented by variable Eta. Beta value of

the distribution was 23.12. Red dashed lined represents x and y coordinates of the characteristic life data point.

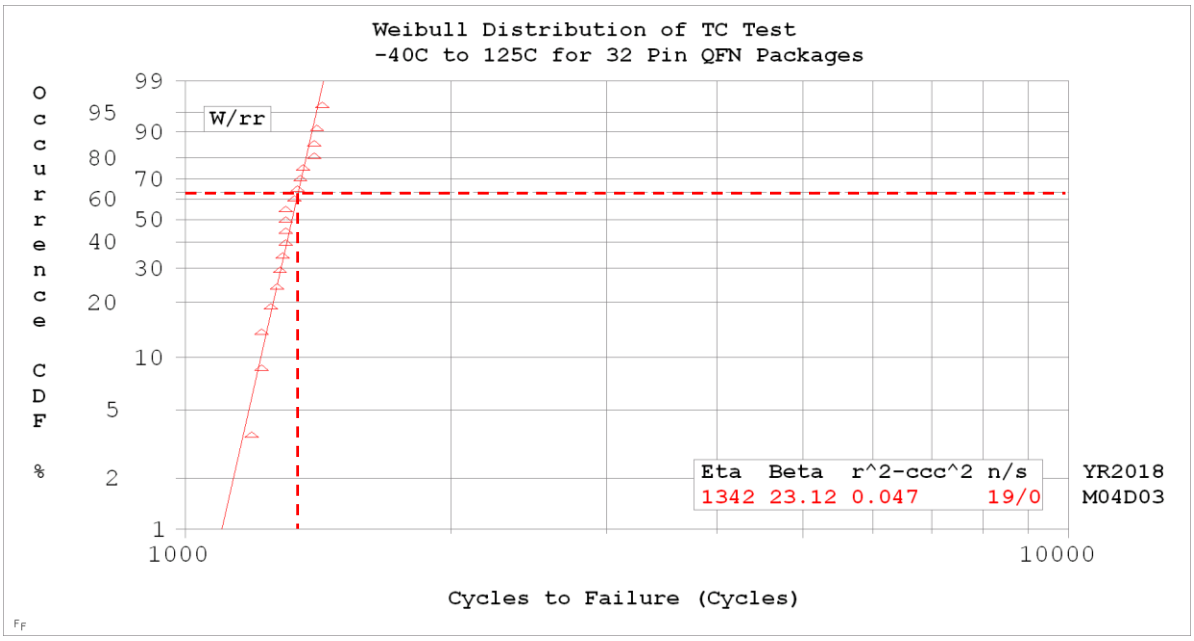

Figure 111: Weibull Plot of experimental dataset

5.1.6 Finite Element Model Results

The meshed hybrid model of CAD modeled geometry and CT to mesh converted geometry was run in ANSYS using an implicit solver. The model was entirely created in Hypermesh and imported into ANSYS. A thermal cycling load from 125°C and -40°C was applied and the model. Two cycles were simulated.

Figure 112 shows the deformation contour plot in Y axis of the QFN quarter model when subjected to a thermal cyclic load.

High temperature (125°C) was considered as reference and stress-free temperature. Since the analysis was non-linear in nature with definition of ANAND viscoplastic material

model, after full cycle residual stresses were observed. Figure shows resultant displacement contour of the package under thermal loading at the end of the first ramp thermal load going from 125^0C to -40^0C. The displacement field was symmetric in nature. Minimum displacement was at the corner of the PCB where nodes were constrained, and maximum deformation was observed at the edges of free length of package. As the assembly cools from 125^0C to -40^0C the PCB bends upwards, raising the QFN package corner. This confirms that all boundary conditions and load conditions along with contact were correctly defined and imposed.

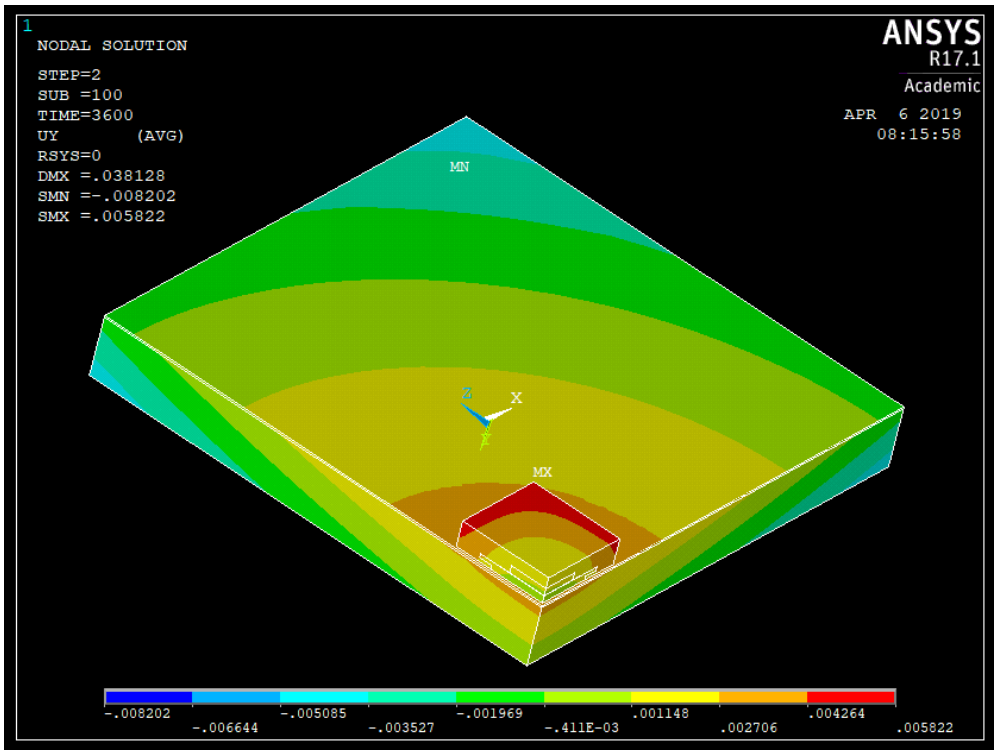

Figure 112: Y axis deformation contour plot

Von Mises stress in the package and the solder joints were studied. It is largely published that upon application of a thermal load the most critical solder joint stresses are found to be in the corner solder ball and this because it is at the highest distance from the neutral

point of the package that is the center of the package. Though, this result is commonly published, the underlying assumption is that there are no voids in the solder joints, all solder in the same package are similar to each other and all packages are of the same type are also similar to each other. These assumptions are not made in this study. Figure 113 shows the contour plot of Von Mises stress on the solder joint on the lead side of the package. The location of maximum stress is pointed out. The most critically stressed solder joint was found to be the one with a long void and the void being close to the interface of solder joint and lead.

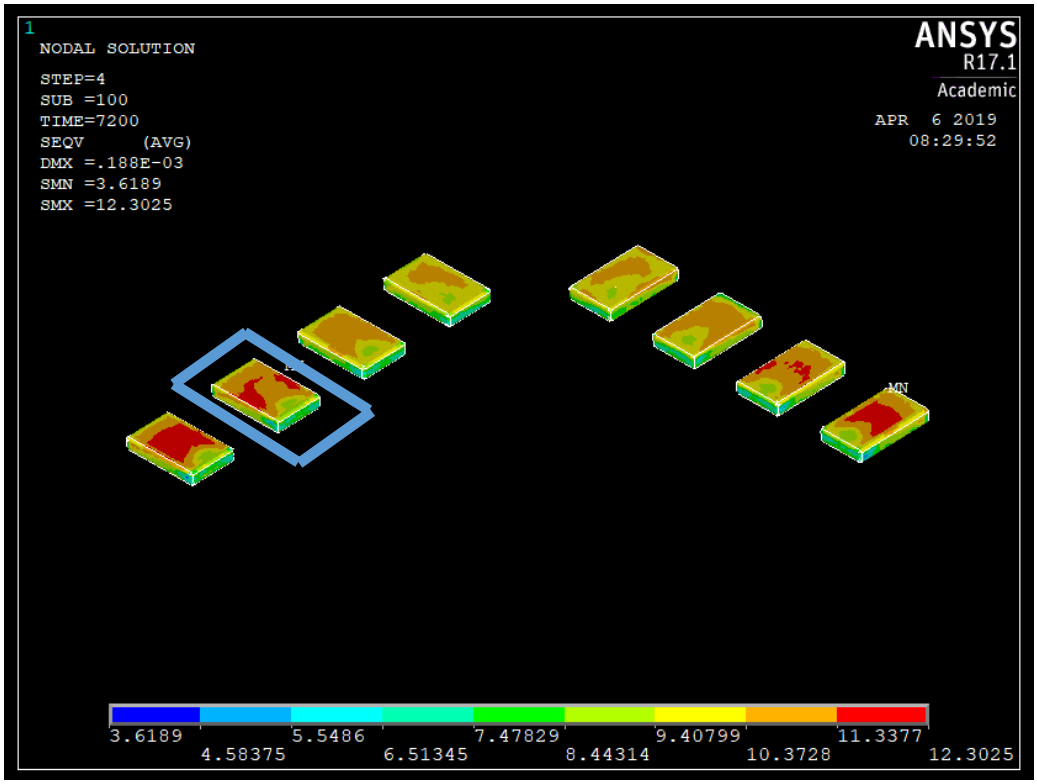

Figure 113: Location of maximum stress, Cycle 1

Figure 114 shows a zoomed in view of the critical solder joint with the void. The lowered stresses observed between the red contours adhere with the shape of the void shown in the Figure 115 . This nature of contour plot is observed because there are minimal stresses

inside the volume of the void which causes the surrounding regions highly stresses from the transfer of shear stresses between the void and the top surface of the solder joint. Figure 115 shows the cross-sectional view of the critical solder with a contour plot of the Von Mises stresses. The location of highest stress was found to be on the apex point of the surface of the void.

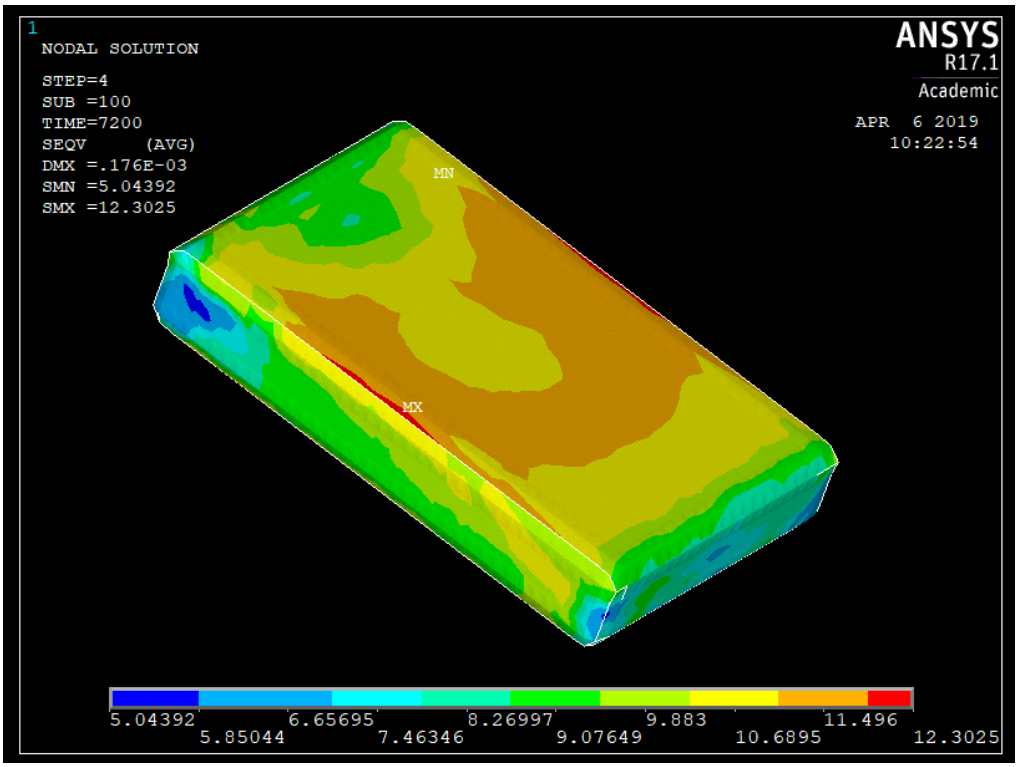

Figure 114: Von Mises contour plot for critical solder joint

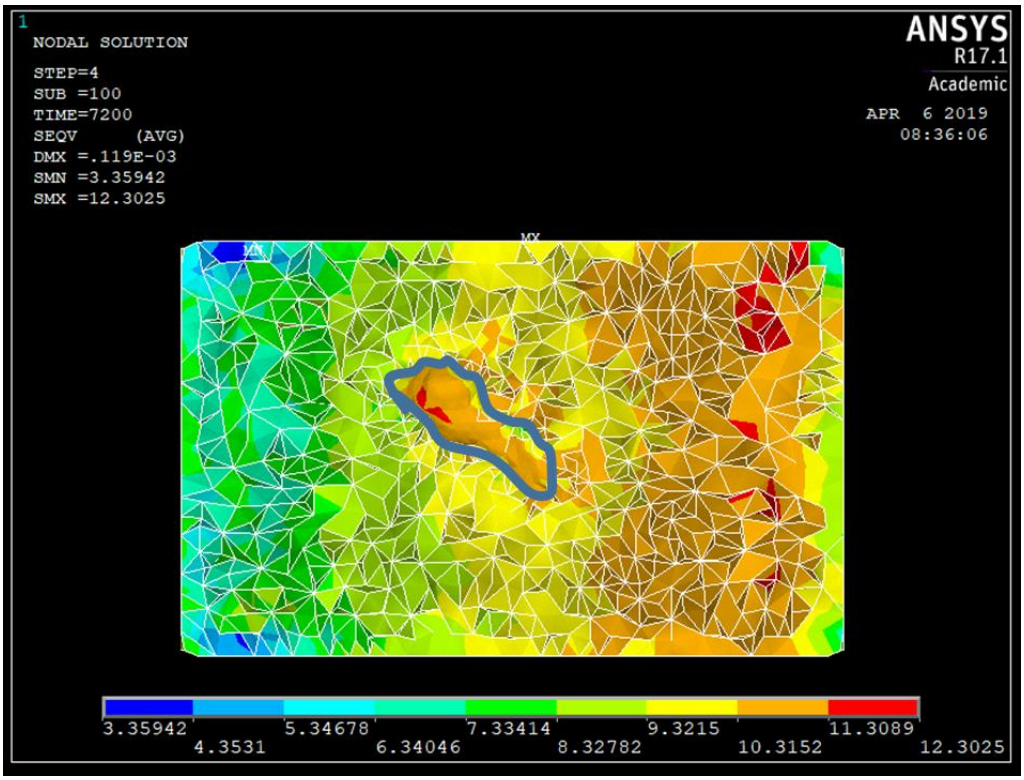

Figure 115: Von Mises contour plot over the cross section of the critical solder joint

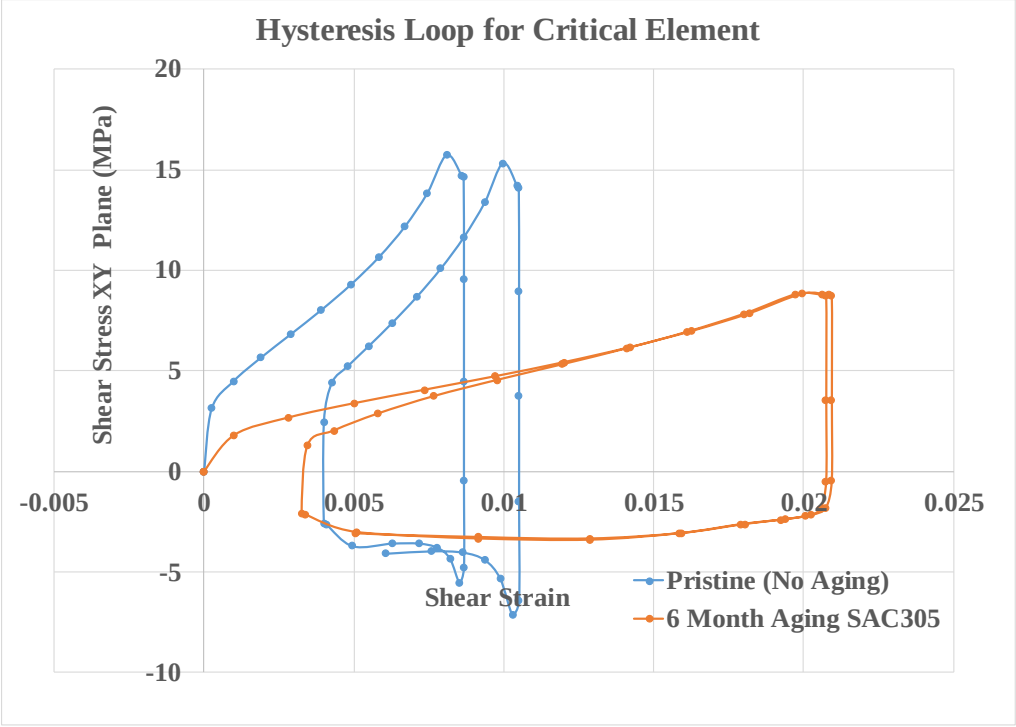

Figure 116: Hysteresis loop for SAC305 solder with no aging

Figure 116 show the hysteresis loop for the Von Mises stress at the critical node for both the cycles for different SAC305 solder Anand parameters, for pristine SAC305 with no ageing and with 6-month ageing. As expected, the peak stress is found at the end of first ramp loads going from 125^0C to -40^0C. The lowest stress is again found at the end of the second ramp, where the temperature goes from -40^0C to 125^0C. This is because the temperature is going towards the reference temperature of 125^0C.

Using this solder joint as the critical solder joint, characteristic life was computed using the Darveaux's model. Darveaux's energy-based model for thermal fatigue life computation in ANSYS is expressed as:

$$N_0 = K_1(\Delta SED)^{K_2} \tag{53}$$

$$\frac{da}{dN} = K_3(\Delta SED)^{K_4} \tag{54}$$

$$\alpha = N_o + \frac{a}{da/dN} \tag{55}$$

Here K1 to K4 are constants related to the finite element model mesh configuration, simulation methodology and constitutive material models. These constant were computed by Mirza et al. by experimentally testing multiple packages to failure with SAC305 solder and regression fit of the log of number of cycles to crack initiation and log of average plastic work density and log of crack initiation growth rate and log of average plastic work density.

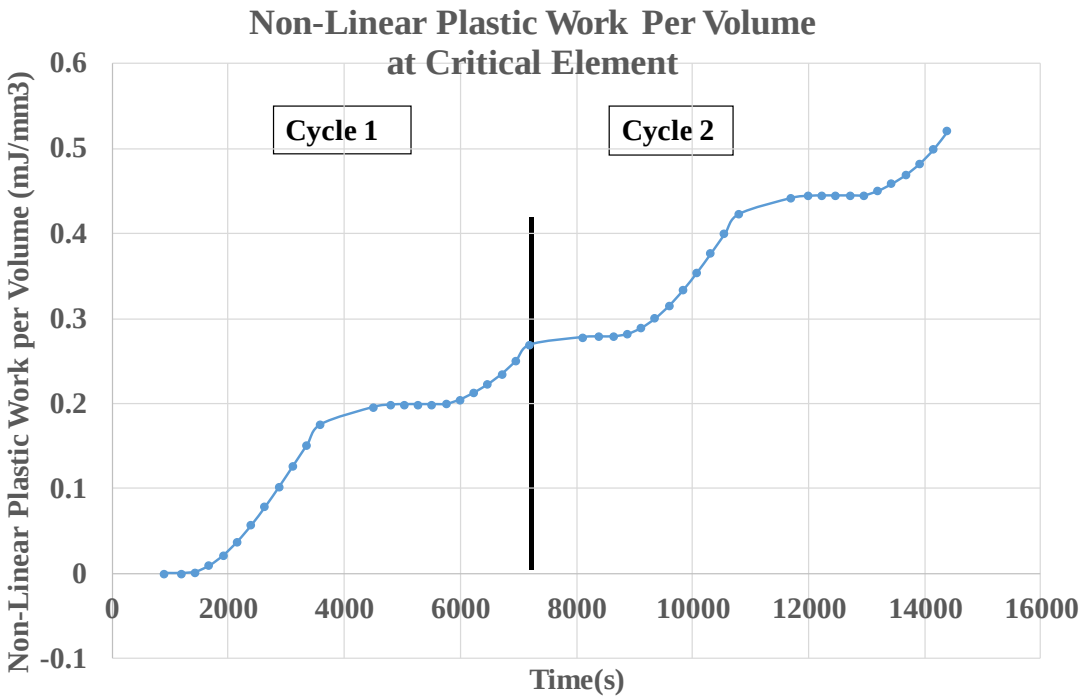

Figure 117: Strain Energy Density over the critical node over 2 cycles

Table 11: Darveaux's Model Constants from [Lall 2017]

K1 (cycles/MPa^{K2})	K2	K3 (mm/cycle-MPa^{K4})	K4
42	-1.3	0.00095	1.3

In this study, the averaged plastic work density accumulated per cycle in solder was extracted from FE model. This value was computed in the top layer of elements, a layer of thickness ~0.4 inch. Using the strain energy density and the constants, number of cycles to

crack initiation, crack propagation rate and number of cycles to failure was computed. Table 12 shows the three values.

Table 12: Darveaux's Model Results

ΔSED	0.2514 mJ/mm^3
N_0	254.64cycles
da/dN	0.0001566 mm/cycle
Characteristic Life	1850.13 cycles

Table 13: Comparison of Experimental and FE Predicted Characteristic Life

Characteristic Life (Experimentally)	Characteristic Life (FE Model)	% Error
1342 Cycles	1850.13 Cycles	37.86

The average characteristic life found experimentally was reported as 1342 cycles.

5.1.7 Summary and Conclusions

In this study, effect of macro-voids on a 32 pin QFN package subjected to thermal cyclic load was studied. The QFN assembly was scanned using micro CT system and the scanned data was used to build FE model to capture the defects in the solder joint. A detailed technique involving image processing algorithms implemented for the conversion of the micro CT data was described in the study. A hybrid FE mesh model of CT data-based solder joints and CAD modeled and meshed PCB and QFN assembly was made. The unique setup of the model allowed for relatively lesser number of elements and thus faster computational times.

The common assumption for the most critical solder joint in a QFN assembly would be the corner solder joint as per the Distance to Neutral Point formula. This DNP formula assumes that the package geometries are free of defect and thus each solder joint is same. Results extracted from FE analysis showed that the corner solder joint was not the most critical solder joint. The most critical solder joint as per the Von-Mises stress generation and amount of non-linear plastic work was the solder joint with the large macro-void. Further, highest stresses were observed at the apex point of the void. Thermal cycling experiment was performed on molded 32 pin QFN packages assembled with SAC305 alloy. 20% change in resistance was defined as failure threshold. Characterize life of the packages was 1342 cycles. Darveaux model for solder joint characteristic life used in the FE model yielded a characteristic life of 2029.74 cycles, within the acceptable error bound, proving the feasibility of this model for computing solder joint fatigue life inclusive of macro-void defects.

5.2 DOE Study to Investigate the Effect of Voids on QFN Solder Joints

5.2.1 Test Matrix

The intent of the study was to evaluate the effect of size and location of the voids in a QFN solder joint.

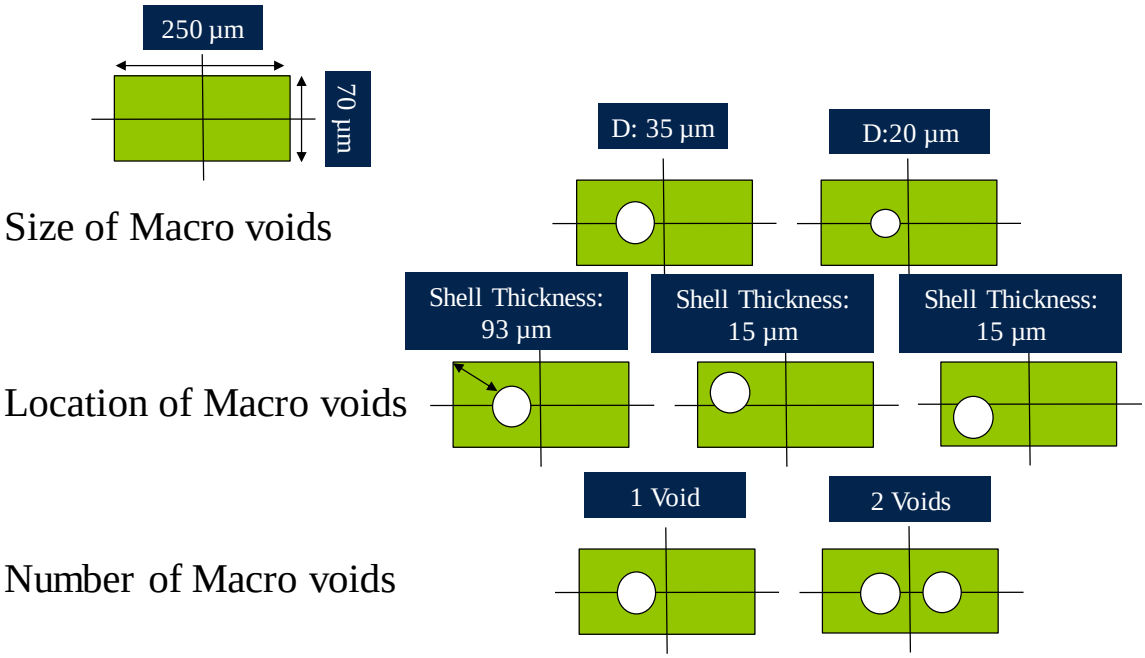

Figure 118: Combinations for size, location and number of voids

Figure 119 and Figure 120 show the test matrix reflective of the same. Two void sizes of 35 microns and 20microns and three void locations were considered as shown in the figures.

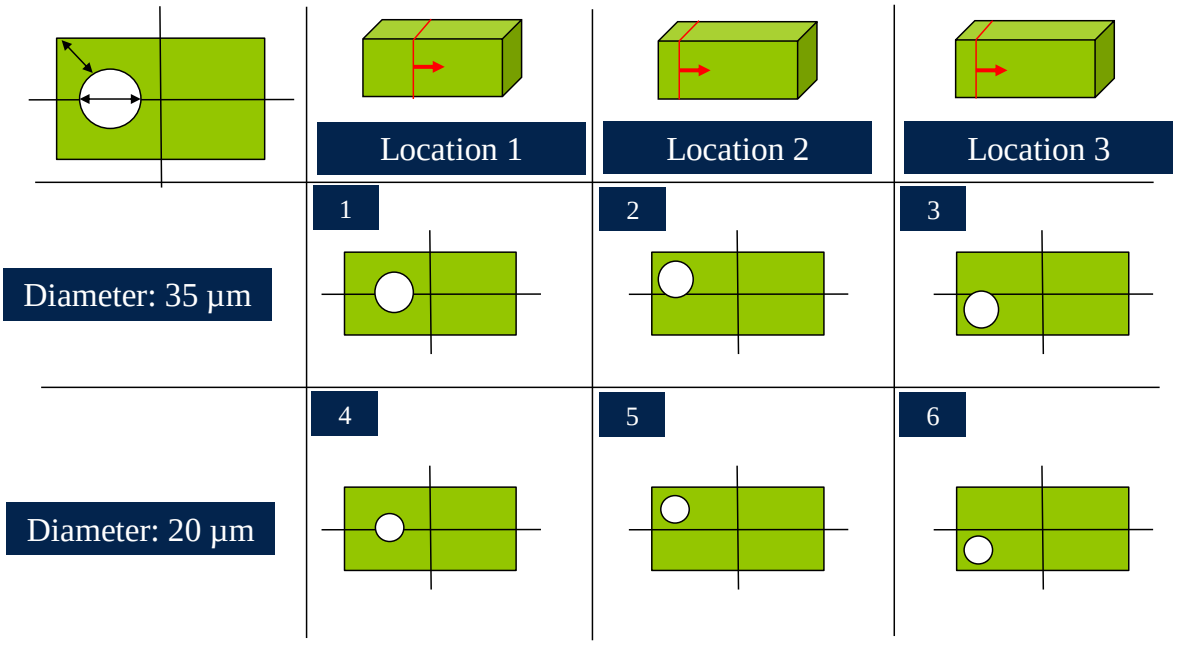

Figure 119: Test Matrix for 1 Void

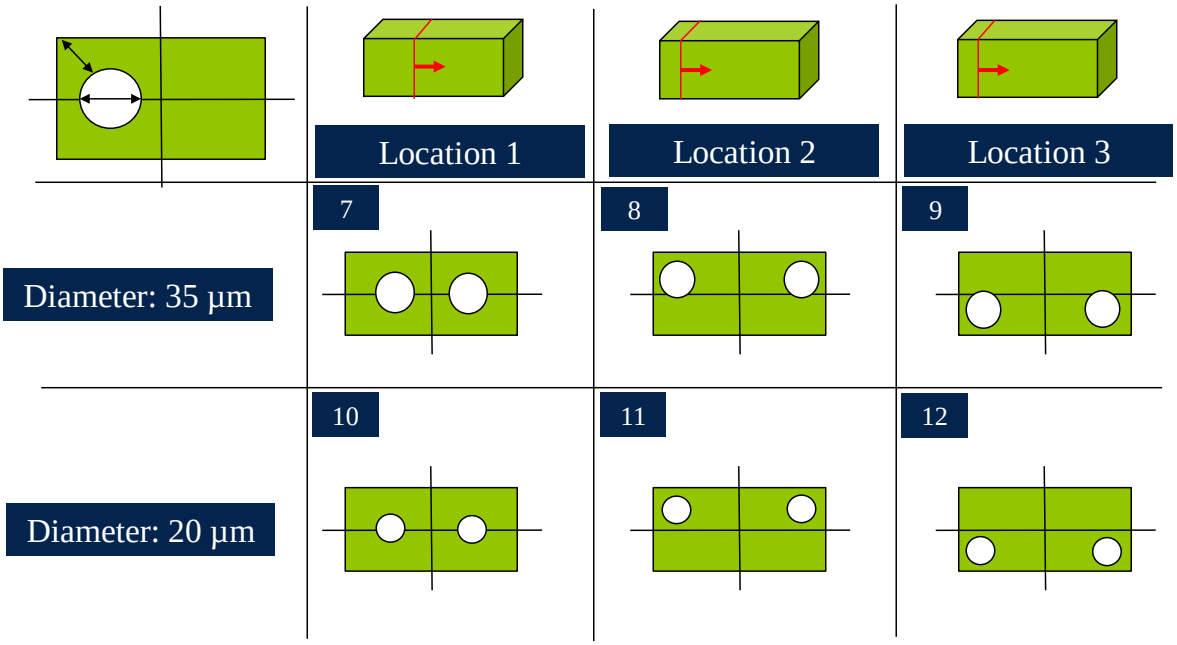

Figure 120: Test Matrix for 2 Voids

The location of the cross section along the out of plane axis was selected on basis of shell thickness, which is the distance between the corner of solder ‘cube’ and the void surface. This distance was kept constant for both the small and the big void.

This matrix would allow to study the effect of size, effect of number of voids and location. 12 combinations were identified and each combination shown the Figure 119 and Figure 120 represent a separate finite element simulation. Alongside these 12 simulations, a solder joint with no void at the corner location was also chosen for the study. This simulation without the void would serve as control. Each simulation run had the corner solder joint with voids as per this test matrix and the other remaining solder joints were modeled without any voids. Maximum non-linear plastic work at the end of two thermal cycles, shear stresses and von mises stresses were chosen to be recorded for comparison across different combinations.

5.2.2 Finite Element Analysis

The 12 finite element models with corner solder joints defined as described earlier were modeled in Hypermesh and imported to ANSYS. Quarter symmetry was exploited to reduce the computational time. The solder joints were modeled with the tetrahedral elements and the rest of the model was meshed with hexahedral elements. This meshing strategy was chosen because meshing a spherical void inside of a solder ‘cube’ with a fine mesh around the void was achievable with relatively lesser number of elements and also easier utilizing Delaunay’s triangulation approach. Figure 121 shows a meshed model of the solder joint with a void.

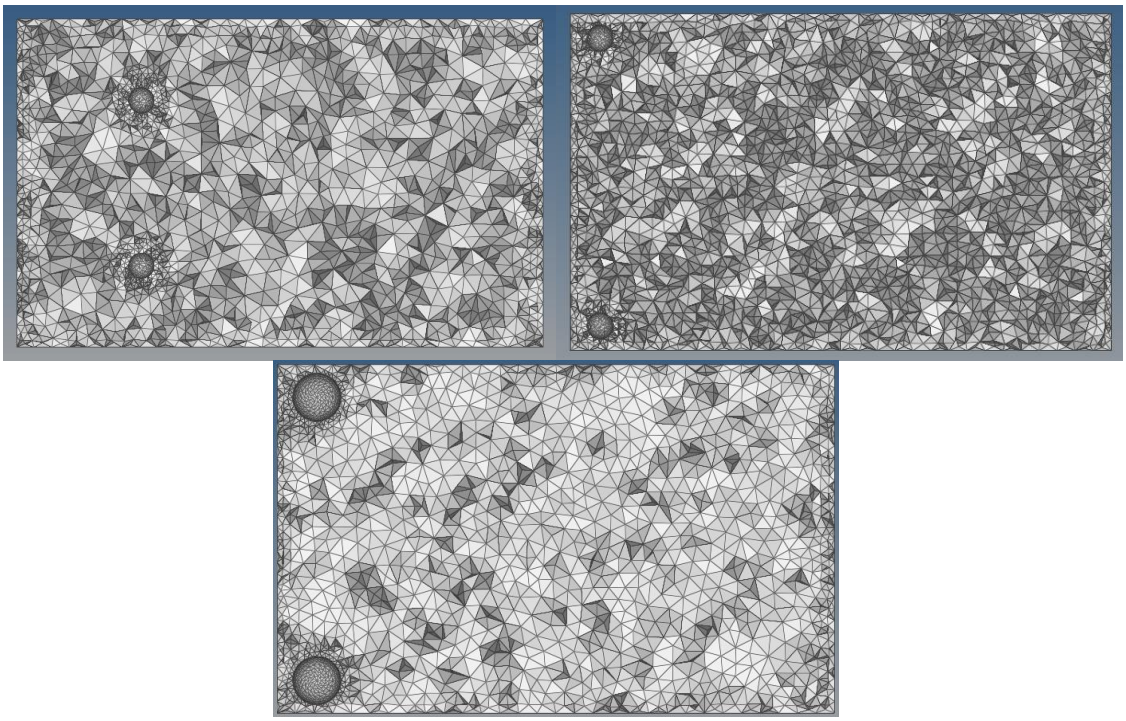

Figure 121: Solder Joint with Voids

As different element types were assembled in the model, multipoint constraints approach was used to establish connectivity between the solder joint and PCB copper pad on the PCB side and solder joint and lead on the package side. A cross section of this assembly is shown in Figure 122

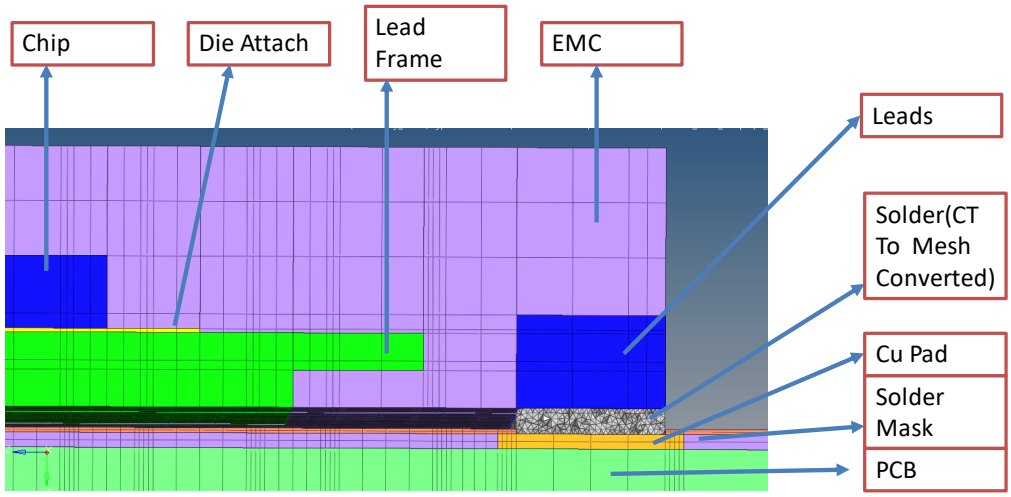

Figure 122: Cross sectional view of the assembly

Linear elastic properties were assigned to all materials except for solder joint. Material properties were applied as listed in Table 9. Die-attach material was identified as CRM-1076NS. This is high CTE silver die-attach specifically designed for QFN applications. The lead frame material was C194 alloy. EMC was green mold compound with very high filler content. This resulted into highest young's modulus and lowest CTE.

Table 10 shows the SAC305 solder Anand Model parameters found using experimental testing [Basit 2014]. SOLID 185 was used to mesh the hexahedral and tetrahedron elements of the solder and the rest of the parts. CONTACT170 and TARGET171 were used as the contact elements for forming the contact pairs for Multipoint constraints. The set of nodes meant for multipoint constraint-based contact definition were used to create Target and Contact elements, namely TARG170 and CONTA171 elements. ANSYS prescribes defining the softer of the materials in contact as the Contact and the relatively harder material as the Target. Other criteria for this definition is based on mesh density. The material with denser mesh is recommended to be defined as Contact and the relatively less dense mesh as the Target. In this model the contact was established between the copper and the solder at the bottom and solder and leads at the top. Figure 123 below shows the location of the contact pairs formed. A fairly course mesh was used for meshing the QFN package and the PCB while a relatively denser mesh was used for modeling the solder joints. This was done to minimize the number of elements as an implicit FE solver was to be used for solving the FE model. The model created also had Anand parameters defined for the solder material further adding to the complexity of the model.

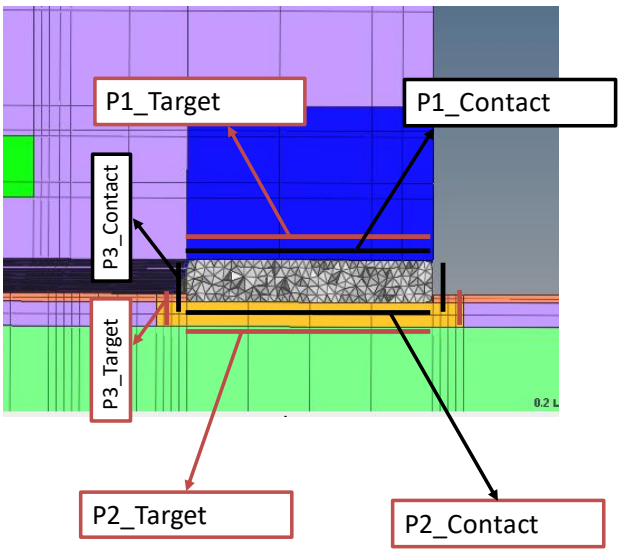

Figure 123: Location of contact pairs

The assembly was then subjected to thermal cyclic loading as shown in the figure above. Constant temperature was applied in stepwise manner to whole assembly. Cycling profile was chosen as per AEC Q-100 standard for grade 0 packages. Peak temperatures were 125°C and -40°C. Higher temperature was defines as reference or stress-free point, and one full cycle was analyzed. Dwell time at highest and lowest point were 10 min. and ramp time was 20 min. The boundary condition applied to the model are shown in the Figure 124. A quarter model with voids was selected to aid computation time. Quarter with highest number of voids was selected for the study.

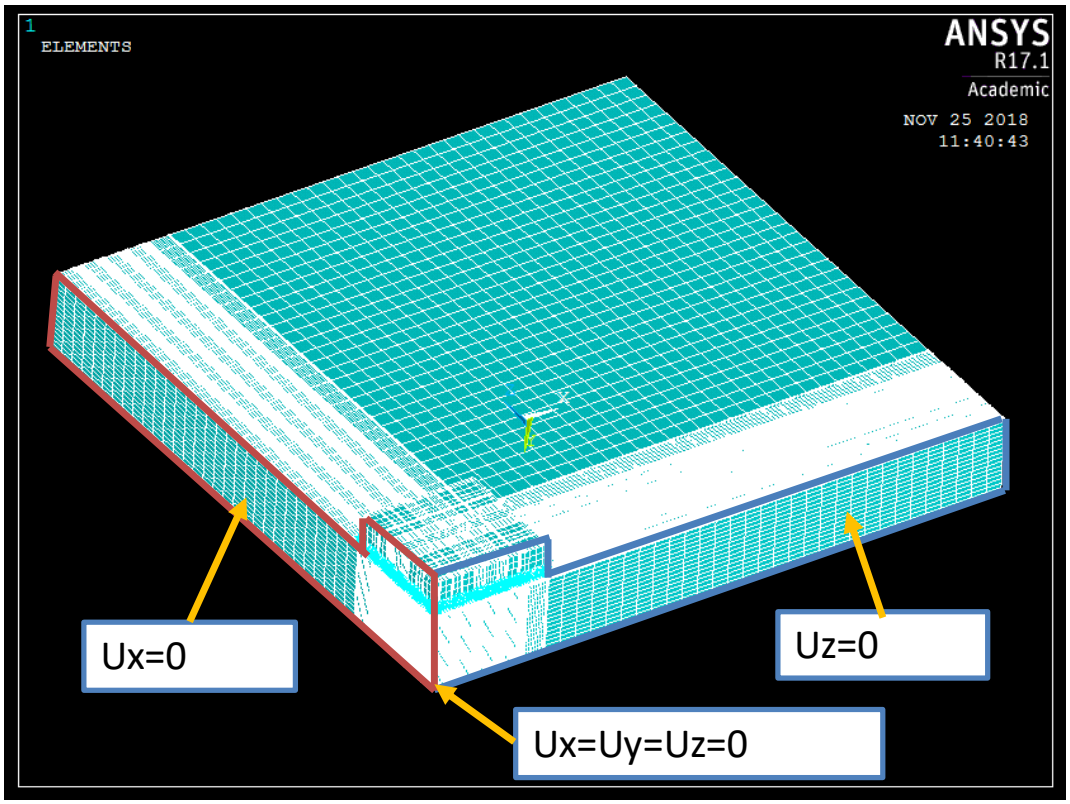

Figure 124: Boundary Conditions for the FE model

5.2.3 Results

Finite Element Model Results

The meshed model was run in ANSYS using an implicit solver. The model was entirely created in Hypermesh and imported into ANSYS. A thermal cycling load from 125°C and -40°C was applied and the model. Two cycles were simulated.

Figure 125 shows the deformation contour plot in Y axis of the QFN quarter model when subjected to a thermal cyclic load.

Higher temperature (125°C) was considered as the reference stress-free temperature. Since the analysis was non-linear in nature with definition of ANAND viscoplastic material model, after full cycle residual stresses were observed. Figure shows resultant displacement contour of the package under thermal loading at the end of the first ramp thermal load going from 125^0C to -40^0C. The displacement field was symmetric in nature. Minimum displacement was at the corner of the PCB where nodes were constrained and maximum deformation was observed at the edges of free length of package. As the assembly cool from 125^0C to -40^0C the PCB bends upwards, raising the QFN package corner ('sad face'). Form this it could be concluded that all boundary conditions and load conditions along with contact were correctly defined and imposed.

Figure 126 to Figure 138 show the maximum non –linear plastic work found in the models from M0 to M12 after two complete thermal cycles. The image shows the top surface of the solder joint at the interface of the solder joint and the leads.

The solder joints were modeled to have two layers of elements in a 25-micron band from the top towards the package side. This was done as per the published literature for solder joint thermo-mechanical reliability. It was seen that location for maximum non-linear plastic work was at the left bottom corner of the solder joint as seen in the figures. This location was found to be constant for all models apart from M2 and M8. Models M2 and M8 were the models with the largest void nearer to the package side. Models M2 and M8 were also found to have the least maximum non-linear plastic work build up in comparison

to all the other models. This comparison is shown in Figure 139. The critical locations for model M2 and M8 were found to be at the center of the left edge.

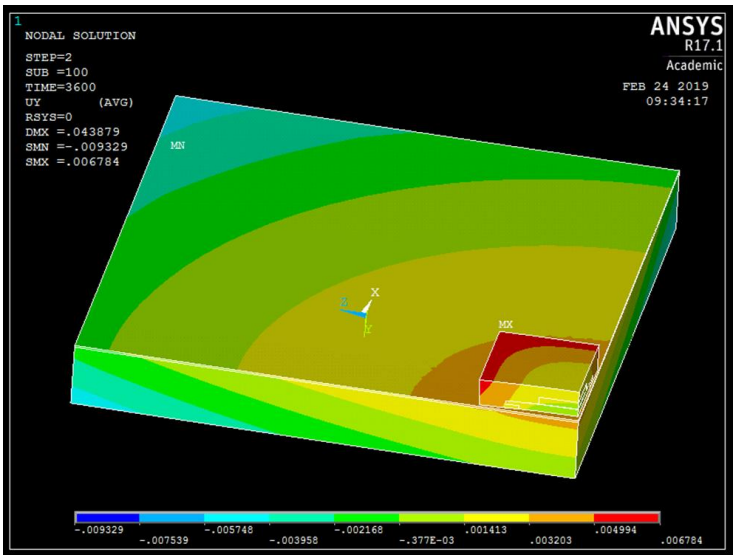

Figure 125: Y axis deformation contour plot

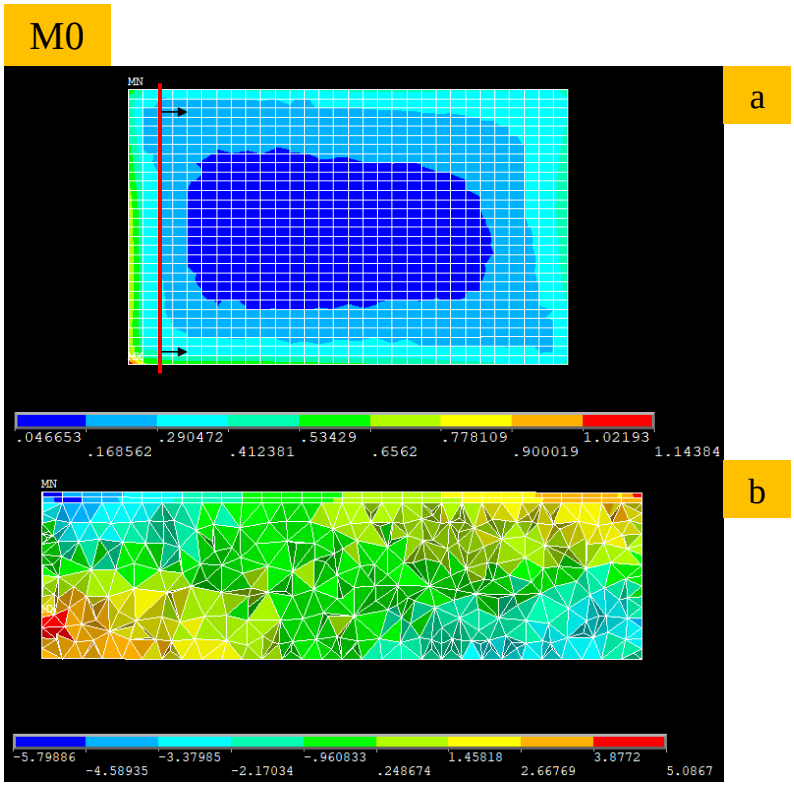

Figure 126: (a) Non-Linear Plastic Work Per Volume (b) YZ Shear Stress

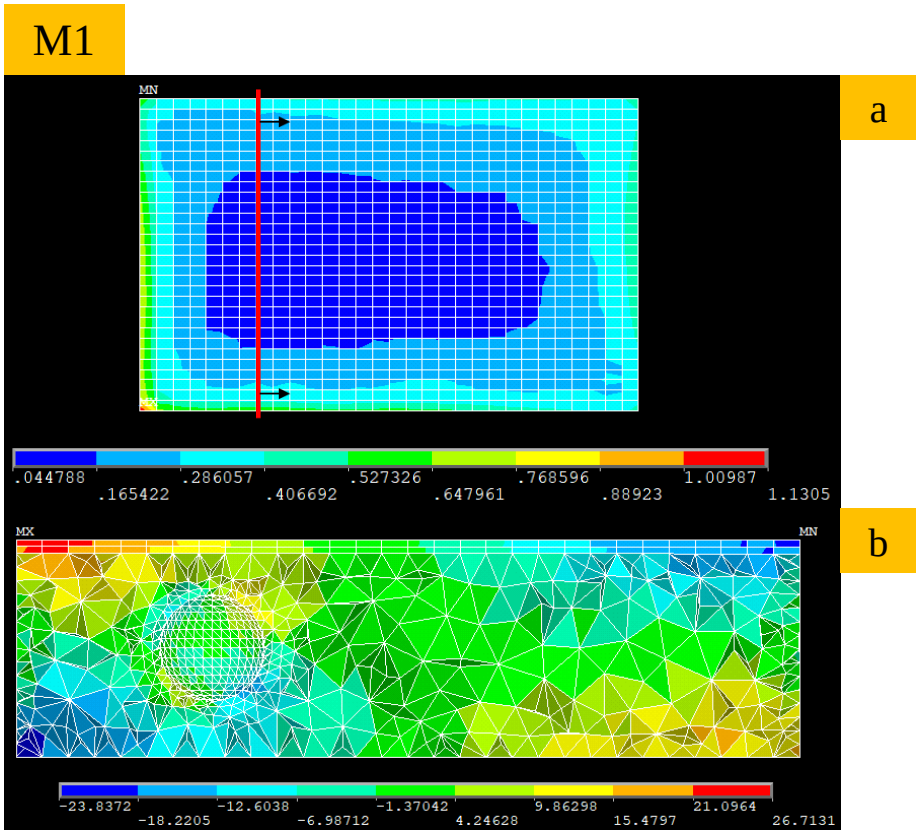

Figure 127: (a) Non-Linear Plastic Work Per Volume

(b)YZ Shear Stress

The change in critical location and the comparison of magnitudes of the non-linear plastic work indicated that a bigger void near the corner location on the package side may show a tendency to arrest crack growth and in turn improve the thermal-cyclic fatigue life. From the YZ shear contour plots, it was observed that the buildup of shear stress was over a larger volume for solder joints with voids near the PCB side in comparison to the joints with voids near the package side. This was observed in figures for M2-M3, M5-M6, M8-M9 and M11-M12 consistently.

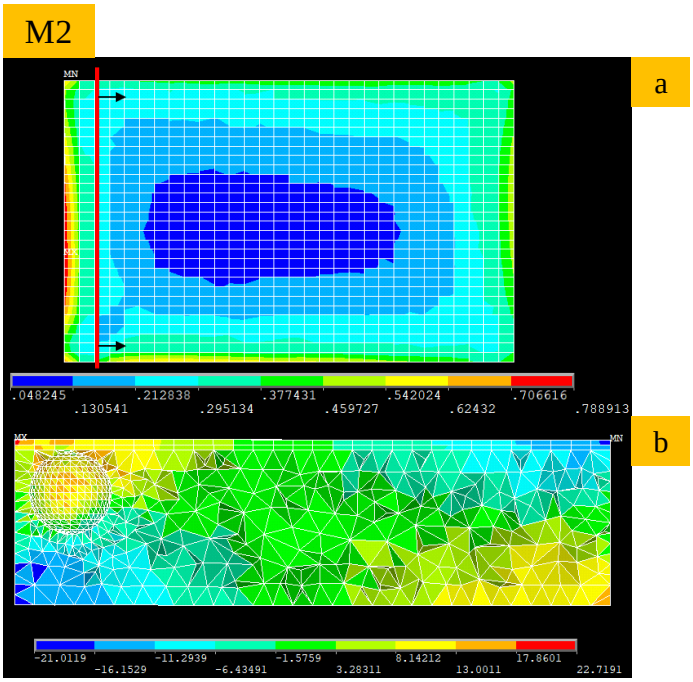

Figure 128: (a) Non-Linear Plastic Work Per Volume (b) YZ Shear Stress

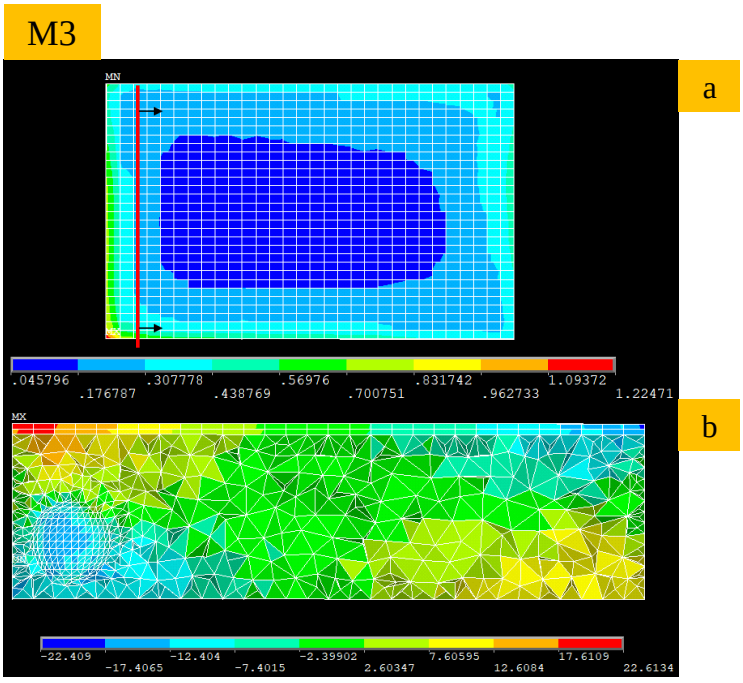

Figure 129: (a) Non-Linear Plastic Work Per Volume (b) YZ Shear Stress

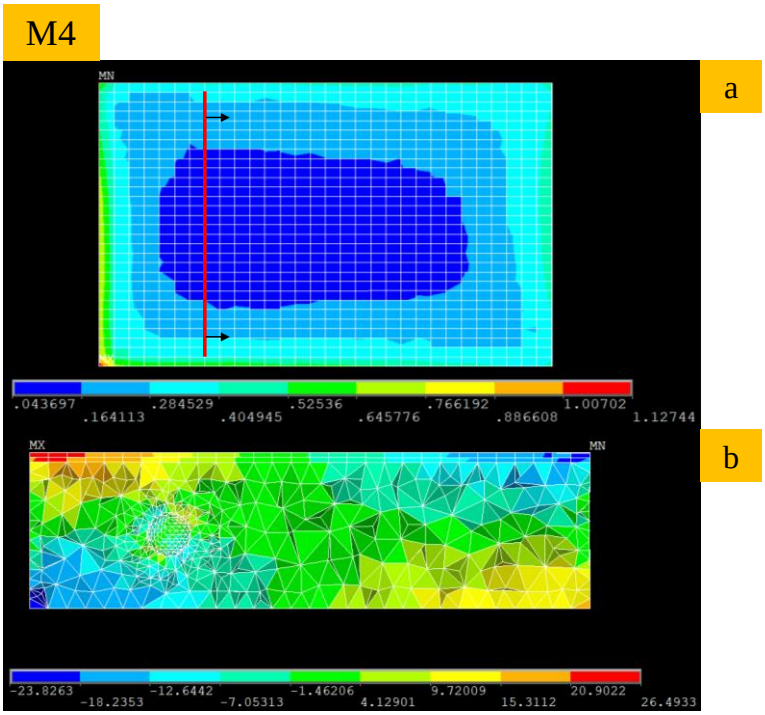

Figure 130: (a) Non-Linear Plastic Work Per Volume (b) YZ Shear Stress

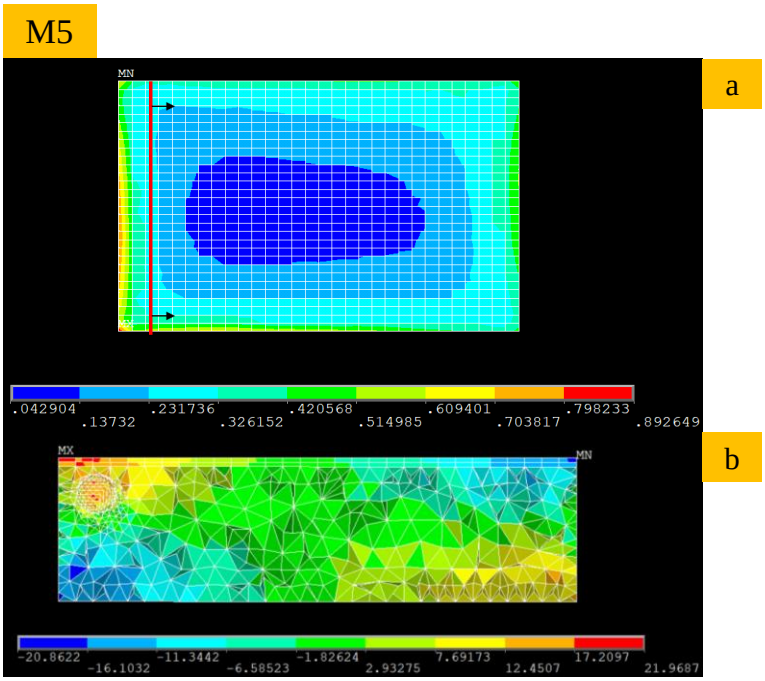

Figure 131: (a) Non-Linear Plastic Work Per Volume (b) YZ Shear Stress

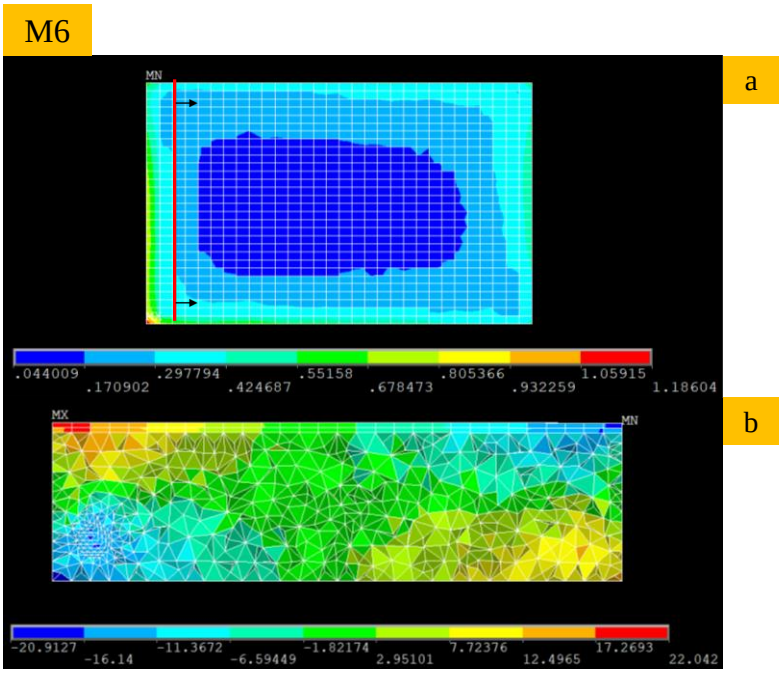

Figure 132: (a) Non-Linear Plastic Work Per Volume (b) YZ Shear Stress

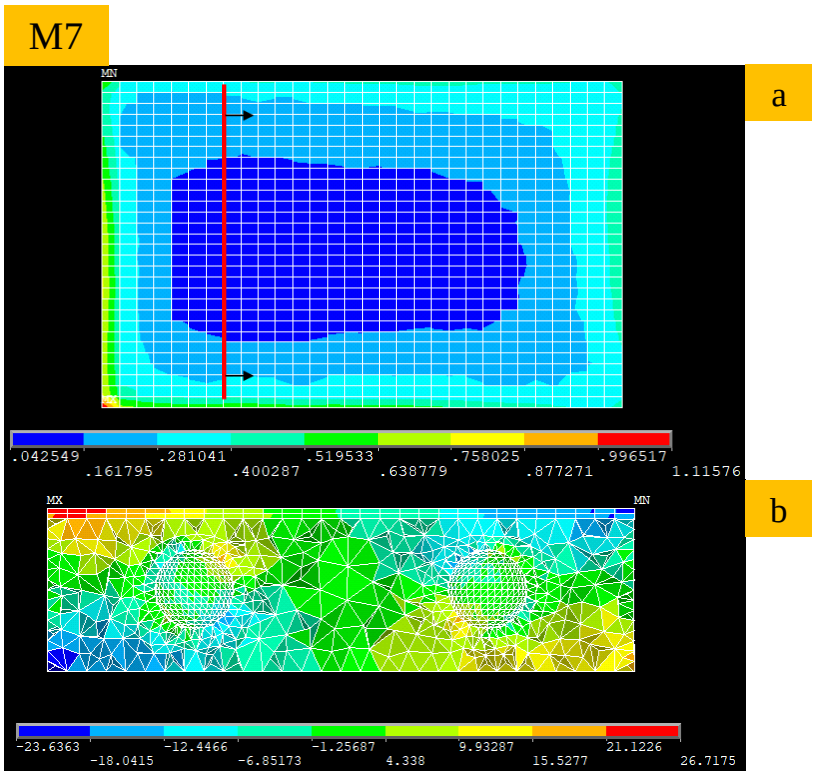

Figure 133: (a) Non-Linear Plastic Work Per Volume (b) YZ Shear Stress

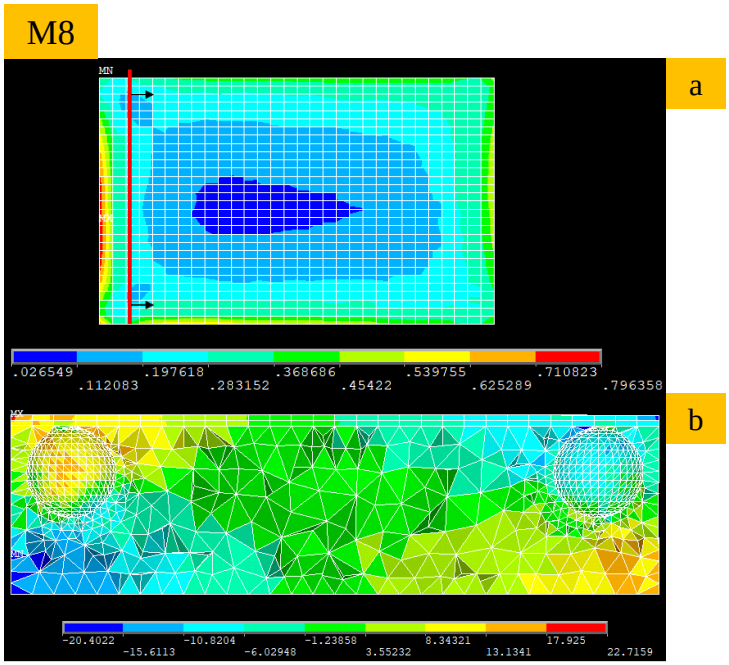

Figure 134: (a) Non-Linear Plastic Work Per Volume (b) YZ Shear Stress

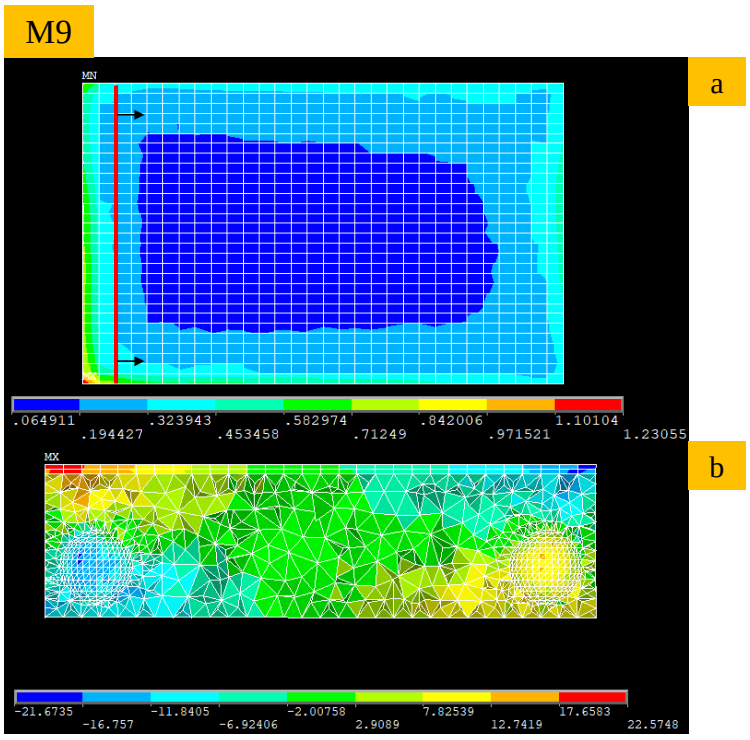

Figure 135: (a) Non-Linear Plastic Work Per Volume (b) YZ Shear Stress

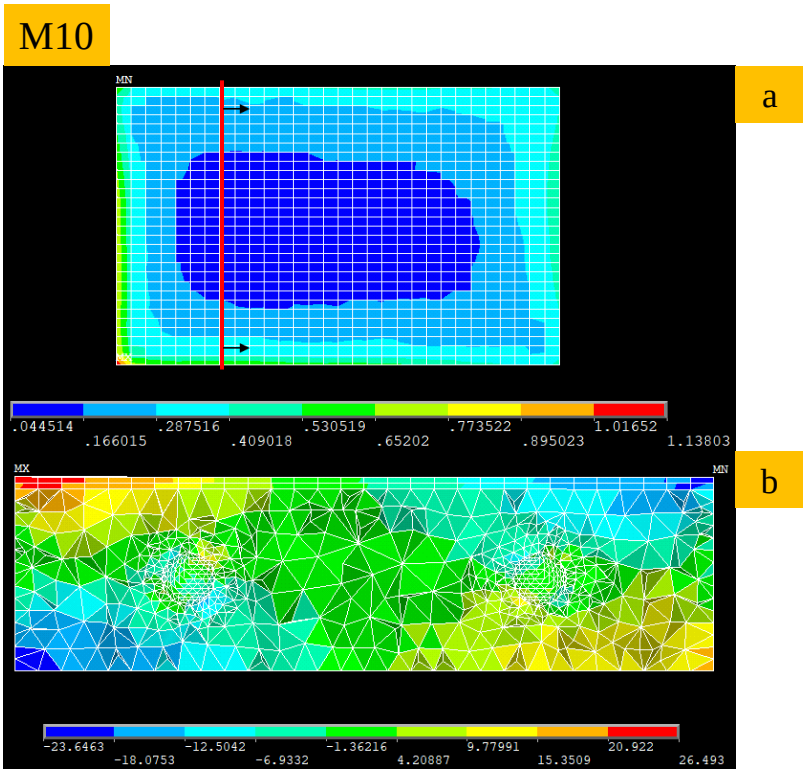

Figure 136: (a) Non-Linear Plastic Work Per Volume (b) YZ Shear Stress

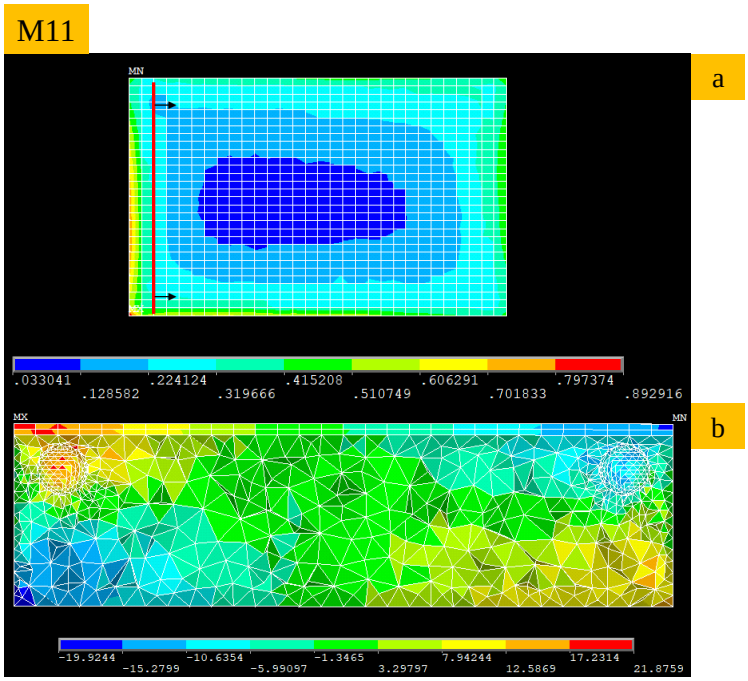

Figure 137: (a) Non-Linear Plastic Work Per Volume (b) YZ Shear Stress

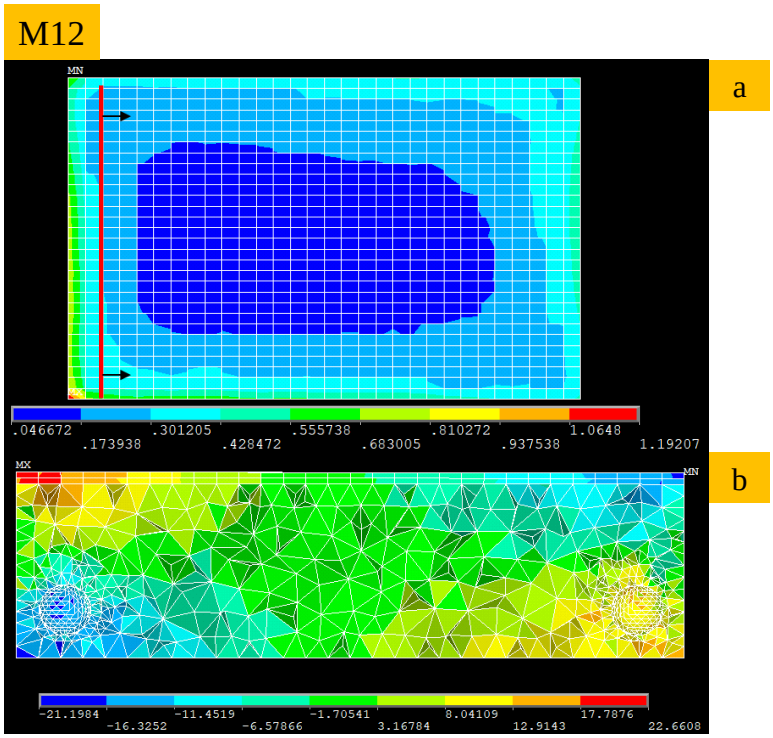

Figure 138: (a) Non-Linear Plastic Work Per Volume (b) YZ Shear Stress

Figure 139 shows a comparison of Maximum non-linear plastic work after two thermal cycles. From the bar graph it was seen that the magnitude of the non-linear plastic work for no voids and that for solder joints with voids along the center axis was found to be very similar. This meant that solder joints without void do not necessarily perform better the solder joint with void. Also void found along the center line may not have much effect of the solder joint thermos-mechanical reliability. Also, the non -linear plastic work per volume was nearly the same irrespective of the void size for solder joints with voids along the center line.

It was further observed that for the solder joints with voids above and below the neutral axis, the build-up for non-linear plastic work was higher for smaller voids than the larger voids. Upon comparing the values for models M2 and M5, M3 and M6, M8 and M11 and

M9 and M12 that because of the closer proximity of the larger void to the critical corner in comparison to the small void, the non-linear plastic work was higher for solder joints with small void, indicating that with increase in the distance from the corner for the same respective position the thermo-mechanical fatigue life may deteriorate. For this trend, it was also observed that the amount of increase in non-linear plastic work was higher for voids below the neutral axis of the solder joint than for the models with voids above the neutral axis.

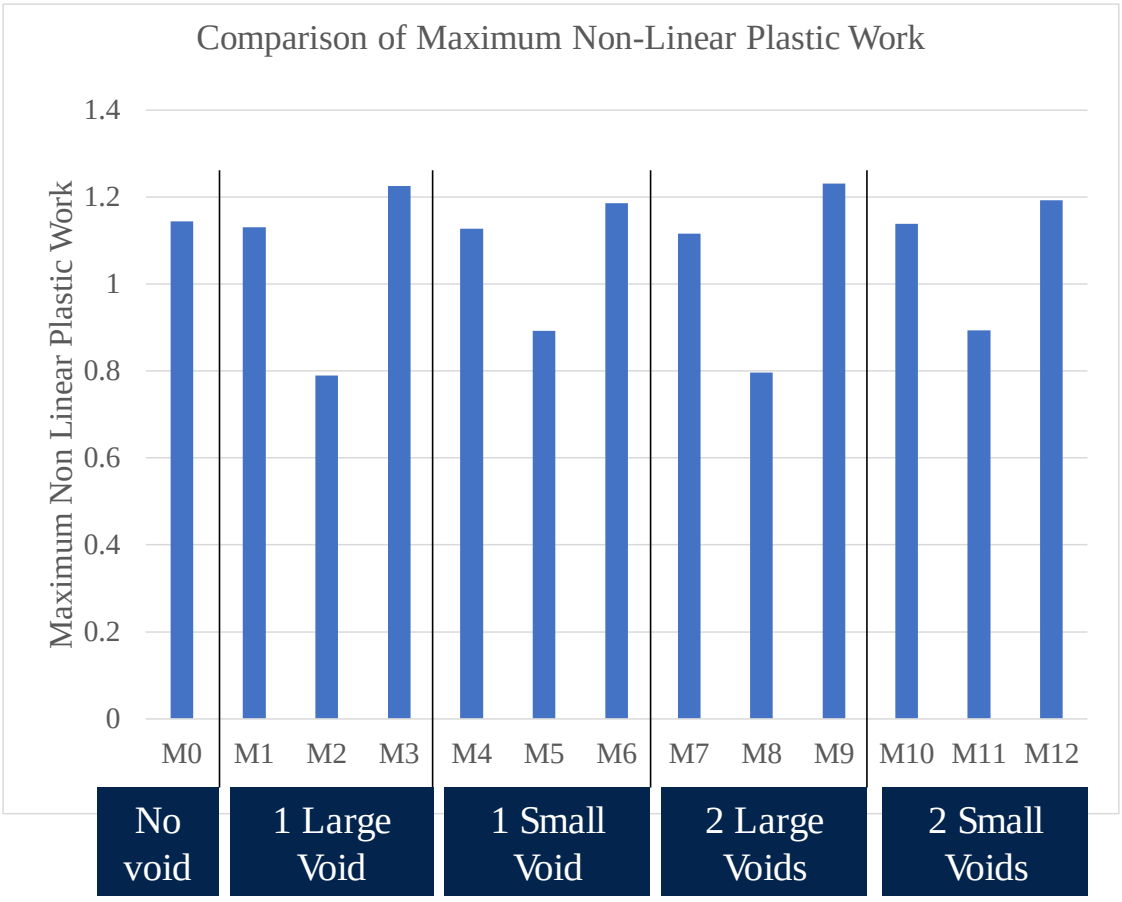

Figure 139: Comparison of Maximum Non-Linear Plastic Work per Volume after 2 cycles

Figure 140 shows a comparison of the hysteresis loops for models. The data for this was extracted from the most critical node on the absolute corner from the most critical region of the solder joint. It was seen that the model M3 had its hysteresis loop extending out the most because of the higher non-linear plastic work as seen from the Figure 139. Model M8 and M2 had their hysteresis loops nearly coincide reiterating the conclusion that irrespective of one void or two voids, it is the location of the voids that caused a significant change in the non-linear plastic work build-up. The same trend could be seen for solder with no void and solder with void along the neutral axis.

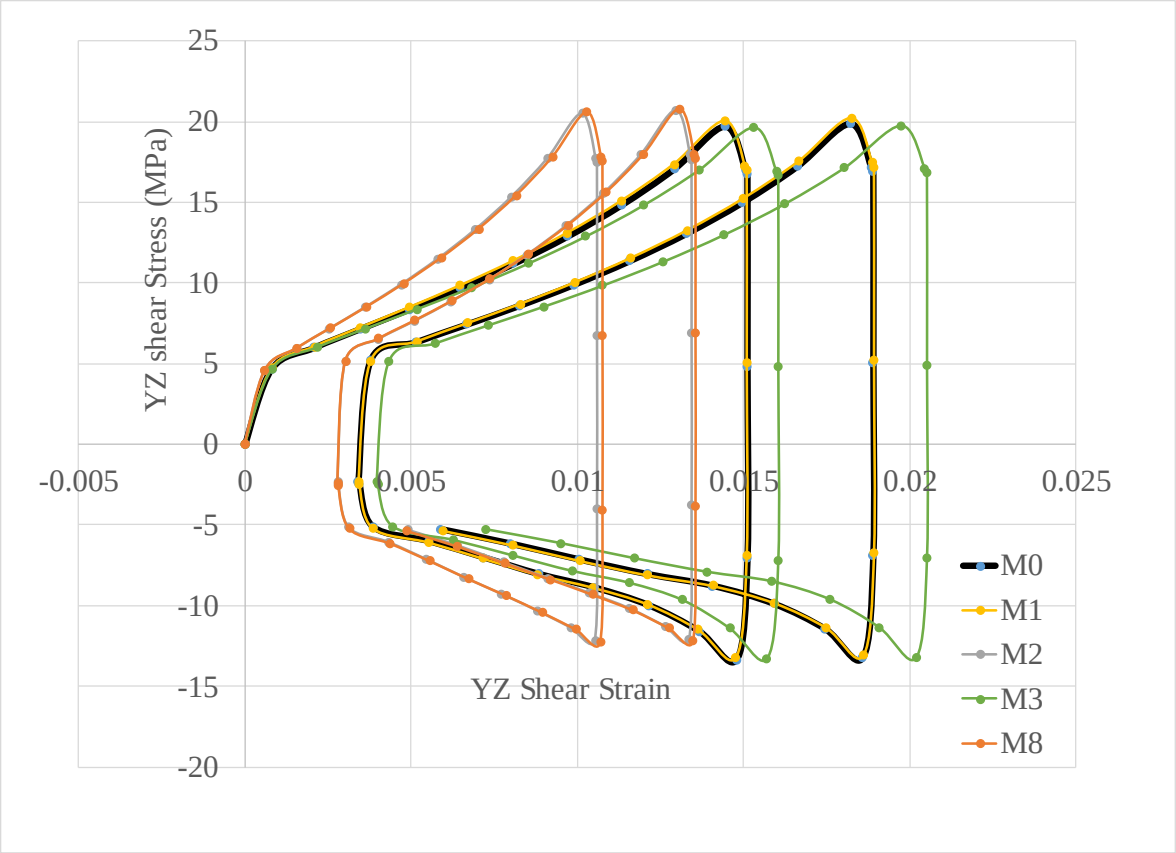

Figure 140: Comparison of solder joint softening response over two thermal cycles via hysteresis loop

In order to further investigate the effect of size, location and number of voids on the thermo-mechanical solder joint fatigue life, the entire test matrix mentioned earlier was repeated for voids located on the cross-section midway through the length of the solder joint as shown in the Figure 141.

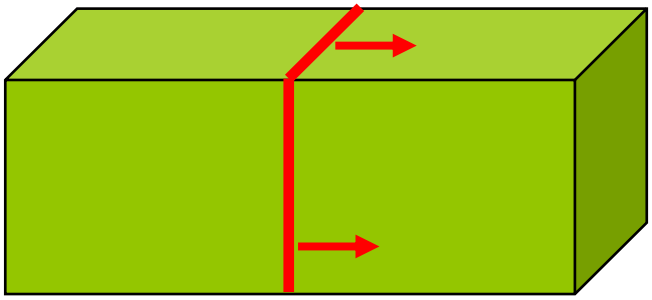

Figure 141: Location of voids along the length of the solder joint

Non-linear plastic work was tracked for all the models and plotted as shown in Figure 142. It can be seen that when the voids centrally located in the solder joint, irrespective of the size, location and number of voids, the non-linear plastic work build up was nearly constant. This could be attributed to the distance between the left top package side corner of the solder joint and the surface of the void was nearly the same.

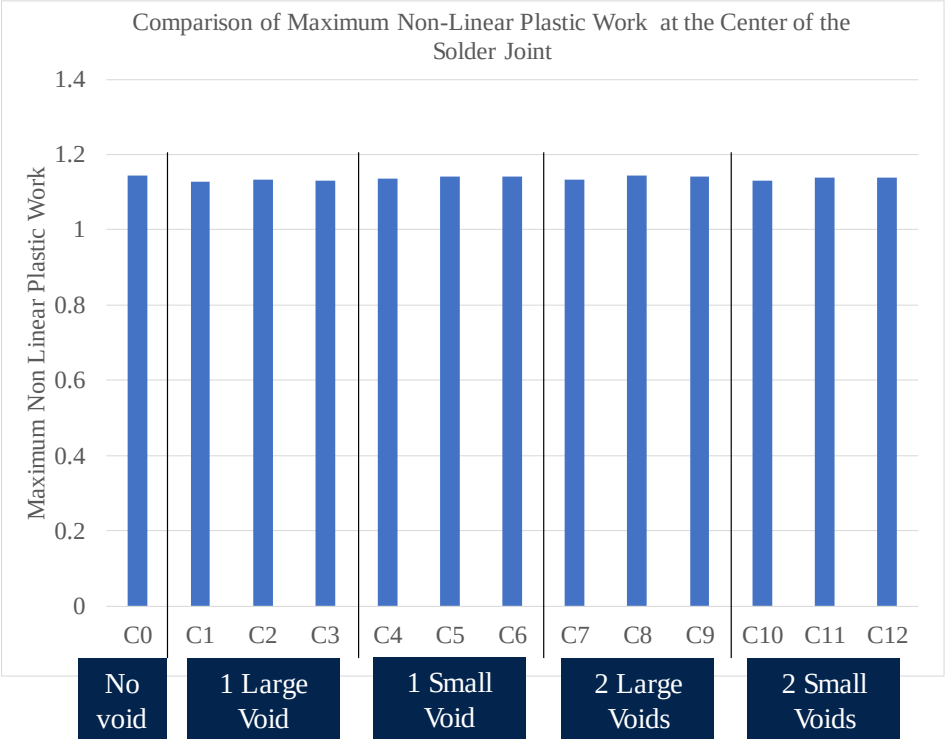

Figure 142: Comparison of Maximum Non-Linear Plastic Work per Volume after 2 cycles for Voids at the Solder Center

From this it could be concluded that voids located around the center vicinity of the solder joint tend to have negligible effect in comparison to voids located closer to the critical corner.

5.2.4 Summary and Conclusion

In summary, this study, investigates the effect of location, size and number of voids on a QFN solder joint. A full factorial design test matrix varying the three factors was executed using finite element analysis. The models were executed in Hypermesh and Ansys. A thermal cyclic load as per AECQ100, standard from 125^0 C to -40^0 C was used. Non-linear plastic work was tracked for different models.

The results showed that presence of voids not always affect the thermo-mechanical reliability of the solder joint. The results showed the voids above the neutral axis closer to the top package corner tend to arrest the non-linear plastic work build-up. Results also showed that as the distance of the void increased from the inner top corner, irrespective of the void size or number, the non-linear plastic work build up was the same as it would be if there was no void. The results also showed that that the number of voids between 1 and 2 had the same effect on the thermo-mechanical reliability of the solder joint.

Chapter 6: Conclusions

In this study, the author has developed a novel technique that is aimed at performing finite element analysis that considers the real geometry of the part in question. This has been showcased by using micro-computed tomography data. The motivation of this work was shown to come from the need to quantify and assess the health of long life, mission critical missile electronics during its field life.

The micro-CT data was acquired for such electronics (fuze) in a non-destructive way and manipulated into a finite element mesh successfully. The mesh was found to have good accuracy with the real measured dimensions. The test cases done were able to showcase good control over the element size and shape, thus capable of running in implicit or explicit finite element solvers as needed.

The developed technique did bypass the cumbersome CAD modeling procedure required in conventional finite element modeling procedure. The technique developed was also tested on multiple other types of system level and component level electronic packages, thus proving the technique being generic and applicable to a wide variety of geometries.

The author showcased use of Digital Volume Correlation to track damage experimentally in electronics and compare it with the results found using micro-CT

data based Finite element modeling. It was shown that DVC used in tandem with Iterative Close Points algorithm allowed for recording damage progression in electronics over its entire 3D domain as a function of time. This helped monitor the physical integrity of the electronics at any instance during its service life. The results of the finite element model were found to be in agreement with the DVC results for the nature of deformation upon application of load.

In order to test the utility of the technique in real engineering problems found in the electronics packaging area, the technique developed was applied to study voids in solder joints of QFN packages. It was found that voids, depending on their location near the corner solder joint could affect the location of failure. This result was further investigated by a detailed full factorial design study to investigate the effect of voids on QFN solder joints depending on size, location and number. This study showed that location of the void was the most crucial factor affecting the thermos-mechanical fatigue life of solder joints amongst size, location and number.

The results from this entire study, point towards utility of the micro-CT data based finite element technique being useful for investigating effects of manufacturing defect and physical damage sustained during field life for electronics. The technique developed finds application in the existing DFR protocols for mission critical analysis of physical integrity of the electronics.

The technique is limited by the resolution of the CT scanner used and the subject matter expertise of the user. The techniques do require prior knowledge of the component being studied and the nature of loads applied to effectively gain valuable insights from the simulation results.

Chapter 7: Discussion

7.1 Discussion on Dimensional Accuracy of Micro-CT to FE Mesh Data

A study on dimensional accuracy of the fuze electronics components was enlisted in Chapter 3 Section 3.3.7. Dimensional accuracy of the components made by the technique is of prime importance and further discussed in this section. It was shown in Chapter 3 that the error % of the components ranged from 0.4% to 2.5%. In this section an additional test case is discussed. A micro-CT scan of an aluminum sheet metal piece of known dimension was acquired and converted into a Finite Element mesh using the technique developed. The dimensions measured from the FE model were compared against the dimensions measured using a digital caliper. Figure 144 shows the aluminum cube and its render after the conversion process. Figure 143 shows the dimensions of the cube measured using caliper.

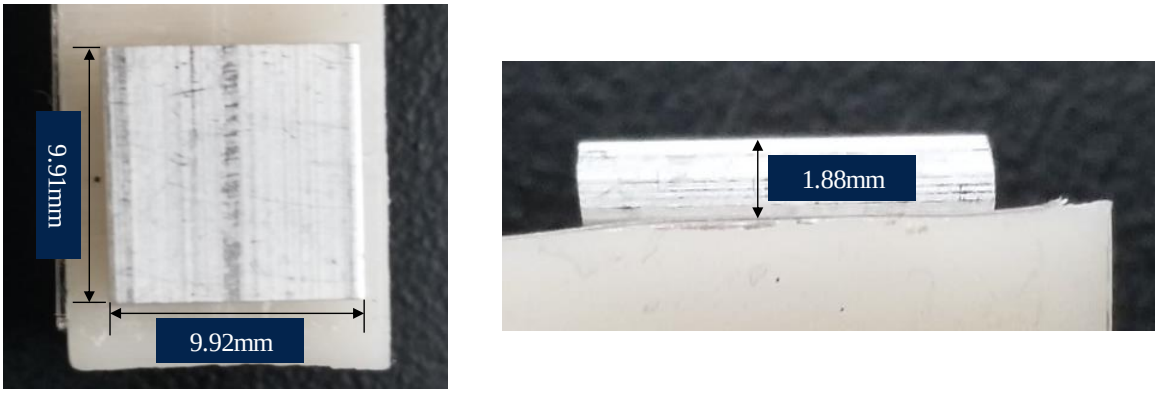

Figure 143: Dimensions of the Al cube measured by Vernier Caliper

Figure 145 shows the dimensions of the Al cube after the CT to mesh conversion process. Table 14 shows the table of comparison of the dimensions measured by the digital caliper and the dimensions measured from the FE mesh.

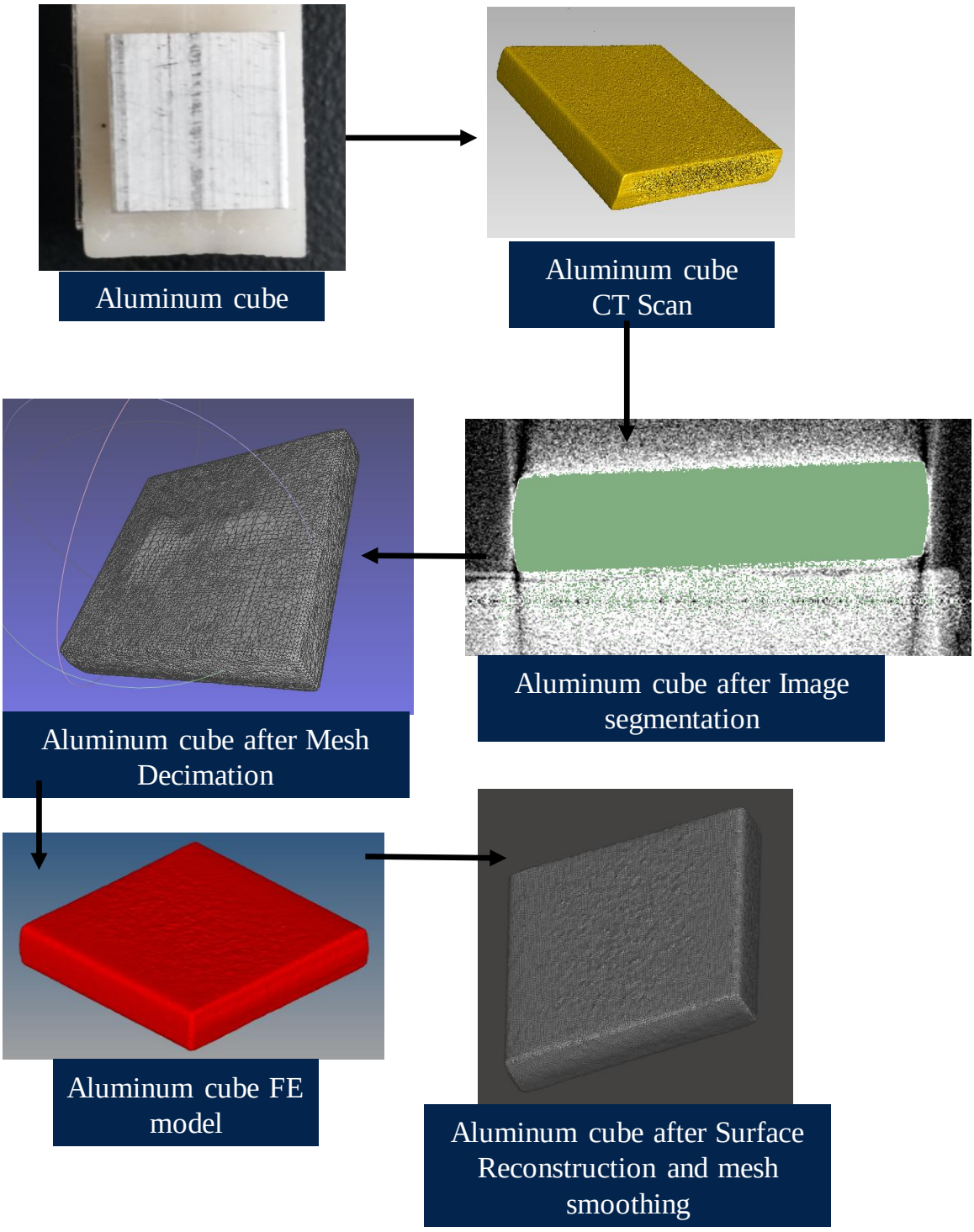

Figure 144: Conversion of the Al cube CT scan to FE mesh

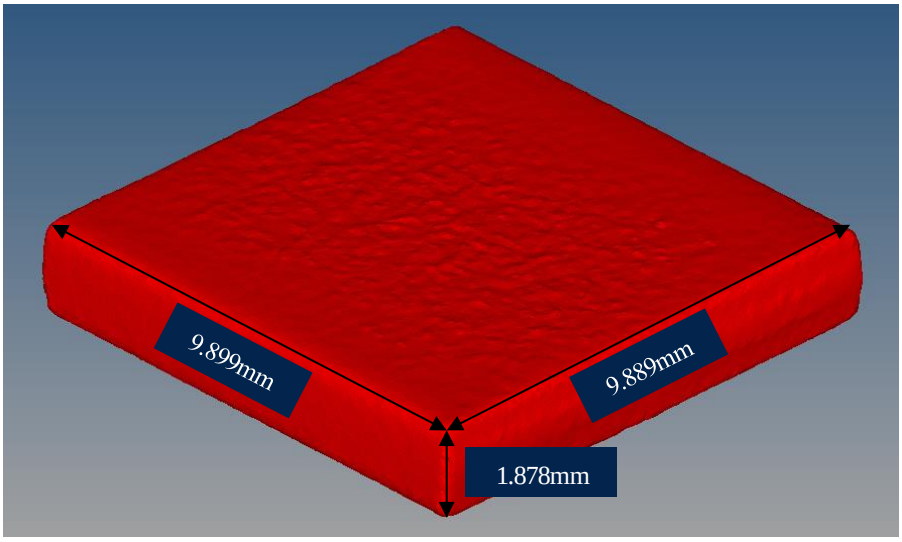

Figure 145: Dimensions of the Al cube measured from the FE mesh

Table 14: Comparison of dimensions of the Al cube

	Dimensions by Digital Caliper	Dimensions from the FE mesh	% Error relative to dimensions from caliper
Length	9.992mm	9.889	1.03%
Breadth	9.991mm	9.899mm	0.92%
Height	1.880 mm	1.878mm	0.106%

A percentage error ranging from 0.1 to 1.03 was found for the test case. The error in dimensions in the CT to mesh conversion process come from various steps. The first source of error comes from the Image segmentation algorithm. This algorithm makes a binary image of the 2D x- ray image on bases of the pixel intensity value. The square shape of

pixel results in the 2D image having ‘blocky’ edges. This data is then converted in to 3D data using Marching cubes algorithm which again relies on a look-up table to create one continues 3D surface. The error in selection of the intensity threshold for image segmentation is another source of error. Accuracy of Otsu segmentation used for selection of the threshold intensity value can be further improved by improving the contrast of the x-ray image. The contrast is further dependent on the number of parts and the material radio density of the parts being CT scanned. Mesh decimation algorithm and the mesh smoothing algorithm result in contraction of the mesh surface. This is another source of error, resulting in the meshed part dimension being smaller than the real part dimension. Poisson surface reconstruction involves fitting a new surface through a vector field of sampled points. The samples created on the surface of the existing surface are using a quad-tree approach which inherently has its own error in locating a sample depending on the level of quadtree /octree selected. The new Poisson surface created from the sampled points, is one closed 3D surface and thus does not precisely bend over sharp edges, if present in the real part. This is the final source of error in the CT to mesh conversion process. The % error seen in Table 14 is inclusive of all the source of error hence discussed.

7.2 Discussion on effect of voids on QFN solder joints

The study undertaken in Chapter 5 addresses the effect of size, location and number of solder joints on QFN solder joints. It has been widely reported that voids do have a significant impact of the solder joint fatigue strength. It is also widely reported that voids are more easily formed in Pb-free solder alloys with respect to Sn-Pb solder alloys. In order to address these findings and IPC Standards (Institute of Printed Circuits) IPC-A-610 and J-STD-001 state the guide lines for maintaining the solder joint integrity for BGA and CSP

solder interconnects. They state that greater than 25% of voiding in any ball in the x-ray image is classified as a defect [IPC-A-610]. The maximum void size considered in the study is 35microns radius. The resultant percentage voiding for area of void to area of solder joint is 3.84% for 1 void and 7.68%. Thus passing the 25% void criteria, though the current standards do not take into consideration the effect of location of the void in the solder joint, which is found to have the most significant impact of the solder joint thermal cycling fatigue life.

Experimental studies to study the effect of voids on solder joints has been scarce and not precise enough as the generation of void is an uncontrollable random process. As discussed earlier, voids are formed in the solder joints during the solder reflow process. The flux and other chemicals outgas into the solder joint forming void during the reflow process. Quality of paste, flux type, solder particle size, ramp temperature and time of each solder reflow phase are control parameters that determine the presence absence and size of void and number of voids.

The conclusions of this study in Chapter 5 show that the location of void is more crucial to the solder joint thermal fatigue life than the size and number of voids. The present Standards do not take this factor into account. The existing standards view the Voiding Criteria currently in place as a check to verify solder joint integrity. It is the intent of the study in Chapter 5 to develop a better understanding of the presence of void in the QFN solder joint, which would be crucial to ensure better survivability of the QFN packages in mission critical applications. It is the intent of the study to add to the existing body of

literature on importance of location, size and number of voids for QFN solder joints, so that the standards may be amended to include a more specific voiding criteria. These findings intend to promote development of better solder paste materials, better reflow processes and manufacturing practices.

7.3 Discussion on computation of Non-Linear Plastic Work per Volume and error in life prediction modeling

Non-linear plastic work per volume is a parameter tracked in Chapter 5 to compute predicted life using finite element modeling. This parameter is based on a Failure theory that states that the failure in material occurs when the strain energy per unit volume exceeds the strain energy per unit volume for the material under a tensile test at the yield point [Li 2001].

Non-linear plastic work per volume is defined as the strain energy found as the area under the curve in the Stress Vs Strain graph per unit volume. This quantity is tracked from the Finite element package as an indicator of damage built into the viscoplastic solder joint. It is widely reported that solder joint is prone to crack initiation and propagation either at component side or PCB side due to higher stress concentration. This stress concentration is caused due to sudden change in cross section area, presence of sharp edges of solder mask on the substrate side in case of Solder Mask Defined configuration and less area offered for ball attachment with Cu pad. The stress concentration could further increase if there is presence of Kirkendall voids at the solder and copper pad interface. Darveaux reported that the strain energy density further increased with decrease in element size

[Darveaux 2000]. In order to reduce this mesh related sensitivity a volume averaging technique is used. The strain energy value of each element is normalized by the volume of each element selected for computation. This is given in equation (1).

$$\Delta W_{ave} = \frac{\sum \Delta W . V}{\sum V} \tag{56}$$

Volume average technique is used to calculate plastic work density. Where ΔW_{ave} is average viscoplastic strain energy density per cycle (Joule/mm3), ΔW is viscoplastic strain energy density per cycle for each element, and V volume of each element (mm^3).

The ΔW_{ave} is computed in Chapter 5.1 by extracting non-linear plastic work of two thermal cycles in the elements in the periphery in the top solder interface for two elements present in top 2 layers. A difference is taken of the non-linear plastic work build up in cycle 1 from cycle 2 and this value is volume averaged as per equation (1). In Chapter 5.2, instead of ΔW_{ave} the author has reported maximum non-linear plastic work found in the most critical element.

The error found in the characteristic life predicted by the finite element model was 37%. There are multiple sources of errors that is discussed hereon. Volume averaging approach stated earlier is introduced to remove the mesh dependency of the strain energy density computation is a source of error as the error involved here is not reflective of the physics of the failure mode whatsoever. Another source of error is use of Anand Viscoplasty material model. The material model used for the Pb-free solder alloy is widely accepted by researchers but introduces the error of how closely it resembles the viscoplastic softening of solder alloy. The K_1 through K_4 constants computed for implementing Darveaux's life

prediction model involves testing of multiple parts with same solder alloy and computing crack initiation time and crack growth rate experimentally.

7.4 Discussion on utility of research findings

The technique developed to convert the CT scanned data to a finite element mesh is directly beneficial to Department of Defense to re-evaluate shelf life of missile electronics.

1. The technique allows for investigating the physical real as-is geometry post manufacturing. Thus allowing the manufacturer to non-destructively investigate the manufacturing defects and there effect on reliability.
2. Life of missile electronics range from 30 to 50 years. The technique developed allows for tracking the physical changes the parts may see during their service life.
3. When coupled with ability to do finite element simulations , the ability to run simulations to study reliability starting from the real as-is geometry is of prime importance to re-evaluate shelf life based on the present condition of the parts.
4. Finite element simulations of Fuze like electronics with many parts is deemed prohibitively time consuming and thus the technique developed effectively bypasses the conventional CAD modeling and meshing step, allowing for a relatively much faster modeling time without loss of considerable accuracy.
5. The ability of the technique to track deformation histories as a function of time or over the life span of the electronics alloys for effective decision making for an engineer to replace parts that may show signs of impending failure as found from the deformation history at critical locations. This is of prime importance in mission critical electronics.

References

1. AMRDEC Public Affairs,2005," Army researchers extend missile system shelf life", https://www.army.mil/article/156942/Army_researchers_extend_missile_system_shelf_life
2. Howard, Truman W. ; Davis, Gary D.,1997," Challenges in Missile Life Cycle System Engineering", Accession Number : ADA329324, ARMY MISSILE COMMAND REDSTONE ARSENAL AL,
3. Department of Archives and Special Collection, "This is Redstone", p.||-0, http://heroicrelics.org/info/redstone/redstone-overview.html
4. Weapons and Systems Engineering Department United States Naval Academy "Fundamentals of Naval Weapons Systems", Chapter 14
5. Alessandro Vallebona, V. Maragliano, E. T. Leddy,Radiology; 1931, "Radiography with Great Enlargement (Microradiography) and a Technical Method for the Radiographic Dissociation of the Shadow", 17:2, 340-341
6. http://www.impactscan.org/background.htm
7. S. Izumi, S. Kamata, K. Satoh and H. Miyai, April 1993, "High energy X-ray computed tomography for industrial applications," in IEEE Transactions on Nuclear Science, vol. 40, no. 2, pp. 158-161
8. F. Maur,2003, "X-ray inspection for electronic packaging latest developments," Fifth International Conference onElectronic Packaging Technology Proceedings, ICEPT2003., pp. 235-239.,Shanghai, China

9. R. Kovacs, 2005, "X-ray inspection of microwire bonds," 28th International Spring Seminar on Electronics Technology: Meeting the Challenges of Electronics Technology Progress, 2005., Wiener Neustadt, pp. 6-9.
10. A. Teramoto, T. Murakoshi, M. Tsuzaka and H. Fujita, 2007, “Automated Solder Inspection Method by Means of X-ray Oblique Computed Tomography," 2007 IEEE International Conference on Image Processing, San Antonio, TX, 2007, pp. V - 433-V - 436.
11. M. Oppermann, T. Zerna and K. Wolter, 2009, "X-ray computed tomography on miniaturized solder joints for nano packaging," *2009 11th Electronics Packaging Technology Conference*, Singapore, pp. 70-75.
12. Tsuritani, H., Sayama, T., Okamoto, Y., Takayanagi, T., Uesugi, K., and Mori, T., June 23, 2011, "Application of Synchrotron Radiation X-Ray Microtomography to Nondestructive Evaluation of Thermal Fatigue Process in Flip Chip Interconnects." ASME. J. Electron. Packag.; 133(2): 021007.
13. Tsuritani, H., Sayama, T., Uesugi, K., Takayanagi, T., and Mori, T. ,May 2, 2007, "Nondestructive Evaluation of Thermal Phase Growth in Solder Ball Microjoints by Synchrotron Radiation X-Ray Microtomography." ASME. *J. Electron. Packag*. December 2007; 129(4): 434–439.
14. Taddei, F.; Martelli, S.; Reggiani, B.; Cristofolini, L.; Viceconti, M., Nov. 2006, "Finite-Element Modeling of Bones From CT Data: Sensitivity to Geometry and Material Uncertainties," Biomedical Engineering, IEEE Transactions on , vol.53, no.11, pp.2194,2200,

15. Wei Yi; Zhensheng Lei; Xiaohu Liu, Oct. 2014, "A domain separate method of developing orthogonal hexahedron finite element mesh model from CT/μCT slice image files," in Image and Signal Processing (CISP), 2014 7th International Congress on , vol., no., pp.645-649, 14-16

16. Rahman, A.; Selmi, S.; Papadopoulos, C.; Papaioannou, G., Nov. 2009, "CT-scan based FEA for the assessment of the effect of bone density on femur's fracture," in Information Technology and Applications in Biomedicine, 2009. ITAB 2009. 9th International Conference on, vol., no., pp.1-2, 4-7

17. Diemente, S.; Lewis, C.G.; Nowak, M.D.; Leone, D.J., Apr 1991, "Finite element modeling from CT scan data," Bioengineering Conference, 1991., Proceedings of the 1991 IEEE Seventeenth Annual Northeast, vol., no., pp.227,228, 4-5

18. Tao Li; Jin Yao; Dake Wu; Jiawei Yang, July 2007, "Data Management and Modeling for Reconstructing 3D Finite Elements of Lungs," Pervasive Computing and Applications, 2007. ICPCA 2007. 2nd International Conference on, vol., no., pp.323,327, 26-27

19. Wei-Chun Chang; Linden, M.J.; Robbins, S.; Mayott, C.; Engler, P., 1993, "Computer aided stress analysis of the femur with prosthetic hip stem utilizing computed tomography," Bioengineering Conference, Proceedings of the 1993 IEEE Nineteenth Annual Northeast , vol., no., pp.60,61, 18-19

20. Battula, S.; Njus, G.O., 17-18 April 2004 ,"A new method to develop the finite element model of the bones in the hand from CT scans," in Bioengineering Conference, 2004. Proceedings of the IEEE 30th Annual Northeast, vol., no., pp.170-171, doi: 10.1109/NEBC.2004.1300049

21. YeeWa Choy; YingPio Lim; Xin Wang; KuanPhang Chan, 6-9 Oct. 2012,"Development CT-based three-dimensional complex skull model for Finite element analysis," in Sustainable Utilization and Development in Engineering and Technology (STUDENT), 2012 IEEE Conference on, vol., no., pp.135-139,

22. Lall, P.; Deshpande, S.; Junchao Wei; Suhling, J., May 2014, "Non-destructive crack and defect detection in SAC solder interconnects using cross-sectioning and X-ray micro-CT," in Electronic Components and Technology Conference (ECTC), 2014 IEEE 64th , vol., no., pp.1449-1456, 27-30

23. Ji-Quan Ma, Fan-Hui Kong, Pei-Jun Ma and Xiao-Hong Su, 2005,"Detection of defects at BGA solder joints by using X-ray imaging," 2005 International Conference on Machine Learning and Cybernetics, pp. 5139-5143 Vol. 8., Guangzhou, China

24. K. Sakai, O. Kikuchi, K. Kitami, M. Umeda and S. Ohno, 2016,"Defect detection method using statistical image processing of scanning acoustic tomography," 2016 IEEE 23rd International Symposium on the Physical and Failure Analysis of Integrated Circuits (IPFA), pp. 293-296, Singapore

25. Lall, P.; Junchao Wei, 26-29 May 2015, "X-ray micro-CT and digital-volume correlation based three-dimensional measurements of deformation and strain in operational electronics," in Electronic Components and Technology Conference (ECTC), 2015 IEEE 65th , vol., no., pp.406-416,

26. Lall and J. Wei, 2016, "Remaining Useful Life Assessment of Field Deployed Electronics Using X-Ray Micro-CT Based Digital Volume Correlation and Finite-Element Analysis," 2016 IEEE 66th Electronic Components and Technology Conference (ECTC), , pp. 1583-1592 ,Las Vegas, NV, USA

27. Gianluca Tozzi, Enrico Dall'Ara, Marco Palanca, Marco Curto, Federica Innocente, Luca Cristofolini, March 2016, "Strain uncertainties from two digital volume correlation approaches in prophylactically augmented vertebrae: Local analysis on bone and cement-bone microstructures", Journal of the Mechanical Behavior of Biomedical Materials, Volume 67, Pages 117-126, ISSN 1751-6161

28. Marco Palanca, Luca Cristofolini, Enrico Dall'Ara, Marco Curto, Federica Innocente, Valentina Danesi, Gianluca Tozzi, 8 December 2016,"Digital volume correlation can be used to estimate local strains in natural and augmented vertebrae: An organ-level study", Journal of Biomechanics, Volume 49, Issue 16, , Pages 3882-3890, ISSN 0021-9290

29. F. Gillard, R. Boardman, M. Mavrogordato, D. Hollis, I. Sinclair, F. Pierron, M. Browne, January 2014, "The application of digital volume correlation (DVC) to study the microstructural behaviour of trabecular bone during compression, Journal of the Mechanical Behavior of Biomedical Materials", Volume 29

30. A. F. M. Yamin, N. M. Shaffiar, W. K. Loh and M. N. Tamin, 2011, "Damage progression in BGA solder joints during board-level drop test," 2011 IEEE 13th Electronics Packaging Technology Conference, pp. 681-685. , Singapore

31. L. J. Ladani, 2010, "Damage initiation and propagation modeling using Energy Partitioning Damage Evolution model for Pb-free solder materials," 2010 12th IEEE Intersociety Conference on Thermal and Thermomechanical Phenomena in Electronic Systems, pp. 1-5., Las Vegas, NV

32. Luhua Xu, J. H. L. Pang and Faxing Che, 2005 "Failure study of Sn-Ag-Cu lead-free solder joint by digital image speckle analysis (DISA)," 2005 7th Electronic Packaging Technology Conference, pp. 4 pp.-. , Singapore

33. Cantatore, A., & Müller, P., 2011," Introduction to computed tomography." ,Kgs.Lyngby: DTU Mechanical Engineering.

34. ASTM E1441 - 00:2005. Standard guide for computed tomography (CT) imaging,Technical report

35. Hayashi, Hiromitsu et al.,2010 "Beam-hardening artifacts on computed tomography images caused by lanthanum carbonate hydrate in a patient on dialysis." Japanese Journal of Radiology 28: 322-324.

36. Brett Muehlhauser,2016, "A New Development for Significantly Reducing Ring Artifacts in CT Scans", North Star Imaging Blog, https://4nsi.com/blog/2016/08/02/a-new-development-for-significantly-reducing-ring-artifact-in-ct-scans/

37. Xiaoxi Guo, Boliang Wang, Shaoyin Duan, Shaohui Huang, Yongjun Chen and Lijun Chen, 2011"The influence of partial volume effect on the finite element modeling of bone," 2011 IEEE International Symposium on IT in Medicine and Education, pp. 477-480. Cuangzhou

38. C. Bao and Q. Meng,2010 "Three-Dimensional Finite Element Analysis of the Tibia Stresses during Jumping Momnet," 2010 International Conference on Computational and Information Sciences, pp. 756-759. Chengdu , China

39. P. Shweta and M. Anburajan, 2011"Finite element analysis of the skull implant using ansys software," 2011 3rd International Conference on Electronics Computer Technology, pp. 420-425. Kanyakumari, India

40. C. Wong, P. M. Gehrchen, T. Darvann and T. Kiaer,June 2003 "Nonlinear finite-element analysis and biomechanical evaluation of the lumbar spine," in IEEE Transactions on Medical Imaging, vol. 22, no. 6, pp. 742-746
41. Nobuyuki Otsu ,1979, "A threshold selection method from gray-level histograms". IEEE Trans. Sys. Man. Cyber. 9 (1): 62–66. doi:10.1109/TSMC.1979.4310076.
42. Lorensen, William E.; Cline, Harvey E. ,1 August 1987, "Marching cubes: A high resolution 3D surface construction algorithm", ACM SIGGRAPH Computer Graphics. 21 (4): 163–1
43. Lorensen, W. E., 1994., "Marching Through the Visible Man," IEEE Visualization, Proceedings of the 6th conference on Visualization '95, pp. 368-373.
44. Lorensen, W. E., Schroeder, W. J. and Zarge, Jonathan A., 1992.,"Decimation of Triangle Meshes," Internationa Conference on Computer Graphics and Interactive Techniques, Proceedings of the 19th annual conference on Computer Graphics and Interactive Techniques, pp. 65-70.
45. Cirne, Marcos & Pedrini, Helio. ,2013," Marching cubes technique for volumetric visualization accelerated with graphics processing units" Journal of the Brazilian Computer Society. 19. 10.1007/s13173-012-0097-z.
46. Michael Hoffmann, Yoshio Okamoto,2005,"The minimum weight triangulation problem with few inner points",Computational Geometry,Volume 34, Issue 3,2006,Pages 149-158,ISSN 0925-7721
47. P. Liepa, 2003,"Filling Holes in Meshes", Proceedings of the 2003 Eurographics/ACM SIGGRAPH Symposium on Geometry processing, pp. 200-205, 2003.

48. Michael Kazhdan, Bolotho Matthew, Hoppe Hogues,2006, "Poisson Surface Reconstruction", Eurographics Symposium on Geometry Processing, pp. 1-10, 2006.
49. Matthew Berger, Tagliasacchi Andrea, M. Seversky Lee, Aliiez Pieere, A. Levine Joshua, Sharf Andrei, T. Silva Claudio, April 2014,"State of the Art in Surface Reconstruction from Point Clouds" in EUROGRAPHICS star report, Strasbourg, France, pp. 161-185
50. M. Garland,1999," Quadric-based Polygonal Surface Simplification", Thesis,Carnegie Mellon University , Pittsburgh, PA 15213-3891
51. Z. Ji, L. Liu, G. Wang, Dec 7–10, 2005, "A global Laplacian smoothing approach with feature preservation", Computer Aided Design and Computer Graphics 2005. Ninth International Conference on, pp. 1-6,
52. Wei, Junchao, 2017," In-situ Electronics Measurement Using X-ray Micro-Computed Tomography System and Data Driven Prognostic Health Management", PhD Dissertation, Auburn University Mechanical Engineering
53. Tao Li, Jin Yao, Dake Wu, Jiawei Yang, 26–27 July 2007, "Data Management and Modeling for Reconstructing 3D Finite Elements of Lungs", Pervasive Computing and Applications 2007. ICPCA 2007. 2nd International Conference on, pp. 323-327
54. P. Lall, Junchao Wei, , May 26–29, 2015, "X-ray micro-CT and digital-volume correlation based three-dimensional measurements of deformation and strain in operational electronics", Electronic Components and Technology Conference (ECTC), pp. 406-416
55. Marco Palanca, Luca Cristofolini, Enrico Dall'Ara, Marco Curto, Federica Innocente, Valentina Danesi, Gianluca Tozzi, , December 2016,"Digital volume correlation can

be used to estimate local strains in natural and augmented vertebrae: An organ-level study", Journal of Biomechanics, vol. 49, no. 16, pp. 3882-3890, ISSN 0021-9290

56. F. Gillard, R. Boardman, M. Mavrogordato, D. Hollis, I. Sinclair, F. Pierron, M. Browne, January 2014, "The application of digital volume correlation (DVC) to study the microstructural behaviour of trabecular bone during compression", Journal of the Mechanical Behavior of Biomedical Materials, vol. 29,
57. Oliver, W., & Pharr, G. ,1992," An improved technique for determining hardness and elastic modulus using load and displacement sensing indentation experiments" Journal of Materials Research, 7(6), 1564-1583. doi:10.1557/JMR.1992.1564
58. A. Schubert, R. Dudek, E. Auerswald, A. Gollbardt, B. Michel and H. Reichl, 2003, "Fatigue life models for SnAgCu and SnPb solder joints evaluated by experiments and simulation," 53rd Electronic Components and Technology Conference, 2003. Proceedings., , pp. 603-610., New Orleans, Louisiana, USA
59. David Bernard, Bob Willis, 2007,"Common Process Defect Identification of QFN Packages Using Optical and Xray Inspection", Proceedings of the SMTA International Conference, pp. 849-857
60. P. Lall, N. Kothari, S. Deshpande and L. Nguyen, 2019, "Study of the Effect of Solder-Joint Voiding using X-ray MicroCT Data-based FE Models with Experimental Validation," 2019 18th IEEE Intersociety Conference on Thermal and Thermomechanical Phenomena in Electronic Systems (ITherm), , pp. 1160-1167. Las Vegas, NV, USA

61. T. Terasaki and H. Tanie, 2005, "Fatigue crack propagation analysis for microsolder joints with void," 2005 International Symposium on Electronics Materials and Packaging, , , pp. 37-42. Tokyo, Japan
62. R. Schwerz, S. Meyer, M. Roellig, K. Meier and K. Wolter, 2011, "Finite element modeling on thermal fatigue of BGA solder joints with multiple voids," Proceedings of the 2011 34th International Spring Seminar on Electronics Technology (ISSE), pp. 380-385., Tratanska Lomnica
63. G. Yubing, L. QuanYong and Y. Daoguo,2005, "Study on the fatigue life of the FC-BGA solder joints with Damage," Conference on High Density Microsystem Design and Packaging and Component Failure Analysis, pp. 1-5. Shanghai
64. N. Lee, , 2002," Reflow soldering processes and troubleshooting: SMT BGA CSP and flip chip technologies" Boston: Newnes
65. K. C. Otiaba, R. S. Bhatti, N. N. Ekere, S. Mallik, E. H. Amalu, M. Ekpu,2011 "Thermal effects of die-attach voids location and style on performance of chip level package", 3rd IEEE InternationalConference on Adaptive Science and Technology (ICAST 2011)
66. L. Biswal, A. Krishna, D. Sprunger,2005 "Effects of solder voids on thermal performance of a high power electronic module", IEEE 7th Electronics Packaging Technology Conference Proceedings, vol. 2, pp. 526-531
67. Qiang Yu, T. Shibutani, Y. Kobayashi and M. Shiratori, 2006, "The Effect of Voids on Thermal Reliability of BGA Lead Free Solder Joint and Reliability Detecting Standard," Thermal and Thermomechanical Proceedings 10th Intersociety Conference

on Phenomena in Electronics Systems, 2006. ITHERM 2006., , pp. 1024-1030, San Diego, CA

68. Y. Y. G. Hoe, Y. G. Jie, V. S. Rao and M. W. Daniel Rhee,2012, "Modeling and characterization of the thermal performance of advanced packaging materials in the flip-chip BGA and QFN packages," 2012 IEEE 14th Electronics Packaging Technology Conference (EPTC), pp. 525-532. Singapore
69. R. Darveaux and A. Mawer,1998 "Solder joint fatigue life of fleXBGA/sup TM/ assemblies," 1998 Proceedings. 48th Electronic Components and Technology Conference (Cat. No.98CH36206), 1998, pp. 707-712, Seattle, WA, USA,
70. YeeWa Choy, YingPio Lim, X. Wang and KuanPhang Chan,2012 "Development CT-based three-dimensional complex skull model for Finite element analysis," 2012 IEEE Conference on Sustainable Utilization and Development in Engineering and Technology (STUDENT) , pp. 135-139, Kuala Lumpur
71. S. Battula and G. O. Njus,2004 "A new method to develop the finite element model of the bones in the hand from CT scans," IEEE 30th Annual Northeast Bioengineering Conference, 2004. Proceedings of 2004, pp. 170-171.
72. Sandeep Kumar Parashar, Jai Kumar Sharma, 2016“A review on application of finite element modelling in bone biomechanics”, In Perspectives in Science, Volume 8, 2016, Pages 696-698, ISSN 2213-0209
73. P. Lall, N. Kothari, J. Deep, J. Foley and R. Lowe,2017 "Development of FE Models and Measurement of Internal Deformations of Fuze Electronics Using X-Ray MicroCT Data with Digital Volume Correlation," 2017 IEEE 67th Electronic Components and Technology Conference (ECTC), pp. 497-506. Orlando, FL

74. P. Lall and J. Wei,2016 "Remaining Useful Life Assessment of Field Deployed Electronics Using X-Ray Micro-CT Based Digital Volume Correlation and Finite-Element Analysis," 2016 IEEE 66th Electronic Components and Technology Conference (ECTC), pp. 1583-1592. Las Vegas, NV
75. B. Zhaowei, Q. Fei, A. Tong, X. Guofeng and L. Chengyan, , 2011"Influence of interfacial delamination on temperature distribution of QFN packages," 2011 12th International Conference on Electronic Packaging Technology and High Density Packaging, , pp. 1-4. , Shanghai
76. S. Abdullah, M. F. Abdullah and A. K. Arifin, 2007"Fatigue Test Method for Observing the Delamination Effect in a QFN Package," 2007 9th Electronics Packaging Technology Conference, Singapore, pp. 670-674.
77. M. Wu and C. Wang,2018 "Effects of Moisture and Temperature on Quad Flat No-lead (QFN) Package," 2018 20th International Conference on Electronic Materials and Packaging (EMAP), pp. 1-2, Clear Water Bay, Hong Kong
78. J. Lau, S. Erasmus and S. Pan,2002 "Effects of voids on bump chip carrier (BCC++) solder joint reliability," 52nd Electronic Components and Technology Conference 2002. (Cat. No.02CH37345), pp. 992-1000. San Diego, CA, USA
79. Qiang Yu, T. Shibutani, Y. Kobayashi and M. Shiratori,2006 "The Effect of Voids on Thermal Reliability of BGA Lead Free Solder Joint and Reliability Detecting Standard," Thermal and Thermomechanical Proceedings 10th Intersociety Conference on Phenomena in Electronics Systems, 2006. ITHERM 2006., 2006, pp. 1024-1030. San Diego, CA

80. L. J. Ladani and A. Dasgupta,2006, "The Successive-Initiation Modeling Strategy for Modeling Damage Progression: Application to Voided Solder Interconnects," EuroSime 2006 - 7th International Conference on Thermal, Mechanical and Multiphysics Simulation and Experiments in Micro-Electronics and Micro-Systems, Como, 2006, pp. 1-6.
81. A. Deshpande, H. Kaeser and A. Dasgupta,2019 "Effect of Stress State on Fatigue Characterization of SAC305 Solder Joints," 2019 20th International Conference on Thermal, Mechanical and Multi-Physics Simulation and Experiments in Microelectronics and Microsystems (EuroSimE), pp. 1-3. Hannover, Germany
82. Do-Seop Kim, Qiang Yu, T. Shibutani, N. Sadakata and T. Inoue,2004 "Effect of void formation on thermal fatigue reliability of lead-free solder joints," The Ninth Intersociety Conference on Thermal and Thermomechanical Phenomena In Electronic Systems (IEEE Cat. No.04CH37543), pp. 325-329 Vol.2. Las Vegas, NV, USA
83. P. Lall, S. Deshpande, N. Kothari, J. Suhling and L. Nguyen, 2018"Effect of Thermal Cycling on Reliability of QFN Packages," 2018 17th IEEE Intersociety Conference on Thermal and Thermomechanical Phenomena in Electronic , San Diego, CA
84. B. Vandevelde, G. Willems,2012 "Early fatigue failures in copper wire bonds inside packages with low CTE green mold compounds", 2012 4th Electronic System-Integration Technology Conference, pp. 1-4,
85. P. Lall, N. Islam, J. Suhling and R. Darveaux,2003 "Model for BGA and CSP reliability in automotive underhood applications," 53rd Electronic Components and Technology Conference, 2003. Proceedings., pp. 189-196.

86. M. M. Basit, M. Motalab, J. C. Suhling and P. Lall,2014 "The effects of aging on the Anand viscoplastic constitutive model for SAC305 solder," Fourteenth Intersociety Conference on Thermal and Thermomechanical Phenomena in Electronic Systems (ITherm), pp. 112-126. Orlando, FL

87. IPC-A-610 Standard https://www.ipc.org/4.0_Knowledge/4.1_Standards/IPC-A-610E-redline-April-2010.pdf

88. Q.M. Li, 2001,"Strain energy density failure criterion,International Journal of Solids and Structures,Volume 38, Issues 38–39,Pages 6997-7013,ISSN 0020-7683

89. R. Darveaux, 2000, "Effect of simulation methodology on solder joint crack growth correlation," Proceedings. 50th Electronic Components and Technology Conference (Cat. No.00CH37070), Las Vegas, NV, USA, 2000, pp. 1048-1058.